

UNCLASSIFIED

in the report

2

ORT DOCUMENTATION PAGE

AD-A200 232

TC

DECLASSIFICATION/DOWNGRADING SCHEDULE

PERFORMING ORGANIZATION REPORT NUMBER 2 1988

1b. RESTRICTIVE MARKINGS

3. DISTRIBUTION/AVAILABILITY OF REPORT
Approved for Public Release;
Distribution Unlimited

5. MONITORING ORGANIZATION REPORT NUMBER(S)

AFOSR-TR- 88-1029

6a. NAME OF PERFORMING ORGANIZATION
UNIVERSITY OF ARIZONA

6b. OFFICE SYMBOL
(If applicable)

7a. NAME OF MONITORING ORGANIZATION

AFOSR/NA

6c. ADDRESS (City, State and ZIP Code)

DEPT. OF CIVIL ENGR. & ENGR. MECHANICS
TUCSON, AZ 85721

7b. ADDRESS (City, State and ZIP Code)

Bldg 416
Bolling AFB, DC 20332-6448

8a. NAME OF FUNDING/SPONSORING
ORGANIZATION AIR FORCE

8b. OFFICE SYMBOL
(If applicable)

9. PROCUREMENT INSTRUMENT IDENTIFICATION NUMBER

OFFICE OF SCIENTIFIC RESEARCH

AFOSR/NA

AFOSR-83-0256

6c. ADDRESS (City, State and ZIP Code)

BOLLING AFB, DC 20332

10. SOURCE OF FUNDING NOS.

PROGRAM
ELEMENT NO.

PROJECT
NO.

TASK
NO.

WORK UNIT
NO.

61102F

2302

11. TITLE (Include Security Classification) CONSTITUTIVE MODELLING
OF JOINTS UNDER CYCLIC LOADING (UNCLASSIFIED)

12. PERSONAL AUTHOR(S)

DESAI, C. S., FISHMAN, K. L., MA, Y., RIGBY, D., KUNDU, T. AND WANG, G.

13a. TYPE OF REPORT

13b. TIME COVERED

14. DATE OF REPORT (Yr., Mo., Day)

15. PAGE COUNT

FINAL-PARTS 1 TO 4

FROM 8/83 TO 7/88

1988, JULY 31

360

16. SUPPLEMENTARY NOTATION PART 2: FURTHER DEVELOPMENT OF HIERARCHICAL PLASTICITY MODEL FOR JOINTS
PART 3: CYCLIC MULTI DEGREE-OF-FREEDOM SHEAR DEVICE WITH PORE WATER PRESSURE.
PART 4: DEVELOPMENT OF SIMULATED ROCK LIKE MATERIAL AND TESTING.

17. COSATI CODES

FIELD GROUP SUB. GR.

18. SUBJECT TERMS (Continue on reverse if necessary and identify by block number)

Constitutive Modeling, Cyclic Loading, Rock Joints,
Testing

19. ABSTRACT (Continue on reverse if necessary and identify by block number)

The research envisages development of constitutive models for joints in rock subjected to cyclic loading. The final objective is to evolve rational models from basic principles so as to obtain realistic and reliable results from solution procedures such as computational methods for dynamics problems involving blast and earthquake type loadings. Behavior of joints under cyclic loading is influenced by a number of factors such as normal and shear stresses and displacements (strains), roughness and asperities, number of loading cycles and effect of fluid pressures. Hence, in addition to consideration of basic mechanics for developing constitutive models, it is essential to develop and use new laboratory test devices that can simulate various factors that influence the behavior.

(CONTINUED ON REVERSE SIDE)

20. DISTRIBUTION/AVAILABILITY OF ABSTRACT

UNCLASSIFIED/UNLIMITED ☒ SAME AS RPT. ☐ DTIC USERS ☐

21. ABSTRACT SECURITY CLASSIFICATION

Unclassified

22a. NAME OF RESPONSIBLE INDIVIDUAL

SPENCER T WU

22b. TELEPHONE NUMBER
(Include Area Code)

(202) 767-6962

22c. OFFICE SYMBOL

AFOSR/NA

DD FORM 1473, 83 APR

EDITION OF 1 JAN 73 IS OBSOLETE.

88 1011 285

UNCLASSIFIED

19 - (Continued)

An hierarchical constitutive model based on the plasticity theory is developed and verified with respect to a comprehensive series of laboratory tests including the above factors. The Cyclic Multi-Degree-of-Freedom shear (CYMDOF) device is used to perform the laboratory tests on simulated joints in concrete with different roughness and asperities. The constitutive models developed allow for associative, nonassociative, directional anisotropy and damage characteristics of joints. They represent a new and unique modelling approach for characterizing behavior of discontinuities in general, and joints in particular. The CYMDOF device is modified to incorporate fluid pressures at joints, and a new simulated rock-like material is developed for future testing of joints so as to allow measurements of deformation and damage with greater accuracy than for the concrete joints.

The research results can provide enhanced understanding of the complex mechanical response of joints under dynamic loadings, and new directions for constitutive modelling of the response. Although further research is needed for additional factors, the models developed in this research can simulate static, quasi-static and cyclic behavior of joints with associative and nonassociative characteristics. The models can be implemented in (numerical) solution procedures for realistic and economical solutions of dynamic problems of interest to the Air Force.

FINAL REPORT: PART 1
CONSTITUTIVE MODELLING OF JOINTS
UNDER CYCLIC LOADING

Approved for public release;
distribution unlimited.

PART 1: MODELLING AND TESTING OF IDEALIZED ROCK JOINTS

AIR FORCE OFFICE OF SCIENTIFIC RESEARCH (AFOSR)
NOTED FOR REVIEW AND APPROVAL OF THE
IT IS REQUESTED THAT THE REPORT BE REVIEWED AND IS
APPROVED FOR RELEASE UNDER AFR 190-12.
DISTRIBUTION IS UNLIMITED.
MATTHEW J. KERPER
Chief, Technical Information Division

Submitted to
Air Force Office of Scientific Research (AFOSR)
Bolling AFB, D. C. 20332
Grant No. AFOSR 830256

Department of Civil Engineering and Engineering Mechanics
University of Arizona
Tucson, Arizona 85721

July 1988

PREFACE

This final report containing research supported by Grant No. 830256 from the Air Force Office of Scientific Research (AFOSR), Bolling AFB, Washington, D. C., consists of four parts: Part 1: Modelling and Testing of Idealized Rock Joints; Part 2: Further Development of Hierarchical Plasticity Model for Joints; Part 3: Cyclic Multi-Degree-of-Freedom Shear Device with Pore Water Pressure; and Part 4: Development of Simulated Rock Like Material and Testing. Previous Progress and Interim Reports were submitted in April 1984, September 1985, January 1986, October 1986 and February 1987. Dr. C. S. Desai acted as the principal investigator at the University of Arizona, Tucson, and the project was monitored by Dr. Spencer Wu and Col. L. D. Hokanson at AFOSR. A number of individuals contributed towards the research results and preparation of these reports: Dr. C. S. Desai, Dr. K. L. Fishman, Mr. Y. Ma, Mr. D. Rigby, Dr. T. Kundu and Mr. S. Wang. Part 1 is based on Dr. Fishman's doctoral dissertation; Part 2 is based on the ongoing doctoral research of Mr. Ma; Part 3 is based on the ongoing Master's and doctoral research of Mr. Rigby, which is also partly supported from a grant from the NSF; and Part 4 is based on the Master's research of Mr. Wang, which is guided by Dr. Desai and Dr. T. Kundu.

Accession No.	
NTIS	✓
DTIC	□
Unannounced	□
Justification	
By	
Date	
Approved	
Date	
A-1	

TABLE OF CONTENTS

	Page
LIST OF ILLUSTRATIONS	viii
LIST OF TABLES	xviii
ABSTRACT	xix
CHAPTER	
1. INTRODUCTION	1
Relevance of Joint Constitutive Matrix	5
Procedure	6
Scope of Research	7
2. LITERATURE REVIEW	9
Rock Joint Testing	9
Failure Models	19
Models for Deformation of Rock Joints	33
3. DESCRIPTION OF TEST DEVICE	39
Upper and Lower Sample Holders	39
Securing Samples to Sample Holders	43
Rail System	47
Load Frame	50
Load System	53
Control System	55
Measurement of Test Variables	57
Vertical and Horizontal Loads	57
Horizontal Displacement	59
Vertical Displacements	59
Outside Front and Back LVDT's	60
Inside Front and Back Displacement Sensors	60
Inductance Coils	60
Data Acquisition System	65
Assembly of Device	67

TABLE OF CONTENTS--Continued

	Page
4. CALIBRATION OF INSTRUMENTS	70
Inductance Coils	71
Linearity of Meter Deflection	74
Precision	78
Effects on Calibration	78
Misalignment	78
Rotations	88
Surrounding Metal	88
5. DESCRIPTION OF SAMPLES	93
Forms	93
Method of Casting	96
Concrete and Grout Mixes	101
6. DESCRIPTION OF TEST SERIES	111
Purpose of Test Series	111
Details of Test Series	111
Normal Stress Tests	112
Method	112
Load Increments	112
Factors	113
Quasi-Static Shear Tests	113
Cycle of Displacement	113
Method	116
Factors	118
Damage	118
Multiple Tests With One Sample	118
Fast Cyclic Tests	120
Displacement Cycle	123
Method	126
Factors	126
Damage	126
Effects on Cyclic Shear Behavior	126
Multiple Tests With One Sample	131
Summary of Test Program	131
7. DESCRIPTION OF PLASTICITY MODEL	135
Specialization of a 3-D Generalized Model	136

TABLE OF CONTENTS--Continued

	Page
Analogies	137
Analogies for Yield Function	138
Analogies for Growth Function	140
Mathematical Specialization	143
Nonassociativeness	145
Elastic-Plastic Constitutive Matrix	146
Load Reversal	147
Displacement Induced Anisotropy	147
Gouge and Damage	151
Application of Plasticity Model to Cyclic Loading . .	151
Cyclic Hardening	153
Parameters	153
Elastic Constants	156
Parameters for Yield Function	156
Ultimate Parameters	156
Parameter n	159
Growth Function	159
Nonassociative Parameter	164
Load Reversal	166
Yield and Growth Function	166
Cyclic Loading	167
Summary	168
8. BACK PREDICTIONS	169
Quasi-Static Loading	169
Determination of Parameters	169
Ultimate Parameter γ	170
Phase Change Parameter n	170
Growth Function Parameters	174
Nonassociative Parameter κ	177
Back Predictions of Quasi-Static Loading	177
Algorithm	178
Results	179
Average Parameters	186
Quasi-Static Loading With Unloading and Load Reversal . .	186
Determination of Parameters	190
Back Predictions of Quasi-Static Loading	
With Unloading and Load Reversal	194
Algorithm	194
Results	194

TABLE OF CONTENTS--Continued

	Page
Cyclic Shear	200
Determination of Parameters	202
Ultimate Parameter γ	202
Phase Change Parameter n	206
Growth Function Constants	206
Nonassociative Parameter κ	209
Back Predictions of Cyclic Shear Tests	218
Algorithm	218
Results	221
9. SUMMARY, CONCLUSIONS, AND RECOMMENDATIONS	228
Summary	228
Conclusions	229
Recommendations	230
APPENDIX I: DERIVATION OF K^{ep} MATRIX	232
APPENDIX II: BACK PREDICTION FIGURES	236
APPENDIX III: COMPUTATIONS FOR κ	276
LIST OF REFERENCES	280

LIST OF ILLUSTRATIONS

Figure	Page
1-1. Typical Problems Involving Jointed Rock Masses	2
1-2. Degrees of Freedom for Rock Joints	4
2-1. Schematic Diagram of Rotary Shear Machine [Kutter (1974)]	14
2-2. Schematic of Direct Shear Apparatus [Martin and Miller (1974)]	15
2-3. Portable Shear Device [Ross-Brown and Walton (1975)]	18
2-4. Device by Goodman and Ohnishi (1973)	20
2-5. Dynamic Direct Shear Apparatus [Gould (1982), Gillette (1983)]	21
2-6. Schematic of Peak and Residual Shear Strengths	24
2-7. Peak and Residual Strengths Envelopes	25
2-8. Empirical Shear Strength Curve [Jaeger (1971)]	26
2-9. Inclined Joint	28
2-10. Model by Patton (1966)	29
2-11. Barton's Model (1973)	31
2-12. Shear Strength Relation for Rough Joints [Ladanyi and Archambault (1970)]	32
2-13. Data from Hypothetical Direct Shear Test on a Rock Joint [Goodman et al. (1968)]	34
2-14. Capped Plasticity Model for Joints [DiMaggio and Sandler (1971), Ghaboussi et al. (1973)]	36
3-1. Picture of Shear Device	40
3-2a. Upper Sample Holder	41

LIST OF ILLUSTRATIONS--Continued

Figure	Page
3-2b. Lower Sample Holder	42
3-3. Schematic of "Burke Stone" Plugs Used to Secure Samples to Holders	45
3-4. Setting of Upper Sample Holder to Upper Sample	46
3-5. Placement of Lower Sample Into Lower Sample Holder	48
3-6. Determination of Angle of an Asperity Trough With Respect to the Rear Edge of the Upper Sample Holder	49
3-7. Load Frame Containing Horizontal and Vertical Force Actuators	51
3-8. Detail of Rail System for Guiding Motion of Upper Sample	52
3-9. Schematic of Load System	54
3-10. Schematic of Control System (Drumm, 1983)	56
3-11. Placement of Instruments	58
3-12a. Pictorial Diagram of Soil Strain Gage (Truesdale and Anderson, 1964)	61
3-12b. Block Diagram of Soil Strain Gage (Truesdale and Anderson)	62
3-13. Bison Model #4101A Soil Strain Indicator	64
4-1. Calibration Instrument for Inductance Coils	72
4-2a. Typical Bison Gage Spacing Calibration Curve	75
4-2b. Typical Bison Gage Meter Deflection Calibration Curve	76
4-3. Misalignment of Inductance Coils	80
4-4. Vertical Offset Caliper	82

LIST OF ILLUSTRATIONS--Continued

Figure	Page
4-5a. Effect of Coil Misalignment on Spacing Calibration	83
4-5b. Effect of Coil Misalignment on Meter Calibration - Case 1	84
4-6. Bison Gages Surrounded by Metal Sample Holder During Testing	89
4-7. Bison Gages Within the Confines of the Upper Sample Holder	90
5-1. Sawtooth Shaped Asperity Pattern	94
5-2. Forms for Casting Concrete Samples	95
5-3a. Sketch of Top Sample Geometry	97
5-3b. Sketch of Bottom Sample Geometry	98
5-4. Casting of Bottom Samples	99
5-5. Casting of Top Samples	100
5-6. Vibration Table Used for Compaction of Concrete Near the Structured Surface of the Bottom Sample . . .	102
5-7. Typical Sample After Cleaning	103
5-8. Gradation Curve for Sand and Aggregate Used in Mix Design	105
5-9a. σ - ϵ Curve for Concrete Mix	109
5-9b. σ - ϵ Curve for Grout Mix	110
6-1. Normal Stress Versus Vertical Displacement From a Typical Normal Stress Test	114
6-2a. Waveform From Function Generator for Quasi-Static Tests	115
6-2b. Motion of Upper Sample Due to Input Function of Fig. 6-2(a)	117
6-3. Typical Results for Quasi-Static Test	119

LIST OF ILLUSTRATIONS--Continued

Figure		Page
6-4.	Comparison of Results From a Quasi-Static Shear Test On a Fresh Sample and a Sample Previously Subjected to 500 Cycles of Displacement	121
6-5.	Comparison of Results From Two Quasi-Static Shear Tests On the Same Sample With Debris Cleaned From the Shear Surface Between Tests	122
6-6a.	Waveform From Function Generator for Cyclic Tests	124
6-6b.	Motion of Upper Sample Due to the Input Function of Fig. 6-6(a)	125
6-7.	Typical Results for a Cyclic Test	127
6-8a.	Comparison of Results From a Quasi-Static Test On a Fresh Sample (Case 1) and the First Cycle From a Cyclic Test On a Fresh Sample (Case 2)	129
6-8b.	Comparison of Results From a Quasi-Static Test Performed After a Cyclic Test (Surfaces Not Cleaned (Case 3) and the Last Cycle of a Cyclic Test (Case 4)	130
7-1.	Typical Plot of the Yield Function	141
7-2.	Comparison of Results From a Hydrostatic Compression Test and a Normal Stress Test	142
7-3.	Right-Handed Coordinate System of Joint Plane	144
7-4.	Failure Envelope for Inclined Surface	149
7-5.	Collapse of Yield Surface During Unloading	150
7-6.	Shift in Yield Surface Between Phases 2 and 3 and Phases 4 and 1	154
7-7.	Overriding Asperities	155
7-8.	k_s as Unloading Portion of τ vs. u_r	157

LIST OF ILLUSTRATIONS--Continued

Figure	Page
7-9. k_n as Initial Portion of σ_n versus u_r	158
7-10. Ultimate Shear Stress	160
7-11. Determination of γ from Best Fit Line of τ_u versus σ_n	161
7-12. Point of Phase Change	162
7-13. Determination of M_{zs} from Plot of σ_n versus τ_{zs}	163
7-14. α versus ξ	165
8-1. Ultimate Envelope; Quasi-Static Test Series; Forward Pass; 9° Surface	172
8-2. Phase Change Envelope; 9° Surface	173
8-3. α versus ξ ; Quasi-Static Test Series; 9° Surface	176
8-4. Test Data and Back Predictions of τ versus u_r ; Quasi-Static Loading; 9° Surface	180
8-5. Test Data and Back Predictions of v_r versus u_r ; Quasi-Static Loading; $\sigma_n = 5$ psi; 9° Surface; Associative and Nonassociative Case	181
8-6. Test Data and Back Predictions of v_r versus u_r ; Quasi-Static Loading; $\sigma_n = 10$ psi; 9° Surface; Associative and Nonassociative Case	182
8-7. Test Data and Back Predictions of v_r versus u_r ; Quasi-Static Loading; $\sigma_n = 20$ psi; 9° Surface; Associative and Nonassociative Case	183
8-8. Test Data and Back Predictions of v_r versus u_r ; Quasi-Static Loading; $\sigma_n = 50$ psi; 9° Surface; Associative and Nonassociative Case	184
8-9. Test Data and Back Predictions of τ versus u_r ; Quasi-Static Loading; Average Parameters; 9° Surface; Nonassociative Case	187

LIST OF ILLUSTRATIONS--Continued

Figure	Page
8-10. Test Data and Back Predictions of v_r versus u_r ; Quasi-Static Loading; Average Parameters; 9° Surface; $\sigma_n = 5$ psi; Nonassociative Case	188
8-11. Test Data and Back Predictions of v_r versus u_r ; Quasi-Static Loading; Average Parameters; 9° Surface; $\sigma_n = 50$ psi; Nonassociative Case	189
8-12. Ultimate Envelope; Reverse Pass, 9° Surface	192
8-13. α versus ξ ; Reverse Pass; 9° Surface	193
8-14. Test Data and Back Predictions of τ versus u_r ; Quasi-Static Tests with Unloading and Load Reversal; 9° Surface	195
8-15. Test Data and Back Predictions of v_r versus u_r ; Quasi-Static Tests with Unloading and Load Reversal; 9° Surface; $\sigma_n = 5$ psi; Associative and Nonassociative Cases	196
8-16. Test Data and Back Predictions of v_r versus u_r ; Quasi-Static Tests with Unloading and Load Reversal; 9° Surface; $\sigma_n = 10$ psi; Associative and Nonassociative Cases	197
8-17. Test Data and Back Predictions of v_r versus u_r ; Quasi-Static Tests with Unloading and Load Reversal; 9° Surface; $\sigma_n = 20$ psi; Associative and Nonassociative Cases	198
8-18. Test Data and Back Predictions of v_r versus u_r ; Quasi-Static Tests with Unloading and Load Reversal; 9° Surface; $\sigma_n = 50$ psi; Associative and Nonassociative Cases	199
8-19. Ultimate Envelopes from Cyclic Test Results at Different Cycles of Displacement (N) for Phases 1 and 3; 9° Surface	204
8-20. γ versus N from Cyclic Test Results; Phases 1 and 3; 9° Surface	205

LIST OF ILLUSTRATIONS--Continued

Figure	Page
8-21. Ultimate Envelope; Phases 2 and 4; Cyclic Tests; 9° Surface; $N = 1$	207
8-22. α versus ξ ; Phase 1; Cycle 1. Cyclic Test; 9° Surface; $\sigma_n = 20$ psi	211
8-23. α versus ξ ; Phase 3; Cycle 1. Cyclic Test; 9° Surface; $\sigma_n = 20$ psi	212
8-24. α versus ξ ; Phases 1 and 3, Cycle 10. Cyclic Test; 9° Surface; $\sigma_n = 20$ psi	213
8-25. α versus ξ ; Phases 1 and 3; Cycle 100. Cyclic Test; 9° Surface; $\sigma_n = 20$ psi	214
8-26. α versus ξ ; Phases 2 and 4; Cycle 1. Cyclic Test; 9° Surface; $\sigma_n = 20$ psi	215
8-27. α versus ξ ; Phases 2 and 4; Cycle 10. Cyclic Test; 9° Surface; $\sigma_n = 20$ psi	216
8-28. α versus ξ ; Phases 2 and 4; Cycle 100. Cyclic Test; 9° Surface; $\sigma_n = 20$ psi	217
8-29. Back Predictions; Cyclic Test; τ versus u_r ; 9° Surface; $\sigma_n = 20$ psi	222
8-30. Test Data and Back Prediction; τ versus u_r ; Cyclic Test; 9° Surface; $\sigma_n = 20$ psi; Cycle 1	223
8-31. Test Data and Back Prediction; τ versus u_r ; Cyclic Test; 9° Surface; $\sigma_n = 20$ psi; Cycle 10	224
8-32. Test Data and Back Predictions; τ versus u_r ; Cyclic Test; 9° Surface; $\sigma_n = 20$ psi; Cycle 100	225
8-33. Test Data and Back Predictions; v_r versus u_r ; Cyclic Test; 9° Surface; $\sigma_n = 20$ psi	226

LIST OF ILLUSTRATIONS--Continued

Figure		Page
II-1.	Ultimate Envelope; Quasi-Static Test Series; Forward Pass; Flat Surface	237
II-2.	Ultimate Envelope; Quasi-Static Test Series; Forward Pass; 5° Surface	238
II-3.	Ultimate Envelope; Quasi-Static Test Series; Forward Pass; 7° Surface	239
II-4.	Phase Change Envelope; 5° Surface	240
II-5.	Phase Change Envelope; 7° Surface	241
II-6.	α versus ξ ; Quasi-Static Test Series; Flat Surface . . .	242
II-7.	α versus ξ ; Quasi-Static Test Series; 5° Surface	243
II-8.	α versus ξ ; Quasi-Static Test Series; 7° Surface	244
II-9.	Test Data and Back Predictions of τ versus u_r ; Quasi-Static Loading; Flat Surface	245
II-10.	Test Data and Back Predictions of τ versus u_r ; Quasi-Static Loading; 5° Surface	246
II-11.	Test Data and Back Predictions of τ versus u_r ; Quasi-Static Loading; 7° Surface	247
II-12.	Test Data and Back Predictions of v_r versus u_r ; Quasi-Static Loading; Flat Surface; Associative Case	248
II-13.	Test Data and Back Predictions of v_r versus u_r ; Quasi-Static Loading; Flat Surface; Nonassociative Case	249
II-14.	Test Data and Back Predictions of v_r versus u_r ; Quasi-Static Loading; $\sigma_n = 5$ psi; 5° Surface; Associative and Nonassociative Case	250
II-15.	Test Data and Back Predictions of v_r versus u_r ; Quasi-Static Loading; $\sigma_n = 10$ psi; 5° Surface; Associative and Nonassociative Case	251

LIST OF ILLUSTRATIONS--Continued

Figure		Page
II-16.	Test Data and Back Predictions of v_r versus u_r ; Quasi-Static Loading; $\sigma_n = 20$ psi; 5° Surface; Associative and Nonassociative Case	252
II-17.	Test Data and Back Predictions of v_r versus u_r ; Quasi-Static Loading; $\sigma_n = 50$ psi; 5° Surface; Associative and Nonassociative Case	253
II-18.	Test Data and Back Predictions of v_r versus u_r ; Quasi-Static Loading; $\sigma_n = 5$ psi; 7° Surface; Associative and Nonassociative Case	254
II-19.	Test Data and Back Predictions of v_r versus u_r ; Quasi-Static Loading; $\sigma_n = 10$ psi; 7° Surface; Associative and Nonassociative Case	255
II-20.	Test Data and Back Predictions of v_r versus u_r ; Quasi-Static Loading; $\sigma_n = 20$ psi; 7° Surface; Associative and Nonassociative Case	256
II-21.	Test Data and Back Predictions of v_r versus u_r ; Quasi-Static Loading; $\sigma_n = 50$ psi; 7° Surface; Associative and Nonassociative Case	257
II-22.	Test Data and Back Predictions of τ versus u_r ; Quasi-Static Loading; Average Parameters; Flat Surface	258
II-23.	Test Data and Back Predictions of τ versus u_r ; Quasi-Static Loading; Average Parameters; 5° Surface; Nonassociative Case	259
II-24.	Test Data and Back Predictions of τ versus u_r ; Quasi-Static Loading; Average Parameters; 7° Surface; Nonassociative Case	260
II-25.	Test Data and Back Predictions of v_r versus u_r ; Quasi-Static Loading; Average Parameters; Flat Surface; Nonassociative Case	261
II-26.	Test Data and Back Predictions of v_r versus u_r ; Quasi-Static Loading; Average Parameters; 5° Surface; $\sigma_n = 5$ psi; Nonassociative Case	262

LIST OF ILLUSTRATIONS--Continued

Figure		Page
II-27.	Test Data and Back Predictions of v_r versus u_r ; Quasi-Static Loading; Average Parameters; 5° Surface; $\sigma_n = 50$ psi; Associative Case	263
II-28.	Test Data and Back Predictions of v_r versus u_r ; Quasi-Static Loading; Average Parameters; 7° Surface; $\sigma_n = 5$ psi; Nonassociative Case	264
II-29.	Test Data and Back Predictions of v_r versus u_r ; Quasi-Static Loading; Average Parameters; 7° Surface; $\sigma_n = 50$ psi; Nonassociative Case	265
II-30.	Back Predictions; Cyclic Test; τ versus u_r ; 9° Surface; $\sigma_n = 5$ psi	266
II-31.	Test Data and Back Predictions; τ versus u_r ; Cyclic Test; 9° Surface; $\sigma_n = 5$ psi; Cycle 1	267
II-32.	Test Data and Back Predictions; τ versus u_r ; Cyclic Test; 9° Surface; $\sigma_n = 5$ psi; Cycle 10	268
II-33.	Test Data and Back Predictions; τ versus u_r ; Cyclic Test; 9° Surface; $\sigma_n = 5$ psi; Cycle 100	269
II-34.	Back Predictions; Cyclic Test; τ versus u_r ; 9° Surface; $\sigma_n = 10$ psi	270
II-35.	Test Data and Back Predictions; τ versus u_r ; Cyclic Test; 9° Surface; $\sigma_n = 10$ psi; Cycle 1	271
II-36.	Test Data and Back Predictions; τ versus u_r ; Cyclic Test; 9° Surface; $\sigma_n = 10$ psi; Cycle 10	272
II-37.	Test Data and Back Predictions; τ versus u_r ; Cyclic Test; 9° Surface; $\sigma_n = 10$ psi; Cycle 100	273
II-38.	Test Data and Back Predictions; v_r versus u_r ; Cyclic Test; 9° Surface; $\sigma_n = 5$ psi	274
II-39.	Test Data and Back Predictions; v_r versus u_r ; Cyclic Test; 9° Surface; $\sigma_n = 10$ psi	275

LIST OF TABLES

Table	Page
4-1. Check on Linearity of Meter Deflection	77
4-2. Verification of Precision of Bison Soil Strain Gage . . .	79
4-3. Comparison of Meter Calibration with Coils Aligned and Misaligned	87
4-4. Comparison of Bison Gage Calibration in the Absence of and Surrounded by Metal Sample Holders	91
5-1. Concrete and Grout Mixes	104
5-2a. Twenty-Eight Day Unconfined Compressive Strength Test Results for Concrete Mixes	107
5-2b. Twenty-Eight Day Unconfined Compressive Strength Test Results for Grout Mixes	108
6-1. Summary of Test Program	132
7-1. Analogous Quantities	139
8-1. Summary of Parameters Obtained From Different Surfaces for the Case of Quasi-Static Loading	171
8-2. Value of n Determined For Each Surface	175
8-3. Summary of Parameters for Reverse Pass, 9° Surface	191
8-4. Parameters for Back Prediction of Cyclic Tests	203
8-5. Growth Function Constants Determined for Cycles of Displacement; 9° Surface, $\sigma_n = 20$ psi	210
III-1. Determination of κ ; Quasi-Static Test Series, Forward Pass	277
III-2. Determination of κ ; Reverse Pass; 9° Surface	278
III-3. Determination of κ ; Cyclic Test; 9° Surface; $\sigma_n = 20$ psi	279

ABSTRACT

A rather novel plasticity based constitutive model to describe the response of simulated (rock) joints under cyclic, quasi-static and static shear is developed. Development of the constitutive model includes both mathematical formalization based on the hierarchical approach and laboratory testing. The mathematical formulation is such that the model is basic and general and is capable of predicting observed behavior of joints. Laboratory test results are used ^{for determining} for the determination of parameters for the model, and ^{for comparison} for comparison with model predictions.

The constitutive model is based on the theory of incremental plasticity. A generalized three-dimensional plasticity model capable of predicting the behavior of geologic solid material such as soil and rock is specialized to describe the behavior of individual rock joints. At this time, the model allows for effects of initial normal stress, states of shear and normal stress, plastic hardening, nonassociativeness, volume changes at joints, and cycles of loading, unloading and reverse loading.

The test program was conducted on simulated joints. The simulated specimens were cast in concrete with a variety of surface geometries (angles of asperities). Specimens were subjected to a series of quasi-static and fast cyclic direct shear tests. Tests were performed with a special device known as the Cyclic Multi-Degree-of-Freedom (CYMDOF) shear device; minor modifications of the device were necessary for the testing of joints. Quasi-static tests included shear loading, unloading and

reverse loading, and fast cyclic tests repeated cycles of shear loading at the frequency of 1.0 Hz. Tests were conducted under different levels of normal stress and amplitudes of cyclic displacement.

The constants for elastic and inelastic responses were found from the laboratory test data. Then typical observed results were predicted by integrating the incremental plasticity equations which were expressed in terms of the constants. The predictions, in general, were found to provide satisfactory correlation with the observations.

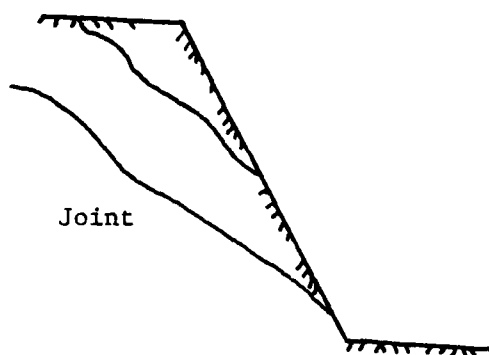
The results of this research have demonstrated that the model described herein is capable of capturing many aspects of rock joint behavior during quasi-static and cyclic shear loading. The model is sufficiently simplified so that it can be easily implemented in numerical techniques such as the finite element method. Such computational procedures can be used to solve practical boundary value problems in rock mechanics involving static and dynamic loads.

CHAPTER 1

INTRODUCTION

This study is concerned with the response of idealized joints in rock masses subjected to quasi-static or cyclic loadings. The cyclic loading may be due to the propagation of stress waves during an earthquake or due to blast loads which can occur either above or below ground. Many times rock masses are considered to be composed of continuous solid material, i.e. discontinuities in the form of cracks (joints) are not considered to be present. This idealization may not be valid. Rock masses are seldom continuous, and discontinuities (joints) of the order of several feet to hundreds of feet long may be present throughout the rock mass, and may have a particular pattern or orientation. These joints may have been created in the rock mass due to a variety of tectonic processes including previous shear along faults during an earthquake which may create a state of stress such that tensile fracture of the rock mass along particular planes occurs. Also, joints may become present during the formation of the rock mass due to temperature gradients, etc.

Figure 1-1 presents some typical problems encountered in rock mechanics where the presence of joints in the rock mass may be significant. Slope stability analysis in rock masses involves the determination of critical planes of weakness (joints) along which sliding may occur, and then the determination of the state of stress along the joint to



a) Rock Slope

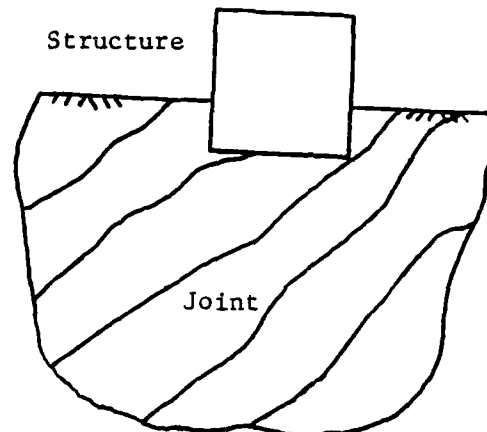
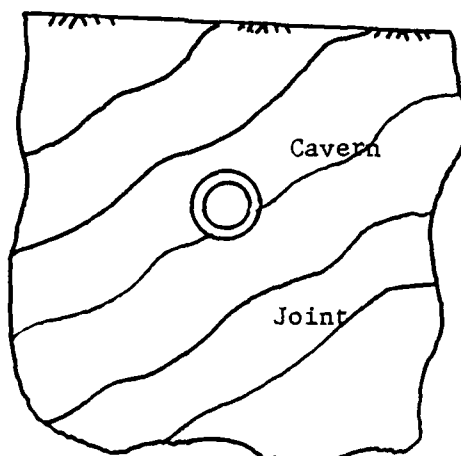
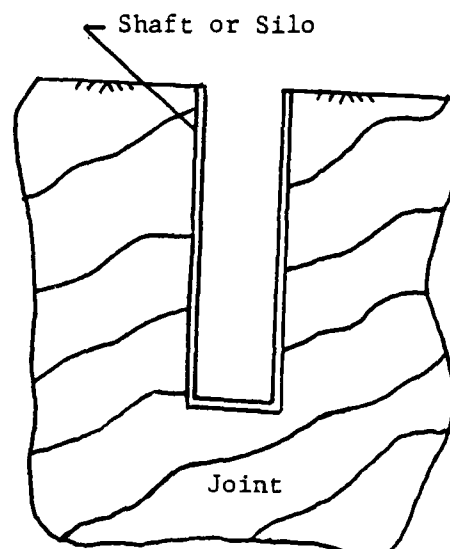
b) Structure Founded on
Jointed Rock Massc) Cavern Embedded in
Jointed Rock Massd) Shaft or Silo
Embedded in
Jointed Rock Mass

Figure 1-1. Typical Problems Involving Jointed Rock Masses

ascertain if failure is imminent. Structures may be founded on rock masses containing joints, and shafts or caverns may be constructed within jointed rock. The response of these systems to various excitation is an interaction type of problem in which the response of the structure is affected by the response of the medium and vice versa.

Analysis involving jointed rock masses may be sensitive to the properties of the individual rock joints (O'Conner et al., 1986). This is particularly true during cyclic loading conditions where relative motion along the joint plane may dissipate energy. An individual rock joint has several degrees-of-freedom, as shown in Figure 1-2. The joint is depicted as a zone of material with thickness, h , (1-2a). The joint may undergo compression or dilation, V_r , due to changes in normal stress across the joint plane, (1-2b). The joint may undergo relative tangential (shear) displacement, U_r , due to the application of shear stress across the joint plane, (1-2c), often accompanied by dilation or compression. Also, due to eccentricities, the joint may undergo rocking and experience a nonuniform distribution of normal stress, (1-2d). At some points the normal stress may become zero and separation of the joint plane may occur. Separation of the joint plane is known as debonding, and if the joint plane comes back into contact, rebonding occurs. Joint planes may undergo cycles of rebonding and debonding as described by Zaman (1982), Nagaraj (1986). In order to describe the behavior of rock joints properly, methods of analysis must consider as many of these modes of deformation as possible.

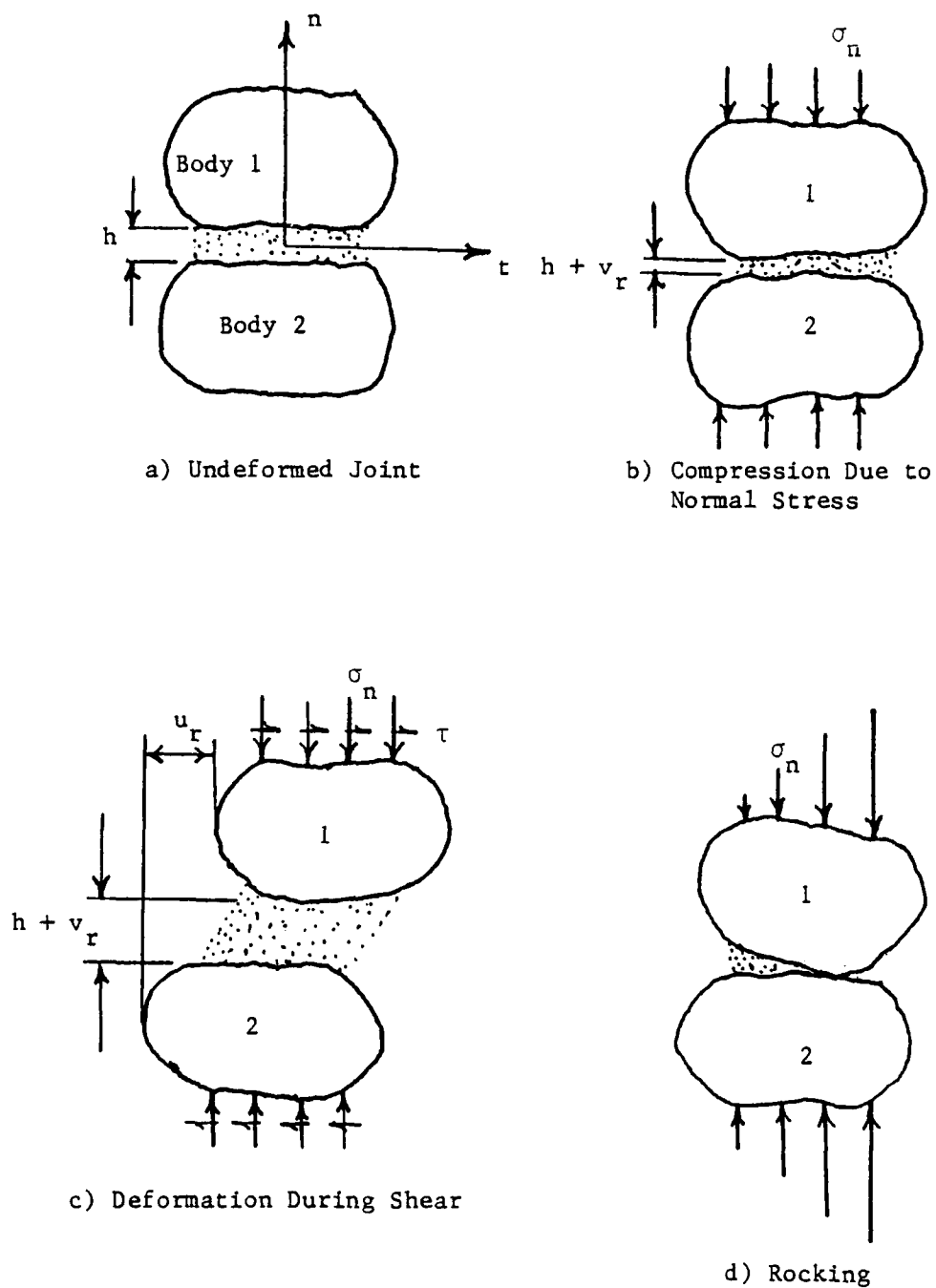


Figure 1-2. Degrees-of-Freedom for Rock Joints

The finite element method is a very versatile method which makes it possible to incorporate many of these factors in the analysis (Desai et al., 1982; Nagaraj, 1986). It is possible to utilize this method, and describe the behavior of the individual rock joints through the use of special joint elements. The joint elements can be based on the idea of the thin-layer element proposed by Desai et al. (1981, 1983a, 1984b). The formulation of these elements is similar to that of the solid elements. The joints are considered to consist of a thin zone of material, the properties of which are determined from appropriate laboratory tests. The joint properties are then described through a constitutive matrix which relates increments of stress to increments of strain. The relevance of the joint constitutive matrix within the framework of the finite element method will be described in the following section.

Relevance of Joint Constitutive Matrix

The governing matrix element equations for general dynamic problems are expressed as (Zienkiewicz, 1971; Desai and Abel, 1972; Bathe, 1982)

$$[m] \{\ddot{q}\} + [c] \{\dot{q}\} + [k] \{q\} = \{Q(t)\} \quad (1-1)$$

where $[m]$ is the global mass matrix, $[c]$ is the global damping matrix, $[k]$ is the global stiffness matrix, $\{q\}$ is the vector of nodal displacements, and $\{Q(t)\}$ is the assemblage nodal load vector which is a function of time. The overdot denotes derivative with respect to time.

Terms in the global stiffness matrix, $[k]$, involve contributions from both solid and joint elements. Joint element stiffness matrices are determined from the following relationship:

$$[k]_j = \int [B]^T [C]_j [B] dV \quad (1-2)$$

where $[k]_j$ is the joint element stiffness matrix, and $[B]$ is the strain-displacement transformation matrix in nonlinear incremental analysis, $[C]_j$ is the joint constitutive matrix relating increments of stress to increments of strain as follows:

$$\{d\sigma\} = [C]_j \{d\epsilon\} \quad (1-3)$$

where $\{d\sigma\}$ is the vector of components of stress increments, and $\{d\epsilon\}$ is the vector of components of strain increments. The development of the joint constitutive matrix is the focus of this research.

Procedure

The constitutive matrix, $[C]_j$, is obtained on the basis of appropriate constitutive laws. The main steps toward the development of appropriate constitutive relationships for a material are as follows (Desai and Siriwardane, 1984):

1. Mathematical formulation
2. Identification of significant parameters
3. Determination of parameters from laboratory tests and verification, which can involve the following two additional steps:

4. Successful prediction of a majority of observed data from which the parameters were determined, and of other test data under different stress paths
5. Satisfactory comparisons between predictions from a solution scheme in which the constitutive law is introduced, and observations or closed-form solutions for relevant practical boundary value problems.

In this investigation the procedure will be carried through the fourth step. Implementation of the model in a numerical (finite element) program will be done at a later time.

Scope of Research

The scope of the research performed in this investigation is as follows:

1. Perform a comprehensive series of tests on individual idealized rock joints. These tests will employ a special shear device known as CYMDOF (Cyclic Multi Degree-of-Freedom), (Desai, 1980a) which has undergone minor modification for rock joint testing.
2. Develop a constitutive model for rock joints during shear based on observations. The model must have physical meaning and obey physical laws.

3. Determine parameters for the model from the test data.
4. Verify the model by performing back predictions of the test data.

Chapter 2 of this report will provide a review of the literature in the area of rock joints. Chapters 3, 4, 5 and 6 provide details of the test program including descriptions of the device, instrumentation, calibration of instruments, preparation of samples, and the test series. Chapter 7 describes the proposed constitutive model, and Chapter 8 describes determination of parameters and back prediction of test data. Finally, Chapter 9 presents conclusions of the investigation.

CHAPTER 2

LITERATURE REVIEW

In this chapter a review will be made of existing literature pertaining to rock joints. The survey will be divided into three sections. The first section will review testing of rock joints. The remaining two sections will deal with modeling of rock joint behavior. Earlier work in this area dealt mainly with predicting slip across the joint plane with little attention paid to deformation of the joint plane; this research considers both in a single framework. Failure models described in section two are all that is necessary to perform analyses such as those based on limiting equilibrium where the main intention is to design against failure. The third and final section describes models developed to describe deformation of rock joints during shear. Development of deformation models is necessary to perform deformation analysis with such advanced techniques as the finite element method.

Rock Joint Testing

A review of various test methods for the study of rock joints, including laboratory and in situ techniques is available in Goodman (1974). The strength of rock joints is usually obtained in the laboratory on the basis of direct shear tests conducted under dry state of joints or drained conditions. Here a joint is subjected to a normal

stress and a shear stress is applied parallel to the plane of the joint. Some experimenters have employed the triaxial cell for the study of rock joint behavior. The following paragraphs discuss previous investigations and provide highlights of results obtained. The relevance of this discussion lies in the fact that the development of a constitutive model should be made on the basis of observed behavior. Although the model may not include all of these features, one should be made aware and be conscious of shortcomings inherent in a model.

Jaeger (1959) studied the frictional properties of rock joints by cutting rock cylinders at various angles to their axes and testing the cylinders in a triaxial apparatus. Different types of joints were created by filling the joints with commercial patching plaster, grinding the joint surfaces and placing them together, or creating natural shear surfaces. Jaeger found that the relationship between the shear stress at failure and normal stress may be nonlinear. Also, the coefficient of friction seems to vary with inclination of the joint.

Horn and Deere (1962) found that the presence of water increased the frictional resistance of smooth mineral surfaces having massive crystal structures, but that of minerals having layer lattice structures was reduced. However, the antilubricating effect on the crystal structured minerals is reduced as the surface roughness increases.

Byerlee (1967a) found that the coefficient of friction for rock joints varied with displacement and normal stress. Also, the effective stress principle was observed to hold for rock joints. In another investigation, Byerlee (1967b) proposed a theory which assumes that sliding

is initiated between surfaces as a result of brittle fracture of asperities.

Krsmanovic (1967) ran a series of direct shear tests on samples of sandstone, conglomerate and limestone in order to study the initial and residual strength of hard rock. Initially, the samples contained no joints or discontinuities, and it was found that the initial shear strength of the specimen was reached after very small deformations. At this point a sharp decrease in shear strength occurred as deformation continued along a developed shear plane. After large deformations, a residual shear strength was attained. It was found that the locus of points defining the residual shear strength of rock joints is linear with respect to normal stress and passes through the origin.

Locher (1968) developed an apparatus to determine the friction angle of rock joints subjected to a quasi-static shear load. Displacement normal to the joint plane was constrained. The device displaced the specimens in both forward and reverse directions, and the normal stress was allowed to vary throughout the test due to the tendency of the joint to compress or dilate. Locher found that the angle of friction for rock joints is in the range of that for parent media such as soil and rock, the difference in strength coming from a "cohesion" term in the failure criteria.

Locher and Rieder (1970) ran a series of quasi-static direct shear tests on discontinuities within Jurassic Limestone. Laboratory

tests with and without a filler material were performed, as well as in situ tests. The filler material decreased the friction angle by about three degrees, and the laboratory friction angles were about five degrees less than those determined in situ.

Coulson (1972) ran a series of quasi-static direct shear tests on flat rock surfaces having different "micro-roughnesses" due to grinding, polishing or sandblasting. Different types of surface damage were studied and correlated with observed variations of the coefficient of friction with displacement. The effects of water on the surfaces were also investigated. The initial coefficient of friction was observed to increase with an increase in "micro-roughness" and to decrease at higher levels of normal stress. At low levels of normal stress the residual shear strengths of rougher surfaces were higher, but as the normal stress was increased, the residual strength was essentially constant with respect to "micro-roughness."

Christensen et al. (1974) studied the dependency of the coefficient of friction for rock joints on the state of stress. A rotary shear apparatus was employed which could apply normal stress as well as confining pressure around the joint. For the same ratio of confining stress to normal stress, the coefficient of friction decreased, and the joint stiffness increased with increasing normal stress. By comparing the states of stress in joints during shear to the failure locus for intact material, it was postulated that the closer the state of stress on the rock joint during shear to the failure locus of the intact material, the higher the coefficient of friction for the joint.

Kutter (1974) developed a rotary shear apparatus in order to study the effect of large displacements on the shear strength of rock joints. A schematic of the device is given in Fig. 2-1. The device is displacement controlled, and the rotation is applied to the upper sample through a chain and sprocket assembly. The lower sample is prevented from rotating but is allowed to pitch and roll during shear, allowing full contact of the shearing surface, and eliminating excessive dilation due to an inclined discontinuity. The torque at the interface is measured with strain gages mounted to the reaction arm that prevents the rotation of the lower part of the sample. Kutter's preliminary study showed that, in general, rock joints do not seem to require large displacements to reach residual strength.

Martin and Miller (1974) used direct shear equipment to test weathered rock or rock joints, and reported results from strength tests of joints in sandstone with different degrees of weathering. A schematic of the device is shown in Fig. 2-2. The results showed decrease in strength with increase in degree of weathering. The study also suggested a procedure for isolating the dilatancy in the rock joints. They adopted the model proposed by Ladanyi and Archambault (1970) to describe the dilatant component of the joint strength.

Mogilevskaya (1974) found that the effect of wetting the shear plane on the strength of rock joints depended on the mineralogy. For crystalline rock, there seemed to be no change, but for other types such as sedimentary or intrusive rock, there was a decrease in the

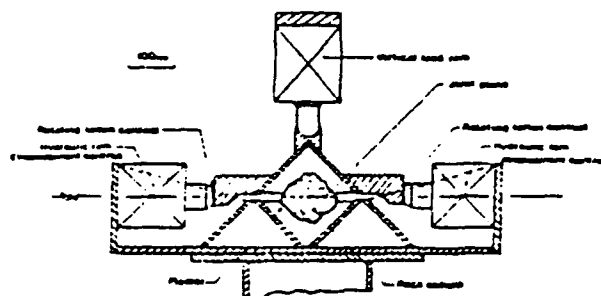


Figure 2-2. Schematic Diagram of Direct Shear Apparatus [Martin and Miller (1974)]

initial friction angle. If a filler material exceeded the height of the macro-asperities, then the shear strength of a rock joint depended on the properties of the filler, and not on the joint morphology.

Nikitin et al. (1974) studied the effects of impulse loading on rock joints, both with and without a filler material. Impulse loads were induced in a direct shear apparatus by applying a shear stress which was near failure for a joint under a given normal stress, and then reducing the normal stress abruptly. This caused the upper sample, which was allowed to translate, to accelerate. The results indicated that for joints both with and without a filler, initially under impulse loading, the shear strength was higher than the peak "static" shear strength. As relative displacements occurred, the shear strength under impulse loading decreased, and became less than peak static strength.

Pratt et al. (1974) performed both laboratory direct shear and in situ shear tests on samples of jointed quartz diorite. The effects of specimen size, loading path, and the orientation of the joint on the shear strength were studied. The specimens with larger joint areas had lower shear strengths. This could be due to differences between the total area of the joint and the 'apparent' contact area. As the angle of the joint with respect to the applied load increased, the shear strength increased. The shear strength seemed to be affected by load path. Angles of friction determined from direct shear tests with constant normal stress were different than those obtained from proportional loading tests.

Based on friction tests on plaster casts of rough fractured surfaces of different rock types (granite, sandstone and limestone), Schneider (1974) found that the geometry of the joint surface has significant influence on the stress-strain response, and the residual strength is dependent upon the surface geometry and material parameters.

Ross-Brown and Walton (1975) describe a portable direct shear box which is schematically shown, Fig. 2-3. The device was designed such that as much data as possible may be gathered in the field. However, the device is not designed for in situ testing. It can be deduced from the figure that the shear and normal stresses are applied by hydraulic rams which react against cables attached to the shear box.

Dieterich (1978a, 1978b, 1979a, 1979b, 1981a, 1981b) and Dieterich and Okubo (1981) presented models and test results for describing fault behavior including stick-slip phenomenon for predicting earthquakes. Although the basic mechanics aspects of these studies are relevant to the mechanisms of joints or interfaces, the present study is more concerned with effect of blast or earthquake-type loadings on joints, resulting in various modes of deformation. Hence, detailed reviews of these studies are not included.

Kane (1981) presented a review of static strength behavior of rock joints and reported direct shear test results for joints with different roughnesses in a granite gneiss. Tests were performed using natural joints and joints created by fracture along existing cleavage planes.

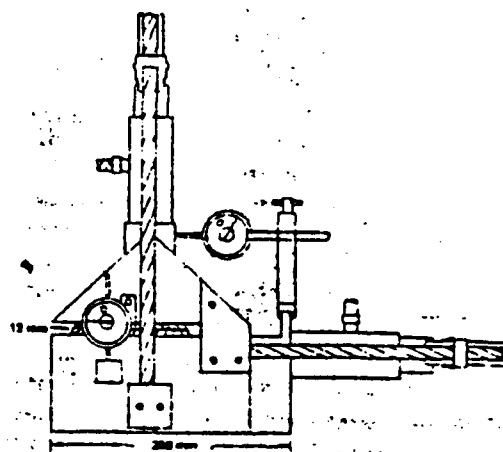


Figure 2-3. Portable Shear Device
[Ross-Brown and Walton (1975)]

The foregoing models involved tests for dry joints without pore fluid (water) pressures. Goodman and Ohnishi (1973) developed a static direct shear device, Fig. 2-4, that permitted undrained shear testing of joints with measurement of pore water pressures. They found that the behavior of joints was affected by compression and closure of joint, dilation and the state of stress.

Most of the previous studies are concerned with static behavior of dry (or wet) joints with major attention to strength behavior of rock joints. Recently, there are a few studies that consider cyclic behavior of joints and effect of pore water pressure. Crawford and Curran (1981) developed a direct-shear device to examine the effect of shear rate on the shear resistance of smooth artificial joints in different rocks. Gould (1982) and Gillette (1983) describe a cyclic direct-shear device, Fig. 2-5, and its use for studying undrained behavior of rock joints.

Failure Models

Reviews on shear strength of rock joints are presented by various investigators, Jaeger (1959, 1971); Barton (1973, 1974); Goodman (1974, 1976); Jaeger and Cook (1976); Kane (1981); the presentation herein has consulted these publications.

Amonton's law (1699) for metals provides a basis for defining shear force, F , parallel to the contact area required to initiate sliding:

$$F = \mu N$$

(2-1)

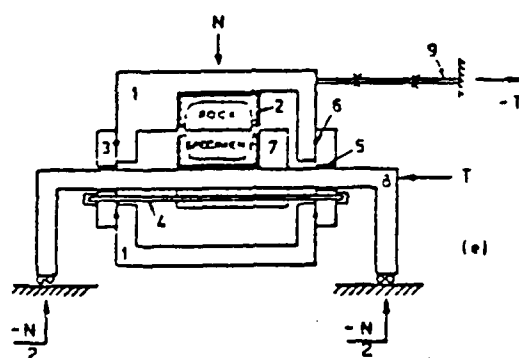


Figure 2-4. Device by Goodman and Ohnishi (1973)

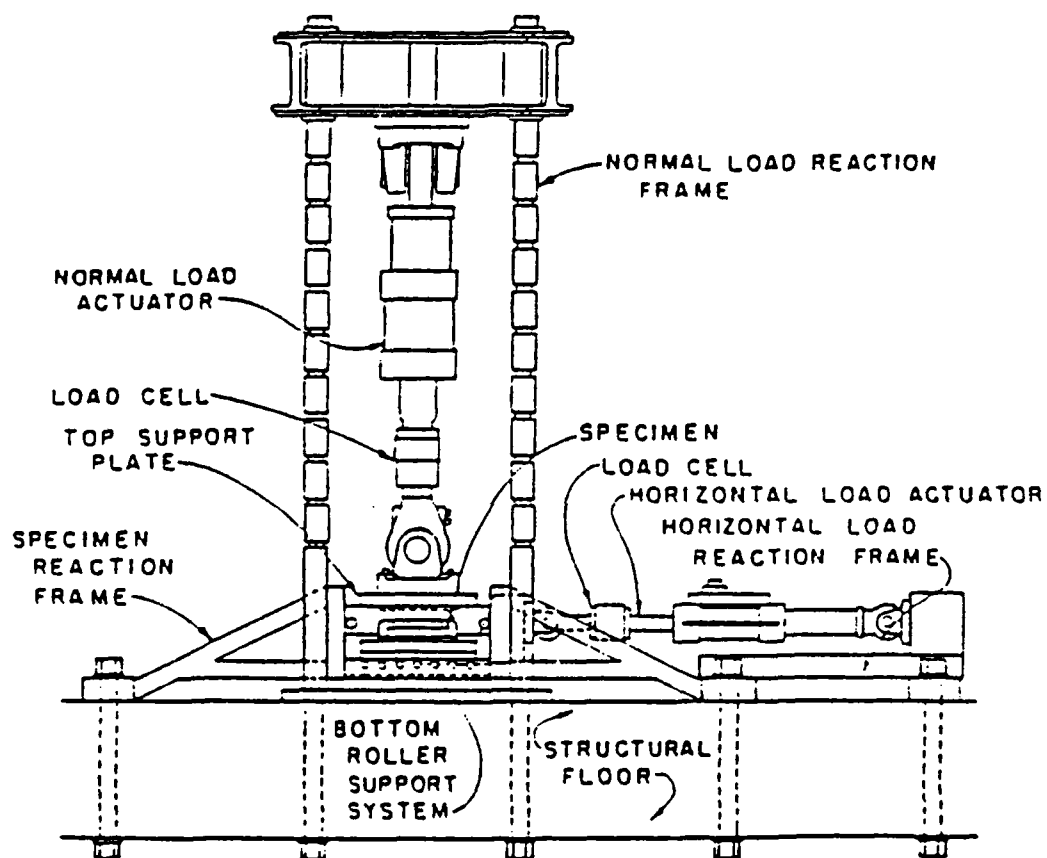


Figure 2-5. Dynamic Direct Shear Apparatus
[Gould (1982), Gillette (1983)]

where N = normal force and μ = coefficient of friction, which is independent of N and the contact area A . The work of Bowden and Taber (1950) for metals has also provided a basis for defining rock friction. In these theories for metals, the shearing force is derived from force required for plowing (force necessary to plow in grooves at contact) and that required to shear asperities. Since in the case of rocks and minerals failure is often caused by brittle fracture with plastic flow and 'welding' of asperities, the above mechanism for metals may not be strictly valid for rock joints, Jaeger (1959).

In order to allow for elastic behavior, Archard (1958) proposed the following expression for F :

$$F = \mu N^m \quad (2-2)$$

where m = exponent whose value varies between $2/3$ and 1 ; for purely elastic behavior, $m = 2/3$ and for ductile contact, $m = 1$. For the latter, Eq. (2-2) reduces to Eq. (2-1).

Jaeger and Cook (1976) presented the following Mohr-Coulomb criterion for shear strength:

$$\tau = s_o + \mu \sigma_n \quad (2-3)$$

where s_o = shear strength (adhesion) of contact surface analogous to cohesion c in solids. Lajtai (1970) suggested that the linear model in Eq. (2-3) may not be sufficient, and he proposed failure mechanisms involving stress dependency and components of stress tensor.

Most rocks exhibit strain softening type behavior, Fig. 2-6, where a residual strength is reached after the peak strength (Goodman, 1974, 1976; Jaeger, 1971; Hoek and Bray, 1974). The schematic of peak and residual envelopes is shown in Fig. 2-7. The residual strength is considered to represent the strength of an uncemented joint. The ratio of peak to residual strength is defined as stress ratio, S_r ; for a filled joint, the ratio can be as high as 4, Barton (1973).

A question arises as to the definition of "failure" because its adoption may depend on various factors such as type of loading and structure to be designed and nature of the (joint) material. Giuseppe (1970) proposed various possible definitions: (a) maximum or peak stress, (b) "knee" of the τ vs. u_r curve (where slope change can occur), (c) "inversion" of vertical deformation (prior to failure) or (d) current deformation greater than previous ones.

Since the strength behavior of joints can be nonlinear, Jaeger (1959, 1971, 1976) proposed the following relation, Fig. 2-8:

$$\tau_p = c_j (1 - e^{-b\sigma_n}) + \sigma_n \tan \phi_r \quad (2-4a)$$

For very large values of σ_n , Eq. (2-4a) becomes

$$\tau_p = c_j + \sigma_n \tan \phi_r \quad (2-4b)$$

and for $\sigma_n = 0$, it gives

$$\frac{d\tau_p}{d\sigma_n} = c_j b + \tan \phi_r \quad (2-4c)$$

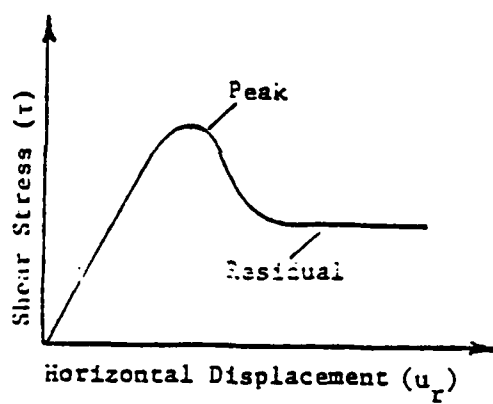


Figure 2-6. Schematic of Peak and Residual Shear Strengths

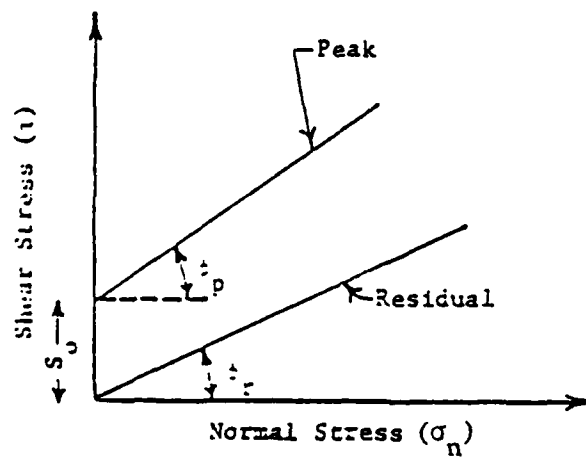


Figure 2-7. Peak and Residual Strengths Envelopes

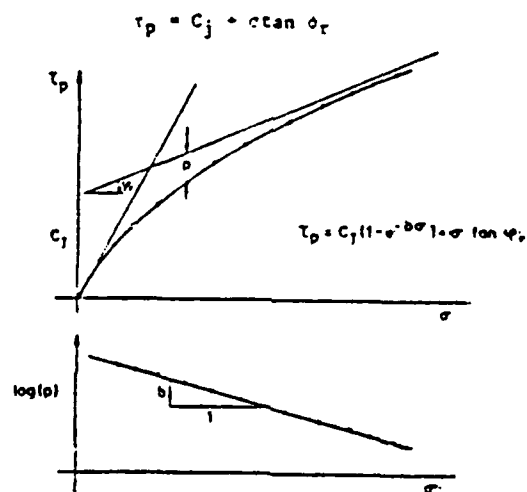


Figure 2-8. Empirical Shear Strength Curve
[Jaeger (1971)]

Until now the discussion has been limited to planar contact surfaces with shear stress parallel to it. Now consider a contact surface such that it is not parallel to the shear stress, but inclined at an angle i , Fig. 2-9. Then the expression for shear stress becomes (without s_o), Patton (1966)

$$\tau = \sigma_n \tan (\phi_\mu + i) \quad (\sigma_n < \sigma_n^*) \quad (2-5a)$$

$$\tau = c + \sigma_n \tan \phi \quad (2-5b)$$

where σ_n^* = critical or yield stress, and ϕ_μ = mineral friction angle between smooth and even surfaces; $\phi = \phi_r$ = residual friction angle; at larger shear strains, $\phi_r \approx \phi_\mu$. It was noted by Patton that an apparent cohesion, c , can exist due to interlocking of asperities. Figure 2-10 shows the bilinear failure envelope proposed by Patton. One of the characteristics of this model is that it predicts normal (relative) displacement, v_r , for any horizontal (relative) displacement, u_r ; in other words, during u_r , the volume of the specimen increases or it dilates. The angle i , which denotes the slope (dv_r/du_r) of v_r vs. u_r plot, can be used to define the measure of the dilation. The tendency to dilate decreases with increasing normal stress. The dilation approaches zero as the normal stress approaches the unconfined compressive strength of the asperities. At this stage, the asperities shear off rather than be ridden over (Barton, 1973; Goodman, 1974, 1976; Martin and Miller, 1974).

Barton (1973) and Barton and Chouby (1977) proposed the following model for strength of rock joints:

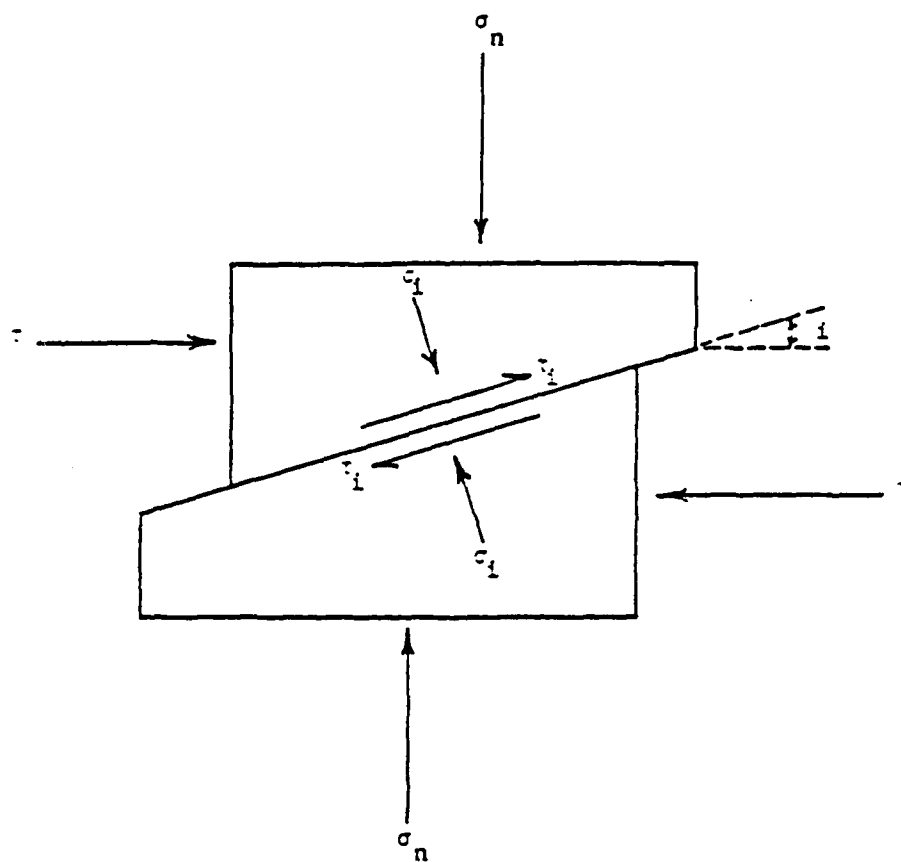
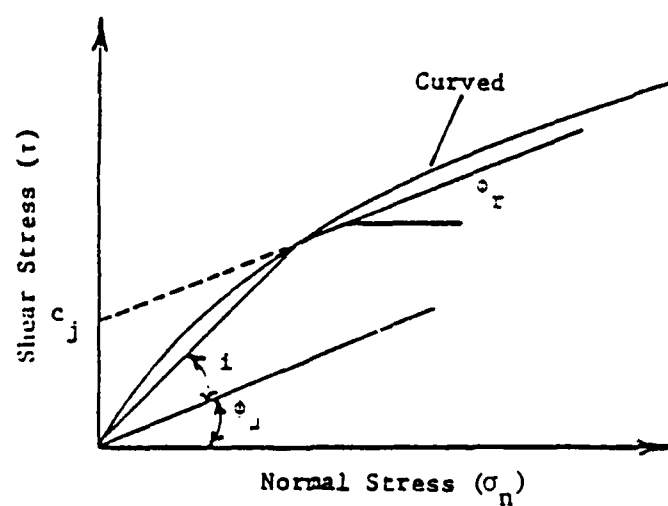


Figure 2-9. Inclined Joint
(Patton, 1966)



Patton's Failure Envelope

Figure 2-10. Model by Patton (1966)

$$\tau = \sigma_n \tan \left(\text{JRC} \log \left(\frac{\text{JCS}}{\sigma_n} + \phi_b \right) \right) \quad (2-6)$$

where JRC = joint roughness coefficient, which is an empirical value between 0 and 20 (for smooth and rough joint), JCS = joint wall (unconfined) compressive strength for low σ_n and confined for high σ_n , ϕ_b = residual shear strength of flat, nondilatant rock (dry or wet) surfaces. A plot of Barton's model is shown in Fig. 2-11. In the context of plasticity, the nonassociative rule at yield (which represents dilation rate at peak) from Barton's model can be expressed as

$$\frac{d\epsilon_n}{d\epsilon_s} = \tan \left(\frac{\text{JRC}}{2} \log \left(\frac{\text{JCS}}{\sigma_n} \right) \right) \quad (2-7)$$

where $d\epsilon_n$, $d\epsilon_s$ = increments of normal and shear strains, respectively. The dilatant behavior of a joint is affected by factors such as width of asperities, roughness and angle of asperities.

Ladanyi and Archambault (1970) developed the following model for rock joint behavior and yield surface, Fig. 2-12:

$$\tau = \frac{\sigma_n (1 - a_s) (\tan i + \tan \phi_\mu) + a_s S_r}{1 - (1 - a_s) \tan i \tan \phi_f} \quad (2-8a)$$

where a_s = relative length of shear through asperities, ϕ_f = statistical average of friction angle with varying i ($\phi_f \approx \phi_\mu + i$ ave.), and S_r = shear strength of asperities. The flow rule with this model is given by

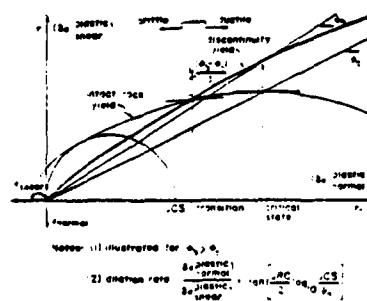


Figure 2-11. Barton Model (1973)

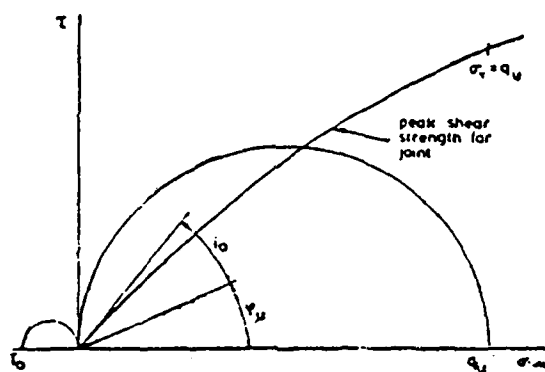


Figure 2-12. Shear Strength Relation for Rough Joints [Ladanyi and Archambault (1970)]

$$\frac{d\epsilon_n^p}{d\epsilon_s^p} = \tan i \text{ for } \sigma_n < \sigma_{nt} \quad (2-8b)$$

where σ_{nt} = stress at which the asperities are sheared off and $i \approx 0$, and the superscript p denotes plastic strain. When $\sigma_n = \sigma_{nt}$, the joint can be considered to have reached a critical state and the behavior can be considered to transit from that of joint to that of intact rock. Equation (2-8b) defines a set of plastic potentials and since they are not equal to the function describing the yield surface, the flow will be nonassociative; hence, $\tan i \neq \frac{d\tau}{d\sigma_n}$.

Models for Deformation of Rock Joints

Goodman et al. (1968) proposed a model for rock joint in which the constitutive or stiffness relation for the joint element is expressed as

$$\begin{Bmatrix} d\sigma_n \\ d\tau \end{Bmatrix} = \begin{bmatrix} k_n & k_{n\tau} \\ k_{\tau n} & k_\tau \end{bmatrix} \begin{Bmatrix} d\epsilon_n \\ d\epsilon_s \end{Bmatrix} \quad (2-9)$$

where $k_{n\tau}$, $k_{\tau n}$ = stiffness for coupling between shear and normal responses. In many applications, it is assumed $k_{n\tau} = k_{\tau n} = 0$. Schematic force displacement curves for the stiffnesses are shown in Fig. 2-13, where w_n (v_r) and w_s (u_r) are (relative) normal and shear displacements.

Ghaboussi and Wilson (1973) utilized a constitutive model which involved normal and shear stiffnesses as above which can be linear or can vary nonlinearly (with stress). They also proposed that dilatancy in

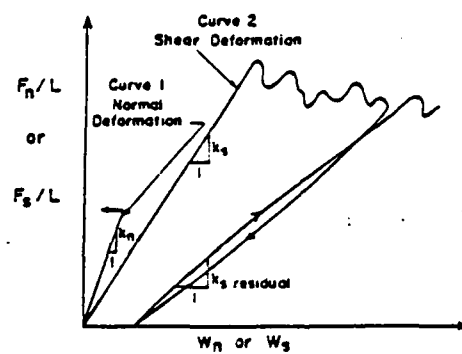


Figure 2-13. Data From Hypothetical Direct Shear Test on a Rock Joint
[Goodman et al (1968)]

rock joints can be incorporated by using the idea of the Cap model (DiMaggio and Sandler, 1971), (Fig. 2-14). The fixed "failure" envelope, f_f , and the yield caps, f_c , are expressed as

$$f_f (\sigma_n, \sigma_s) = 0 \quad (2-10a)$$

$$f_c (\sigma_n, \sigma_s, \kappa) = 0 \quad (2-10b)$$

where κ = strain hardening parameter. Although the above plasticity model was implemented for boundary value problems, the question of determination of required parameters remained.

Zienkiewicz et al. (1977) proposed an elastic-viscoplastic model for joint behavior. A Mohr-Coulomb yield criteria was employed with both associative and nonassociative flow rules. The nonassociative flow rule adopted a potential function, Q , of the form

$$Q = \hat{\sigma}_{pq} + \hat{\sigma}_q \tan \psi - \kappa = 0 \quad (2-11)$$

where $\hat{\sigma}_{pq}$ = shear stress, $\hat{\sigma}_q$ = normal stress, ψ (between 0 and ϕ) the internal angle of friction, and κ = parameter.

Roberds and Einstein (1978) presented a model that can include elastic, plastic and viscous effects in rock discontinuities. The concept is based on using two or multisurface plasticity models such as critical state or cap. The model appears to be essentially in a qualitative form, and includes qualitative comparisons with other available models for joints.

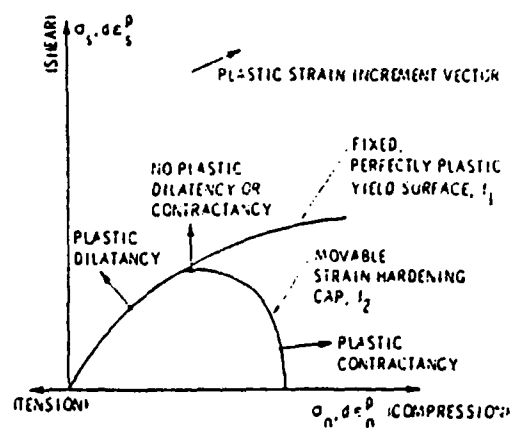


Figure 2-14. Capped Plasticity Model for Joints
[DiMaggio and Sandler (1971),
Ghaboussi et al (1973)]

Hsu-Jun (1979) proposed a plasticity based model for joints in which the Mohr-Coulomb criterion is used as the yield function.

Pande (1979) presented a model for rock mass behavior derived from individual representation of joint behavior by using, for instance, Barton's equation (Eq. 2-6), and "solid" rock behavior by using a yield function expressed in terms of stress invariants.

Heuze and Barbour (1982) presented a review of some of the available models for joints.

Plesha (1986) describes an incremental plasticity model which may be used to model joints with dilatancy and contact surface degradation (damage). The model distinguishes between macroscopic and microscopic features of a discontinuity. Through macroscopic considerations, an incremental constitutive law is derived which is applicable to a large class of contact friction problems. By idealizing the microstructure to consist of interlocking asperity surfaces, the constitutive equations are specialized for the description of rock joints including effects such as dilatancy, asperity surface degradation and bulking. Asperity degradation is described using a simple tribological relationship which assumes that degradation is a function of the plastic tangential work, W_t^P .

Barton and Bandis (1987) modified Barton's model further to consider the variation in shear strength and dilation angle during the course of shearing. These effects are incorporated on the basis of a "mobilized roughness" concept. Roughness is mobilized at the onset of dilation, has its maximum contribution at peak shear displacement, and then declines due to surface mismatch and wear.

Drumm and Kane (1987) describe the nonlinear inelastic response of rock joints utilizing an incremental plasticity based model, similar to the Cap model of DiMaggio and Sandler (1971), but formulated in terms of natural joint coordinates. Elliptical caps or moving yield surfaces are determined from experimentally observed dilation rates. The customary fixed yield surface is replaced by a pair of slip surfaces which describe peak and residual strengths of the joint plane.

Divakar et al. (1987) model the shear behavior of rough interfaces using a crack stiffness matrix formulation. The behavior is considered to be nonlinear elastic, and expressions are formulated for shear stress vs. slip and slip vs. dilation at constant normal stress. Coupling is incorporated by relating normal stresses to peak shear stresses by means of a "failure surface." Introducing this coupling effect provides off-diagonal terms in the elastic stiffness matrix.

From the above review, it appears that major attention in the past has been given to characterizing strength behavior of joints. Limited attention has been given to define deformation behavior by using linear or piecewise linear idealization, and this is limited to cases of monotonic loading. There are hardly any models that include the entire deformation, failure and softening in a single framework. A major objective of this research is to begin to develop such a general concept on the basis of laboratory tests, including quasi-static and cyclic loadings on simulated joints in concrete.

CHAPTER 3

DESCRIPTION OF TEST DEVICE

Large-scale fast and slow or quasi-static direct shear tests were performed on (idealized) rock joint surfaces using the translation portion of the cyclic multi-degree-of-freedom shear device (CYMDOF). The CYMDOF device is described by Desai (1980a, 1981), Drumm and Desai (1983), and Desai et al. (1983b). Minor modification of the test box was undertaken such that vertical displacement and rotation of the upper sample about an axis in the plane of shear perpendicular to the direction of the shear were permitted.

The device, as shown in Fig. 3-1, consists of an upper and lower sample holder, a load frame, a system for guiding the motion of the upper sample holder, a hydraulic system for applying loads, a control system, a measurement system for measuring loads and displacements, and a data acquisition system.

Upper and Lower Sample Holders

The upper and lower sample holders are shown in Figs. 3-2 (a) and (b). The upper sample holder is smaller than the lower sample holder so that during shear testing no loss of contact area of the upper sample shear surface will occur. Also depicted are the plates required for the rail system which guides the upper sample motion with respect to the lower sample while allowing for appropriate degrees-of-freedom.

Figure 3-1. Picture of Shear Device

Figure 3-2 (a). Upper Sample Holder

Figure 3-2 (b). Lower Sample Holder

The upper sample holder has a pair of plates protruding near the bottom, centered on the front face, for attachment of the horizontal actuator which exerts the shear force on the sample. These plates are as close to the bottom of the sample holder as possible in order to reduce the moment that the shear force exerts on the upper sample. Holes at the front of the sample holder allow instrumentation wiring to pass through.

The lower sample holder has a cutout portion on one side and in the front, although only the front cutout is shown in Fig. 3-2 (b). These cutouts allow for observation of the joint during shear testing, and also provide access to instrumentation to be discussed later. A leveling plate was placed on the inside bottom of the holder such that the bottom sample could be leveled prior to testing. The bottom sample holder is bolted at the bottom to the test frame so that it is held fixed during testing.

Securing Samples to Sample Holders

Samples are secured to sample holders with a commercially available, quick-setting, nonshrinking cement known as "Burke Stone," manufactured by the Burke Company, San Mateo, California. Samples are cast with slightly undersized dimensions with respect to the sample holders. Upper and lower sample holders have inside dimensions (L x W) of 12 in. x 12 in. (30.5 cm. by 30.5 cm.) and 16 in. x 16 in. (40.64 cm. x 40.64 cm.), respectively, while upper and lower samples have inside dimensions of 11.5 in. x 11.5 in. (29.2 cm. x 29.2 cm.) and

15.5 in. x 15.5 in., respectively. This allows the samples to be leveled and centered within the sample holders, then cemented into place by filling the gap between the sample and sample holder with Burke Stone. Since removal of the samples from the sample holders after testing would be very difficult if the entire gap is filled with Burke Stone, only intermittent lengths of the gap are filled, forming cement plugs around the periphery of the specimen. The cement plugs, depicted in Fig. 3-3, are 1.0 to 1.5 in. deep and 1.0 to 1.5 in. (2.54 to 3.81 cm) long. The spaces between the cement plugs are used as an aid in removing the plugs after testing.

The top sample is placed in the upper sample holder in such a manner that both the sample and the holder are level prior to placing the cement plugs. Initially the top sample is set on a level plate with its structured surface facing down, and the upper sample holder is suspended above the lower sample by means of a winch, Fig. 3-4. The upper sample holder is lowered around the upper sample until contacting two protruding metal plates at the bottom side of the sample. Set screws are placed around the periphery for leveling the upper sample holder. After centering and leveling the upper sample holder, cement plugs are placed around the upper periphery as depicted in Fig. 3-3. After allowing the cement to set, the upper sample and holder are overturned and cement plugs are placed around the bottom periphery as well.

The bottom sample is placed in the bottom sample holder in such a manner that it is level with respect to the horizontal,

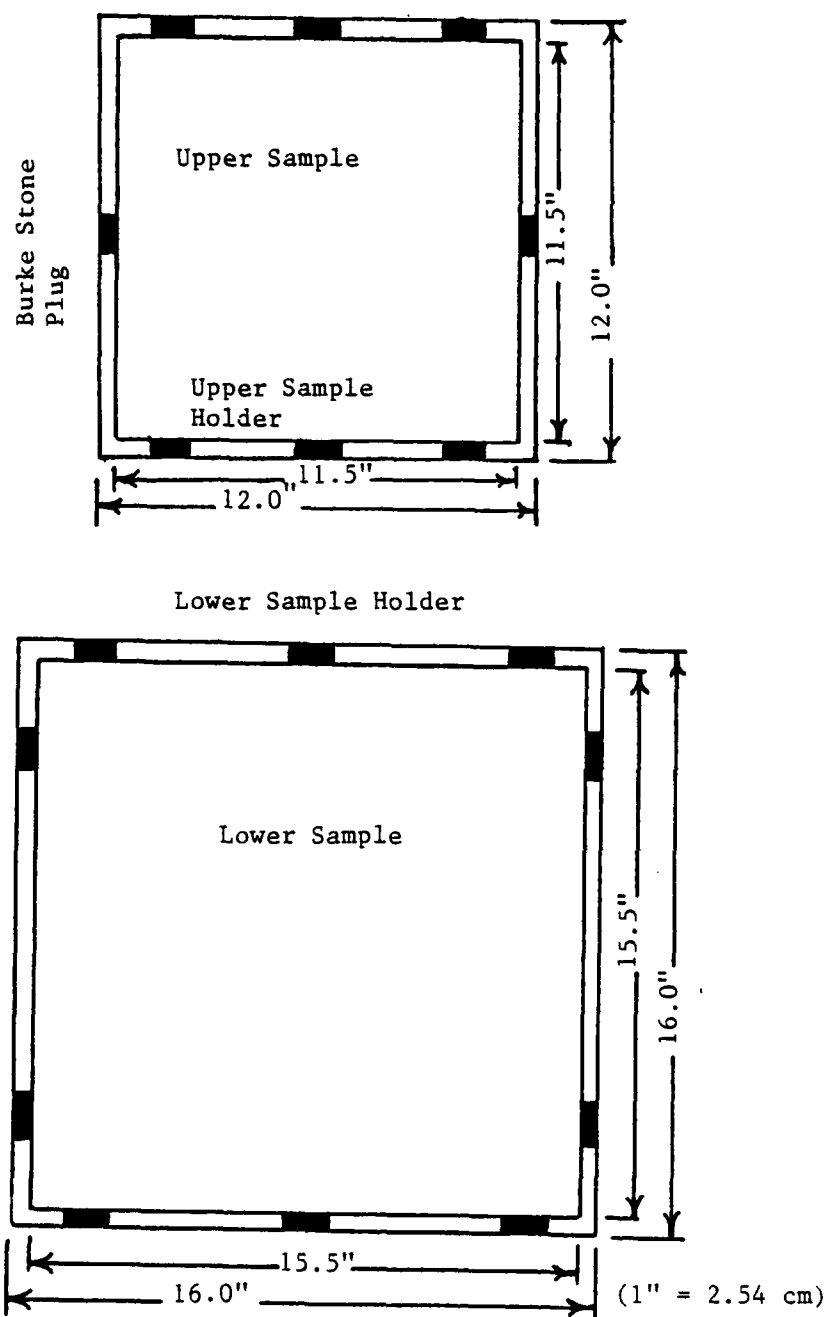


Figure 3-3. Schematic of "Burke Stone" Plugs Used to Secure Samples to Holders

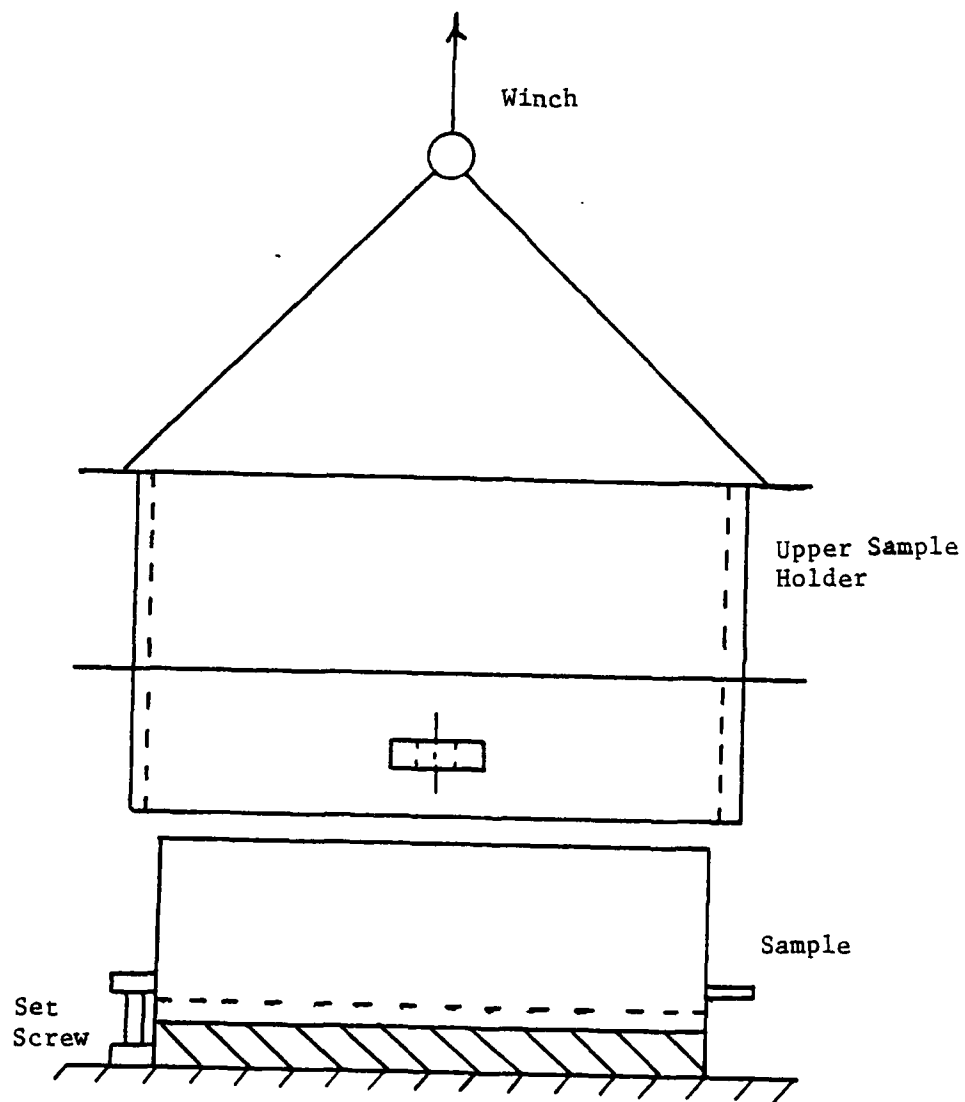


Figure 3-4. Setting of Upper Sample Holder to Upper Sample

and the asperities on the surfaces of the upper and lower samples will mate when the device is assembled. The bottom sample is lowered into the bottom sample holder by means of a winch (Fig. 3-5). A level plate at the base of the bottom sample holder is used to level the sample.

The position of the bottom sample is adjusted such that asperities on the surfaces of the top and bottom samples run in the same direction after assembling the device. This is necessary for proper mating of the joint at the onset of testing. The rear edge of the upper sample holder is used as a reference and the angle of an asperity trough on the surface of the upper sample with respect to this edge is determined as shown in Fig. 3-6. Then the bottom sample is positioned in the bottom sample holder such that its asperity peaks make the same angle with respect to a reference line on the bottom sample holder. This reference line is such that it will be parallel to the rear edge of the upper sample holder after assembling the device. After positioning and leveling the lower sample, cement plugs are placed around the periphery.

Rail System

The device is designed to shear an interface or rock joint by applying shear and normal forces to a top sample. With respect to the bottom sample, which is held fixed, the top sample is allowed to displace horizontally, vertically and rotate about an axis in the plane of shear perpendicular to the direction of shear. Top and bottom samples are secured to sample holders which are then placed in a load frame containing actuators for applying vertical and horizontal forces as shown in

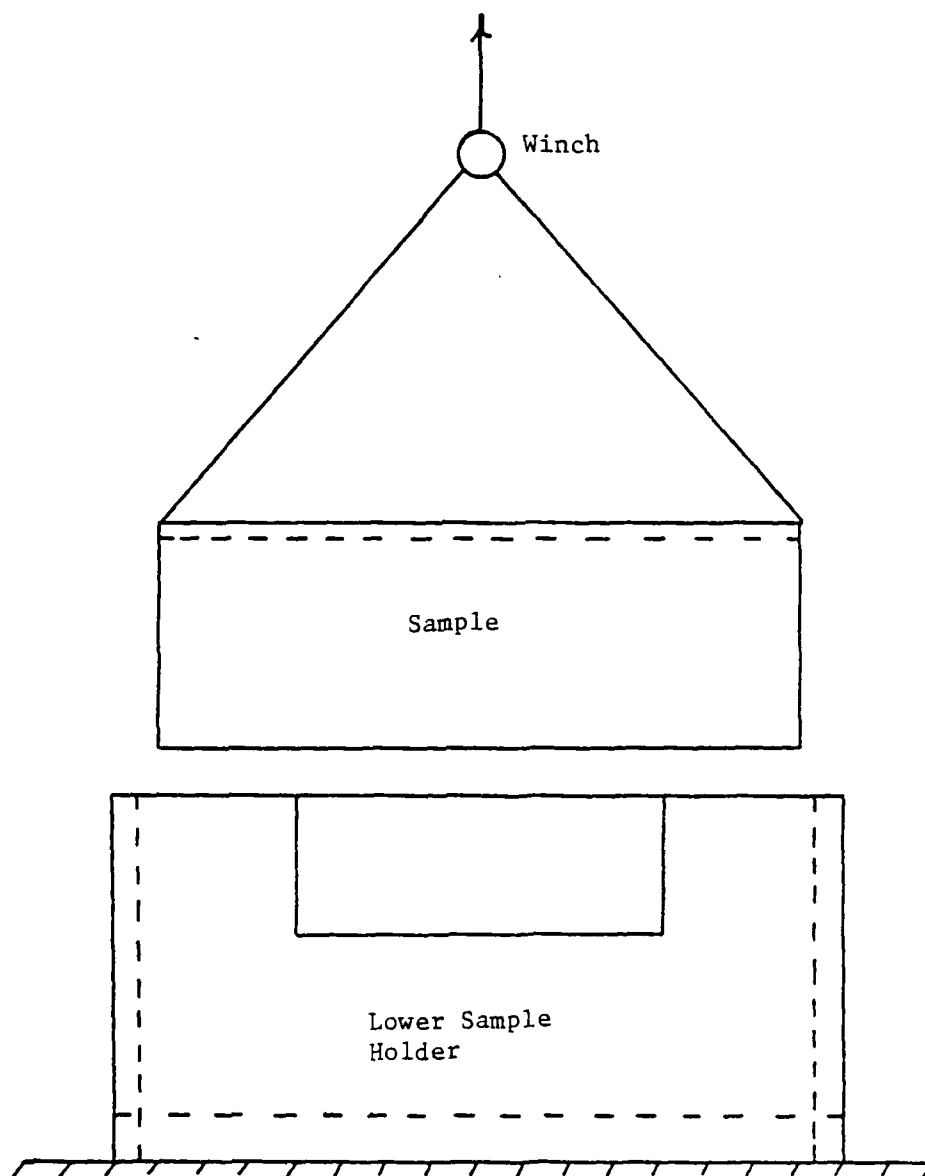


Figure 3-5. Placement of Lower Sample Into Lower Sample Holder

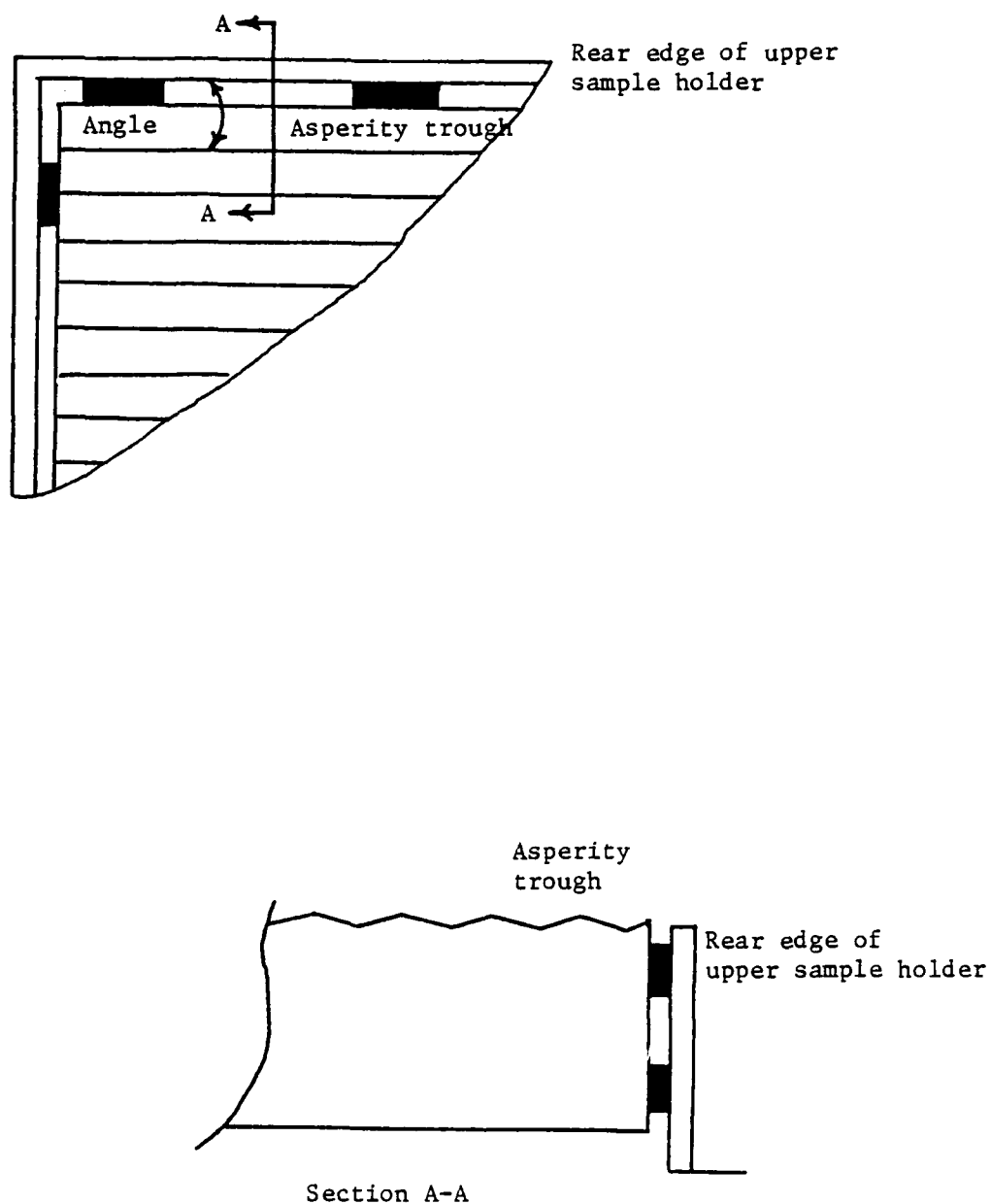


Figure 3-6. Determination of the Angle of an Asperity Trough with Respect to the Rear Edge of the Upper Sample Holder

Fig. 3-7. Motion of the upper sample is guided by means of a rail system depicted in Fig. 3-8. The rail system consists of two 1 in. (2.54 cm.) hardened steel rods, one on either side of the sample holders, which are constrained by four slotted bearings, two on each side of the bottom sample holder. The slotted bearings are made from oil impregnated bronze. Details of the slotted bearings can be seen, Fig. 3-8. These bearings allow translation, vertical (upward or downward) displacement up to 0.25 in. (0.635 cm.), and rotation about an axis in the plane of shear, perpendicular to the direction of shear, of the top sample with respect to the bottom sample. Lateral motion of the upper sample or rotations other than those considered above are constrained.

Load Frame

The load frame is depicted in Fig. 3-7. Wide flange beams (W 10 x 45) were used in the construction of the load frame. The frame was designed to withstand a vertical or horizontal load up to 30 tons and a frequency of about 2 Hz.

The load frame is self-supporting and no attachment to the floor is necessary. Provision is made in the frame for securing the lower sample holder and for the vertical and horizontal hydraulic actuators used for application of normal and shear loads. A winch and trolley system is installed on the load frame to aid in the assembly of the specimen in the shear device.

Figure 3-7. Load Frame Containing Horizontal
and Vertical Force Actuators

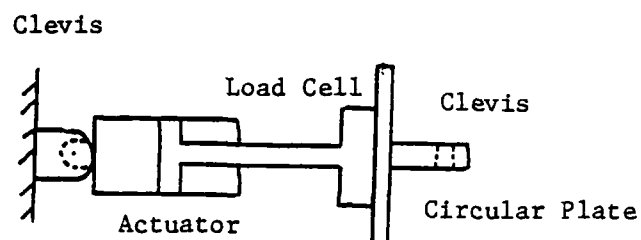
Figure 3-8. Detail of Rail System for
Guiding Motion of Upper
Sample

Load System

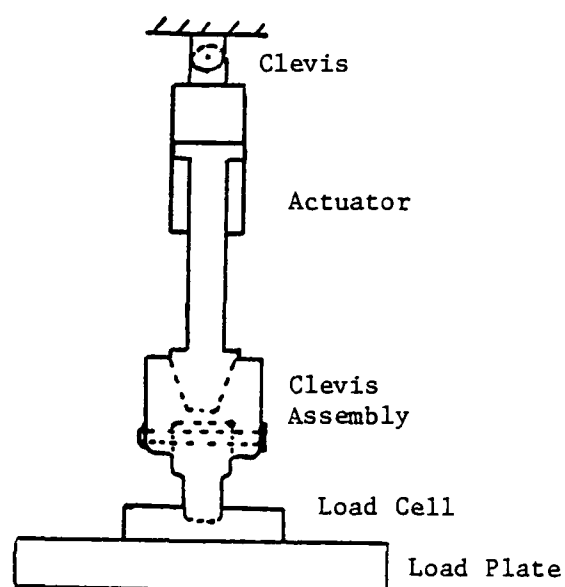
The loading system consists of the hydraulic system used to apply loads including the vertical and horizontal hydraulic actuators and all attachments necessary to secure the actuators to the load cells and the upper sample holder. The system is shown schematically in Fig. 3-9.

At the heart of the load system is a hydraulic pump capable of providing a fluid pressure up to 3000 psi (21 MPa) at a flow rate of 25 gallons/min. This pump services a servo-controlled electro-hydraulic system, to be discussed subsequently, which controls the flow of hydraulic fluid to two hydraulic actuators. One actuator is mounted to the load frame such that it reacts against a vertical member of the frame and provides the shear force transmitted to the upper sample. The other actuator mounts to the top of the load frame in the center and provides the normal force transmitted to the upper sample. Both actuators have a stroke of 8 in. (20 cm.). The horizontal actuator is capable of applying a force of 12 kips (53 KN) and the vertical actuator is capable of applying a 30 kip (133 KN) force.

The actuators are connected to the load frame and load cells using connections and fittings as shown in Fig. 3-9. The connections are designed to provide a tight fit while not allowing the load system to inhibit the motion of the upper sample box. Both the horizontal and vertical actuators are pinned to the load frame using clevises which fix the end of the actuator with respect to translation but allow rotation about any axis. Thus the ends of the actuators which contact the



(a) Horizontal Load System



(b) Vertical Load System

Figure 3-9. Schematic of Load System

upper sample are allowed to move with the upper sample as they rotate about fixed ends. The horizontal actuator piston threads directly into a load cell which is mounted to a circular plate. Another clevis assembly joins the circular plate to the upper sample holder at the center of the front face, 2 in. (5.08 cm.) up from the bottom. The vertical actuator piston feeds directly into a clevis assembly that is threaded to a vertical load cell. Both clevis assemblies at the load cell end of the horizontal and vertical actuators contain ball bearings which allow the ends of the actuators to rotate about any axis.

Control System

The hydraulic actuators are controlled with a closed-loop servo-controlled electro-hydraulic system. This system consists of an MTS model #436 control unit, an MTS service manifold, two MTS model #406 controllers (one for each actuator), a frequency generator, and a Moog model #A076 servovalve in line with each actuator. The system is shown schematically in Fig. 3-10.

The hydraulic actuators may be controlled by the closed-loop electro-hydraulic system in either a displacement-controlled mode or a load-controlled mode. The system compares a command signal generated by the frequency generator with a feedback signal from instruments measuring loads or displacements realized by the test arrangement. The command signal describes the desired motion or force of the actuator while the feedback signal indicates the actual motion or force of the actuator. A command signal, in terms of amplitude and frequency of the controlled

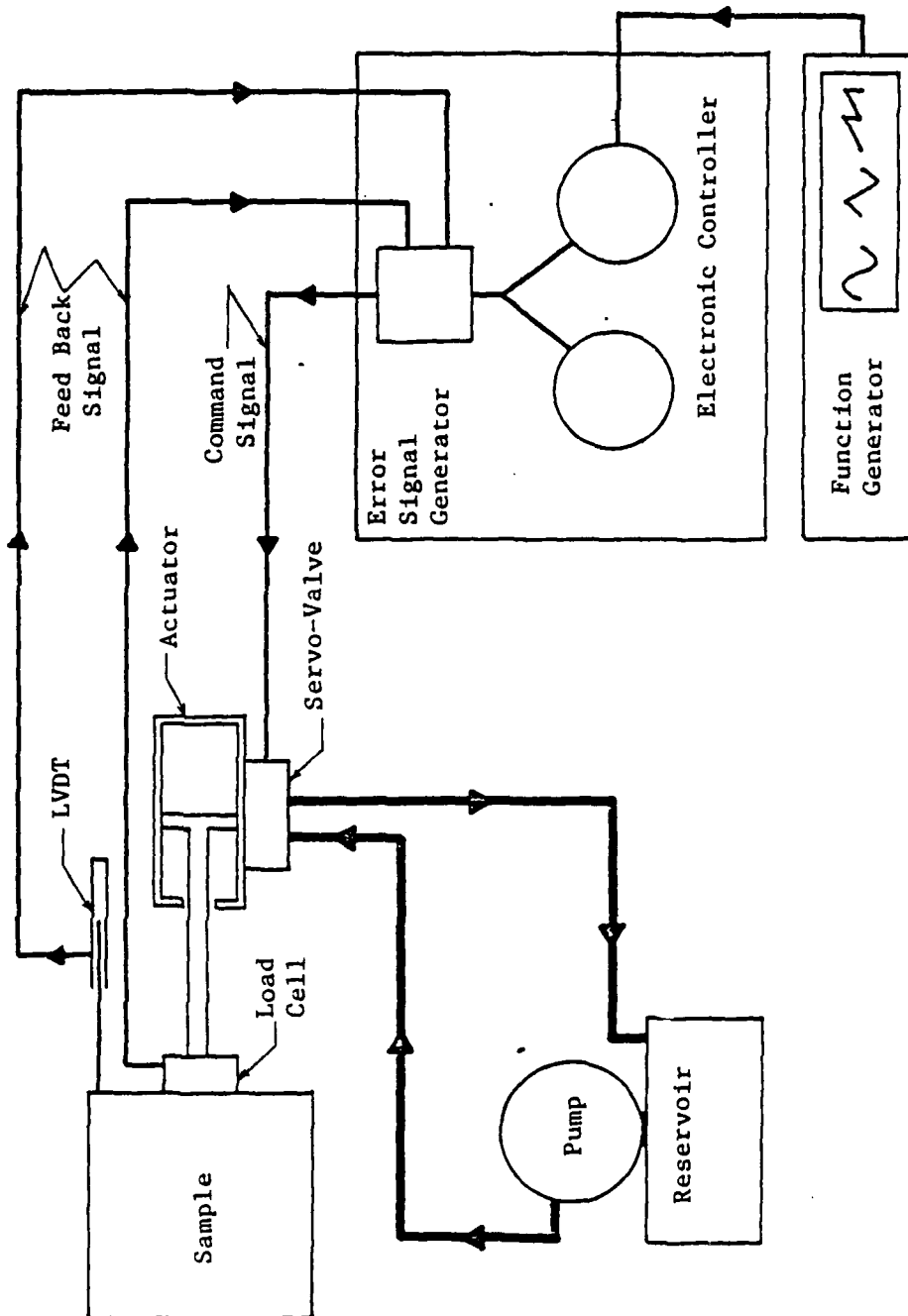


Figure 3-10. Schematic of Control System (Drumm, 1983)

variable, either load or displacement, is sent from the electronic controller to the servovalve mounted on the hydraulic actuator. A feedback signal indicating the value of the controlled variable is returned to the controller and compared with the command signal. A deviation between the command signal and the feedback signal results in an error signal that is returned as a command signal to reduce the error to zero, or close the loop.

Measurement of Test Variables

Measurements made during testing consist of the vertical and horizontal forces transmitted to the upper sample via the hydraulic actuators, as well as the horizontal motion, the vertical displacement, and rotation about an axis in the plane of shear perpendicular to the direction of shear of the upper sample. Figure 3-11 indicates the placement of instrumentation, and the variables measured.

Vertical and Horizontal Loads

Vertical loads are measured with a Strainert load cell, Model #FFL (45/±30) U(C)-SPKT which has a capacity of 30,000 lbs. (133 kN) in both tension and compression. Horizontal loads are measured with a Strainert load cell Model #FFL (18/±12) U-(3/±2) which has a capacity of 12,000 lbs. (53 kN) in both tension and compression. Both load cells are bolted to load plates and measure loads through the use of strain rosettes.

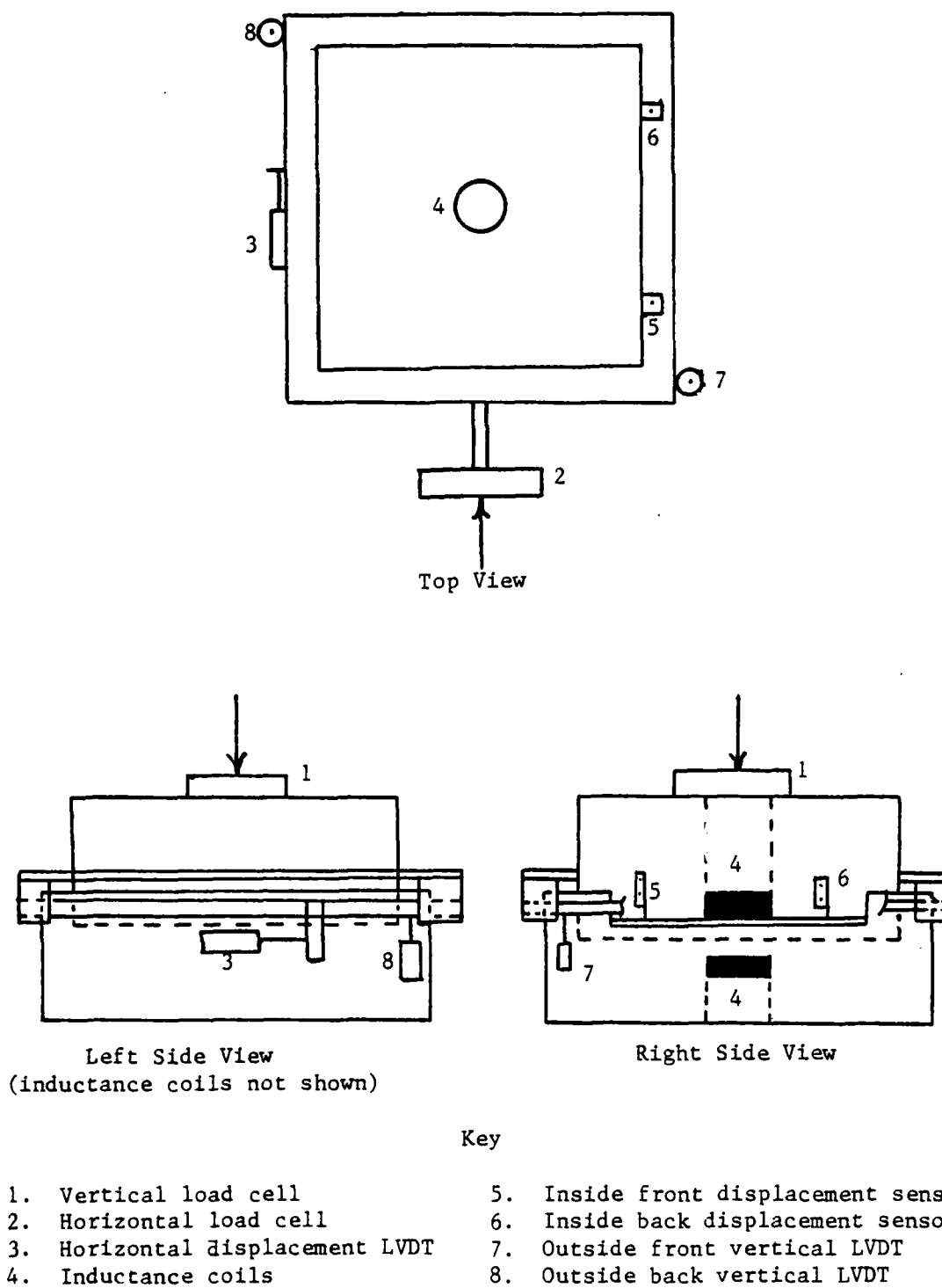


Figure 3-11. Placement of Instruments

Horizontal Displacement

Horizontal displacement of the upper sample is measured using a Scheavitz linear variable differential transformer (LVDT) Model #PCA-117-1000. This LVDT is spring loaded and has a stroke of plus or minus 1 in. (2.54 cm.). Attachment of the LVDT is made at the side of the bottom sample holder, and the gage head of the LVDT contacts a plate which is suspended from the rail that guides the upper sample. Locating the LVDT in this manner bypasses measurement of displacements which are extraneous to the motion of the upper sample. These extraneous displacements include some small amount of slip occurring in the clevises used in the actuator connections, and any motion of the lower sample holder.

Vertical Displacements

Vertical displacements of the upper sample holder are made at five locations as shown in Fig. 3-11. These include two LVDT's at the far corners of the bottom sample which are attached to the lower sample holder and contact the rail guiding the upper sample (outside front and back vertical LVDT's), two displacement sensors which attach to plates protruding from the side of the front sample near the bottom and contact a smooth aluminum plate attached to the cutout portion on the side of the lower sample holder (inside front and back displacement sensors), and a pair of inductance coils which are placed in cavities formed in the center of the top and bottom samples. Measuring the vertical displacement at five locations allows measurements of vertical displacement as well as rotations, if any, of the upper sample.

Outside Front and Back LVDT's. The outside front and back LVDT's are Sheavitz Model #PCA-116-300. This model is externally spring loaded and has a stroke of plus or minus 0.30 in. (76.2 mm).

Inside Front and Back Displacement Sensors. The inside front and back displacement sensors are Model #9610 Spring Return Linear Position Modules purchased from Duncan Electronics, Costa Mesa, California. These displacement sensors have a stroke of plus or minus 0.5 in. (1.27 cm.) and are DC-operated instruments which utilize a Wheatstone Bridge arrangement. Displacements are measured via a change in resistance induced as the piston of the instrument extends or retracts.

Inductance Coils. The inductance coils used to measure vertical displacements near the center of the joint by placing them in cavities formed at the center of the upper and lower structured surfaces were purchased from Bison Instruments, Minneapolis, Minnesota. The coils come as part of a system which includes the coils (sensors) and an external instrument package (Bison Model #4101A Soil Strain Gage Indicator). The system is similar in concept to one described by Selig (1964), and a full description can be found in the Bison Gage Instruction Manual. Strain is measured as a change in spacing between two reference points divided by the original spacing (gage length). The system is depicted schematically in Fig. 3-12 (a) and (b).

The sensors, each of which is a disk-shaped coil, are placed in near parallel and coaxial alignment. One sensor is placed in the cavity of the upper sample, and the other is placed in the cavity of the bottom sample. They are separated a distance over which the strain is to be

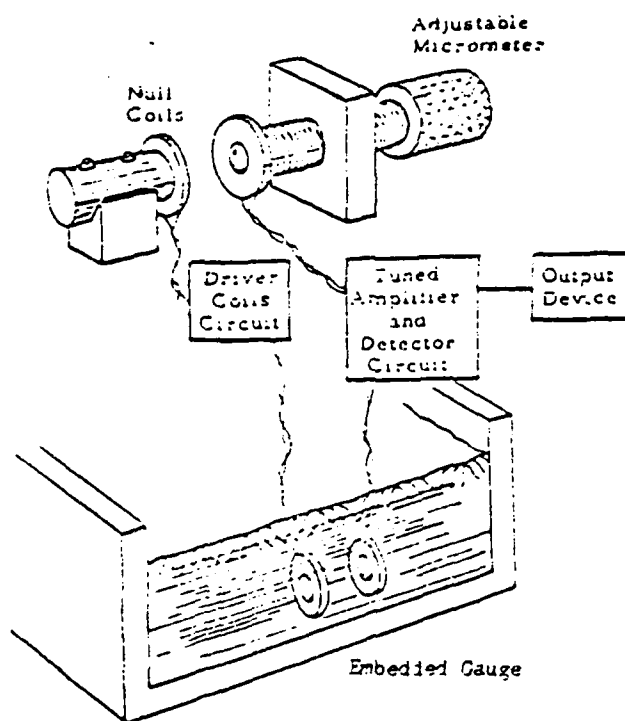


Figure 3.12 (a). Pictorial Diagram of Soil Strain Gage (Truesdale and Anderson, 1964)

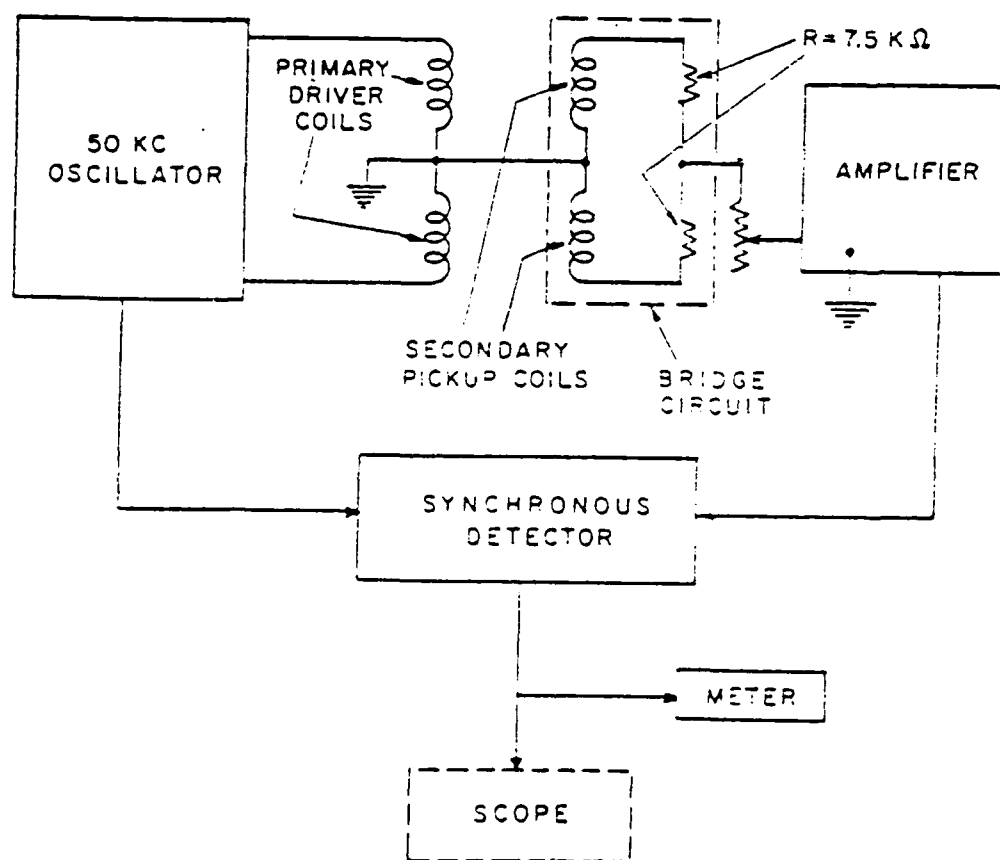


Figure 3.12 (b). Block Diagram of Soil Strain Gage (Truesdale and Anderson, 1964)

averaged. The sensors are 2.0 in. (5.08 cm.) in diameter, which is a standard size currently manufactured. One inch (2.54 cm.) diameter coils are also available. The separation of the sensors is related to the electro-magnetic coupling between the two. By means of an inductance bridge, Fig. 3-12 (b), an output voltage as a function of strain may be obtained since a change in spacing from the initial spacing produces an imbalance. The sensors operate at any spacing between one and four times the nominal sensor diameter. The effects of rotational or transverse movement, to be discussed later, and moisture and temperature are usually negligible. The proximity of metals may affect the output. This will be discussed in Chapter 4, Calibration of Instruments.

The Model #4101A Soil Strain Indicator to which the coils are connected contains all necessary driving, amplification, balancing, read-out and calibration controls and a self-contained power supply, Fig. 3-13. The bridge balance is accomplished by means of the phase and amplitude controls using the meter to indicate null. The amplitude dial reading corresponds to the sensor spacing. Changes in spacing may be determined by meter deflection from zero or by voltage output recorded by a data acquisition system connected to the rear panel. The calibration control is used to set up the output sensitivity so that it corresponds to the desired amount of strain, about 0.4 percent in this research. This particular instrument was designed for dynamic strain measurement and it has the ability to sense changes as fast as 0.25 microseconds.

Figure 3-13. Bison Model 4101A Soil Strain Indicator

Data Acquisition System

A Digital Electronic Corporation MINC-11 (Micro Instrumentation Computer) was used for data acquisition for tests with the CYMDOF device. The MINC-11 consists of a 64 K RAM microcomputer system designed for laboratory data acquisition and data reduction. The MINC used in conjunction with the CYMDOF device is equipped with two preamplifiers and an analog to digital (A/D) converter. The preamplifiers step up or down all voltage signals so that they are between 1 and 5 volts and the A/D converter allows for analog data such as the voltage output from load cells, LVDT's, displacement sensors, and inductance coils to be converted into digital form for storage and manipulation by the computer. The system may accommodate up to eight preamplified channels, and up to 64 channels with no amplification. The accuracy of readings using the preamplifier is plus or minus 0.005 volts. The system is capable of reading a channel every microsecond, and the A/D converter takes about 40 microseconds to process the signal.

The MINC utilizes 8.0 in. (20.3 cm.) floppy magnetic disks for data and program storage, and both BASIC and FORTRAN programming languages can be used.

The operation of the MINC and the data acquisition program are fully described elsewhere (Drumm and Desai, 1983). The major features of the data acquisition and data reduction programs will be briefly described here.

Acquisition of data is triggered by an internal time clock, which is also a part of the MINC system. During a slow (quasi-static) cyclic test data from all the instruments are sampled every three seconds. During a fast cyclic test readings of all instruments are taken continuously for cycles 1 through 10, then continuously for two cycles after cycles number 20, 50, 100, 150, 200, 250, 300, 350, 400, 450 and 500. Data from all the instruments may be sampled up to sixteen times during a given fast cycle. The voltage signal from each instrument contains some "noise" or high-frequency variation in voltage. Since these deviations in the voltage signal may be recorded by the MINC, two voltage readings are taken for each sampling and averaged during the data reduction process. Thus, during a fast cyclic test, for each load cycle for which data is recorded, thirty-two actual voltage readings per cycle are taken and stored in the memory of the microcomputer for the duration of the test. Upon completion of the test, the computer writes all the test data onto a floppy disk for permanent storage. The voltages may then be printed out to obtain a hard copy of the raw data, or the data may be submitted to a data reduction program.

The data reduction program computes an arithmetic average of the two data readings taken at each sampling to yield one voltage sample. From the average voltage values, the shear stress, relative tangential displacement, normal stress, and vertical relative displacement are determined. Stresses are calculated by dividing loads by the area of the

rock joint (idealized) surface, which gives an average value for stress. The maximum and minimum shear stress and the maximum and minimum relative displacement within a given cycle are also determined.

The results of the data reduction program may be printed out to yield a listing of all the computed stresses and relative displacements for each cycle for which readings were taken. The maximum and minimum shear stresses and relative tangential displacements are also output.

Assembly of the Device

After securing the upper and lower samples to their respective holders, the structured surfaces of the samples are cleaned and the top sample placed on top of the bottom sample in the load frame with a winch and trolley system. By suspending the upper sample slightly above the lower sample, the rail system can be installed and the horizontal actuator connected to the upper sample holder without disturbing the structured surface. Before lowering the upper sample completely, the centers of the top and bottom samples are aligned with the horizontal actuator using center marks placed on the samples before they are secured to their sample holders. Aligning the samples in this manner assures as close a mating as possible between the upper and lower structured surfaces. Also, the Bison gages placed in the center of the top and bottom samples need to be coaxially aligned as close as possible prior to testing. After lowering the upper sample to its proper position, the horizontal actuator is leveled.

The vertical load system is installed such that the load plate is placed level on top of the upper sample and the vertical load actuator is directly above the center of the samples prior to testing. In order to accomplish this, a leveling plate is placed atop the upper sample, and leveled. The vertical load plate with the load cell is placed on this level plate. The vertical actuator is then trolleyed into position above the center of the samples and secured. Vertical loads can now be applied to the sample by lowering the piston of the actuator into a yoke which is connected to the load cell.

Once the device is assembled, electrical connections are made between the measurement instruments, the control units, readout devices, and any excitation or signal conditioners required by the instruments. The vertical and horizontal load cells, the horizontal LVDT, and the two (front and back) outside LVDT's are connected to MTS 406 controllers. These controllers provide excitation and signal conditioning required by the instruments and can monitor device outputs to be used for motion or force control. The control units can also direct the output signals to the MINC-11 data acquisition system.

The Bison gages used to measure vertical displacements at the center of the joint are connected to a Bison Model 4101A Soil Strain Indicator. This instrument provides signal conditioning and excitation to the coils and directs the output signals to the MINC-11 data acquisition system.

The two (front and back) linear motion sensors placed on the protruding plates of the upper sample receive excitation of 10 volts from a DC power supply. Sensor outputs are wired directly to the MINC-11 data acquisition system.

CHAPTER 4

CALIBRATION OF INSTRUMENTS

The instruments employed including load cells, LVDTs, displacement sensors, and inductance coils respond to a change in the quantity to be measured, be it load or displacement, with a change in voltage output. Calibration of instruments involves the establishment of a definite relationship between the voltage output of the instrument and the quantity measured. The recorded voltage output of the instruments may also be affected by factors other than the quantity of interest. These factors include changes in temperature, the proximity of metals or magnetic fields, capacitance of cables used in making connections, the excitation provided to the instruments, signal conditioning, and characteristics of the data acquisition system. These effects must either be shown to be negligible, compensated for, or controlled in some manner such that the change in voltage due to the measured quantity alone is essentially realized. The degree to which this may be accomplished, and how well a definite relationship between the measured quantity and the voltage output is established will determine the accuracy and the repeatability of the instrument.

Knowledge of the accuracy and repeatability of instruments is especially important when studying the shear behavior of rock joints, particularly with regard to displacements. The tangential displacement

which occurs prior to reaching the proportional limit, and the amount of compression which occurs prior to dilation during direct shear testing of rock joints are extremely small quantities. The constitutive model requires determination of certain parameters such as the initial shear stiffness, and parameters which are a part of the yield and potential functions employed in the plasticity formulation, which are determined using these small quantities. How accurately these parameters are evaluated is directly related to the accuracy and repeatability of the instruments used to make measurements during testing.

Details of instrument calibrations are included in part II of the final report for this project submitted to the Air Force Office of Scientific Research. This report is entitled "Constitutive Modeling of Idealized Rock Joints Under Cyclic Loading; Final Report, Part II." Only calibration of inductance coils will be discussed in this chapter.

As justification for including this chapter, results from inductance coil measurements are shown to be reliable. To the author's knowledge, this is the first time these instruments have been used for the measurement of vertical displacement during direct shear testing. Proper calibration procedures must be established as well as the precision, accuracy and repeatability of the instrument.

Inductance Coils

The Bison Instrument Inductance Coils (Bison Gages) were calibrated using the calibration fixture depicted in Fig. 4-1. The

Figure 4-1. Calibration Instrument
for Inductance Coils

calibration fixture is made of wood such that the fixture does not affect the magnetic field surrounding the coils. Coils are mounted to the calibration fixture such that they are coaxially aligned. One coil is held fixed and the other coil, attached to a sliding wooden rod, may be translated by turning a micrometer at the end of the fixture. The micrometer is manufactured by Schaevitz and has a total throw of 1.0 in. (2.54 cm.) and an accuracy of 0.0001 in. (0.0025 mm.). During calibration the coils are connected to the Bison Model #4101A Soil Strain Indicator which supplies excitation and signal conditioning required by the coils, and directs output to the MINC-11 data acquisition system.

The calibration of the Bison gages involves two phases of calibration, spacing calibration and meter calibration. Both are fully described in the "Bison Instruments Soil Strain Gage Model 4101A Instruction Manual." The spacing calibration consists of mounting the coils on the calibration fixture and determining settings (amplitude dial) on the indicator unit required to balance the instrument (inductance bridge) at different coil spacings. The meter calibration is intended to determine the displacement that will cause the meter to deflect 100% (5.0 volts) from an initially balanced condition which is termed as 100% full scale displacement. The resulting calibration allows determination of the initial spacing of the coils placed in the test specimens (idealized rock joints), and accumulated deformation from the voltage output (meter deflection) at a given time. The displacement is calculated by multiplying the per cent meter deflection by the 100% full scale deflections

determined from the calibration. Typical calibration plots for both the spacing and meter calibrations are presented in Fig. 4-2 (a) and (b).

The procedure for using these plots for measurements during testing is as follows:

- After assembly of the device, the strain indicator is balanced. The initial coil spacing is determined from Fig. 4-2 (a) corresponding to the amplitude dial setting shown on the indicator unit. For example, if the amplitude reading is 900, the initial spacing is 3.35 in. (8.51 cm.).

- When the coils move during testing, the indicator shows a positive (extension) or negative (compression) reading. The ordinate in Fig. 4-2 (b) shows 100% full scale displacement. Then, depending upon the meter deflection (some percentage of 5.0 volts), displacements are calculated as a percentage of the full scale displacement for the given initial spacing. For example, if the meter reading is x , the measured displacement for a spacing of 3.35 in. would be $(0.013) (x)/100$, where 0.013 corresponds to an amplitude dial setting of 900.

Linearity of Meter Deflection

The calibration assumes the deflection to be a linear function of coil displacement. This was verified by setting a pair of coils on the calibration fixture, and by comparing voltage outputs with applied displacements. This verification was found to be satisfactory, particularly for displacements above 0.0008 in. (0.02 mm.). For displacements as small as 0.0003 in. (.0076 mm.), the error is as high as 40%.

Table 4-1 shows details of this verification.

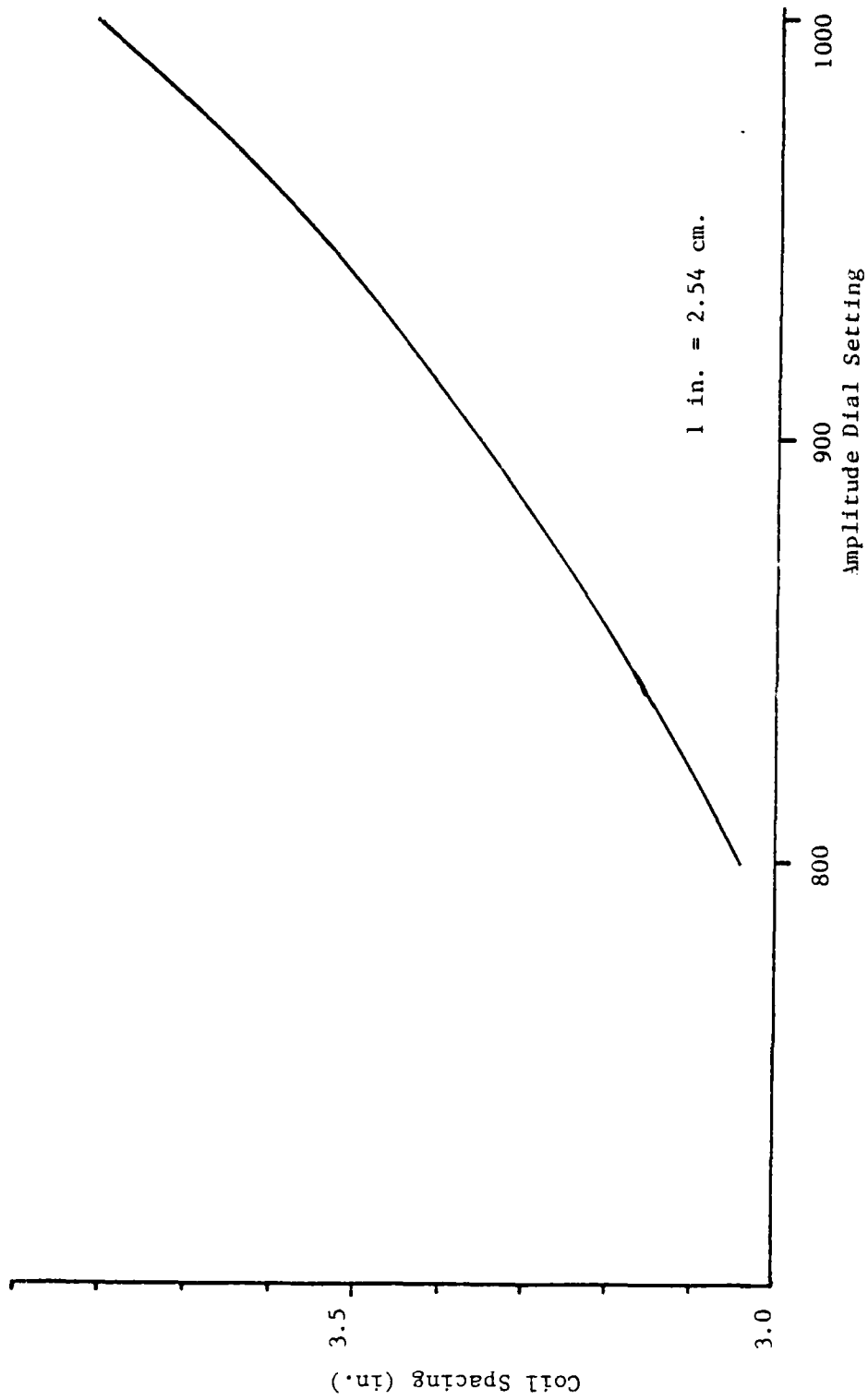


Figure 4-2(a). Typical Bison Cage Spacing Calibration Curve

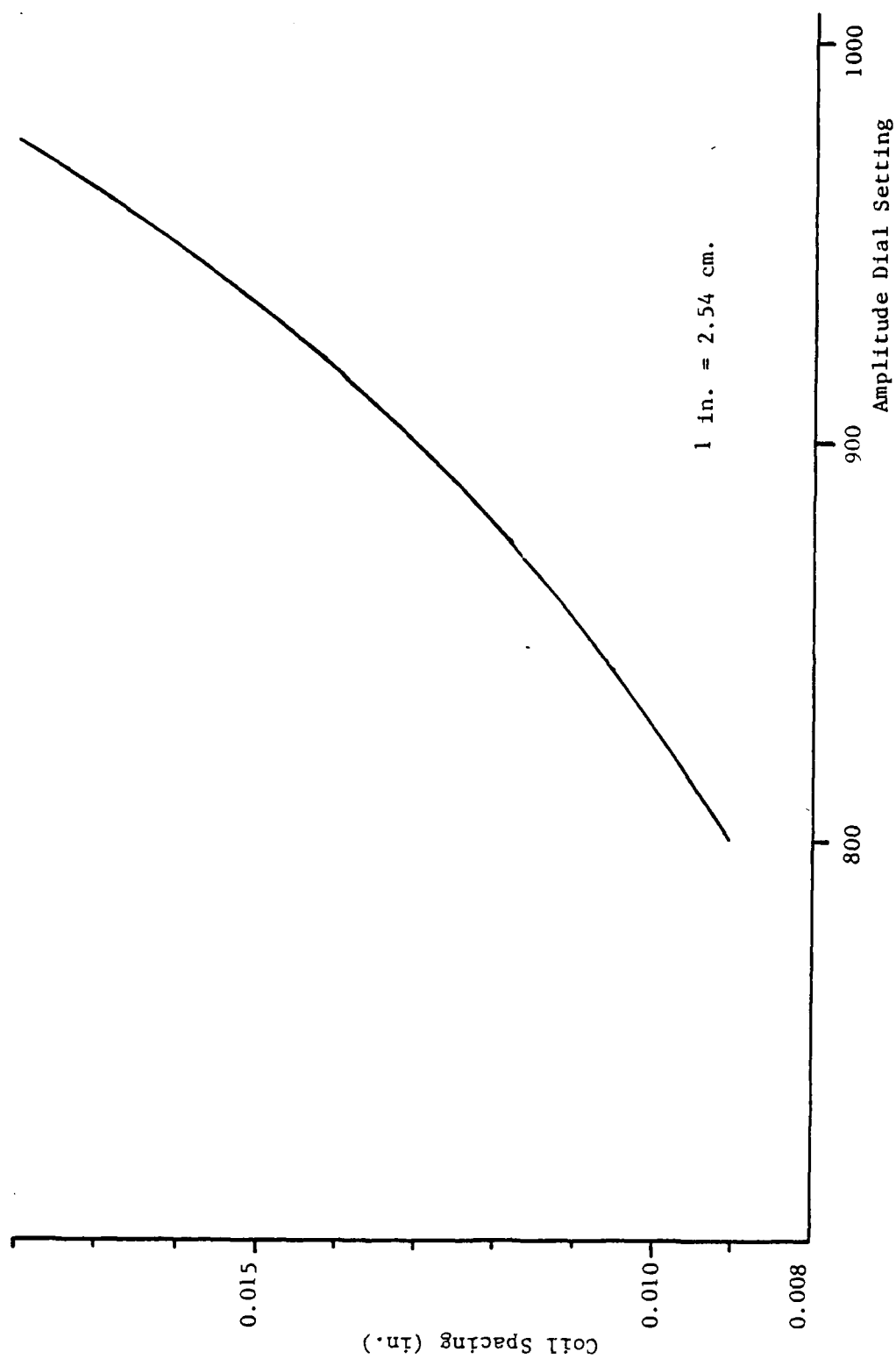


Figure 4-2(b). Typical Bison Gage Meter Calibration Curve

Table 4-1. Check on Linearity of Meter Deflection

Amplitude = 950
Cal = 150

True Displacement	Measured Displacement	% Error
0.0000	0.0000	
0.0005	0.0003	40
0.0010	0.0008	20
0.0015	0.0015	0
0.0020	0.0016	20
0.0025	0.0020	20
0.0030	0.0028	7
0.0035	0.0034	3
0.0040	0.0038	5
0.0045	0.0043	4
0.0050	0.0049	2
0.0055	0.0052	5
0.0060	0.0058	3
0.0065	0.0063	3
0.0070	0.0069	1
0.0075	0.0073	3
0.0080	0.0080	0
0.0085	0.0083	2
0.0090	0.0090	0
0.0095	0.0094	1
0.0100	0.0100	0
0.0105	0.0104	1
0.0110	0.0110	0
0.0115	0.0115	0
0.0120	0.0120	0
0.0125	0.0125	0
0.0130	0.0132	2
0.0135	0.0137	1
0.0140	0.0143	2
0.0145	0.0148	2
0.0150	0.0153	2
0.0155	0.0158	2
0.0160	0.0164	3

Precision

The precision of the Bison gages was checked by repeatedly mounting the same pair of coils on the calibration fixture and comparing results. Table 4-2 summarizes these results. The precision of the instrument is within 0.1%, based on a full scale output of 5 volts.

Effects on Calibration

The voltage output of the Bison gages may be affected by factors such as misalignment of the coils, rotations of the coils during deformation, and nearby metals or magnetic fields.

Misalignment. Misalignment of the Bison gages, as depicted in Fig. 4-3, is a shift in the relative position of the coils such that they are no longer coaxial. The effect of coil misalignment on the calibration of the Bison gages is of interest for two reasons. First, the coils may not be perfectly coaxial when placed within the specimens due to errors in measurement. Secondly, as the upper sample is displaced during direct shear, the coils displace with respect to one another and become misaligned. The calibration assumes that the coils are initially coaxially aligned. The purpose for studying the effect of coil misalignment is twofold:

1. To determine the accuracy of the Bison gage readings, given the uncertainty involved in their initial position; i.e., misalignment due to errors in measurement during placement within shear test specimens.
2. To determine a correction factor to be applied to readings after a known amount of misalignment has taken place; i.e., misalignment due to tangential displacement imposed during direct shear testing.

Table 4-2. Verification of Precision of Bison Soil Strain Gage

Amplitude Setting = 900

Reading #	Initial Spacing (in.)	Strain % F.S. Compression	Strain % F. S. Extension
1	4.504	-5.45	7.04
2	4.504	-5.56	6.98
3	4.507	-5.49	7.03
4	4.502	-5.55	7.02
5	4.513	-5.51	7.04

F.S. = Full Scale

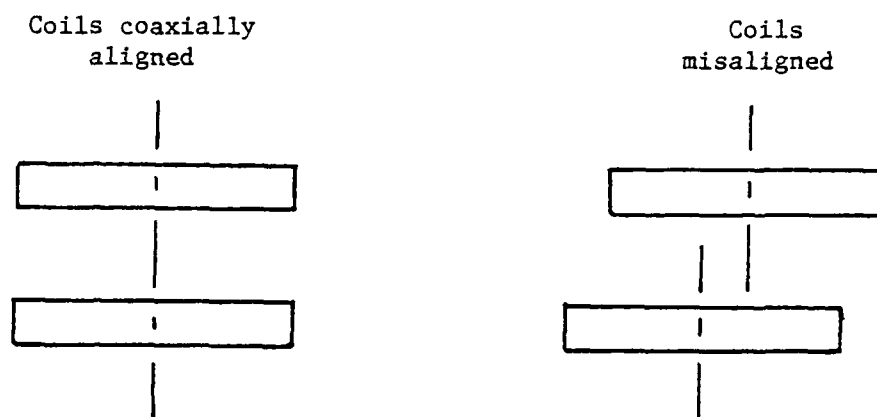


Figure 4-3. Misalignment of Inductance Coils

The effect of coil misalignment on the calibration was studied using a special vertical offset caliper, fastened to the calibration fixture as shown in Fig 4-4. One Bison gage is secured to the calibration fixture as before. The other is fastened to the vertical offset caliper. The vertical offset caliper enables one Bison gage to move up or down vertically in measured increments with respect to the other, initially coaxially aligned, coil. The Bison gage calibration was performed with the gages coaxially aligned, misaligned by 0.1 in. (2.54 mm.), and misaligned by 0.5 in. (1.27 cm.).

The meter calibration at different offsets was performed considering two different cases. In one case, the Bison gages were balanced in the coaxially aligned configuration, and then offset. This case corresponds to direct shear test conditions where the coils may be initially coaxially aligned when the instrument is balanced, and then misaligned due to tangential displacement during shear. For the second case, the Bison gages were balanced in the offset position, and this case was used to ascertain any errors which may be present due to uncertainties involved in the initial alignment of the coils.

Figures 4-5 (a) and (b) present results from the meter and spacing calibrations at the various degrees of alignment. Figure 4-5 (a) indicates that the spacing calibration is not significantly affected by offsets as high as 0.5 in. (1.27 cm.). The difference between the spacing calibration for the coaxially aligned case and the case of 0.1 in. (1.27 cm.) offset differs from the others by 1% at a spacing of around 3.8 in. (9.65 cm.).

Figure 4-4. Vertical Offset Caliper

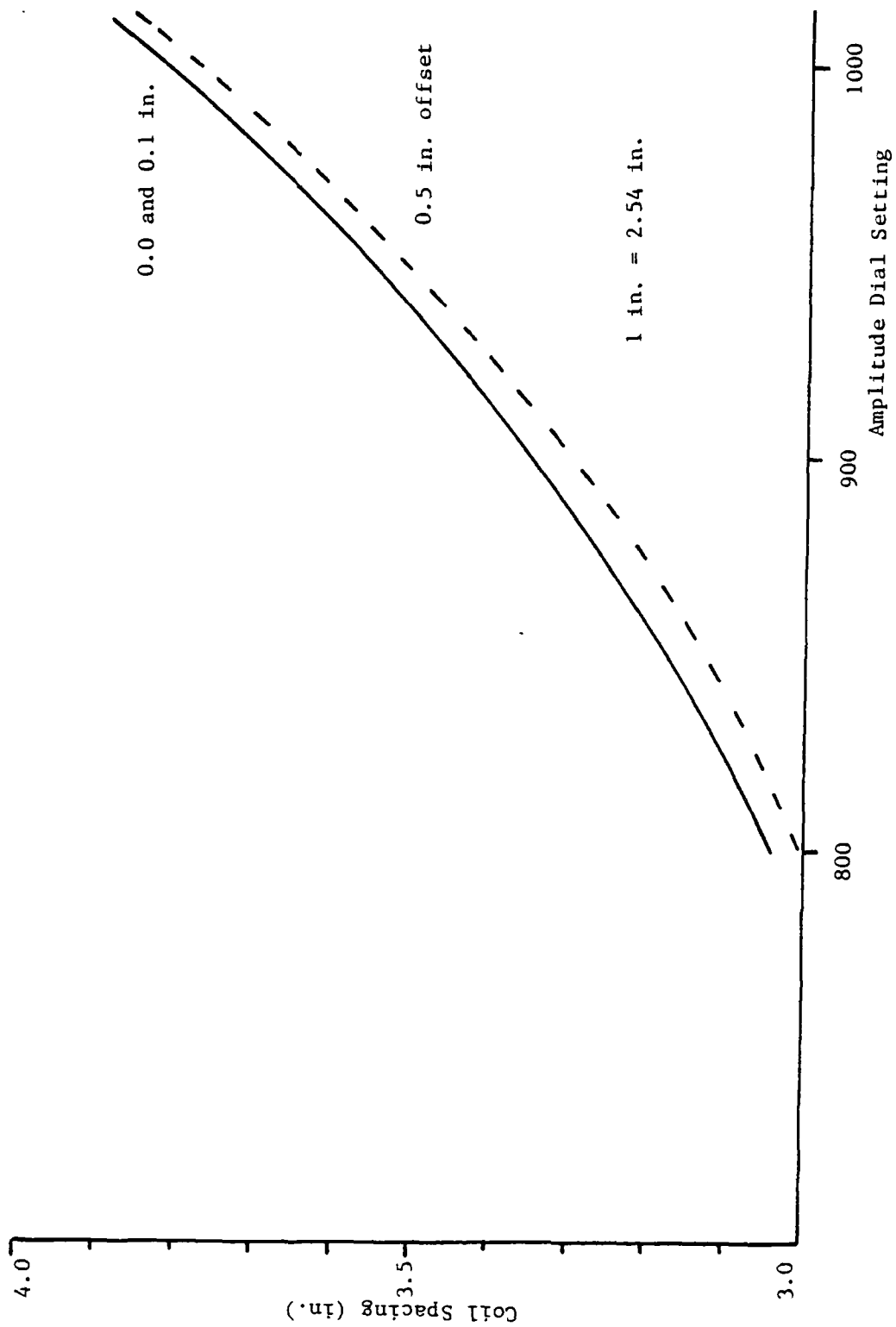


Figure 4-5(a). Effect of Coil Misalignment on Spacing Calibration

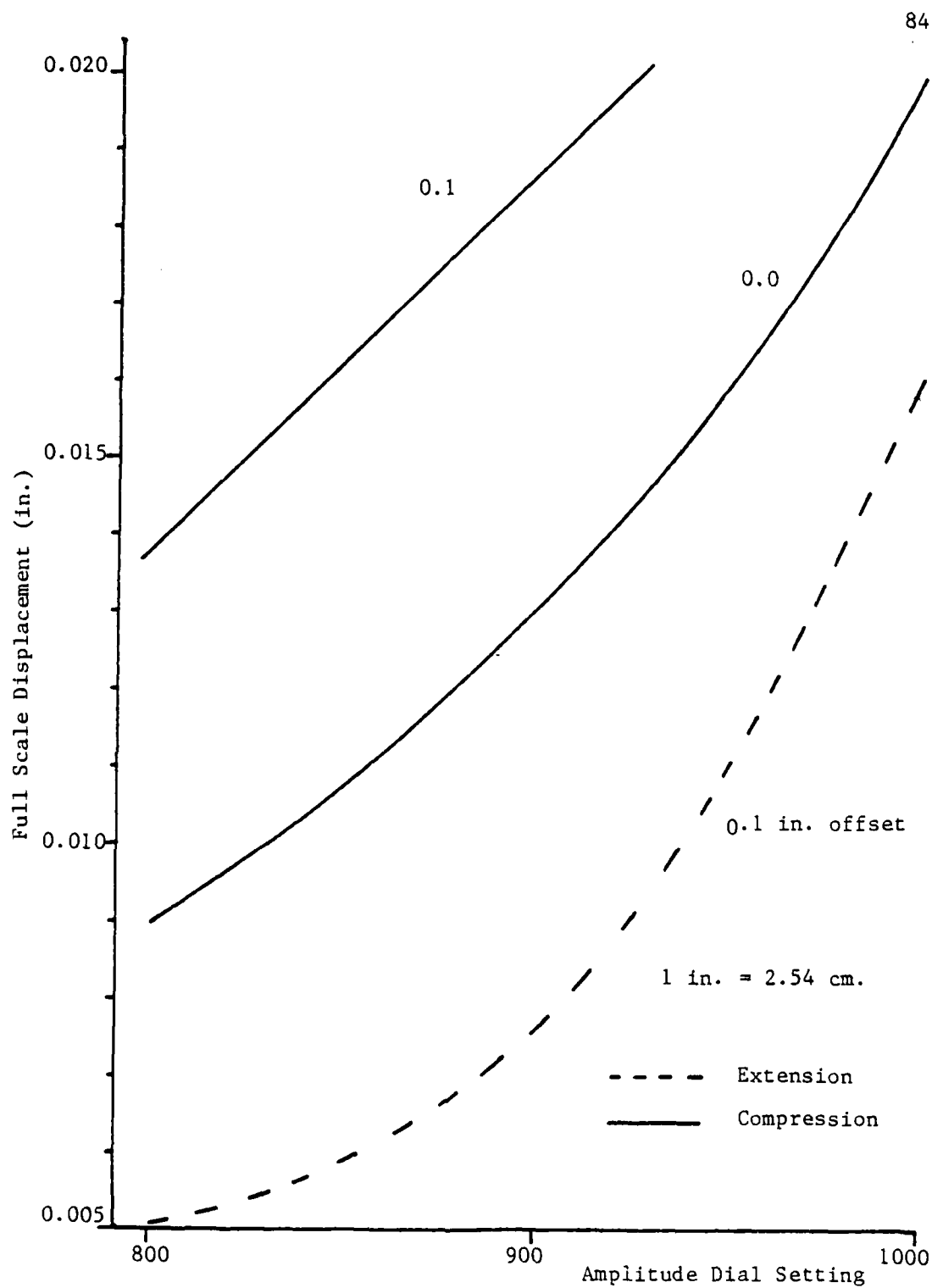


Figure 4-5(b). Effect of Coil Misalignment on Meter Calibration: Case 1

Figure 4-5(b) indicates that when the Bison gages are balanced in the initial coaxially aligned position and then offset by 0.10 in. (2.54 cm.), the calibration is shifted by 0.005 in. (0.127 mm.) from the coaxially aligned case. The shift is such that during extension (positive displacement), the 100% full scale displacement at a given amplitude dial setting is decreased by 0.005 in. (0.127 mm.) above the 100% full scale displacement at the same amplitude dial setting for the case when the coils remain in the coaxial alignment. During compression (negative displacement) the absolute value of the 100% full scale displacement at a given amplitude dial setting when the coils are offset 0.10 in. (2.54 mm.) is increased 0.005 in. (0.127 cm.) from the coaxially aligned case. The shift in the calibration curve for an offset of 0.5 in. (1.27 cm.) is not presented since this shift was so large that the needle of the voltage meter displaced the full amount due to the offset alone.

Using this data, an adjustment to the meter calibration was determined which could account for the effects of coil misalignment, given the misalignment occurred with respect to an assumed initial coaxially aligned configuration. The adjustment assumes that the shift in the calibration curve between the case when the coils remain in the coaxial alignment and when they are misaligned is linear with respect to misalignment for misalignments between 0.0 and 0.1 in. (0.0 to 2.54 cm.). The adjustment was incorporated into the calibration as follows:

1. After assembly of the shear device, as discussed in Chapter 3, the Bison gages are initially balanced.
2. Using the amplitude dial reading, and assuming the coils are initially in coaxial alignment, the 100 per cent full-scale displacement is determined from the meter calibration.
3. During a direct shear test, the tangential displacement and the voltage output (meter deflection) of the Bison indicator unit are determined.
4. The 100 per cent full-scale displacement determined in Step 2 is multiplied by the per cent meter deflection determined in Step 3 to yield the unadjusted vertical displacement.
5. An adjustment is calculated based on the tangential displacement (coil misalignment) which corrects the vertical displacement determined in Step 4. The adjustment is equal to the ratio of the tangential displacement, determined in Step 2, to 0.1 in. (2.54 mm.), multiplied by 0.005 in. (0.127 mm.). This adjustment is only valid for offsets between 0.0 and 0.1 in. (0.00 to 2.54 mm.).

Table 3 presents results from the meter calibration of the Bison gages when misaligned by 0.10 in. (2.54 mm.), and balanced in this offset configuration, and compares these results with the meter calibration of the coils when coaxially aligned. The table indicates that when the Bison gages are initially balanced in the offset configuration, the difference in 100 per cent full-scale displacement for a given amplitude dial setting from the coaxially aligned case is within 0.001 in.

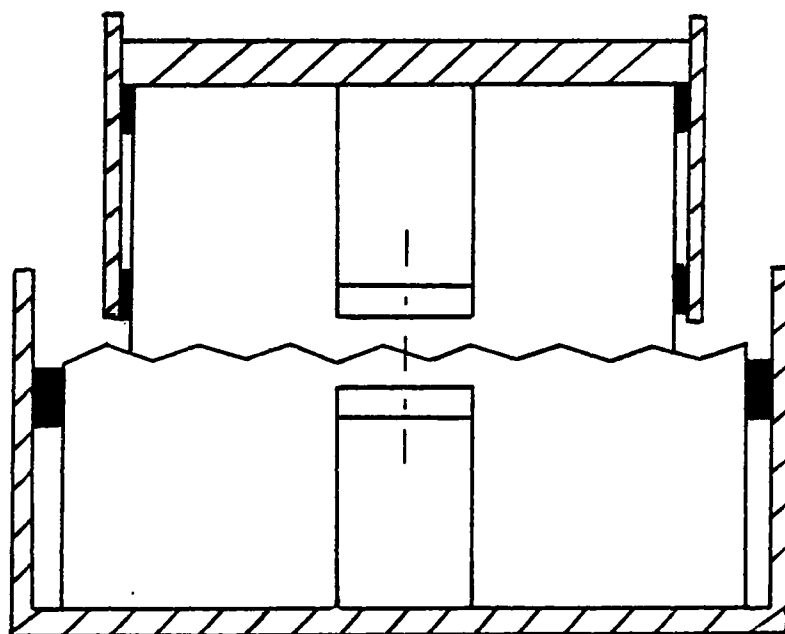
Table 4-3. Comparison of Meter Calibration
With Coils Aligned and Misaligned

Amplitude Setting	Full Scale Displacement			
	Offset			
	0.0 in.		0.1 in.	
	Exten.	Comp.	Exten.	Comp.
800	0.009	0.010	0.010	0.009
850	0.010	0.011	0.011	0.010
900	0.014	0.013	0.014	0.013
950	0.018	0.014	0.018	0.015
1000	0.019	0.015	0.020	0.020

(.025 mm.). Therefore, the uncertainty involved with the initial position of the coils relative to one another is not considered significant for offsets less than 0.10 in. (2.54 mm.).

Rotations. During direct shear testing, not only does the upper sample translate with respect to the lower sample, but a (small) amount of rotation of the upper sample about an axis in the plane of shear perpendicular to the direction of shear may also be present. Effects of coil rotations on the Bison gage calibration are harder to evaluate than the effects of coil misalignment because of the difficulty in producing rotation without axial movement. Truesdale and Schwab (1965) found that for angular rotation less than plus or minus 10 degrees, the effect was not significant. Angular rotation in excess of this amount is not anticipated during direct shear testing.

Surrounding Metal. With the Bison gages placed within the samples, and the shear device assembled as described in Chapter 3, the coils are surrounded by the metal sample holders as shown in Fig. 4-6. The effect of surrounding metal on the calibration of the Bison gages was checked by placing the gages, mounted to the calibration fixture, within the upper sample holder as depicted in Fig. 4-7. Since the upper sample holder has inside dimensions of 12 in. by 12 in. (30.5 cm. by 30.5 cm.), the boundaries of the metal box were 6 in. (15.25 cm.) from the center of the inductance coils, or about three coil diameters away. With the coils in this configuration, a spacing and meter calibration was performed with the instrument. Table 4-4 presents results



 Metal

Figure 4-6. Bison Gages Surrounded by Metal Sample Holder During Testing

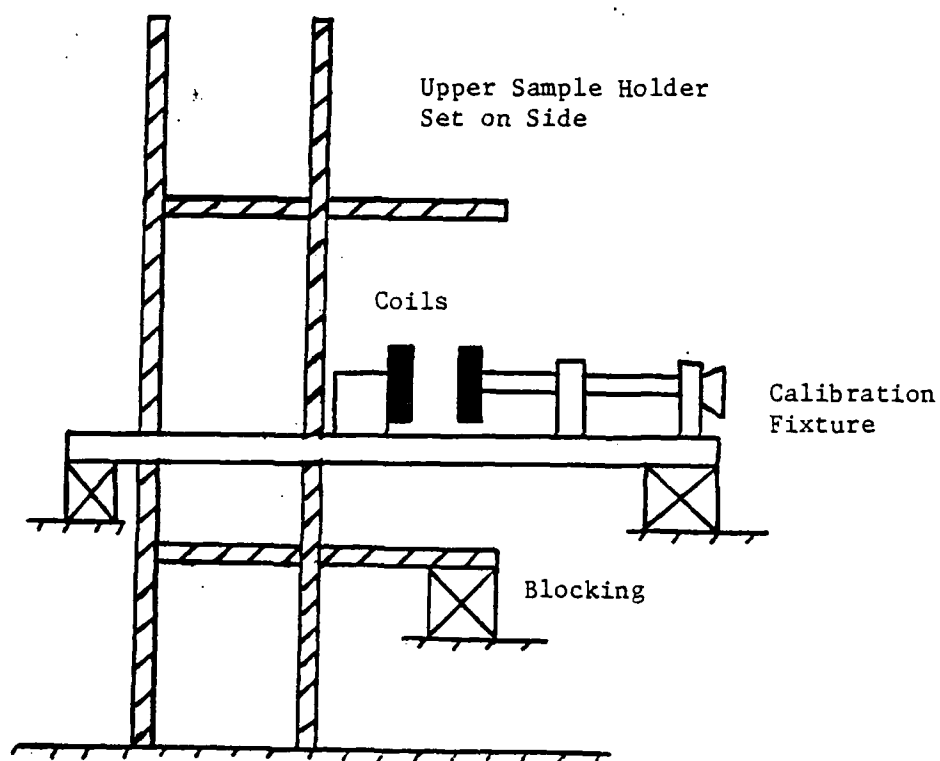


Figure 4-7. Bison Gages Within the Confines of the Upper Sample Holder

Table 4-4. Comparison of Meter Calibration in the
Absence Of and Surrounded by Metal
Sample Holders

Amplitude Setting	Spacing			
	No Metal		Metal	
976	3.7900		3.5665	
950	3.550		3.4550	
900	3.3500		3.2695	

Amplitude Setting	Full-Scale Displacement			
	No Metal		Metal	
	Exten.	Comp.	Exten.	Comp.
976	0.019	0.015	-	0.016
950	0.018	0.014	0.016	0.013
900	0.014	0.013	0.012	0.011

of the calibration performed in the presence of the surrounding metal, and compares them to the results of the calibration performed in the absence of the surrounding metal.

The coil spacing at a given amplitude dial setting in the presence of surrounding metal differed by less than 5 per cent from the coil spacing at the same amplitude dial setting, but in the absence of surrounding metal. Results from the meter calibrations indicate that the 100 per cent full-scale displacements at a given amplitude dial setting in the presence of surrounding metal differed between 6 per cent to 15 per cent from the 100 per cent full-scale displacements at the same amplitude dial setting, but in the absence of surrounding metal. This difference is less at higher amplitude dial settings. The errors in the calibration of the Bison gages due to the presence of surrounding metal appear to be acceptable, and the calibrations performed in the absence of surrounding metal were used.

CHAPTER 5

DESCRIPTION OF SAMPLES

Ideally, laboratory testing intended to study rock joint behavior should be performed on rock joint samples obtained from the field. Due to the size, number, and consistency of samples required for this study, obtaining samples from the field was neither practical nor economical. Artificial rock joint surfaces were prepared by casting concrete against a structured surface. The structured surface had a "sawtooth" shaped pattern intended to simulate asperities on the rock joint surface. Figure 5-1 depicts the "sawtooth" shaped asperity pattern. Idealized rock joints were constructed by casting top and bottom samples such that when placed together, the asperities from the top and bottom produce a closely mated joint, as shown in Fig. 5-1. Different rock joint roughnesses were simulated by varying the angle of the "sawtooth" asperity side with respect to the horizontal. Samples were cast having asperity angles of 0, 5, 7, 9 and 15 degrees; the first denotes "smooth" surface.

Forms

Forms for casting concrete samples were constructed, as shown in Fig. 5-2. Bottom sample forms had inside dimensions of (L x W x H) 15.5 in. x 15.5 in. x 5.5 in. (39 cm. x 39 cm. x 14 cm.). Top sample forms had inside dimensions of 11.5 in. x 11.5 in. x 5.5 in. (29 cm. x 29 cm. x 14 cm.). Chamfer strips were placed around the perimeter of the

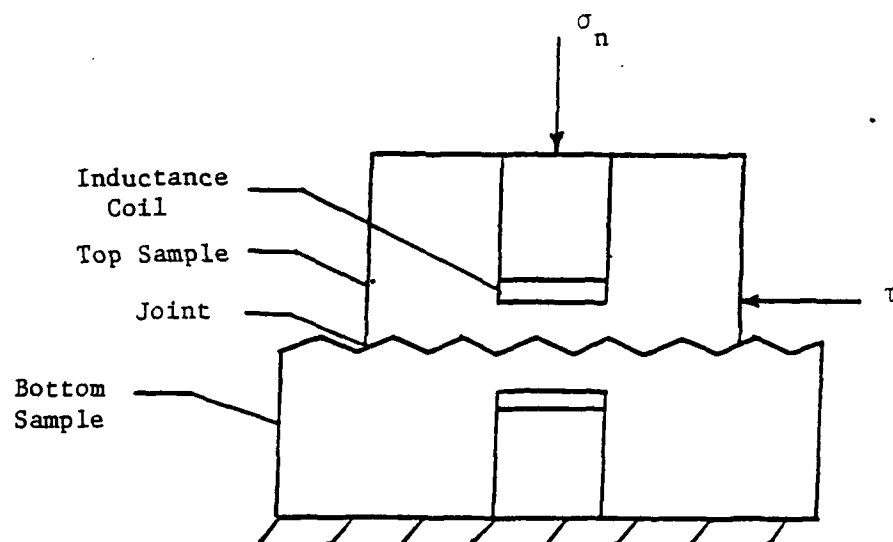


Figure 5-1. Sawtooth Shaped Asperity Pattern

Figure 5-2. Forms for Casting Concrete Samples

bottom of each form to reduce stress concentrations on the leading edges of the samples during shear. The form bottom for each sample consisted of the structured surface.

Provisions were made in the formwork such that instrumentation could be placed on the specimens. Cylindrical cavities were formed in the center of the top and bottom samples so that inductance coils could be placed for measurement of normal displacement close to the joint surface. These cavities were formed so that one-half inch (1.27 cm.) of concrete covered the bottom of the cavity. Also, metal plates were attached front and back on the bottom of a side form for the top sample. When partially embedded in concrete, these plates allowed attachment of linear voltage sensors to the top sample. Figure 5-3(a) and (b) is a sketch of the sample geometry.

Method of Casting

Using six sets of forms, as described in the preceding section, six specimens were cast at a time. Initially, six bottom specimens were cast, as shown in Fig. 5-4. After one day of curing, samples were removed from the forms and overturned. A piece of corrugated sheet metal, previously used as the structured surface at the form bottom, was then placed on the top of each sample, covering the newly exposed surfaces, which exhibited "sawtooth" shaped asperities. The top sample was then cast against the structured surface of the bottom sample, Fig. 5-5. In this manner, a close fit between the asperities of the top and bottom samples was assured.

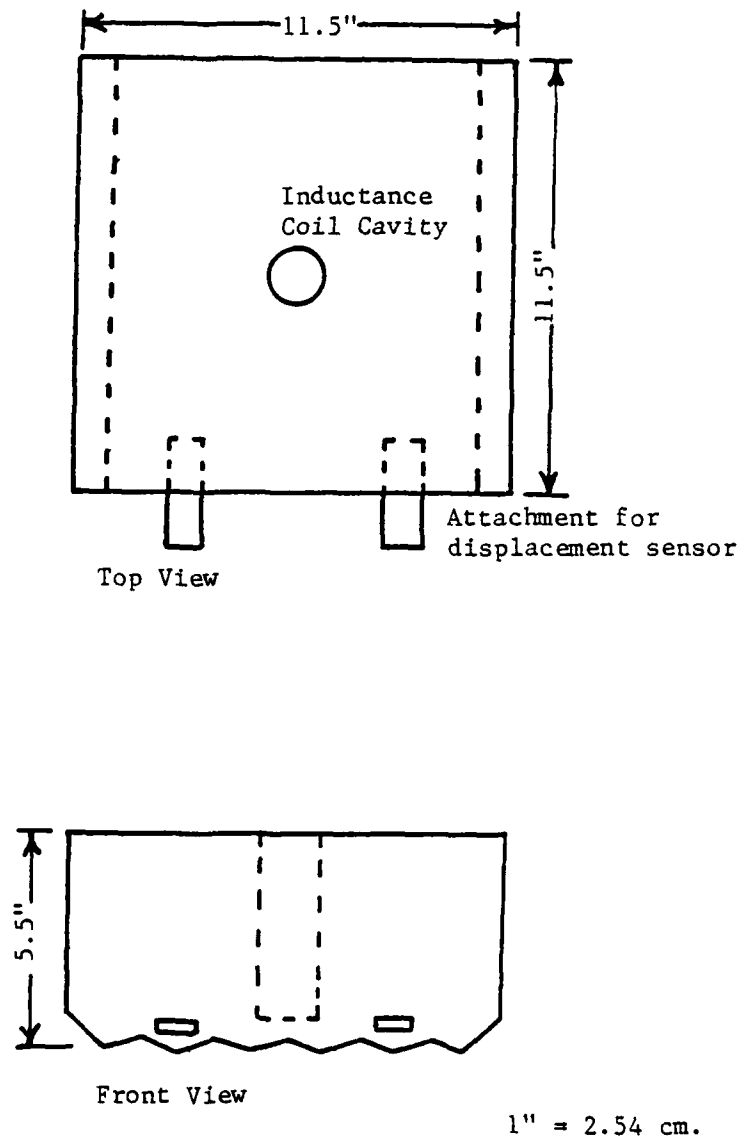
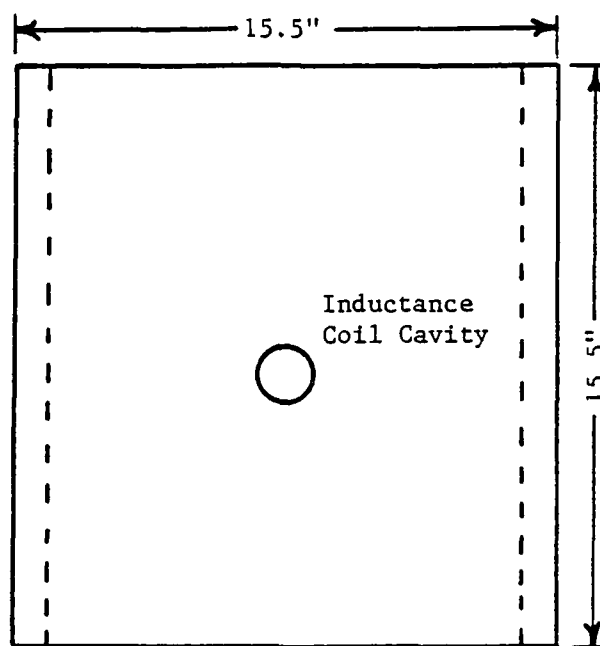
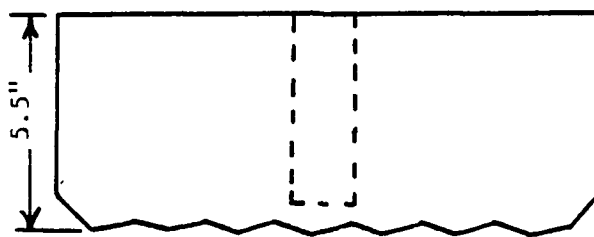


Figure 5-3(a). Sketch of Top Sample Geometry



Top View



Front View

 $1" = 2.54 \text{ cm.}$

Figure 5-3(b). Sketch of Bottom Sample Geometry

Figure 5-4. Casting of Bottom Samples

Figure 5-5. Casting of Top Samples

A concrete and a grout mix were employed. Details of the mixes are provided in the next section. The grout mix was placed for the first one-half inch (1.27 cm.) near the joint surface for both the top and bottom samples. This was to ensure that none of the larger aggregates used in the concrete mix were near the joint surface since these might dislodge during testing and affect the results.

Compaction of grout and concrete during casting was accomplished with a vibration table and a hand held concrete vibrator. Grout placed near the structured surface of the bottom samples was compacted with the vibration table, Fig. 5-6. The concrete used in the rest of the sample was compacted with the hand held concrete vibrator. Compaction of grout placed near the structured surface of the top sample was accomplished by touching the hand held concrete vibrator to the corrugated sheet metal. The concrete used in the rest of the sample was compacted with the hand held concrete vibrator as before.

Samples were cured for one day after casting the top samples, and forms were removed. Samples were then placed in a moist room to cure for 28 days. Upon removal from the curing room, the joint structured surfaces were cleaned with a sponge and a wire brush to remove debris or residue from the surfaces. Figure 5-7 is a picture of a typical sample after cleaning.

Concrete and Grout Mixes

Table 5-1 shows the proportions of materials used in the concrete and grout mixes. Figure 5-8 shows gradation curves for the sand and

Figure 5-6. Vibration Table Used for Compaction of
Concrete Near the Structured Surface
of the Bottom Sample

Figure 5-7. Typical Sample After Cleaning

Table 5-1. Concrete and Grout Mixes

(a) Cement Mix

cement: sand: coarse agg.: water

1: 3.26: 2.9: 0.75

(b) Grout Mix

cement: sand: water

1: 2: 0.55

Note: Ratios are determined by weight

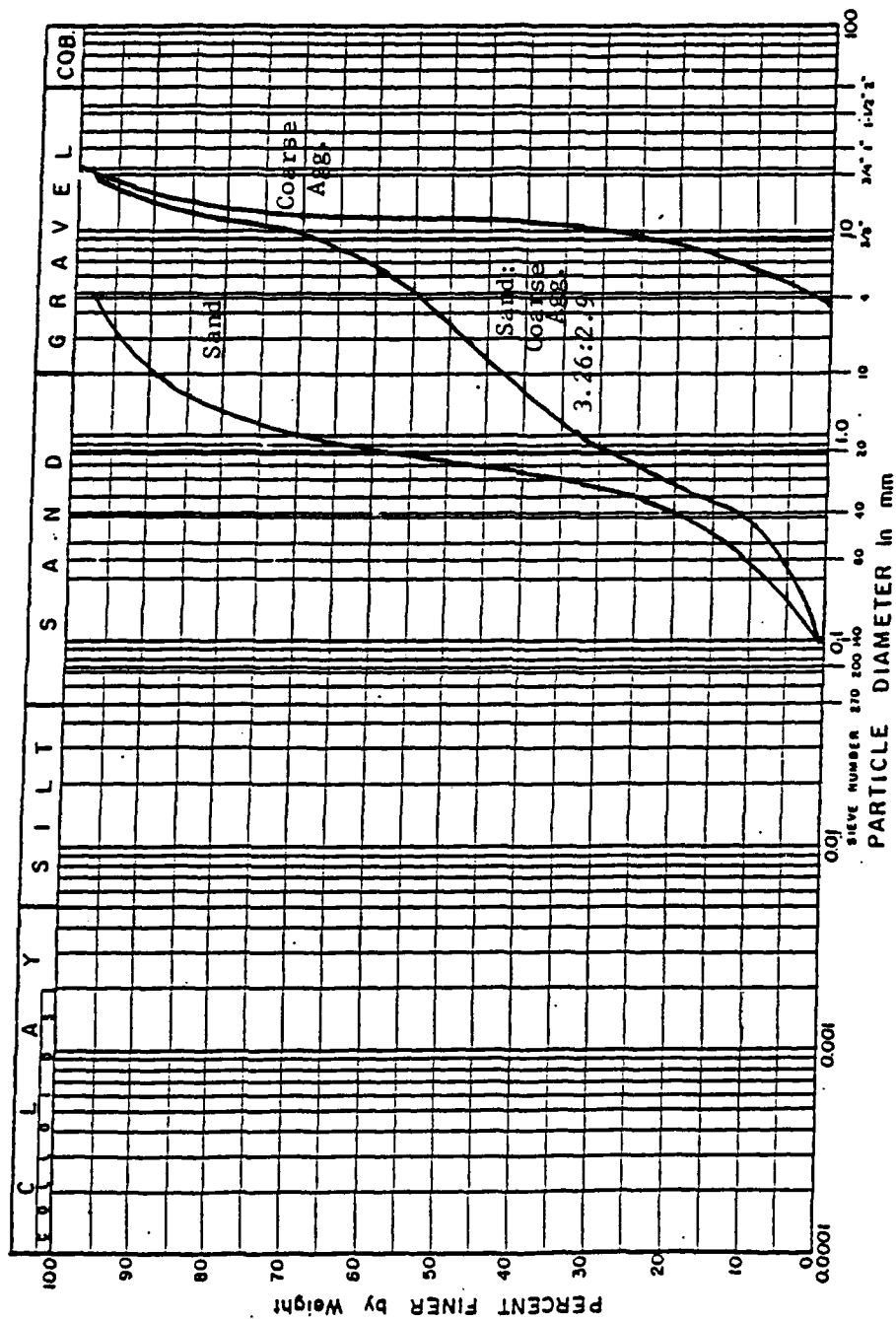


Figure 5-8. Gradation Curve for Sand and Coarse Aggregate Used in Concrete Mix Design

aggregates. The concrete mix used was the same as that used by Salami (1985), so that the model he developed for solid concrete could be used with the model developed here for joints to characterize an idealized jointed rock mass system at a later time.

Both the concrete and grout mixes were designed for a 28-day unconfined compressive strength of around 2500 psi (17.25 MPa). Cylinders for testing the 28-day unconfined compressive strength of both concrete and grout mixes were prepared during sample casting. Each strength determination involved testing three such samples. The results of the three tests were averaged to yield the 28-day unconfined compressive strength for a given mix. Displacement readings were taken during testing of one of the three cylinders so that a determination of Young's modulus after 28 days for a given mix can be made. Table 5-2(a) and (b) presents 28-day unconfined compression test results for grout and concrete mixes. Figures 9(a) and (b) present stress-strain data. An average 28-day unconfined compressive strength of 2500 psi (17.25 MPa) prevailed for both concrete and grout mixes. Young's modulus for the concrete and grout was determined as 3,500,000 psi and 2,000,000 psi (24,000 and 13,780 MPa), respectively.

Table 5-2(a). Twenty-Eight Day Unconfined Compressive
Strength Test Results for Concrete Mixes

Date of Cast	Cylinder	f'c (psi)	f'c (ave for cast)
4/26/84	1	2759	2948
	2	2936	
	3	3148	
5/10/84	1	2511	2582
	2	2405	
	3	2830	
6/19/84	1	2582	2511
	2	2405	
	3	2830	
10/25/85	1	1875	1934
	2	1981	
	3	1946	
11/8/85	1	1592	1592
	2	1592	
	3	1592	
2/6/86	1	3325	3278
	2	3272	
	3	1592	
6/9/86	1	1627	1981
	2	2476	
	3	1839	
7/2/86	1	3537	3384
	2	3537	
	3	3077	

1 psi = 6.89 KPa

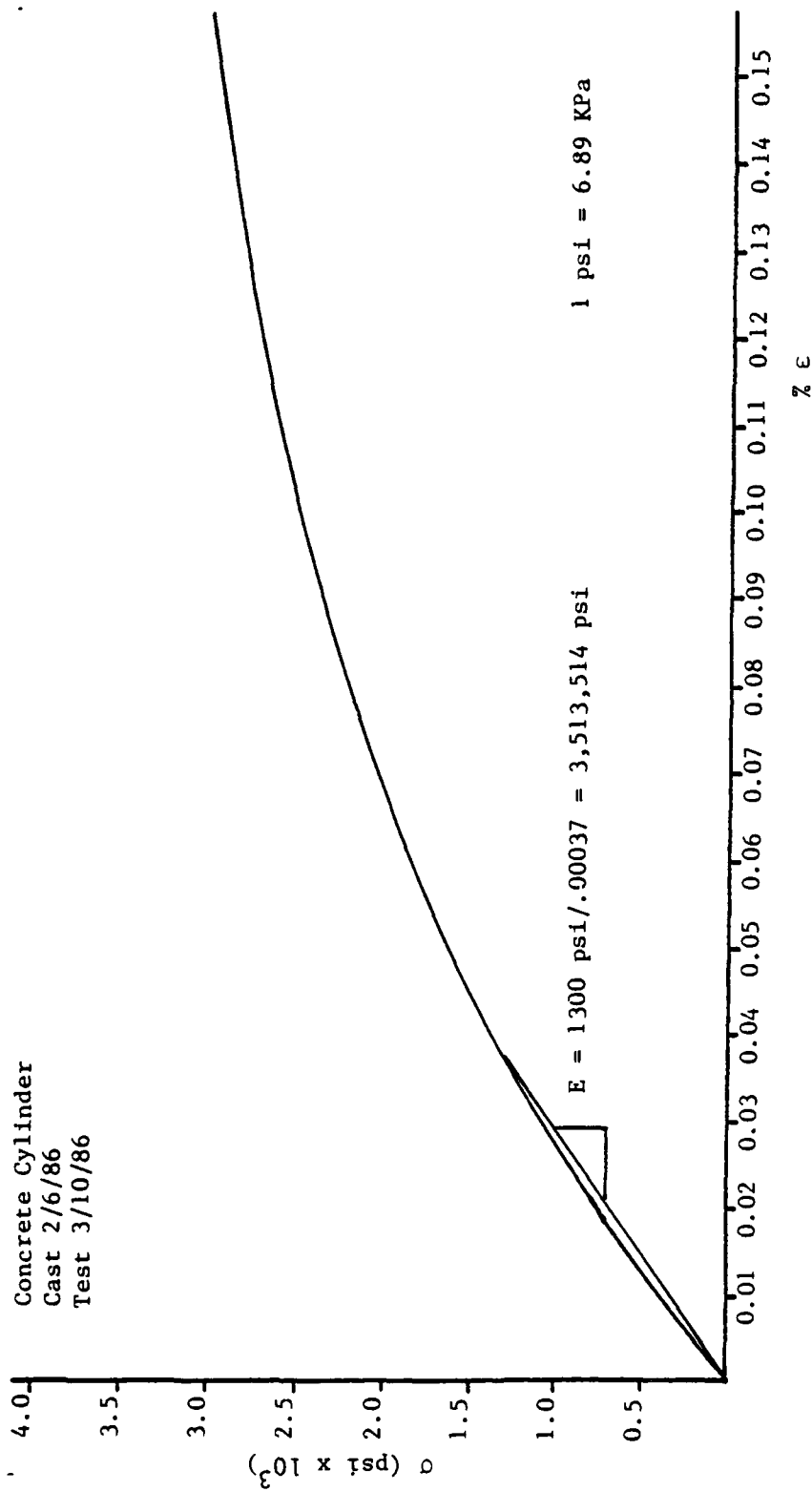
average = 2526 psi

Table 5-2(b). Twenty-Eight Day Unconfined Compressive
Strength Test Results for Grout Mixes

Date of Cast	Cylinder	f/c (psi)	f'c (ave. for cast)
2/11/86	1	1704	1627
	2	1627	
	3	1450	
6/13/86	1	2724	2100
	2	1733	
	3	1839	
7/9/86	1	3962	3868
	2	3750	
	3	3891	

1 psi = 6.89 KPa

average = 2531 psi

Figure 5-9(a). σ - ϵ Curve for Concrete Mix

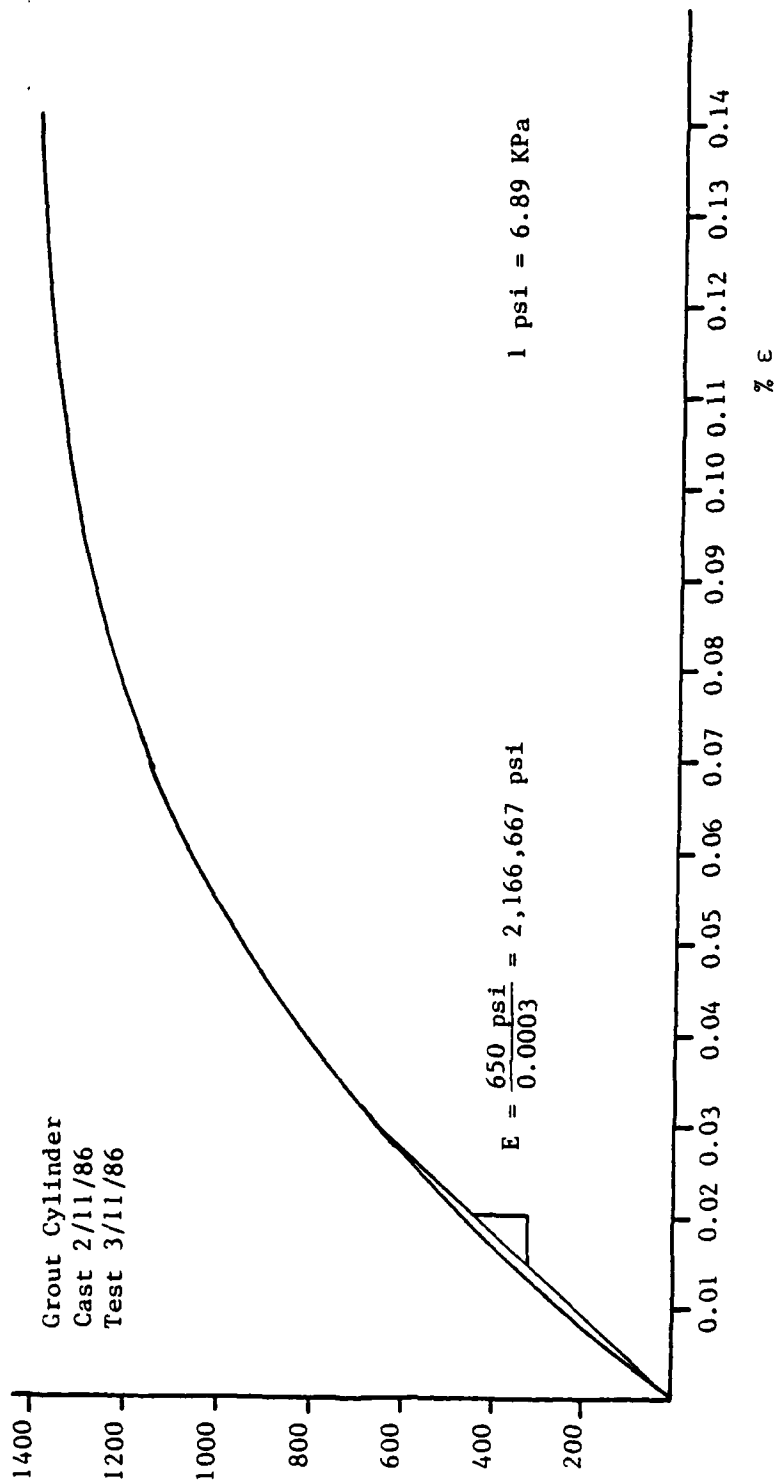


Figure 5-9(b). σ - ϵ Curve for Grout Mix

CHAPTER 6

DESCRIPTION OF TEST SERIES

A test program was undertaken to investigate the behavior of joints during quasi-static and cyclic shear loading by varying factors such as initial normal stress, roughness (asperity angles), rate of loading, and amplitude of displacements. This chapter describes the purpose of the investigation, and details of the tests.

Purpose of the Test Series

The purpose of the tests was to investigate the effects of different factors on the shear behavior of rock joints and to use this data base for defining the parameters in the plasticity model described in Chapter 7. Also, test results not used to find parameters for the plasticity model were provided, and back predictions of these test results using the plasticity model serve as a necessary, though not sufficient, condition for verification of the plasticity model.

Factors studied include the rate of loading, roughness of the joint, relative displacement during shear, the number of cycles during cyclic loading, and state of stress.

Details of the Test Series

The test series investigated both normal and shear behavior of the joints. Normal behavior of the joints was investigated by performing

normal load tests, described in the next section. Shear behavior was studied by performing large-scale direct shear tests. Fast cyclic and slow cyclic or quasi-static tests were performed in order to ascertain the effects of rate of loading as well as number of cycles on the shear behavior. Most of the direct shear tests were displacement-controlled. Some force-controlled testing was performed for validation purposes.

Normal Stress Tests

The objective of the normal stress tests was to study the response of the joints to normal stress. This entailed applying increments or decrements of normal stress and measuring the vertical compression or expansion of the joint.

Method. Normal load tests were performed by assembling the device so that the joint was mated. Initial readings of the vertical displacement measuring devices were taken. At this point, a small initial normal load was present due to the weight of the upper sample, and the vertical load plate. Increments of normal load were applied to the upper sample in the absence of shear forces in the plane of the joint. Average normal stresses were calculated by dividing the normal load by the cross-sectional area. As each increment of normal stress was applied, vertical displacement readings were taken.

Load Increments. In order to determine the elastic normal stiffness and plastic deformation of the joint, cycles of loading, unloading and reloading were applied. A plot of normal stress versus vertical

displacement for a typical normal stress test (9-degree surface) is presented in Fig. 6-1. Starting from the initial state of stress, normal stress increments of 5 psi (34 KPa) were applied until a normal stress of 20 psi (138 KPa) was reached (0-1). Then the sample was unloaded in decrements of 5 psi (138 KPa) until the initial state of stress was reached (1-2). Another cycle of loading was applied in increments of 10 psi (68.9 KPa) until a stress level of 40 psi (276 KPa) was attained (2-3-4), and once again the sample was unloaded to the initial state of stress, but this time in decrements of 10 psi (68.9 KPa) (4-5). Finally, the sample was reloaded in increments of 10 psi (68.9 KPa) until a normal stress of 50 psi (345 KPa) was reached (5-6).

Factors. Normal stress tests were performed on samples with different asperity side angles, including 5, 7, 9 and 15 degrees. In this manner, the effect of joint roughness on normal behavior was investigated.

Quasi-Static Shear Tests

The purpose of the quasi-static shear tests was to subject the joint to one slow cycle of displacement in direct shear. The tests were displacement-controlled with a rate of displacement of 0.05 in./min. (1.27 mm/min.).

Cycle of Displacement. The tests were displacement-controlled via the control unit which received a triangular displacement function from the function generator. The phase and amplitude of the function were adjusted to obtain the waveform depicted in Fig. 6-2(a). The

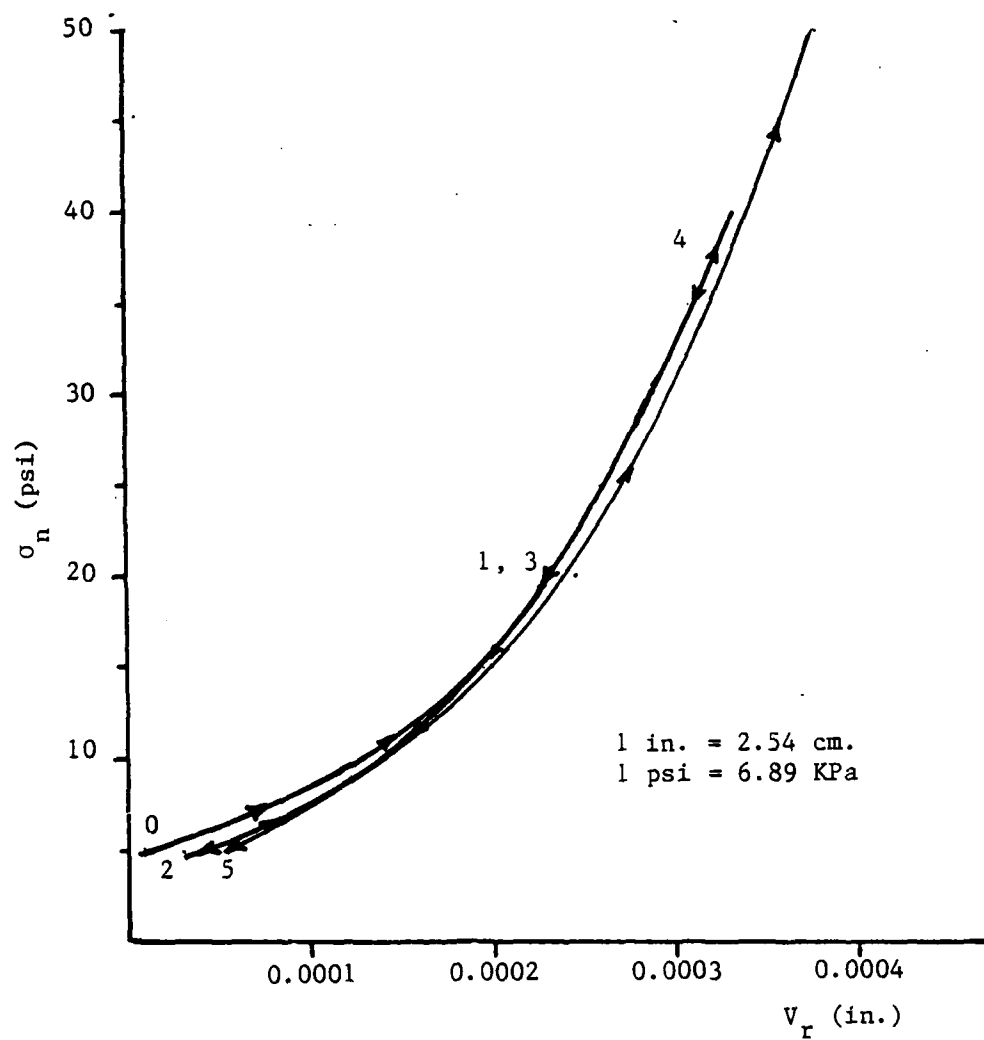


Figure 6-1. Normal Stress versus Vertical Displacement
From a Typical Normal Stress Test

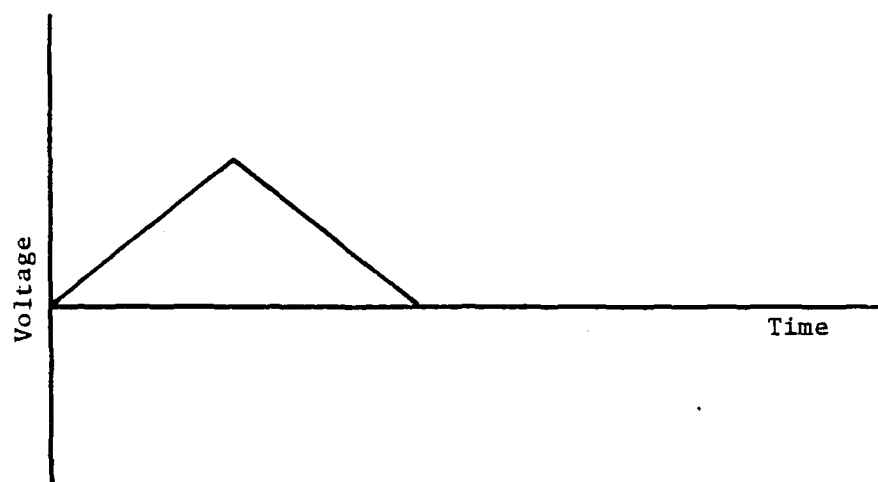


Figure 6-2(a). Waveform from Function Generator
for Quasi-static Tests

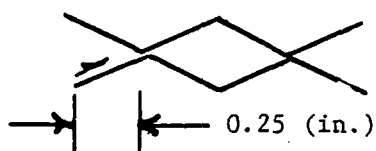
frequency was set so that the rate of displacement was .05 in./min. (1.27 mm./min.) given the maximum amplitude of displacement, 0.25 in. (6.35 mm.).

Figure 6-2(b) shows the motion of the upper sample due to the input function of Fig. 6-2(a). Initially, the upper sample was in a position such that the joint was fully mated, shown as datum in Fig. 6-2(b). The upper sample was then displaced in the horizontal direction (forward pass), about 0.25 in. (6.35 mm.), to a point where the peaks of the asperities from the top and bottom surfaces were almost in contact. During the forward pass, the upper sample traveled up the asperity sides of the bottom sample. The upper sample was then returned to its initial position (reverse pass). During the reverse pass, the upper sample traveled down the asperities of the bottom sample. The sample was initially loaded in shear, unloaded after the upper sample was displaced to its forward position, and then load reversal in direct shear occurred as the sample was displaced back to the initial position.

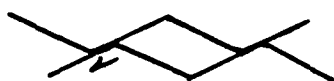
Method. To perform quasi-static shear tests, the device was assembled and initial readings of the horizontal and vertical displacement measuring devices were taken. A normal stress was applied, and vertical displacement due to the application of the normal stress was recorded. A cycle of displacement was applied via the input function received from the function generator. Readings of horizontal load and the vertical and horizontal displacement were taken during the test. Average shear stress was computed by dividing the horizontal load by the



(i) Datum



(ii) Forward Pass



Unloading in Shear



Shear Load Reversal

(iii) Reverse Pass

Figure 6-2(b). Motion of Upper Sample Due to
Input Function of Fig. 6-2(a)

projected cross-sectional area of the joint. Figures 6-3(a) and (b) are typical plots from a quasi-static direct shear test showing the variation of shear stress (τ), and normal displacement (v_r), respectively, with horizontal displacement (u_r).

Factors. Quasi-static shear tests were performed on surfaces with different roughnesses, including cast-smooth, ground-smooth, and asperity side angles of 5, 7, 9 and 15 degrees. For each roughness, tests were performed using normal stresses of 5, 10, 20, and 50 psi (34.5, 69, 138, and 345 KPa). A test with a normal stress of 100 psi (690 KPa) was also performed on the cast-smooth joint.

Damage. During shear the surfaces of rock joints may become damaged or worn. This damage may be visible on the joint surfaces in the form of striations, broken asperities, and/or gouge. The effects of shear on the joint surface were studied by comparing measurements made on the joint surface before shearing to measurements made on the joint surface after shear. These measurements include profilometer measurements, similar to those described by Farrington (1983), photographs of the joint surfaces, and measurements of the weight of the gouge material after shear.

Multiple Tests With One Sample. Between tests with a different normal stress, the device was disassembled, and the samples were cleaned of debris. In this manner, the same sample was used for all tests having a different normal stress. This assumes that previous testing did not cause significant damage to the joint surface.

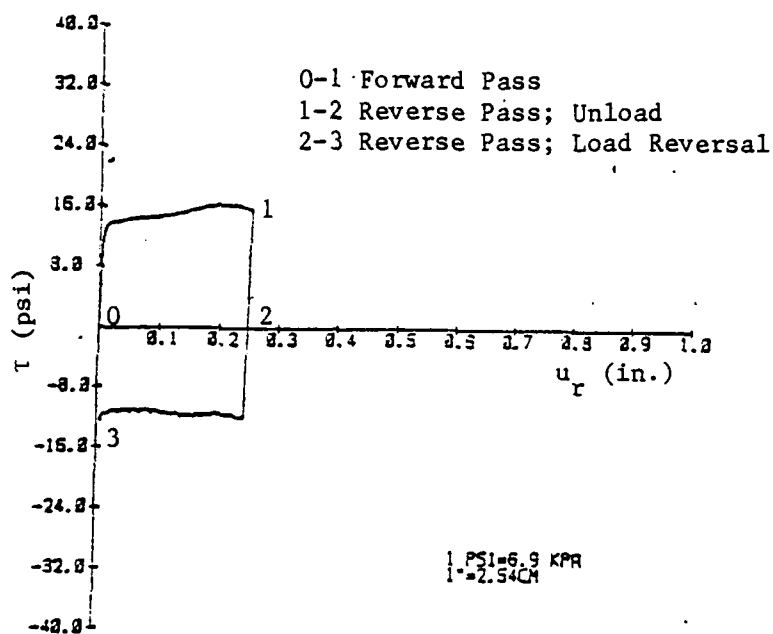
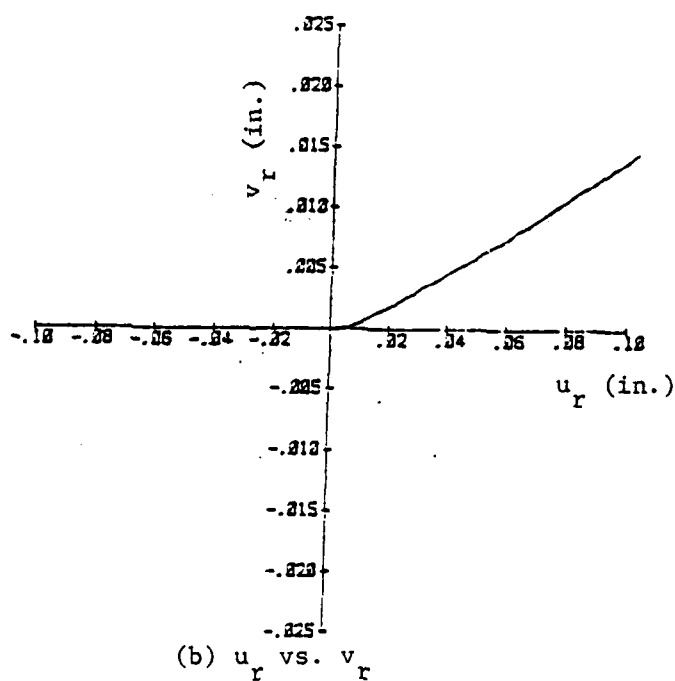
(a) u_r vs. τ (b) u_r vs. v_r

Figure 6-3. Typical Results for Quasi-static Test

This assumption was verified by performing a test with a normal stress of 20 psi (138 KPa) on a fresh, cast-smooth sample, and comparing these results with results of a similar test performed on a sample which had been subjected to 500 cycles of displacement with an amplitude of 0.8 in. (2.03 cm.) under a normal stress of 50 psi (345 KPa). Figure 6-4 shows no significant difference in the results of the two tests.

As a further check, a quasi-static shear test was repeated on the same sample to see if the first cycle of displacement affected the results of the second cycle. The device was disassembled between the tests and any gouge present removed. This investigation was done on a sample with an asperity side angle of 5 degrees under a normal stress of 50 psi (345 KPa). The comparison of results can be seen in Fig. 6-5. These results indicate that if the surfaces are cleaned of debris between the tests, the results of the second test are not significantly different from the results of the first test.

Fast Cyclic Tests

The purpose of the fast cyclic tests was to study the effects of rate of displacement and number of cycles on the shear behavior of joints. Joints were subjected to up to 500 cycles of displacement at a frequency of 1 Hz. Results from fast cyclic tests can be compared to results from quasi-static tests to investigate the effect of rate of displacement. Measurements taken from different cycles of displacement during the test can be compared to study the effect of the number of cycles on the shear behavior.

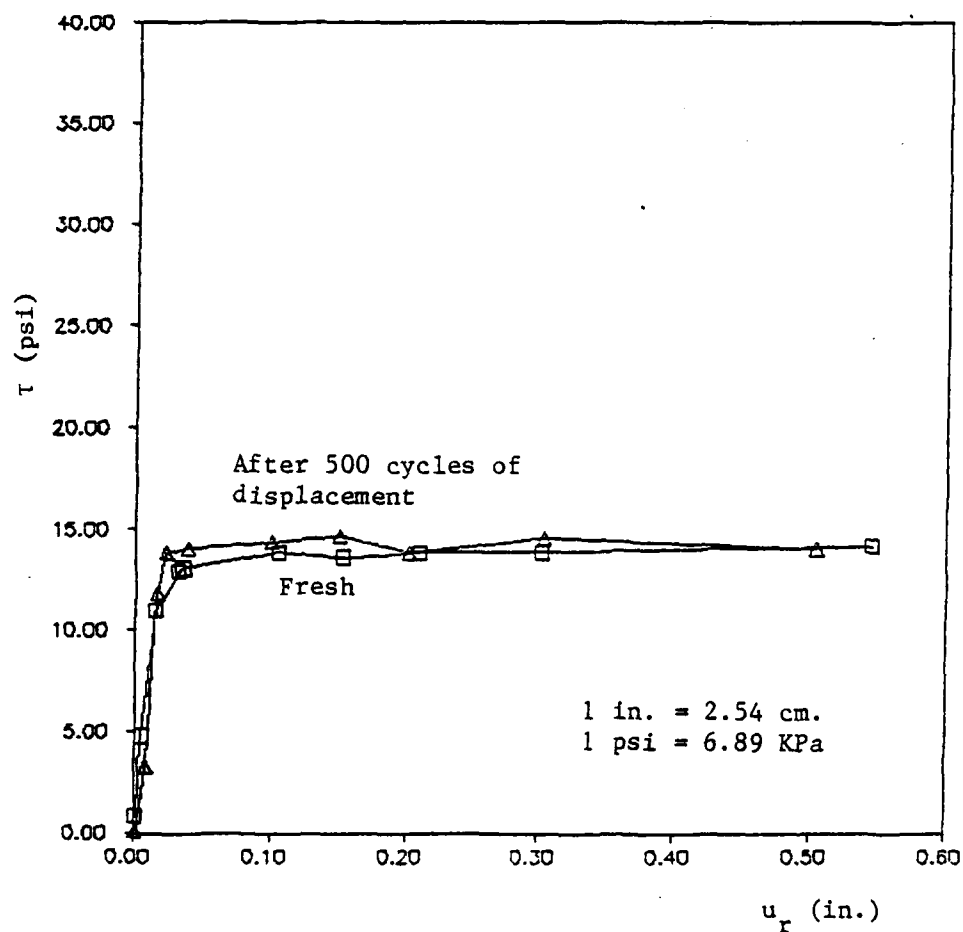


Figure 6-4. Comparison of Results from Quasi-static Shear Testing On a Fresh Sample and a Sample Previously Subjected to 500 Cycles of Displacement

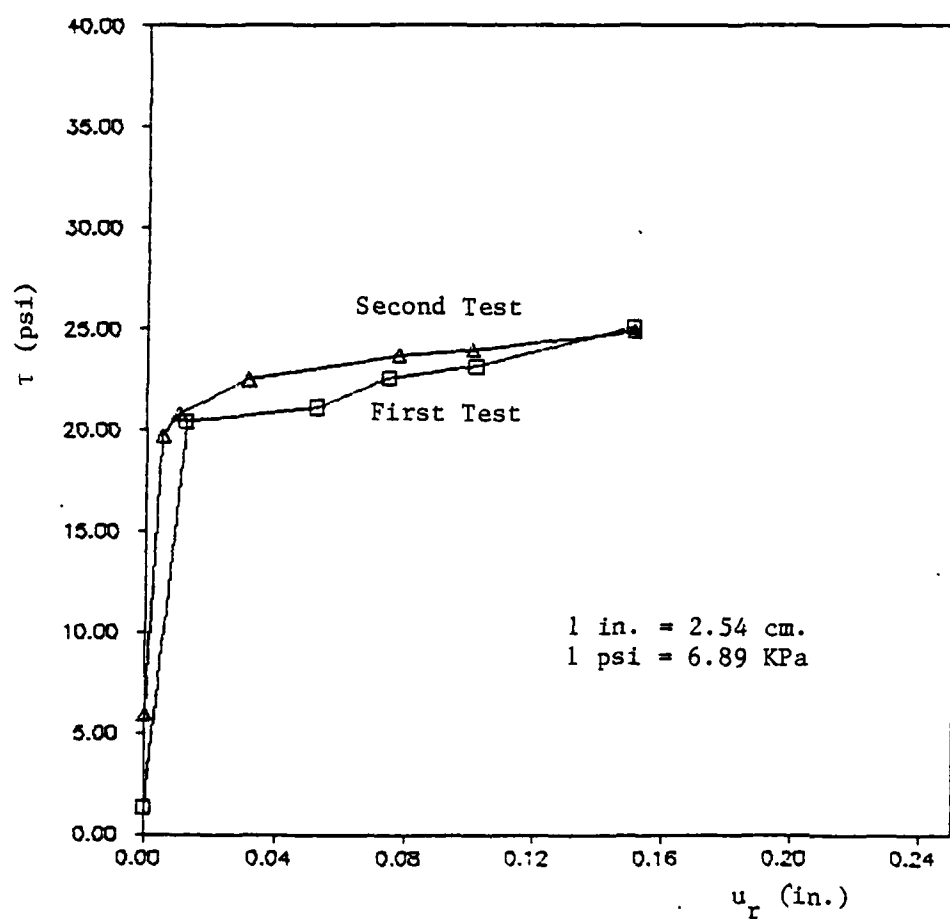


Figure 6-5. Comparison of Results from Two Quasi-Static Shear Tests On the Same Sample With Debris Cleaned From the Shear Surface Between Tests

Displacement Cycle. The tests were displacement-controlled via the control unit which received a sinusoidal displacement function from the function generator. The displacement function had a frequency of 1 Hz. The amplitude and phase of the function were adjusted to obtain the symmetric waveform depicted in Fig. 6-6(a).

Figure 6-6(b) shows the motion of the upper sample due to the input function of Fig. 6-6(a). Initially, the upper sample was in a position such that the joint was fully mated (datum). The displacement during one cycle can be considered to be composed of four phases:

Phase 1 - The upper sample was displaced in the positive horizontal direction until the maximum positive amplitude of cyclic displacement, U_r^m , was reached. During this part of the displacement cycle, the top sample rode up the right asperities of the bottom sample.

Phase 2 - The displacement was reversed, corresponding to unloading and load reversal. During this part of the displacement cycle, the upper sample rode back down the asperities of the bottom sample until returning to the datum.

Phase 3 - Displacement continued in the negative direction as in Phase 2. After passing through the datum, the upper sample traveled up the left asperities in the negative direction until reaching the negative extreme of the maximum amplitude of cyclic displacement.

Phase 4 - Once again the displacement was reversed corresponding to unloading and load reversal. The upper sample traveled down the asperities of the bottom sample in the positive direction until

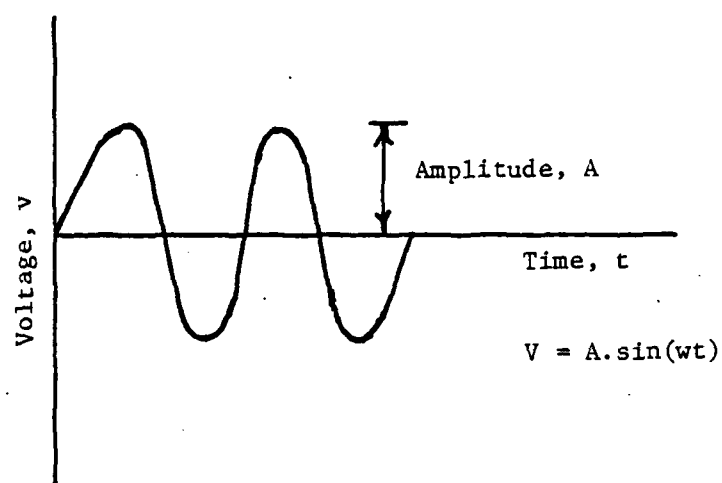


Figure 6-6(a). Waveform From Function Generator
for Cyclic Tests

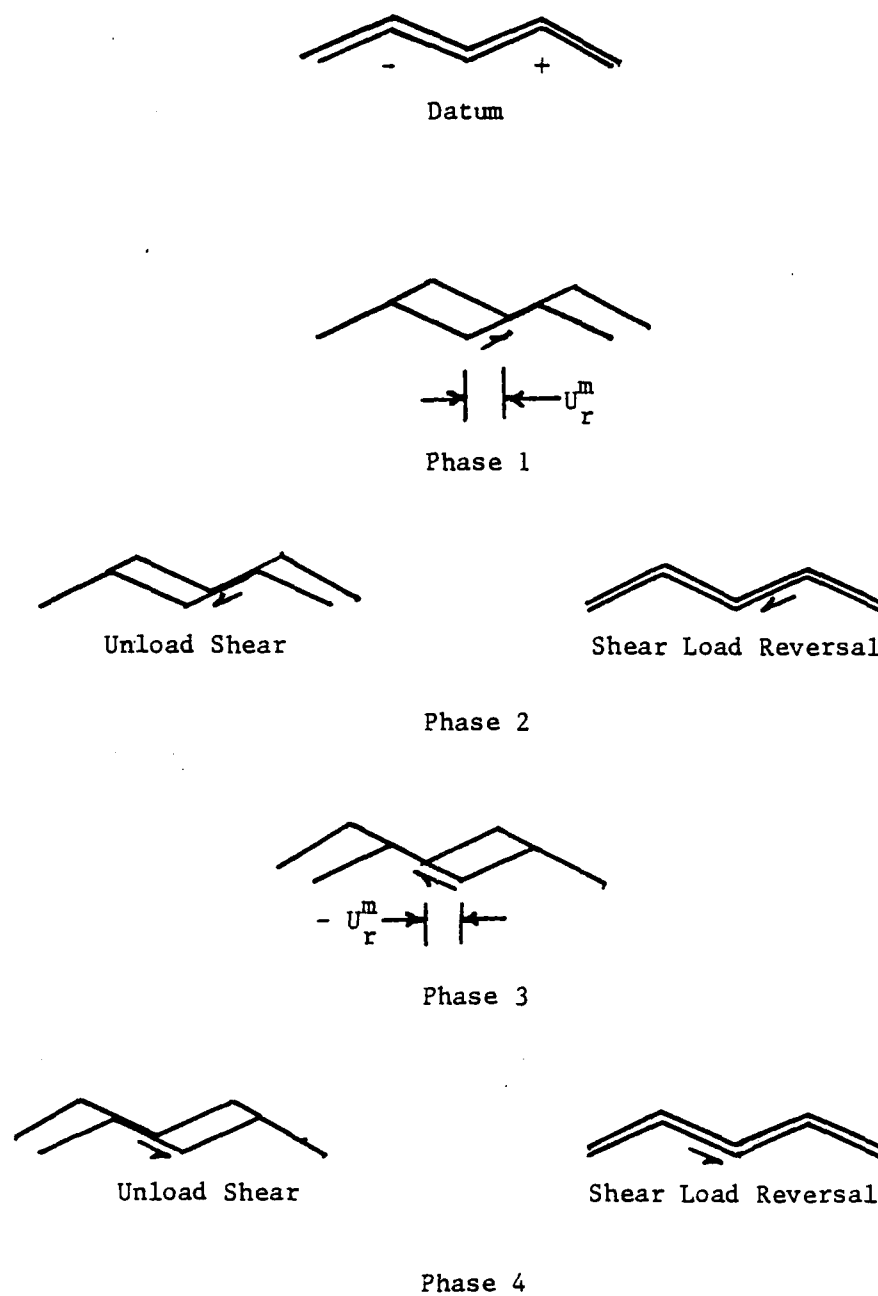


Figure 6-6(b). Motion of Upper Sample Due to the Input Function of Fig. 6-6(a)

returning to the datum. Overtopping of asperities did not take place at any time during the displacement cycle.

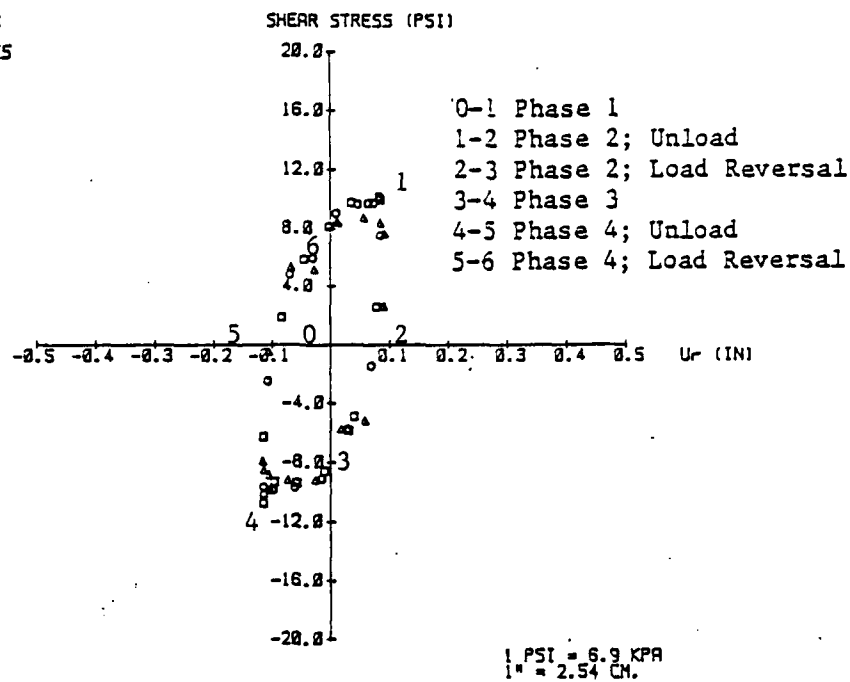
Method. After adjustment of the displacement function, the procedure for running a fast cyclic test was similar to the procedure for running a quasi-static test, described in the previous section. However, for the fast cyclic tests, 500 cycles of displacement were applied. Figures 6-7(a) and (b) are typical plots from a fast cyclic test showing the variation of shear stress and normal displacement, respectively, with horizontal displacement for different cycles.

Factors. Fast cyclic tests were performed on surfaces with different roughnesses including cast-smooth, ground-smooth, and asperity side angles of 5, 7, and 9 degrees. Tests were performed for normal stresses of 5, 10, 20 and 50 psi (34.5, 69, 138, and 345 KPa) and maximum amplitudes of cyclic displacement of 0.05, 0.10, and 0.15 in. (1.27, 2.54, and 3.81 mm.).

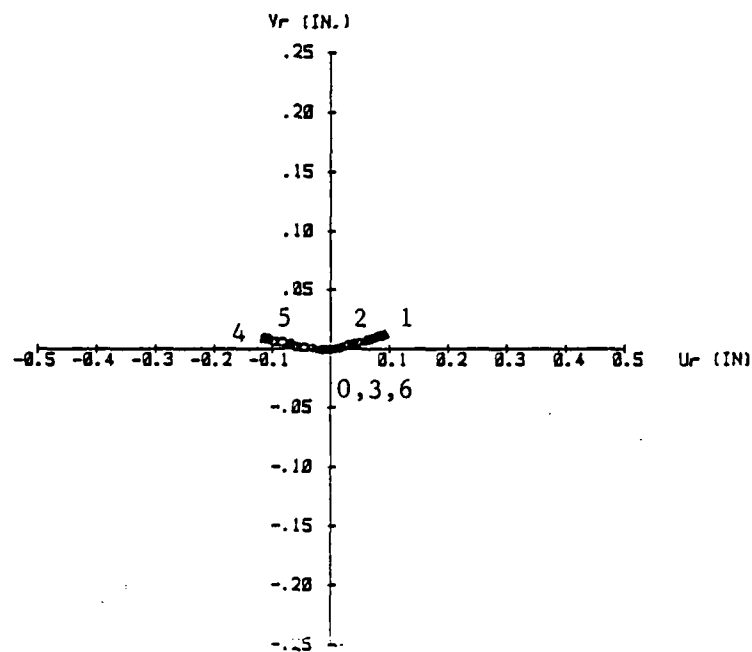
Damage. Damage which may occur to the joint surface due to the cyclic shear displacement was studied in a manner similar to that described for the slow cyclic tests. Profilometer measurements and pictures of the joint surface were taken before and after shear. Gouge material present on the joint surface after testing was weighed. These measurements were compared for different tests.

Effects on Cyclic Shear Behavior. The effects of rate of loading or gouge generated on the joint surface due to cyclic shear displacement

- ▲ N= 1 CYCLES
 ○ N= 10 CYCLES
 □ N= 101 CYCLES



(a) u_r vs. τ



(b) u_r vs. v_r

Figure 6-7. Typical Results for a Cyclic Test

on the cyclic shear behavior of the rock joint were also investigated. After performing a fast cyclic test, a quasi-static test under the same normal stress was performed without cleaning debris on the joint surface generated during the fast cyclic test. Comparisons were made between results from the following "cases:"

"Case 1" - A quasi-static test performed prior to fast cyclic testing on a joint with the same roughness and under the same normal stress (debris not present)

"Case 2" - The first cycle of the fast cyclic test (debris not present)

"Case 3" - The quasi-static test performed after the fast cyclic test (debris present)

"Case 4" - The last cycle of the fast cyclic test (debris present).

Figures 6-8(a) and (b) present typical results from testing with a 9-degree surface with normal stress 20 psi (138 KPa) and $U_r^m = 0.10$ in. (2.54 mm.). Figure 6-8(a) shows that there is no significant difference between results in terms of strength from Case 1 and Case 2. Figure 6-8(b) indicated the same for Cases 3 and 4. Since the rate of loading in Cases 1 and 2 or Cases 3 and 4 was different, it may be concluded that the rate of loading did not have a significant effect on the shear behavior within the range of rates investigated. The accumulation of gouge may affect the peak shear stress by as much as 40 percent, as evidenced by the difference in results between the tests with no debris present (Cases 1 and 2) and the tests with debris present (Cases 3 and 4).

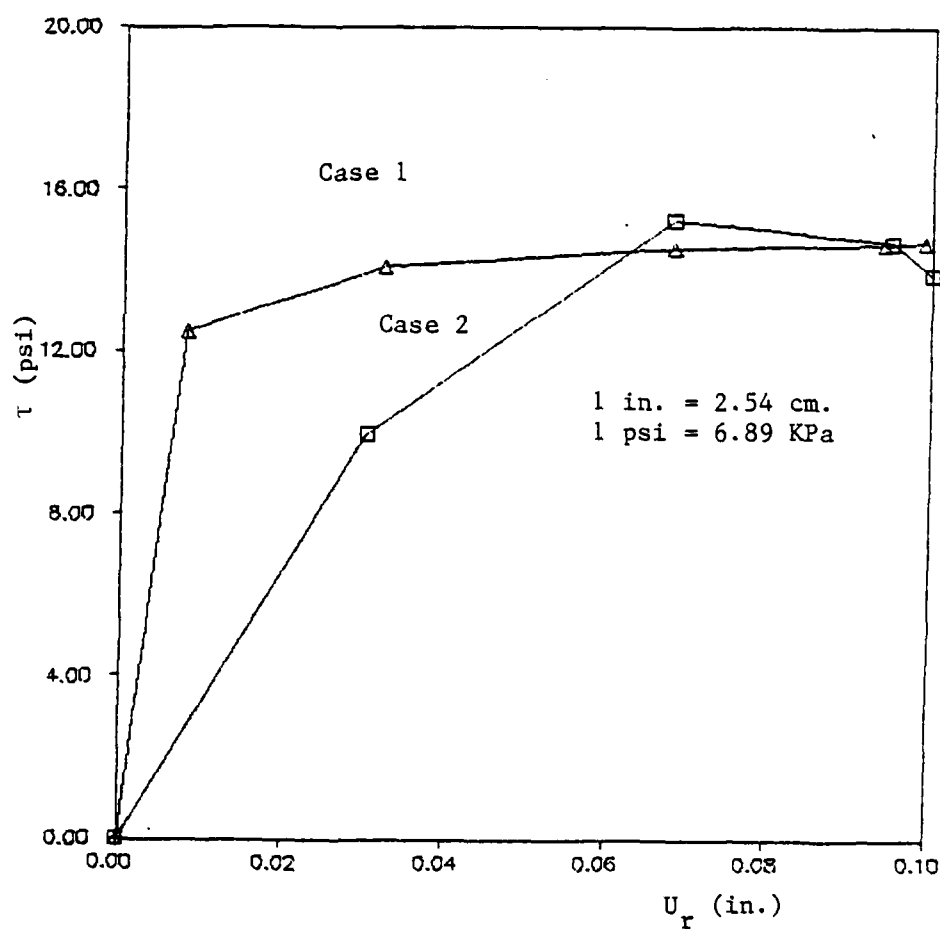


Figure 6-8(a). Comparison of Results From a Quasi-static Test On a Fresh Sample (Case 1) and the First Cycle From a Cyclic Test (Case 2)

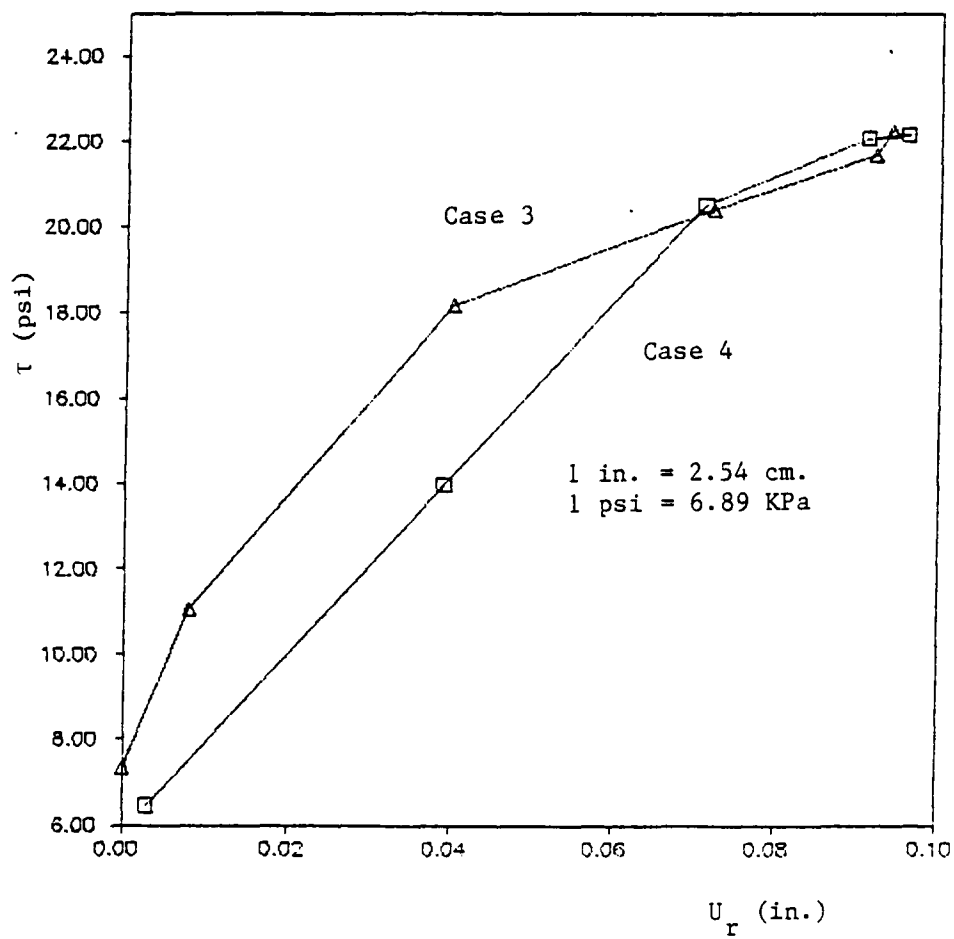


Figure 6-8(b). Comparison of Results From a Quasi-static Test Performed After a Cyclic Test (Surfaces Not Cleaned, Case 3) and the Last Cycle of a Cyclic Test (Case 4)

Multiple Tests With One Sample. On the basis of the above comparison, it was assumed that changes in the shear behavior of the rock joints tested in this program were largely due to the formation of gouge material. Therefore, a series of cyclic tests at various normal stresses can be performed on a single sample as long as the debris is cleaned from the joint surfaces between tests because no significant damage to the structure of the surfaces occurs as a result of gouge formation.

Summary of Test Program

Table 6-1 summarizes the tests performed during this investigation including quasi-static and cyclic shear tests. Each test has a designation which identifies the test series, the roughness of the joint, type of test and amplitude of cyclic displacement if applicable, and the normal stress. Descriptions of these designations can be found at the bottom of Table 6-1. In addition to shear testing, normal stress tests were performed on each surface. Results from this testing program will be discussed in Part II of the final report for this project entitled "Constitutive Modeling of Idealized Rock Joints Under Cyclic Loading; Final Report, Part II." In this report, test results will only be discussed with respect to determination of parameters for the plasticity model and back prediction of results with the model.

Table 4, Continued

Test	Roughness	u_r (in)	σ_n (psi)
<u>STATIC</u>			
I-5-S-05	7° Cast	0.25	5
I-5-S-10		0.25	10
I-5-S-20		0.25	20
I-5-S-50		0.25	50
<u>CYCLIC</u>			
I-5-C2-10		0.10	10
I-5-C2-20		0.10	20
<u>STATIC</u>			
I-6-S-05	9° Cast	0.25	5
I-6-S-10		0.25	10
I-6-S-20		0.25	20
I-6-S-50		0.25	50
<u>CYCLIC</u>			
I-6-C1-05		0.05	5
I-6-C1-10		0.05	10
Static Test After I-6-C1-10		-	-
I-6-C1-20		.05	20
I-6-C2-05		0.10	5
I-6-C2-10		0.10	10
I-6-C2-20		0.10	20
Static Test After I-6-C1-20			
<u>STATIC</u>			
I-2-S-05	15° Cast	0.5	5
I-2-S-20		0.5	0
I-2-S-50		0.5	50

Table 4, Continued

Test Series Designation

I-1-S-10 Series I - Roughness 1 - Static - $\sigma_n = 10$ psi
I-2-C1-20 Series I - Roughness 2 - Cyclic Test Type 1 -
 $\sigma_n = 20$ psi, and so on.

Roughness

Smooth, Cast - Cast on smooth glass - 1
Ground, Flat - Ground smooth using grinding machine - 0
5° Cast - Asperity angle = 5° - 4
7° Cast - Asperity angle = 7° - 5
9° Cast - Asperity angle = 9° - 6
15° Cast - Asperity angle = 15° - 2

Table 6-1. Summary of Test Program

Explanations given below.

Test	Roughness	u_r (in)	σ_n (psi)	
<u>STATIC</u>				
I-1-S-10	Smooth Cast	0.5	10	
I-1-S-20		0.5	20	
I-1-S-50		0.5	50	
I-1-S-100		0.5	100	
<u>CYCLIC</u>				
I-1-C1-10		0.05	10	
I-1-C1-20		0.05	20	
I-1-C2-10		0.10	10	
I-1-C2-20		0.10	20	
I-1-C2-50		0.10	50	
<u>STATIC</u>				
I-0-S-05		Ground Flat	0.25	5
I-0-S-20			0.25	20
I-0-S-50			0.25	50
<u>CYCLIC</u>				
I-0-C2-05			0.10	5
I-0-C2-10			0.10	10
I-0-C2-20			0.10	20
<u>STATIC</u>				
I-4-S-05	5° Cast	0.15	5	
I-4-S-10		0.25	10	
I-4-S-20		0.25	20	
I-4-S-50		0.15	50	
<u>CYCLIC</u>				
I-4-C2-10		0.10	10	

CHAPTER 7

DESCRIPTION OF PLASTICITY MODEL

In order to describe the behavior of jointed rock masses properly, it is necessary to describe the behavior of the individual rock joints.

Rock joints in nature may contain filler materials, and may be saturated with water. The surface features of a rock joint can be highly irregular, and the asperities of the top and bottom portions of the joint may be mated, or there may be some initial offset in the mating surfaces. The state of stress to which the rock joint is subjected may be such that shear takes place in any arbitrary direction with respect to the asperities, and the response of the joint may be affected by initial stress and state of stress. Cyclic or quasi-static loading may be applied. During shear the joint may tend to harden or soften, to compress or dilate, and rotation may occur causing contact pressures to vary. Development of a constitutive model which considers all of these features is a difficult task.

Constitutive models based on the theory of incremental plasticity have been proposed by Ghaboussi and Wilson (1973), Roberds and Einstein (1978), Hsu-Jung (1979), Plesha (1986), Drumm and Kane (1987). By employing the theory of plasticity, normal and shearing behavior of the joint during shear are coupled. In this study, use of a generalized

yield function which can model hardening behavior through a series of continuous yield surfaces which expand towards an ultimate surface during deformation is suggested. To simplify the formulation in this initial study, the effects of filler material, pore water pressure, irregular surface features, initial offset, and softening are not considered. Some of these aspects will be considered in subsequent studies.

The model allows for effects of initial normal stress, states of shear and normal stress, plastic hardening, nonassociativeness, volume changes at joints, load reversal and cyclic loading.

This chapter describes the specialization of a three-dimensional generalized plasticity model to describe shear behavior of individual rock joints. The specialization is described in terms of monotonic shear loading, and then adaptations are described such that the model may be used for unloading, load reversal, and cyclic shear loading. The physical significance of parameters as well as salient details of parameter determination will be discussed.

Specialization Of a 3-D Generalized Model

The following generalized yield function written in terms of stress invariants was proposed by Desai (1980b), Desai and Faruque (1984), Desai et al. (1986), Desai et al. (1987):

$$F = J_{2D} - (-\alpha J_1^n + \gamma J_1^2) (1 - \beta S_r)^m = J_{2D} - F_b F_s = 0 \quad (7-1)$$

where J_1 is the first invariant of the stress tensor, J_{2D} is the second invariant of the deviatoric stress tensor, S_{ij} . The parameters α , n , γ , β and m are the response functions, and S_r equals stress ratio such as $J_{3D}^{1/3}/J_{2D}^{1/2}$ and Lode angle, where J_{3D} is the third invariant of S_{ij} . F_b and F_s are called basic and shape functions, respectively.

Presently γ , β and m are treated as constants associated with the ultimate envelope, which is defined as the locus of points corresponding to asymptotic stress to stress-strain curves for different tests. The parameter α is chosen as a growth or hardening function of specific internal variables such as plastic strain trajectory $\xi = \int (d\epsilon_{ij}^p d\epsilon_{ij}^p)^{1/2}$, where ϵ_{ij}^p equals the plastic strain tensor.

The above function describes a series of continuous yield surfaces which expand towards an ultimate surface during deformations. It has been shown by Desai et al. (1986) that the function is convex when plotted in any stress space, gives orthogonal intersection with the J_1 axis when plotted in J_1 versus $\sqrt{J_{2D}}$ space, and is equal to zero on the ultimate surface which intersects the J_1 axis at infinity. Details of the hierarchical approach are given by Desai et al. (1986) and Desai et al. (1987).

Analogies

In this investigation the shear behavior of idealized rock joints is studied. The form of Eq. (7-1) is specialized to describe yielding of the joint plane. Since yield is to occur on a specified plane, the function is written in terms of the normal, σ_n , and shear, τ , components of stress across the joint plane, instead of the stress invariants. For

solids, F_s controls the shape of the yield function plotted in principal stress space. When specialized to the joint plane, the function is only plotted in σ_n versus τ space. Therefore, F_s will be taken as unity. The parameter n will control the shape of the yield function plotted in σ_n versus τ space and act as the phase change parameter denoting transition from contractive to dilative response.

In order to accomplish the specialization, several analogies will be drawn between quantities that are defined for a three-dimensional state of stress and for the state of stress across a joint plane. Table 7-1 summarizes the analogies which involve quantities appearing in the yield and growth functions. The reasoning behind the analogies is discussed in the following sections.

Analogies for Yield Function. Shear stress, τ , on a joint plane is considered to be analogous to $\sqrt{J_{2D}}$, and normal stress, σ_n , on a joint plane is considered to be analogous to J_1 . The reason for this analogy is the similar manner by which these quantities affect the failure condition for different states of stress. When a three-dimensional state of stress is considered, J_{2D} may cause distortion of materials and J_1 may add confinement which increases the resistance of a material to deviatoric stress. Similarly, the shear stress, τ , across a joint plane may induce relative tangential displacement of the joint and application of normal stress, σ_n , may increase resistance to shear stress. Using this analogy between $\sqrt{J_{2D}}$ and τ , and J_1 and σ_n , Eq. (7-1) may be written as

Table 7-1. Analogous Quantities

Solid	Joint
J_1	σ_n
$\sqrt{J_{2D}}$	τ
$\epsilon_{ii} = \epsilon_v$	v_r
$e_{ij} = \epsilon_{ij} - \frac{\epsilon_{kk}}{3} \delta_{ij}$	u_r
$\xi = \int (d\epsilon_{ij}^p d\epsilon_{ij}^p)^{1/2}$	$\int [(dv_r^p)^2 + (du_r^p)^2]^{1/2}$
$\xi_v = \frac{1}{\sqrt{3}} \int d\epsilon_{kk}^p$	$\int [(dv_r^p)^2]^{1/2}$
$\xi_d = \int (de_{ij}^p de_{ij}^p)^{1/2}$	$\int [(du_r^p)^2]^{1/2}$
J_1 - first invariant of stress tensor	
J_{2D} - second invariant of deviatoric stress tensor	
ϵ_{ij} - strain tensor	
ϵ_{ii} - volumetric strain	
e_{ij} - deviatoric component of strain tensor	
ϵ_{ij}^p - plastic strain tensor	
ϵ_{kk}^p - volumetric plastic strain	
e_{ij}^p - deviatoric component of plastic strain tensor	
σ_n - normal stress	
τ - shear stress	
v_r - relative vertical displacement	
u_r - relative tangential displacement	
v_r^p - plastic relative vertical displacement	
u_r^p - plastic relative tangential displacement	
ξ - plastic strain trajectory	
ξ_v - volumetric component of ξ	
ξ_d - deviatoric component of ξ	

$$F = \tau^2 + \alpha \sigma_n - \gamma \sigma_n^2 = 0 \quad (7-2)$$

Since Eq. (7-2) is of the same form as Eq. (7-1), all of the properties of Eq. (7-1) are retained including $\alpha = 0$ on the ultimate surface, convexity, and orthogonality of the intersection with the σ_n axis. Figure 7-1 presents a plot of a typical function in τ versus σ_n space for a joint to be described later.

Analogies for Growth Function. The growth function needs to be expressed in terms of internal state variables which are believed to be related to the hardening process. In order to accomplish this, two more analogies need to be drawn between quantities which describe deformation for rock joints and those for general three-dimensional states of stress. It is proposed that relative vertical displacement, v_r , of rock joints is analogous to volumetric strain, ϵ_v , in general 3-D problems, and relative tangential displacement, u_r , of rock joints is analogous to deviatoric strain, $e_{ij} = \epsilon_{ij} - 1/3 \epsilon_{kk} \delta_{ij}$. These analogies are based upon similar stress-deformation relationships when the stress analogies discussed in the preceding section are considered.

Typical results from a hydrostatic compression test performed on a granular material and a normal stress test on a rock joint are compared in Fig. 7-2. The shape of the J_1 versus ϵ_v is similar to that of the σ_n versus v_r curve.

Next consider the analogous stress quantities J_{2D} and τ . An initially isotropic material requires the application of deviatoric stress for deviatoric strain to occur. In rock joints shear stress induces relative horizontal displacement.

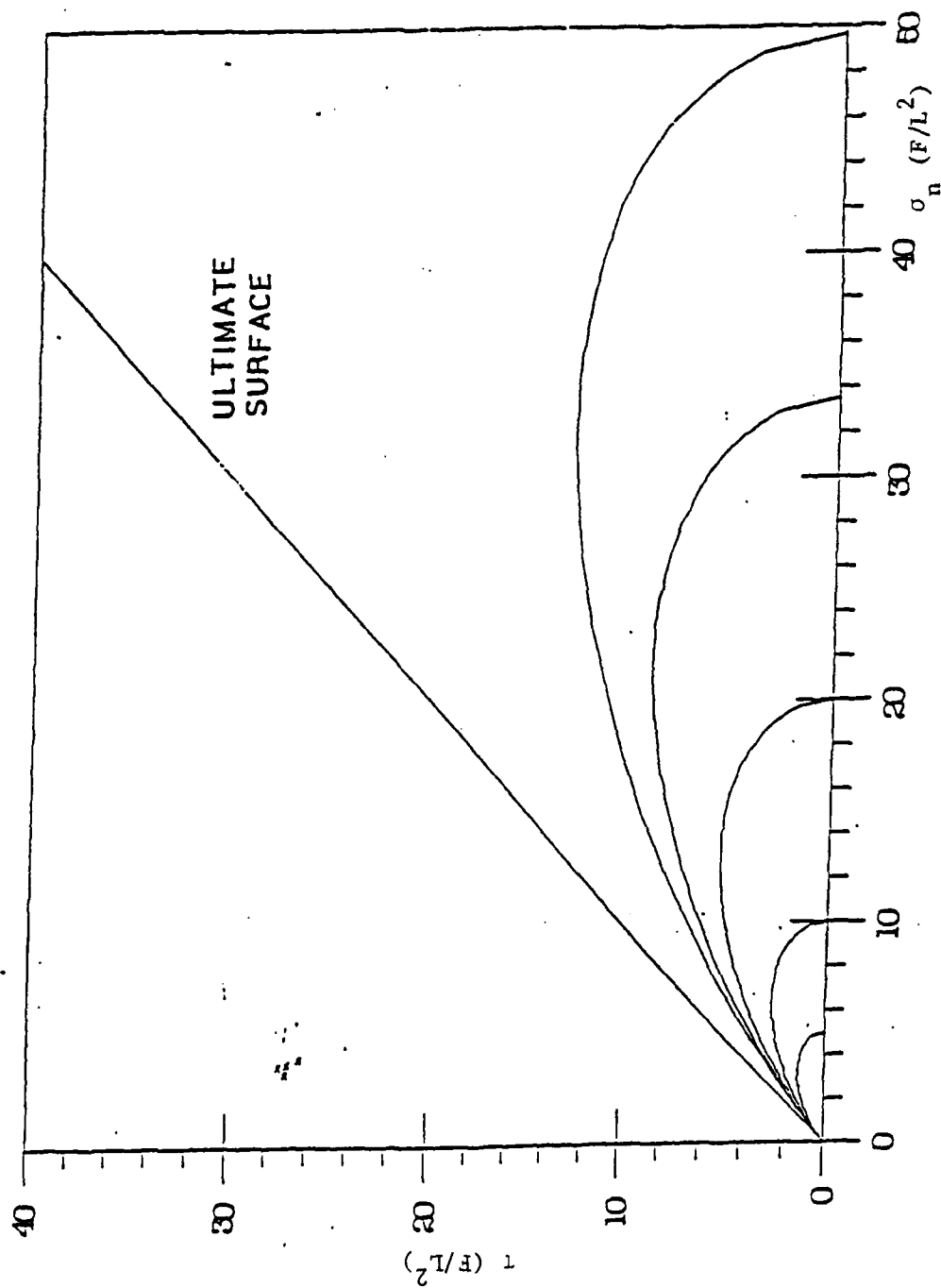


Figure 7-1. Typical Plot of the Yield Function

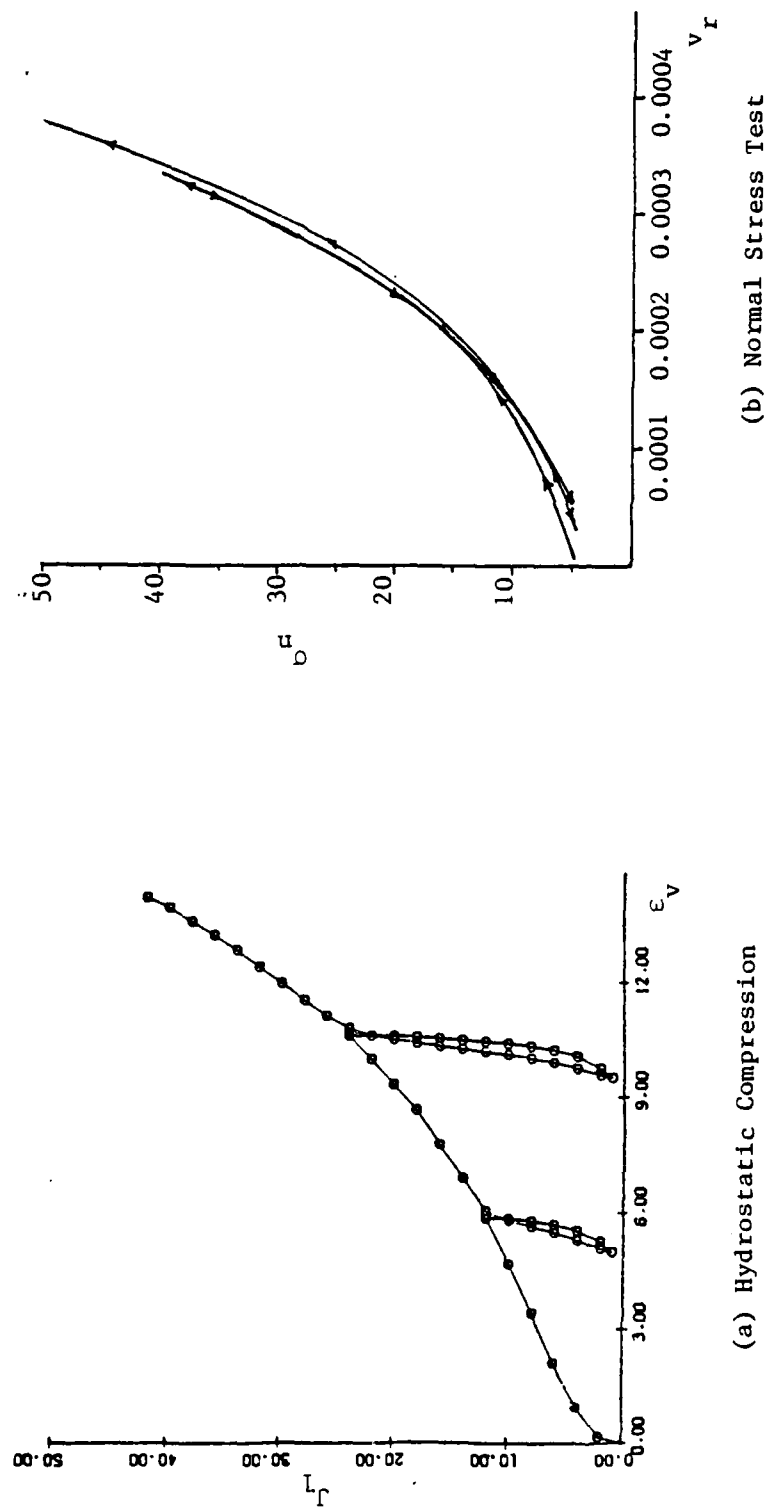


Figure 7-2. Comparison of Results From a Hydrostatic Compression Test and a Normal Stress Test

Mathematical Specialization

It is possible to derive Eq. (7-2) without the analogy of the preceding sections. Consider a right handed coordinate system, as shown in Fig. 7-3, where z is the direction of normal load application on the joint plane, x is the direction of shear, and the y axis is in the joint plane perpendicular to the direction of shear. For the case of direct shear, $\tau_{xy} = \tau_{yz} = 0$ since it is assumed that there is no relative displacement of the joint in the y direction, and shear strain across the joint plane is defined in terms of relative displacement. Also, it is assumed that body forces are negligible. Thus, the following equilibrium equations for stress may be written:

$$(a) \frac{\partial \sigma_x}{\partial x} + \frac{\partial \tau_{xz}}{\partial z} = 0 \quad (7-3)$$

$$(b) \frac{\partial \sigma_y}{\partial y} = 0$$

If the joint plane is considered to be thin, $\frac{\partial \tau_{xz}}{\partial z}$ is approximately zero and Eq. (7-3) becomes

$$\frac{\partial \sigma_x}{\partial x} = 0 \quad (7-4a)$$

$$\frac{\partial \sigma_y}{\partial y} = 0 \quad (7-4b)$$

Assuming for the case of direct shear that σ_x and σ_y are zero on the boundaries, and $\tau_{xy} = \tau_{zy} = \sigma_x = \sigma_y = 0$, and $\sigma_z = \sigma_n$ and $\tau = \tau_{xz}$, then

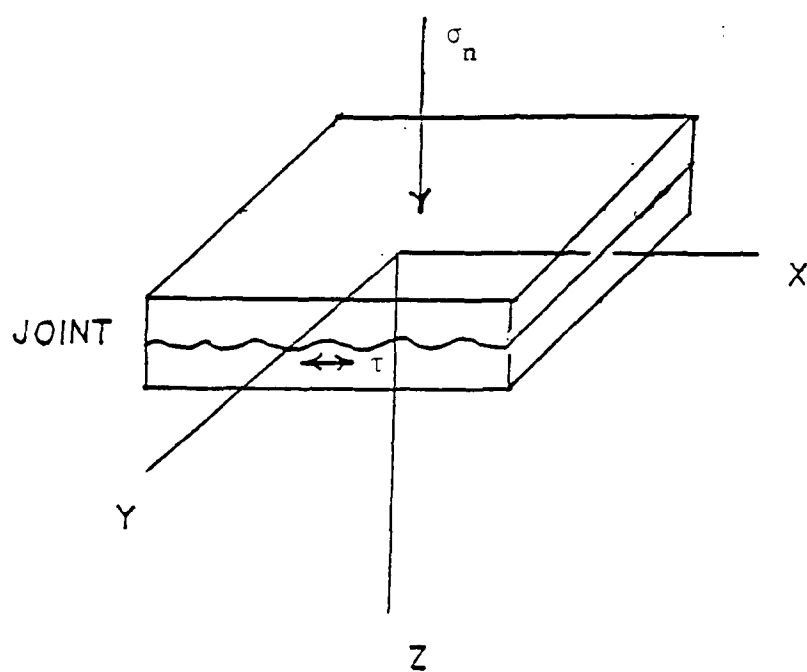


Figure 7-3. Right Handed Coordinate System of Joint Plane

$$J_1 = \sigma_n \text{ and} \quad (7-5a)$$

$$J_{2D} = \frac{\sigma_n^2}{3} + \tau^2 \quad (7-5b)$$

Substitution of Eq. (7-5) in Eq. (7-1) with $F_s = 1$ yields

$$\frac{\sigma_n^2}{3} + \tau^2 + \alpha \sigma_n - \gamma \sigma_n^2 = 0 \quad (7-6)$$

which reduces to

$$\tau^2 + \alpha \sigma_n - \gamma' \sigma_n^2 = 0 \quad (7-7)$$

where $\gamma' = \gamma - \frac{1}{3}$, which is the same as Eq. (7-2).

Nonassociativeness

It has been shown that for many geologic materials, the plastic strain increment is not normal to the yield surface as assumed with the associative flow rule. This can lead to a nonassociative flow rule where the plastic strain increment is assumed to be normal to the plastic potential function, Q . A simple approach has been proposed in which Q is obtained by correcting the growth function, α , in the yield surface F during plastic straining (Desai and Siriwardane, 1980; Frantziskonis et al., 1986). In this case, Q is written as

$$Q = \tau^2 + \alpha_Q \sigma_n - \gamma \sigma_n^2 \quad (7-8)$$

where

$$\alpha_Q = \alpha + \kappa (\alpha_I - \alpha) (1 - r_v) \quad (7-9)$$

κ is a material constant and α_I is the value of α at the initiation of nonassociativeness, which, for a direct shear test, is considered to be just after the normal stress has been applied prior to the initiation of shear. The parameter r_v is equal to ξ_v/ξ .

Elastic-Plastic Constitutive Matrix

In an elastic-plastic constitutive law, incremental stresses and incremental strains are related through an elastic-plastic constitutive matrix. The derivation involves decomposition of deformations into elastic and plastic parts, and a stress-elastic strain relationship. These, together with either an associative or nonassociative flow rule, which relates plastic strains to the state of stress, the consistency condition, and considering α to be a function of the history of plastic strain trajectories, yield the following expression for the elastic-plastic constitutive matrix:

$$[K]^{ep} = \begin{bmatrix} K_{nn} & K_{ns} \\ K_{sn} & K_{ss} \end{bmatrix}^{ep} \quad (7-10)$$

which is symmetric for the associative case and nonsymmetric for the non-associative case. Details of this derivation can be found in Appendix I. In this formulation, relative displacements are treated as strains. For

input in a finite element program, strain would be computed from relative displacements by considering the joint to be of finite thickness and dividing relative displacements by this thickness (Desai et al., 1982).

Load Reversal

Load reversal causes the shear direction of the upper sample with respect to the lower sample to be reversed. The response of the joint after load reversal depends on two factors:

1. Displacement-induced anisotropic response of the joint with respect to shear displacement.
2. The accumulation of gouge and damage which occurred as a result of shear displacement prior to load reversal.

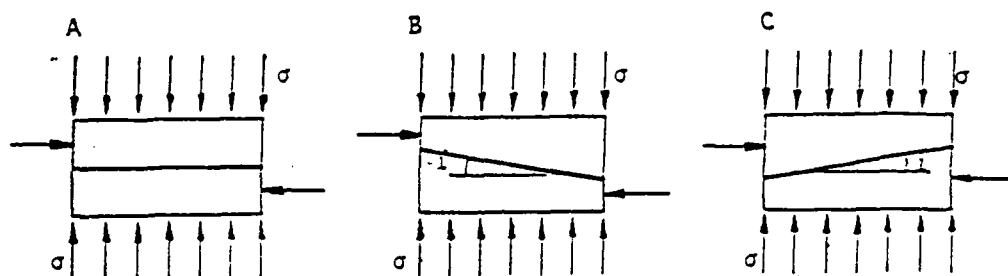
Displacement-Induced Anisotropy. The displacement-induced anisotropic response of rock joints will be discussed with reference to the slow cyclic tests described in Chapter 6. Consider the cycle of displacement depicted in Fig. 6-2(b). Initially, the upper sample is in a position such that the rock joint is considered fully mated. At this instant, the response of the joint during shear is independent of the direction of shear, and the joint is considered to be isotropic with respect to the direction of shear. As the upper sample is displaced during the forward pass, it travels up the asperity sides of the bottom sample. When the direction of the upper sample is reversed, the vertical displacement that is coupled to the shear displacement is also reversed as the upper sample travels back down the asperities of the bottom sample returning to the datum.

The reversal of travel up or down an asperity side not only changes the deformation characteristics of the joint, but also the shear strength. This can easily be realized by referring to Fig. 7-4, which depicts a plane inclined to the direction of the driving force. The failure criteria relates the shear strength of the joint to the normal stress, asperity angle and direction of travel (up or down incline). Hence, after shifting the upper sample from the initial mated joint condition, the shear behavior of the joint depends upon the direction of shear, and the joint must be considered to be anisotropic with respect to shear.

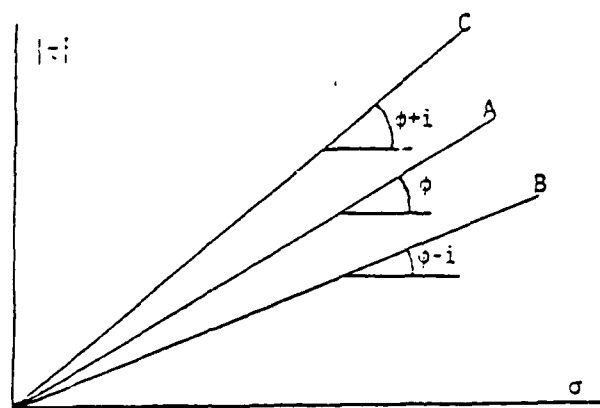
Displacement-induced anisotropy is modeled by adaptation of the isotropic hardening model, as shown in Fig. 7-5. After the joint is displaced from the mated position (0-1), parameters for the yield and growth functions are for a forward or reverse direction. Determination of these parameters will be discussed in the next section. Thus, a different function denoted F_0 , F_1 , F_2 or F_3 is used to define yield, depending on the sign of the shear stress. Note that there is no discontinuity in the yield between unloading and load reversal (2-3) because yield functions for both forward and reverse passes have orthogonal intersections with the abscissa.

Prior to load reversal, the joint is unloaded in shear (1-2), as depicted in Fig. 7-5. Currently, unloading is considered to be elastic. However, after unloading, the yield surface collapses. Thus, when the

Plane inclined at an angle to the driving force.



TOP BLOCK DISPLACED FROM LEFT TO RIGHT



$$C: |\tau| = \sigma \cdot \tan(\phi + i)$$

$$A: |\tau| = \sigma \cdot \tan \phi$$

$$B: |\tau| = \sigma \cdot \tan(\phi - i)$$

Figure 7-4. Failure Envelope for Inclined Surface

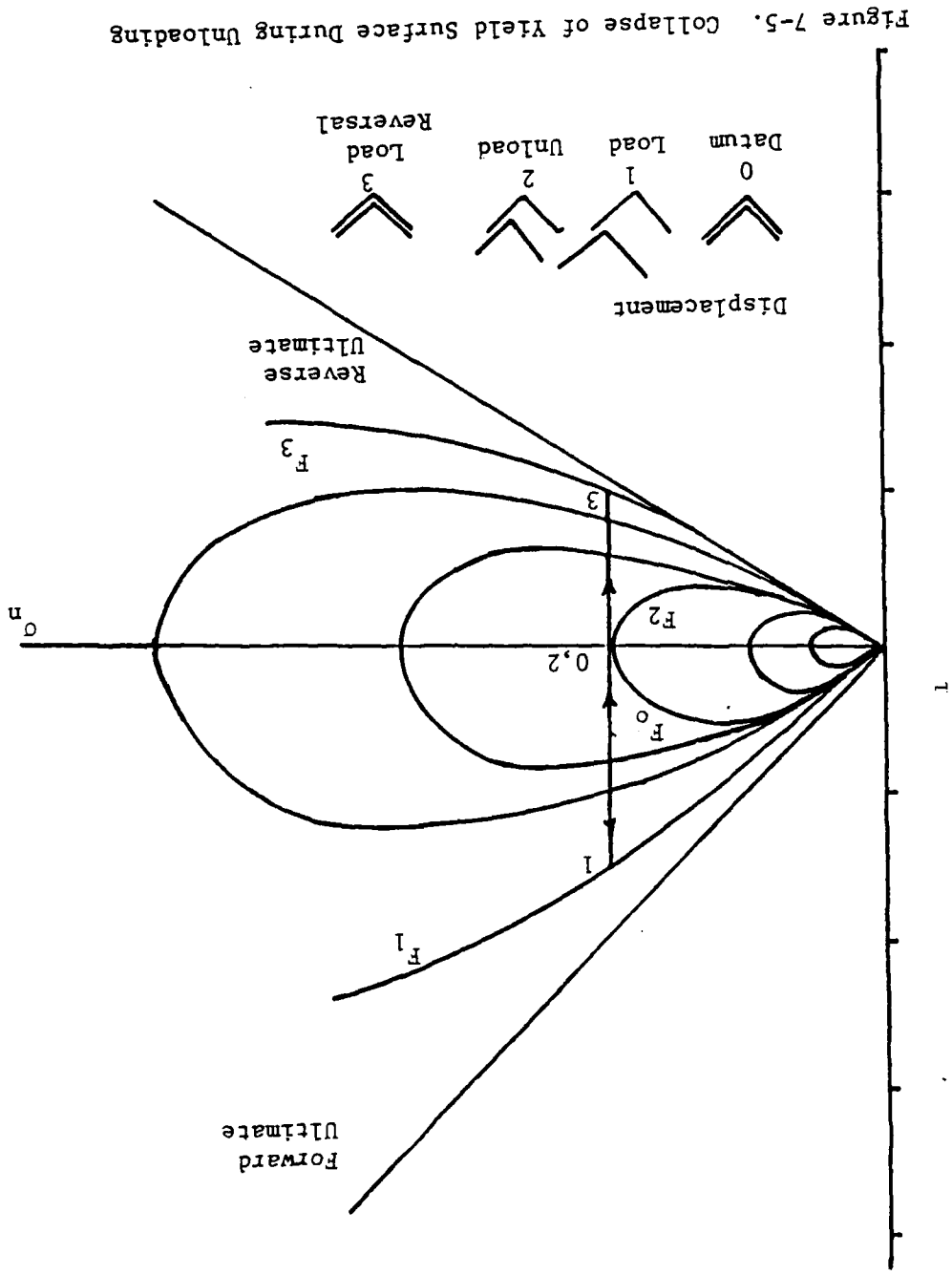


Figure 7-5. Collapse of Yield Surface During Unloading

shear stress is reduced to zero, the joint is under the action of the applied normal stress, and just prior to load reversal (2-3), the stress point lies on a current yield surface.

Gouge and Damage. Gouge and damage generated on the joint surfaces due to shear displacement prior to load reversal tend to change the state of the joint, affecting the shear behavior. In order to describe the shear behavior after load reversal properly, the model must consider the change in state which has occurred to the joint surface as a result of the forward pass. This is considered since the evaluation of parameters for the reverse pass are determined from test data obtained after the sample has been subjected to shear from the forward pass.

Application of the Plasticity Model to Cyclic Loading

In this section development of the aforementioned plasticity model to the case of cyclic shear loading is presented. Each cycle of displacement is considered to consist of four phases, as discussed in Chapter 6. These phases describe the direction of travel of the top sample with respect to the bottom sample. The isotropic hardening model is applied to each phase of the displacement cycle. Parameters are determined for each phase of a given cycle, and then parameters for a given phase may be expressed as functions of number of cycles.

For the sake of completeness, descriptions of each phase of the displacement cycle for a cyclic shear test are given here. This discussion is with reference to Fig. 6-6(b).

Phase 1: Starting from an initially mated condition (datum), the upper sample is displaced up the right asperities (positive direction) an amount equal to the maximum amplitude of cyclic displacement.

Phase 2: The upper sample is unloading in shear, and the direction of shear is reversed (negative direction). During this phase, elastic shear displacement occurs first. Then elasto-plastic deformations due to load reversal develop and continue until the upper sample returns to the datum.

Phase 3: Displacement continues in the negative direction until the maximum amplitude of cyclic displacement is reached. During this phase, the upper sample travels up the left asperity sides of the bottom sample in the negative direction. With the exception of cycle one, to be discussed later, this phase is similar to Phase 1, only the direction of tangential displacement is reversed.

Phase 4: Once again, the direction of travel is reversed (positive direction), during which initial elastic unloading, followed by plastic deformation, occurs until the upper sample returns to the datum. This phase is similar to Phase 2.

As previously discussed, after unloading the yield surface is assumed to collapse so that upon load reversal the stress point lies on a current yield surface. Between Phases 2 and 3 and 4 and 1, the parameters change to reflect the transition from down to up asperity side travel. No unloading occurs, but there is a shift in the yield surface

depicted in Fig. 7-6. This shift in the yield surface occurs because prior to the phase transition the response is approaching ultimate, but the instant after the phase transition the response is no longer near ultimate.

It is important to point out that in the present testing, at no time during the deformation history do the asperities of the top sample override the asperities of the bottom sample as depicted in Fig. 7-7. This would cause an instability with regard to the state of stress, which is not currently built into the model.

Cyclic Hardening. Changes in the behavior of the joint plane as a result of cyclic shear loading are assumed to be described primarily through a change in the ultimate response. This is based on observations made from the cyclic test series. The results of this test series indicate that the ultimate stress during Phases 1 and 3 (up asperity travel) increases with number of cycles. The history of deformation which occurred during previous cycles is considered since the parameters determined during a given cycle are based on deformations which occur to a joint surface that has experienced deformation the previous cycles.

Parameters

The elastic-plastic model discussed herein requires constants for the elastic response of the joint as well as parameters which appear in the yield and potential functions. The elastic response of the joint is described through two constants, k_s and k_n , the elastic shear and normal stiffnesses, respectively. The yield and potential function utilize

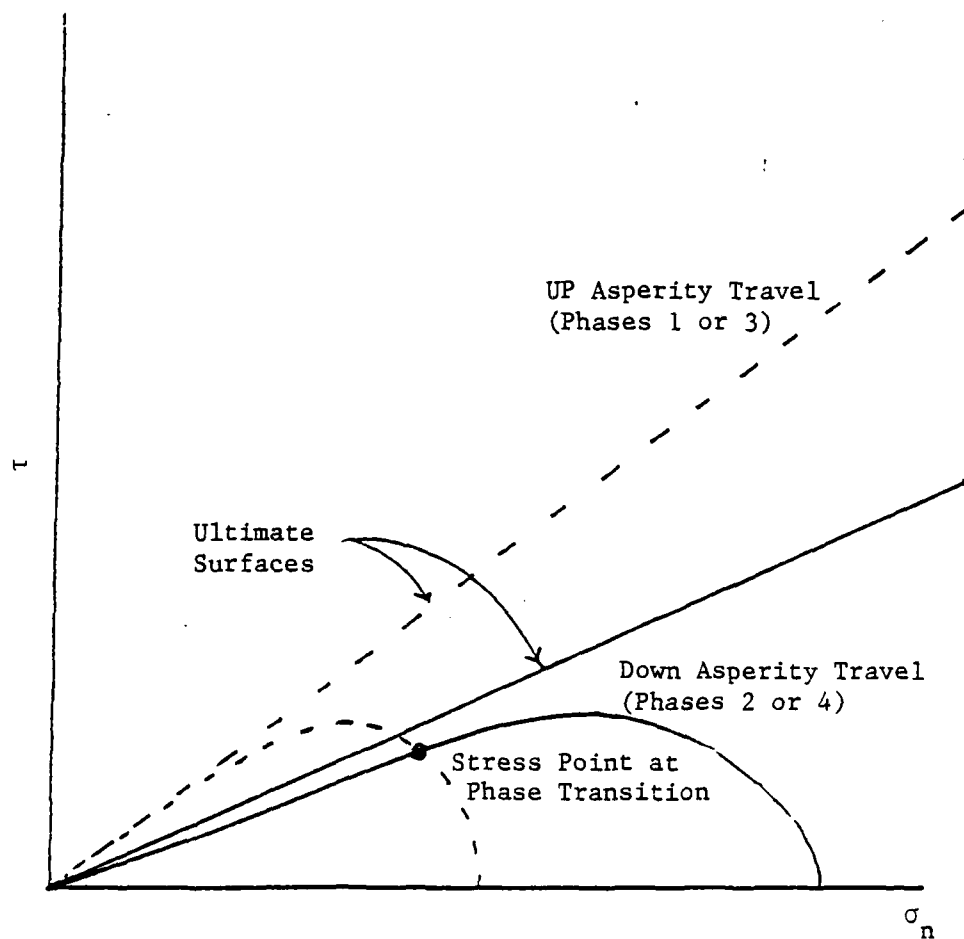


Figure 7-6. Shift in Yield Surface Between Phases 2 and 3 and Phases 4 and 1

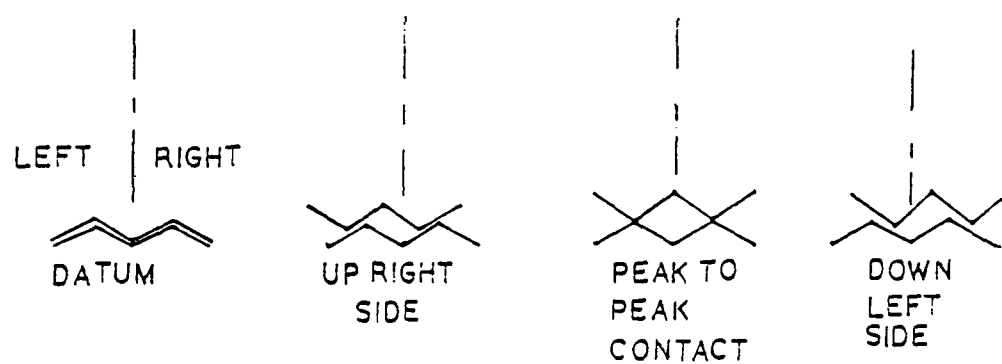


Figure 7-7. Overriding Asperities

parameters which describe the ultimate state, the growth or hardening behavior, and nonassociativeness. The physical significance of the various parameters and salient details of their determination are discussed in this section. Parameter determination from test data will be discussed in Chapter 8.

Elastic Constants

The elastic shear stiffness, k_s , is the slope of the unloading part of the shear (τ) versus relative tangential displacement (u_r) curve obtained from a direct shear test, as shown in Fig. 7-8. This value varies depending on the normal stress across the joint plane at the initiation of shear.

The elastic normal stiffness, k_n , is the initial slope of a normal stress (σ_n) versus relative vertical displacement (v_r) curve obtained from a normal stress test, as depicted in Fig. 7-9.

Parameters for the Yield Function

The following sections describe procedures for finding parameters for the yield function including the ultimate parameter γ , the phase change parameter n , and the growth function.

Ultimate Parameters. As previously discussed, the growth function is equal to zero on the ultimate surface. Thus Eq. (7-2) specializes to

$$\tau_u^2 - \gamma \sigma_n^2 = 0 \quad (7-11)$$

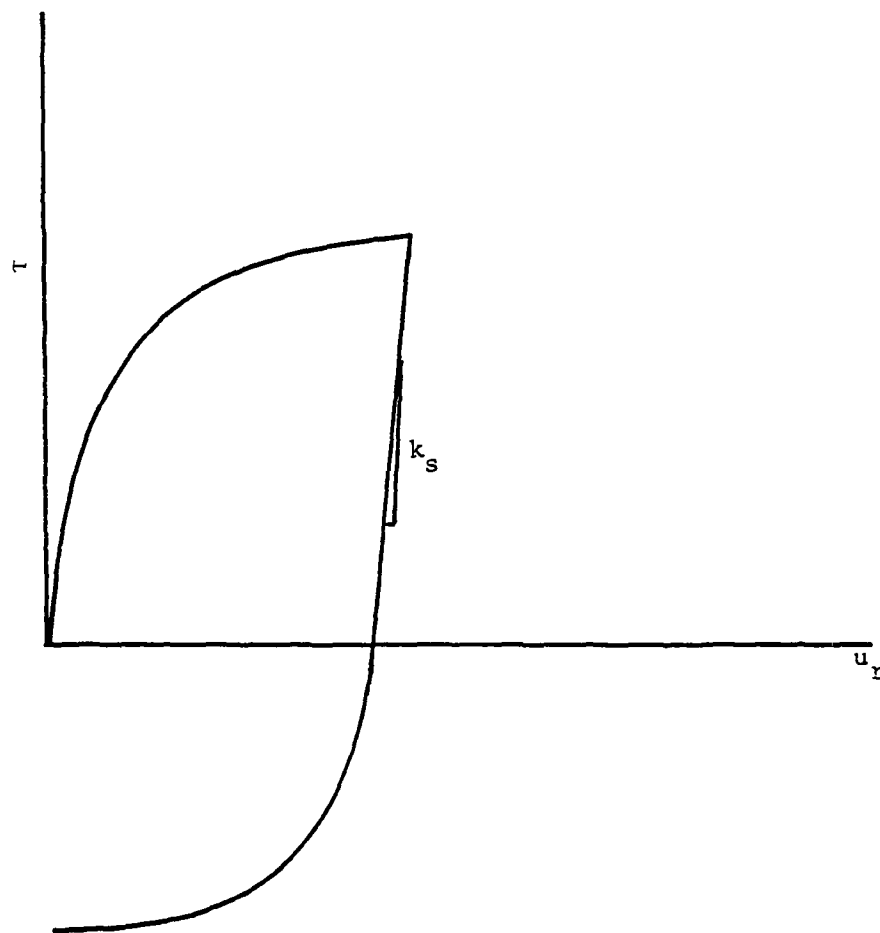


Figure 7-8. k_s as Unloading Portion of τ versus u_r

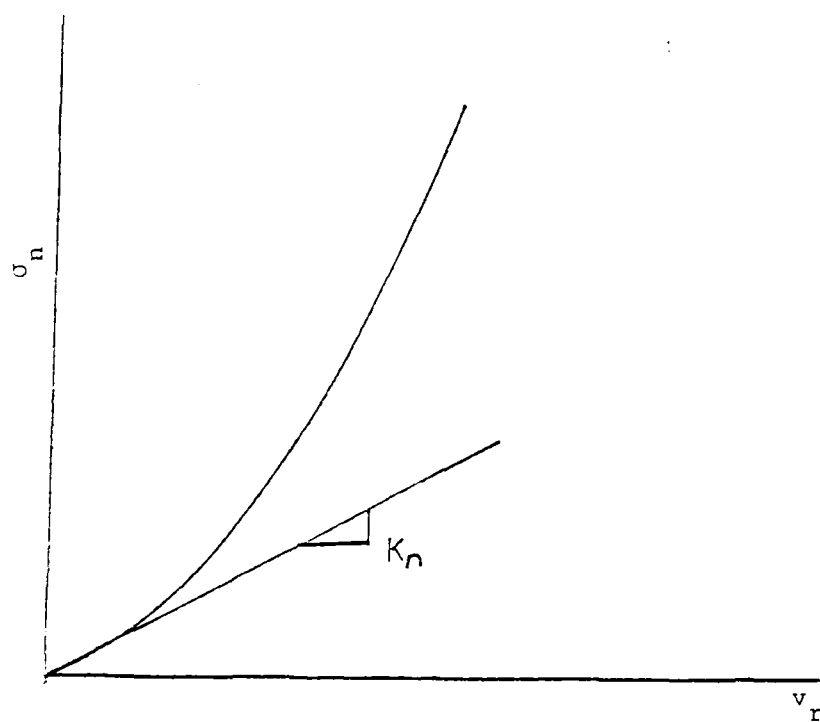


Figure 7-9. k_n as Initial Portion of σ_n versus v_r

where τ_u is usually ten to twenty percent greater than the peak shear stress, as shown in Fig. 7-10. The only parameter which needs to be determined is γ . It is found by squaring the slope of the "best fit" line from a plot of τ_u versus σ_n (Fig. 7-11).

Parameter n. The parameter n may be found by considering the point during shear where the change in vertical displacement is zero, as shown in Fig. 7-12. The shear stress at this point is τ_{zs} . If the plastic strain increment is assumed to be normal to the yield surface, then at this point $\frac{\partial F}{\partial \sigma_n} = 0$. From Eq. (7-2)

$$\frac{\partial F}{\partial \sigma_n} = n\alpha\sigma_n^{n-1} - \partial\gamma\sigma_n = 0 \quad (7-12)$$

and

$$\sigma_n = \left(\frac{\partial\gamma}{n\alpha}\right)^{\frac{1}{n-2}} \quad (7-13)$$

If M_{zs} is defined as the slope of the line yielding the locus of points on a plot of τ_{zs} versus σ_n (Fig. 7-13), then

$$\frac{\tau_{zs}^2}{\sigma_n^2} = M_{zs}^2 = -\alpha\sigma_n^{n-2} + \gamma = \gamma \left(1 - \frac{2}{n}\right) \quad (7-14)$$

The value of n may be determined from this expression once M_{zs} is known.

Growth Function. In general, the growth function can be considered a function of the history of plastic strain, plastic work, and internal state variables (Desai and Faruque, 1984; Desai et al., 1986;

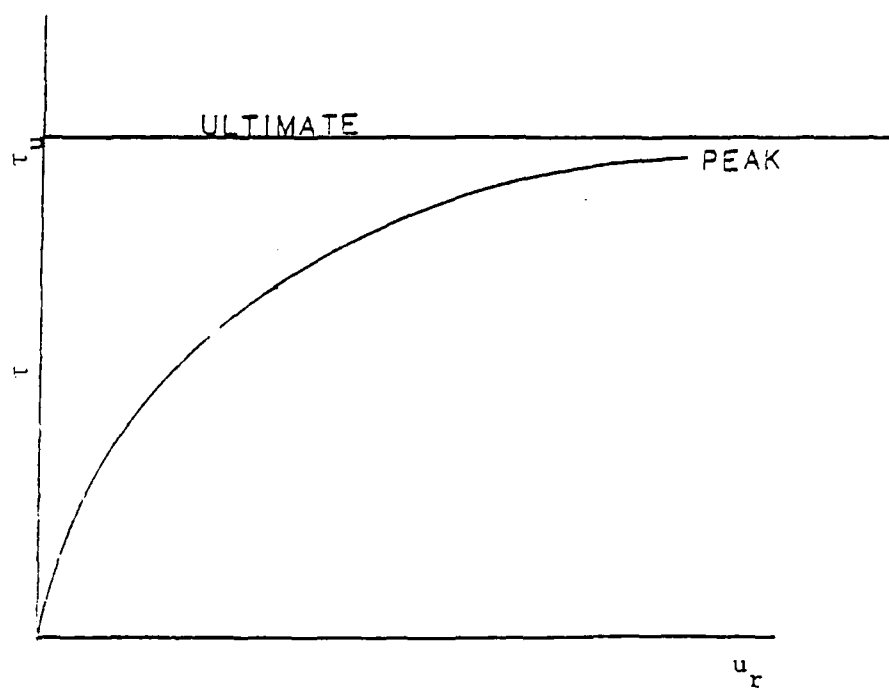


Figure 7-10. Ultimate Shear Stress

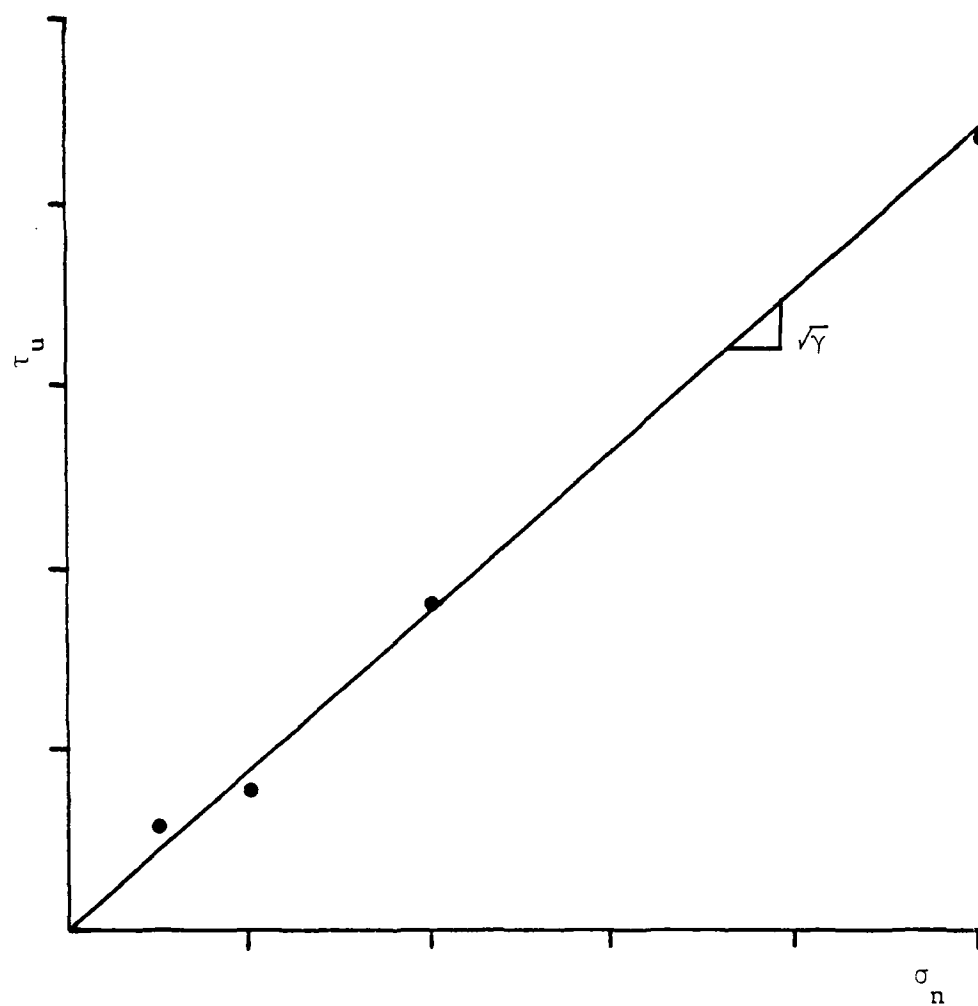


Figure 7-11. Determination of γ from Best Fit Line of τ_u versus σ_n

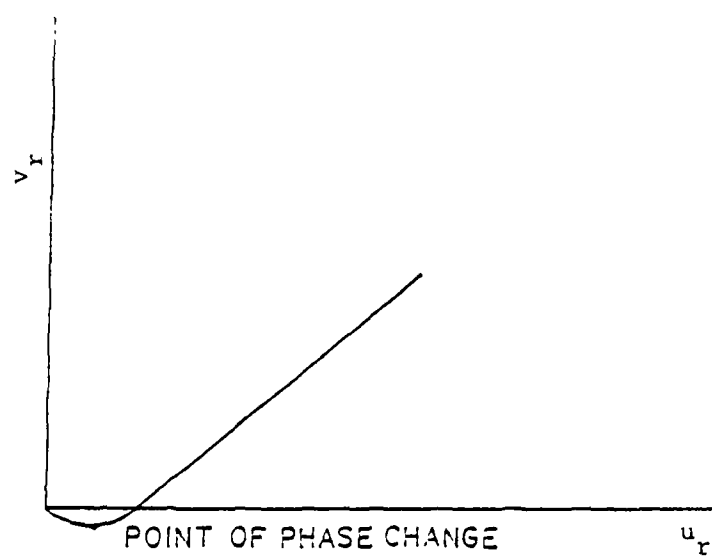


Figure 7-12. Point of Phase Change

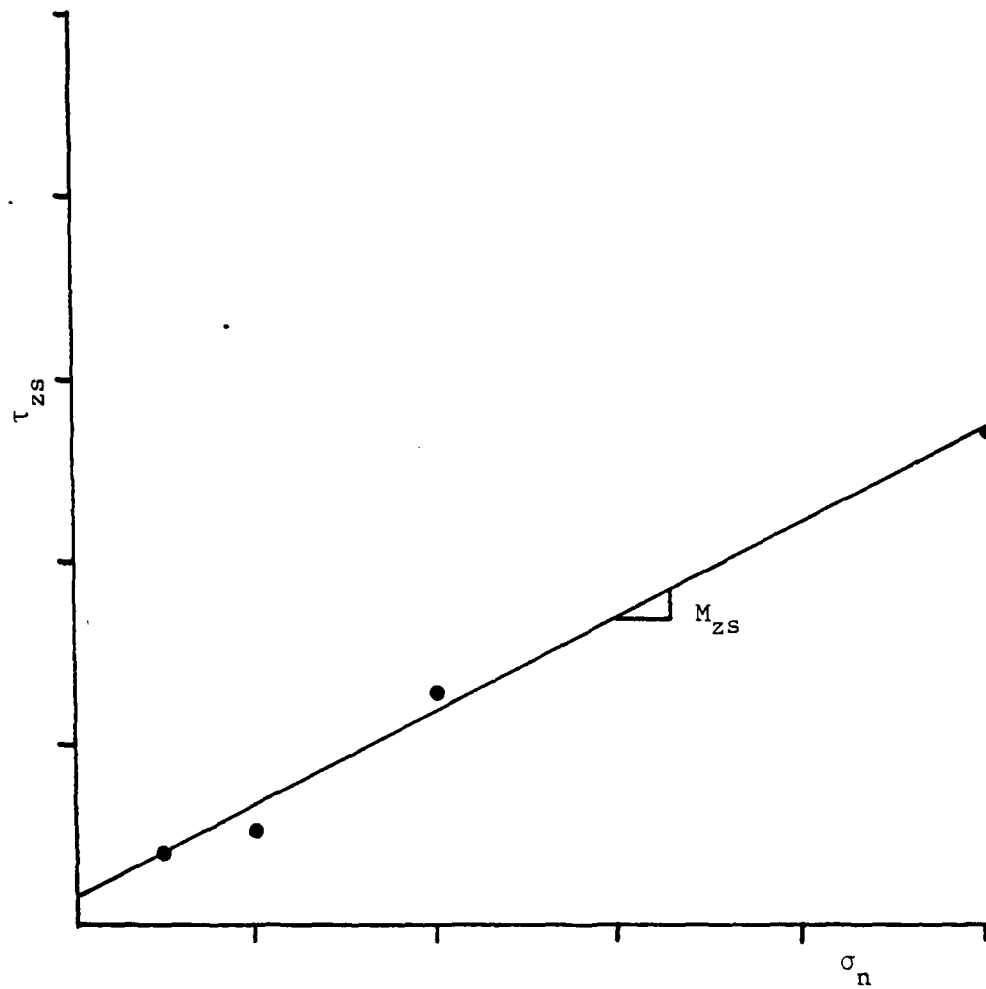


Figure 7-13. Determination of M_{zs} from Plot of σ_n Versus τ_{zs}

and Desai et al., 1987). In this study, relationships between α and the history of plastic strain trajectories, and relationships between α and plastic work were investigated. It was found that plotting α versus the total trajectory of plastic strains, $\xi = \int (u_r^p)^2 + (v_r^p)^2)^{1/2}$, yielded the most consistent trends. A plot of α versus ξ can be seen in Fig. 7-14. The shape of this plot indicates that a relationship of the form

$$\alpha = a \xi^b \quad (7-15)$$

where a and b are material constants can be appropriate. The constant b is negative such that α becomes smaller as ξ increases.

Nonassociative Parameter

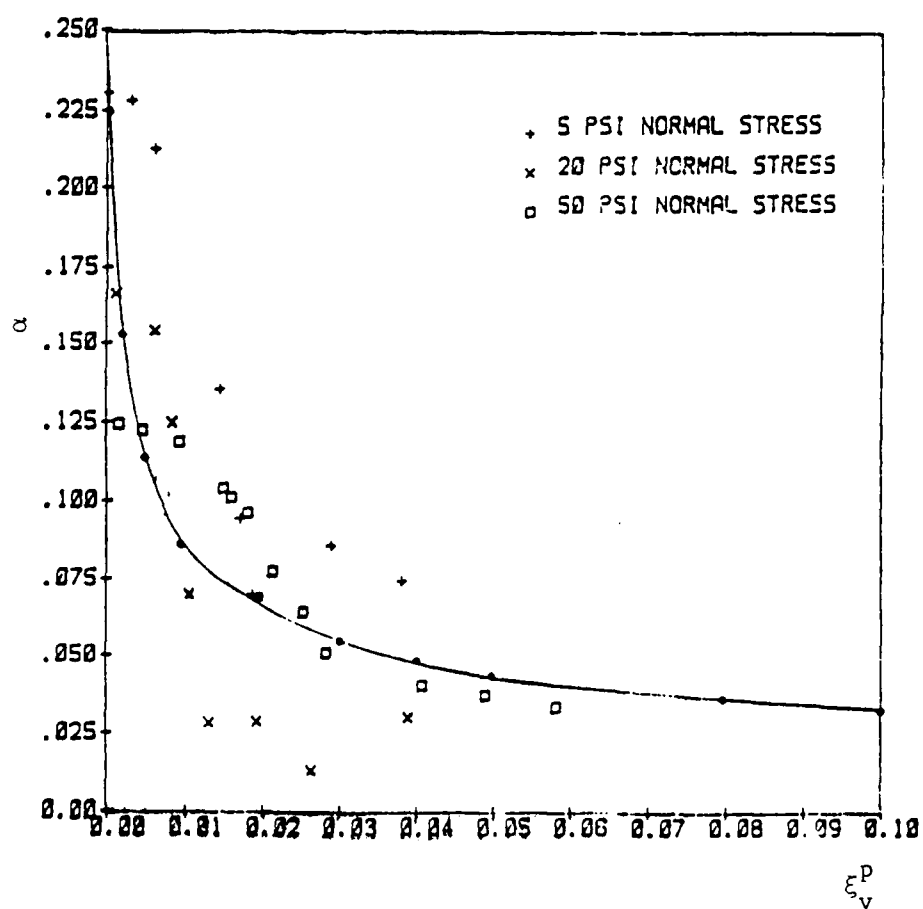
The nonassociative parameter, κ , may be determined by considering the relation between the vertical and horizontal displacement; as a simplification, the slope near ultimate conditions can be used (Frantziskonis et al., 1986). This may be shown as follows:

Consider Eq. (7-8)

$$\alpha_Q = \alpha + \kappa (\alpha_I - \alpha) (1 - r_v)$$

at ultimate conditions α equals zero, hence

$$\alpha_Q = \kappa \alpha_I (1 - r_v)$$

Figure 7-14. α versus ξ

so that

$$\kappa = \alpha_Q / \alpha_I (1 - r_v) \quad (7-16)$$

Now, from the flow rule

$$\left(\frac{dv_r}{du_r} \right)^p_{ult} = \left(\frac{\partial Q}{\partial \sigma_n} / \frac{\partial Q}{\partial \tau} \right)_{ult} \quad (7-17)$$

and we obtain

$$\left(\frac{dv_r}{du_r} \right)^p_{ult} = (\alpha_Q n \sigma_n^{(n-1)} - 2\gamma \sigma_n) / 2\tau_{ult}$$

Therefore,

$$\alpha_Q = \left[\left(\frac{dv_r}{du_r} \right)^p_{ult} 2\tau_{ult} + 2\gamma \sigma_n \right] / n \sigma_n^{(n-1)} \quad (7-18)$$

Load Reversal

As previously discussed, after load reversal, parameters for the yield and growth function must be determined for the reverse pass. The procedure is similar to that for the forward pass.

Yield and Growth Function. The ultimate state parameter γ , the parameter n , and the constants a and b in the growth function must be determined for the reverse pass. The value of γ for the reverse pass is

found in the same manner as γ for the forward pass. The ultimate shear stress, τ_u , is plotted versus σ_n for the reverse pass, and γ is taken as the square of the slope of the "best fit" line passing through these points.

The same value for the parameter n which was used during the forward pass is adopted for the reverse pass. This is because the phase change behavior is assumed to be related to damage occurring to smaller asperities superimposed on the sides of the larger sawtooth asperities. These smaller asperities, or microasperities, are related to the components of the concrete mix as discussed by Kulhawy and Peterson (1979).

Parameters a and b for the growth function during the reverse pass are found after γ is determined for the reverse pass. The procedure is identical to that for the forward pass. The parameters are determined from a plot of α versus ξ for the reverse pass.

Cyclic Loading

Parameters to be determined for each phase of displacement during a given cycle include the ultimate parameter, γ , the phase change parameter, n , and parameters for the growth function. Due to the similarities between Phases 1 and 3, and Phases 2 and 4 (Fig. 6-6(b)), only two sets of ultimate parameters are needed to describe a given cycle of displacement. The same is true of the parameters for the growth function with the exception of Phase 1 during the first cycle of displacement. The same value for n is used for all phases since the phase change behavior is assumed to be similar for all phases of the displacement cycle.

Growth function parameters are determined based on the values of the ultimate parameters used for a given cycle of displacement and may be functions of number of cycles themselves.

Summary

This section has described the specialization of a 3-D Generalized Plasticity Model to describe the behavior of rock joints under the action of shear and normal stresses. The model was extended beyond the case of monotonic shear loading to include shear load reversal and cyclic shear loading. Methods for the determination of parameters were detailed. In the next chapter, parameters will be determined from a set of test data and back predictions performed in order to demonstrate application of the model.

CHAPTER 8

BACK PREDICTIONS

Parameters for the plasticity model discussed in Chapter 7 are determined from the test data. These parameters characterize the behavior of the joint plane during shear as generally as possible. Using these determined parameters, back predictions of experimental results were performed for three cases of shear: quasi-static loading, quasi-static loading with unloading and load reversal, and cyclic shear loading, or displacement with the frequency of 1 Hz, as described in Chapter 6. This chapter describes the determination of parameters for these three cases of shear. Back predictions of test results from the three cases are presented and discussed. Because of the large number of figures depicting back predictions, only results from the 9-degree surface will be presented in this chapter. Other back predictions are presented in Appendix II.

Quasi-Static Loading

The case of quasi-static loading was investigated with test results for four different surfaces. These include the ground flat surface, and surfaces with asperity side angles of 5, 7 and 9 degrees.

Determination of Parameters

Five parameters need to be determined in order to describe the case of quasi-static loading. These include the ultimate parameter, γ ,

the phase change parameter n , growth function parameters a and b , and, for the case of the nonassociative flow rule, the parameter κ . The procedures for determination of these parameters were discussed in Chapter 7. In this section, the data used to determine the parameters is presented, and the values from various surfaces are compared and discussed. Table 8-1 presents a summary of parameters obtained from the different surfaces.

Ultimate Parameter γ . Figure 8-1 is a plot of ultimate shear stress versus normal stress obtained from quasi-static shear tests performed with the 9-degree surface. A "best fit" line is passed through the data points based on a linear regression analysis. This line defines the ultimate surface, and the square of its slope yields the value of γ . Table 8-1 presents the values of γ obtained for the different surfaces. The parameter γ is lowest for the flat surface and consistently increases with roughness.

Phase Change Parameter n . Figure 8-2 is a plot of the shear stress at the point of phase change versus normal stress (Phase Change Envelope) for the 9-degree surface. It should be noted that the point of phase change during testing of rock joints is not always a well defined point. Many times, only an initial flat portion of the curve is evident prior to dilatation rather than a measured compression. This accounts for the evident scatter in the data.

Using a linear regression analysis, a "best fit" line was determined from the data points for each surface. Based on the slope of this line and the values of γ already determined, a value of n was

Table 8-1. Summary of Parameters Obtained From
Different Surfaces for the Case of
Quasi-Static Loading

Parameter	Surface			
	Flat	5°	7°	9°
γ	0.36	0.42	0.78	0.31
n	2.50	2.50	2.50	2.50
a	0.02312	0.01063	0.03053	0.04736
b	-0.116	-0.293	-0.223	-0.162
κ	0.70	0.70	0.70	0.55

Average Values of Growth Function Parameters
a and b, and Nonassociative Parameter κ

$a = 0.02791$

$b = -0.1985$

$\kappa = 0.66$

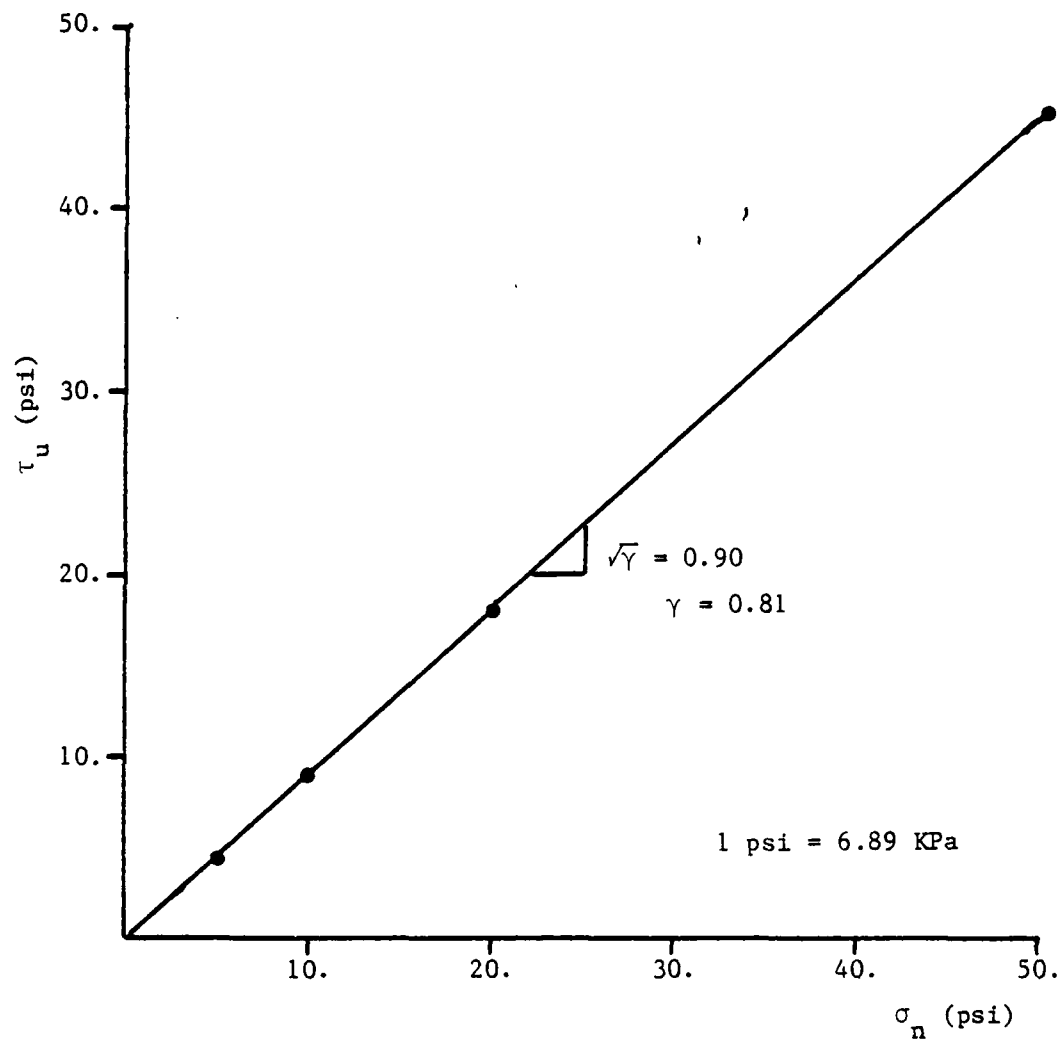


Figure 8-1. Ultimate Envelope; Quasi-Static Test Series
Forward Pass; 9° Surface

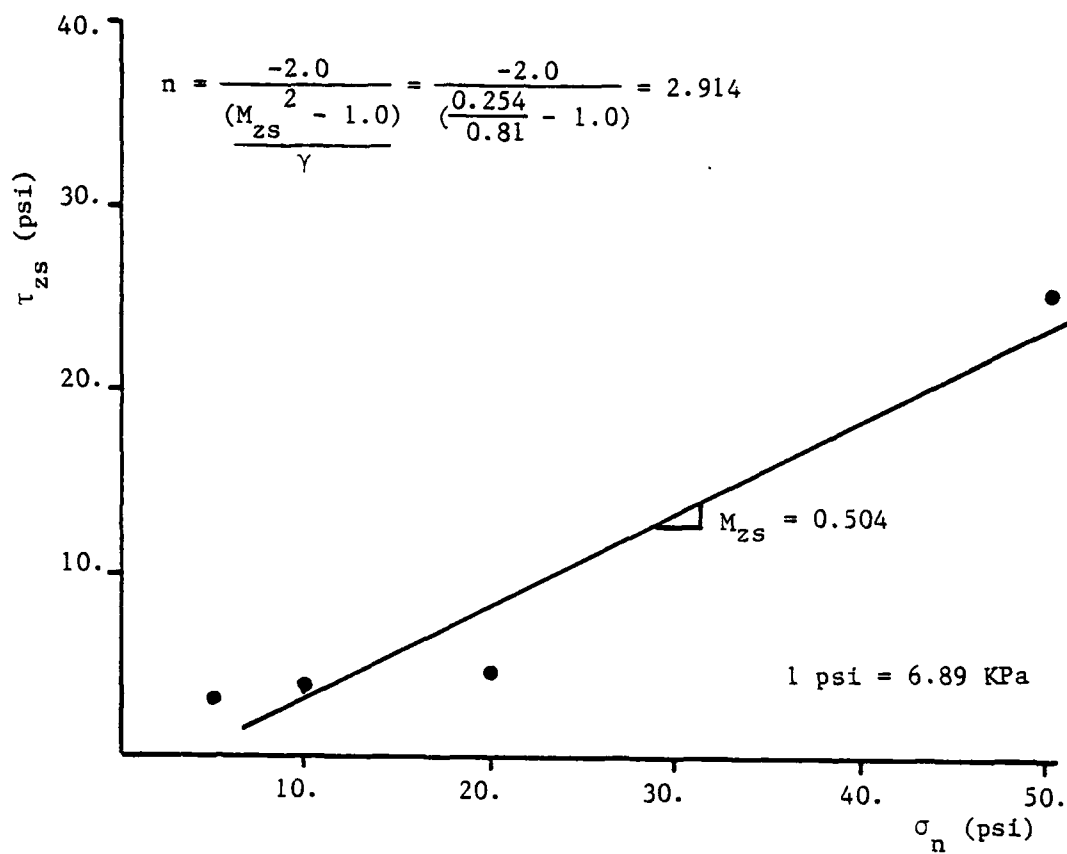


Figure 8-2. Phase Change Envelope; 9° Surface

computed for each surface. No measurable dilation or compression occurred during the testing of the ground flat surface, and this indicates that a value of n equal to 2.0 should be used for this case since M_{zs} is zero [see Eq. (7-14)]. Table 8-2 presents the value of n determined for each surface. Due to the scatter in the data, and the small variation in n between surfaces, an average value of $n = 2.5$ was used for all surfaces. By using the same value of n for all surfaces, it is assumed that the point of phase change during shear of rock joints is more related to the microasperity structure, which may be similar between these surfaces, and the manner in which the macroasperities of the top and bottom samples "fit" prior to the initiation of shear, than to variations of the sawtooth (macroasperity) structure apparent between the surfaces investigated during this study.

Growth Function Parameters. Figure 8-3 is a plot of growth function values, α versus the trajectory of the total plastic displacements ξ , plotted from data for the 9-degree surface. The figure presents data from tests performed under different levels of normal stress.

Assuming a form for the growth function $\alpha = a\xi^b$, as discussed in Chapter 7, the parameters a and b were determined via a linear regression analysis of the data points plotted on a transformed logarithmic plot. The parameters a and b are considered as constants over the range of applied normal stresses for a given surface. Table 8-1 presents the values of the growth function constants a and b for different surfaces.

Table 8-2. Value of n Determined
for Each Surface

Surface	n
Flat	2.000
5°	2.224
7°	3.050
9°	2.914

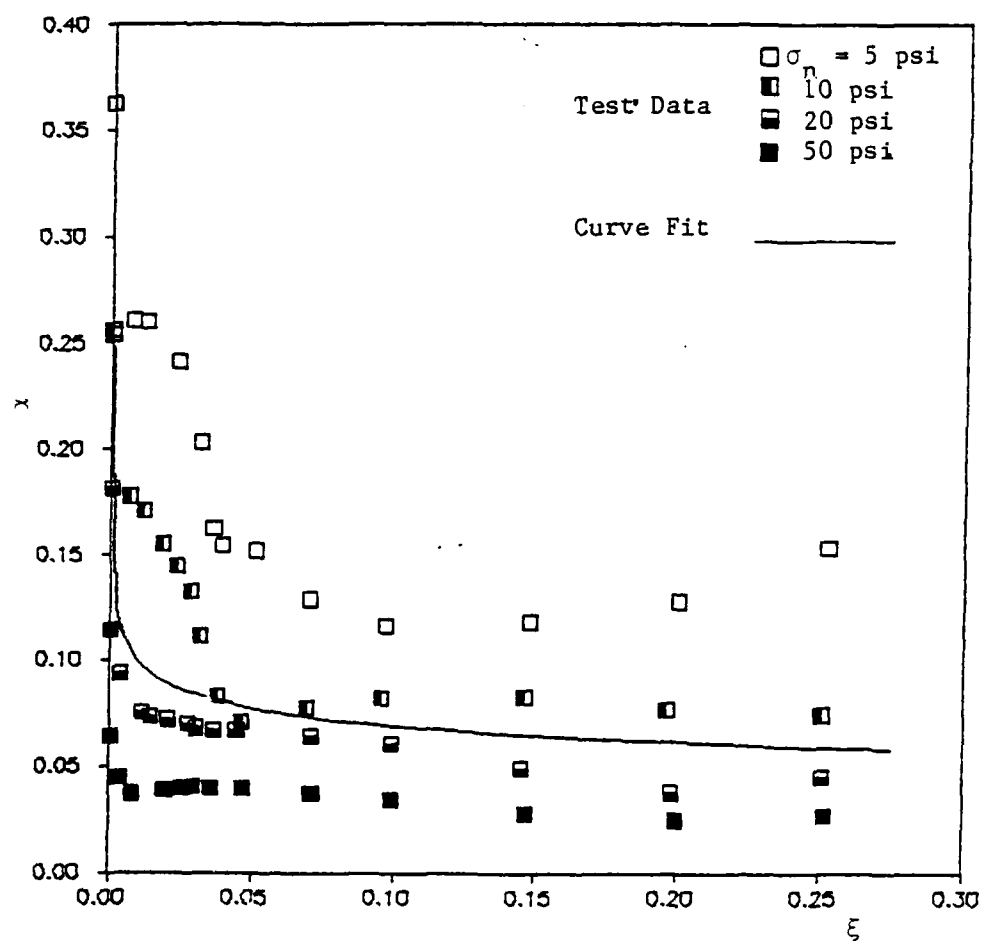


Figure 8-3. α versus ξ ; Quasi-Static Test Series; 9° Surface

The values of a and b for the different surfaces presented in Table 8-1 may be averaged to yield growth function constants to be used for all the different roughnesses. These values are shown at the bottom of Table 8-1. By using the same growth function constants for all the roughnesses, it is assumed that the hardening process is more related to the microasperity structure than to the difference in macroasperities between the surfaces. Back predictions using growth function constants determined for each roughness and for all the surfaces will be compared in the next section.

Nonassociative Parameter κ . The nonassociative parameter κ is computed from test results based on the slope of the vertical relative displacement versus tangential relative displacement near ultimate conditions, as outlined in Chapter 7. These computations are presented in Appendix III. During back predictions, it was found that for best results, these computed values may need to be adjusted slightly. This may be due to the fact that the procedure for the determination of κ assumes it to be a constant where in reality it may not be. Table 8-1 presents the values of κ used in the back prediction of test results for the different roughnesses.

Back Predictions of Quasi-Static Loading

Using the parameters discussed in the preceding section, back predictions were made and compared with experimental results. Both associative and nonassociative flow rules were employed. Also, back predictions were performed with averaged growth function constants and nonassociative parameter κ .

Algorithm. The back predictions were performed by numerical integration of the elastic-plastic constitutive, K^{ep} , matrix, described in Chapter 7. Because of the hierarchical nature of the plasticity model, the same formulation was used for both the associative and non-associative cases. For the associative case, $\kappa = 0$. The integration is performed using an incremental technique similar to one described by Desai and Faruque (1984). Small increments of relative tangential displacements are input and the corresponding increments of shear stress and relative vertical displacement are computed under the condition of constant normal stress. As with all numerical techniques, the solution obtained in this manner is an approximate one, the accuracy of which increases with a decrease in the increment size. In this study, relative tangential displacement increments of 0.0001 in. (0.0025 mm.) were found to yield acceptable results. The algorithm employed for these back predictions is as follows:

1. Input the normal stress, increments of relative tangential displacement, parameters for the joint plane including γ , n , a , b , κ , and the elastic shear and normal stiffnesses.
2. Starting from a state of zero displacement and stress, apply the normal stress and compute the value of the growth function, α , based on the state of stress.
3. Set the value of α at the initiation of nonassociative behavior, α_I , equal to the value of α just after the application of normal stress, but prior to the initiation of shear. At this point, the

vertical component of the trajectory of the history of plastic strain, ξ_v , is equal to the total trajectory of the history of plastic strain, ξ (computed from α), and the ratio of ξ_v/ξ , r_v , is equal to unity.

4. Using values of α , α_I , r_v and the inputted parameters, compute the modified growth function, α_Q , used in the potential function. Compute the derivatives of the yield and potential surfaces, and form the K^{ep} matrix.

5. Solve the system of equations and determine the increment of shear stress and relative vertical displacement.

6. Update the total stress and relative displacement vectors.

7. Compute increments of plastic relative displacement using the flow rule, associative or nonassociative.

8. Obtain updated values for ξ , ξ_v , r_v , and α .

9. If this is the first increment of shear displacement, check the value of the yield function, F . If F is negative, adjust the shear stress to make $F = 0$. This is done by changing the elastic shear stiffness on the first increment such that F is equal to zero at the end of the increment.

10. If the total relative tangential displacement is not reached, return to Step 4. If the total tangential displacement is reached, stop.

Results. Figures 8-4 to 8-8 present back predictions of quasi-static shear tests. Both test data and back predicted results are shown. Parameters utilized in this analysis are presented in Table 8-1, where the growth function constants and κ are found for each surface.

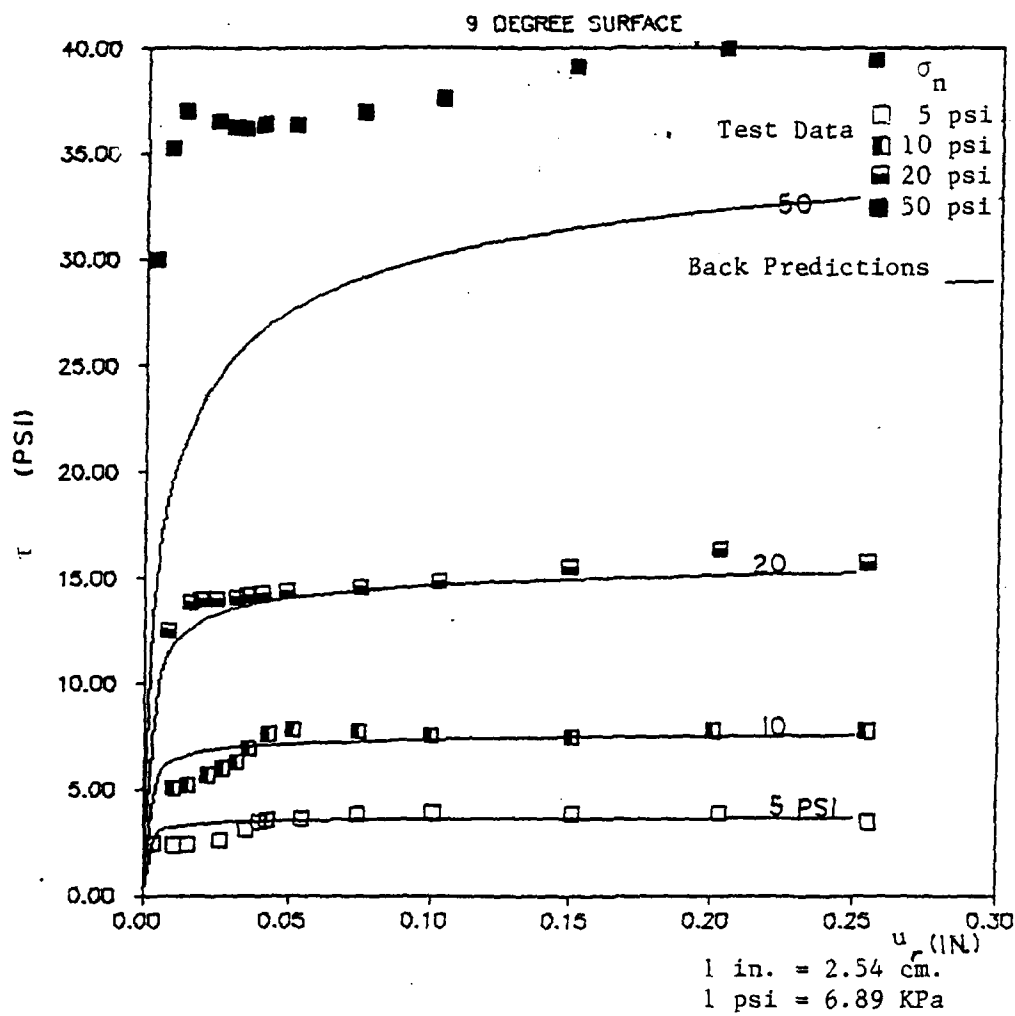


Figure 8-4. Test Data and Back Predictions of τ versus u_r , Quasi-Static Loading; 9° Surface

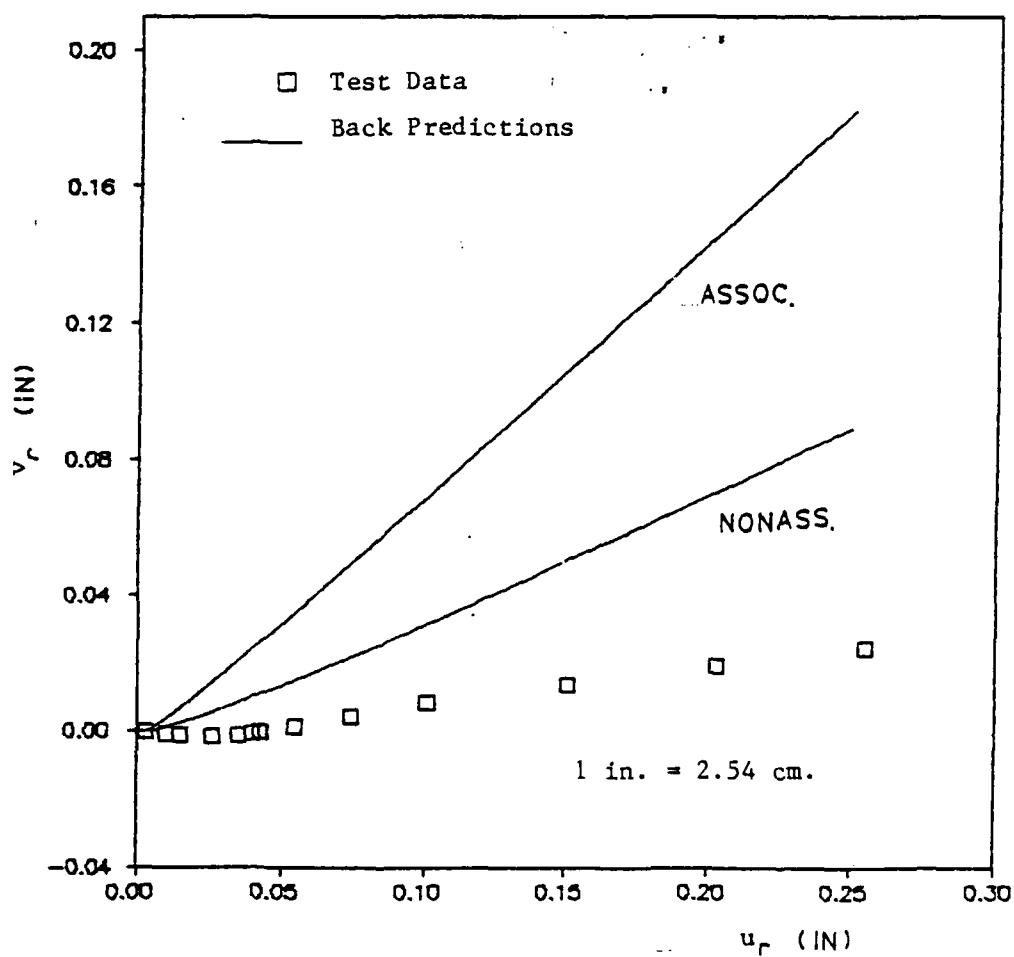


Figure 8-5. Test Data and Back Predictions of v_r versus u_r ; Quasi-Static Loading; $\sigma_n = 5$ psi; 9° Surface; Associative and Nonassociative Case

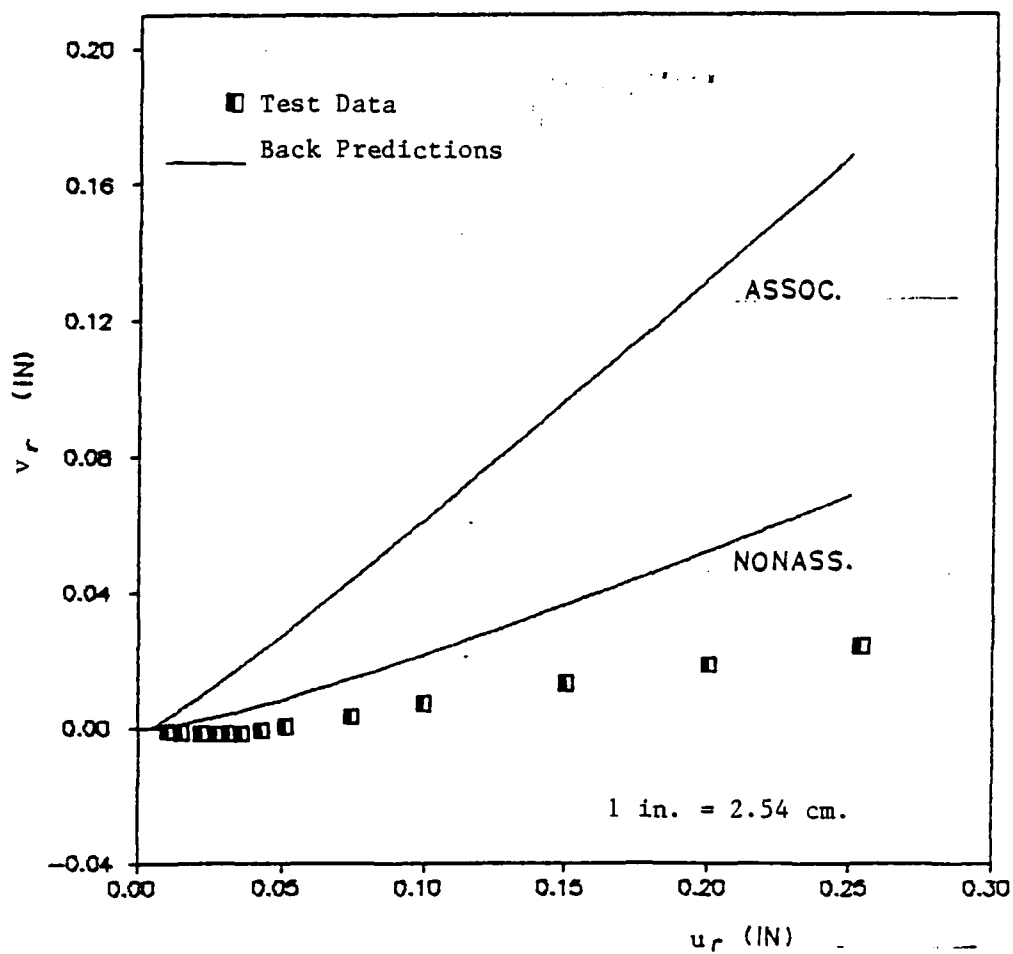


Figure 8-6. Test Data and Back Predictions of v_r versus u_r ; Quasi-Static Loading; $\sigma_n = 10$ psi, 9° Surface; Associative and Nonassociative Case

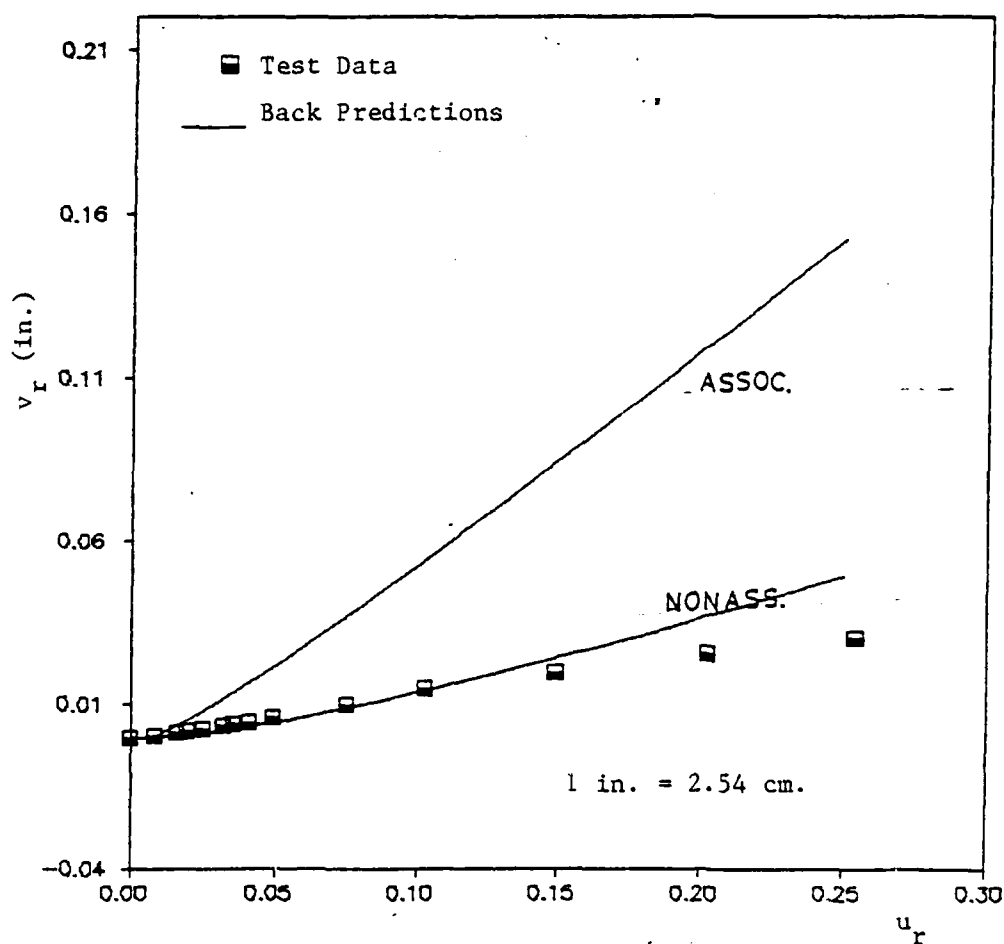


Figure 8-7. Test Data and Back Predictions of v_r versus u_r ; Quasi-Static Loading; $\sigma_n = 20$ psi; 9° Surface; Associative and Nonassociative Case

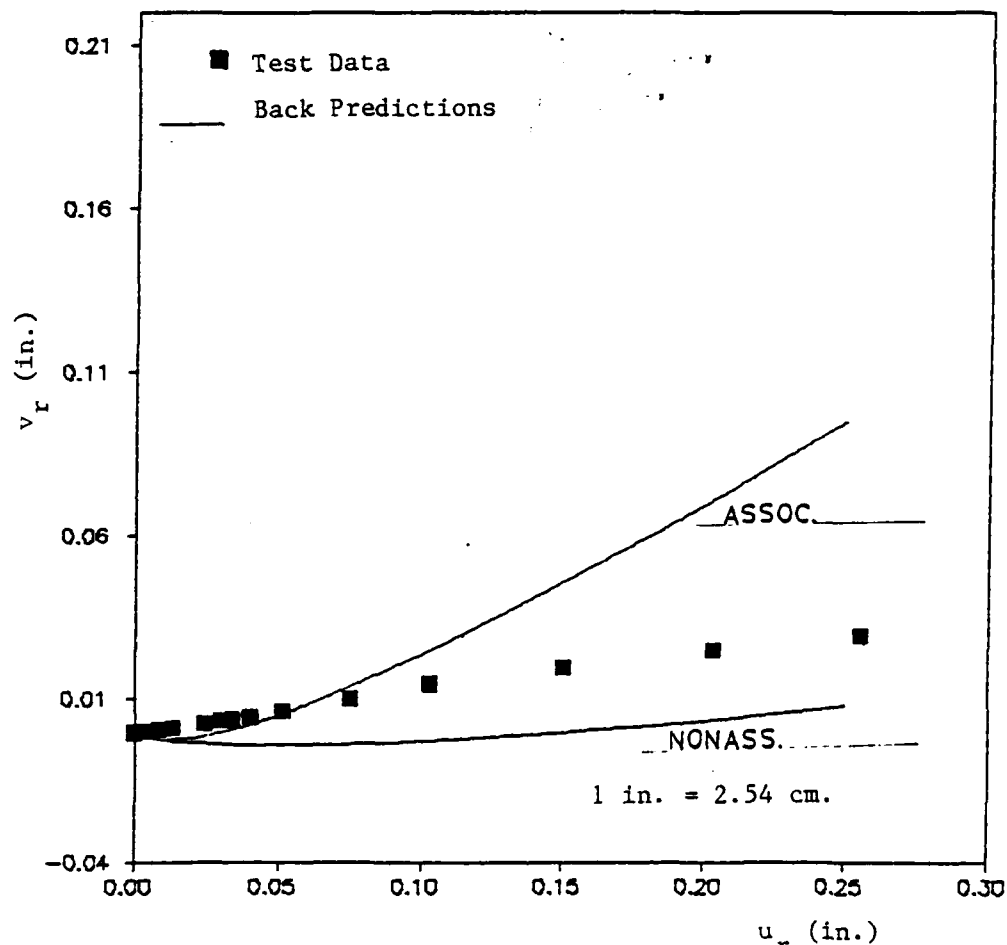


Figure 8-8. Test Data and Back Predictions of v_r versus u_r ; Quasi-Static Loading; $\sigma_n = 50$ psi; 9° Surface; Associative and Nonassociative Case

Figure 8-4 presents plots of shear stress versus relative tangential displacement for the 9-degree surface under different levels of normal stress. Use of the associative or nonassociative flow rule does not significantly alter the back prediction of these curves; hence, only back predictions utilizing the associative flow rule are presented here. The model captures the effect of different levels of normal stress and hardening behavior quite well. Back predicted curves appear to be in reasonable agreement with test data. The only significant discrepancy is at a normal stress of 50 psi (344.5 KPa).

Figures 8-5 to 8-8 are plots of relative tangential displacement, u_r , versus relative vertical displacement, v_r . Each figure depicts results from different levels of normal stress including back predictions using associative and nonassociative flow rules and the test data. In all cases, the back predictions which employ the associative flow rule significantly overpredict dilation. The back predictions which utilize the nonassociative flow rule are in better agreement with test data. However, some error between experiment and theory still exists. The model appears to be much more sensitive to the effect of changes in levels of normal stress on the prediction of relative vertical displacements during shear than experimental results indicate. At normal stresses of 5 and 10 psi (34.5 and 68.9 KPa), the back predictions utilizing the nonassociative flow rule still overpredict dilation. At 20 psi (137.8 KPa), the back prediction is good, and at 50 psi (344.5 KPa), not quite enough dilation is predicted.

Average Parameters. In this case, growth function constants, a and b , and the parameter κ are averaged over the range of surface roughnesses considered. The ultimate parameter γ is still determined separately for each roughness. Therefore, in this discussion, it is implicitly assumed that γ is significantly affected by the macroasperity characteristics of the surface, while hardening and nonassociativeness are more affected by characteristics of the microasperities.

Figures 8-9 to 8-11 present results of back predictions utilizing the average parameters presented in Table 8-1. Only back predictions utilizing a nonassociative flow rule are considered. Results are presented for normal stresses of 5 and 50 psi (34.5 and 344.5 KPa). Comparing the results utilizing average parameters with the results of the previous section, it appears that there are some differences, but the differences are not striking for the 9-degree surface.

Quasi-Static Loading with Unloading and Load Reversal

The case of quasi-static loading with unloading and load reversal was investigated with test results from the 9-degree surface. As described in Chapter 7, this case is modeled by considering two distinct phases of displacement, the forward and reverse passes. During the forward pass, the joint is dilating as "up asperity travel" takes place (Fig. 6-2(b)). Parameters for this phase are identical to those discussed in the preceding section on quasi-static loading. During the reverse pass, the joint is compressing as "down asperity travel" takes place (Fig. 6-2(b)). Parameters for this pass are found in a manner similar to

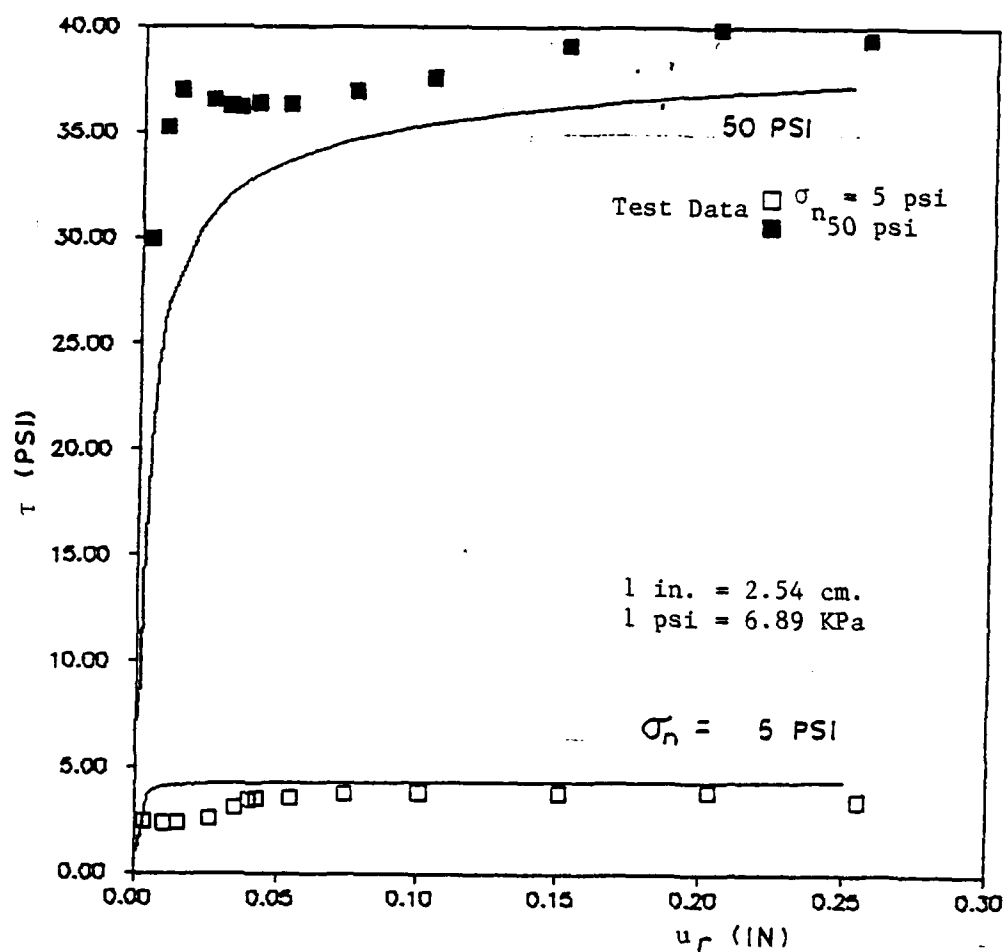


Figure 8-9. Test Data and Back Predictions of τ versus u_r ; Quasi-Static Loading; Average Parameters; 9° Surface; Nonassociative Case

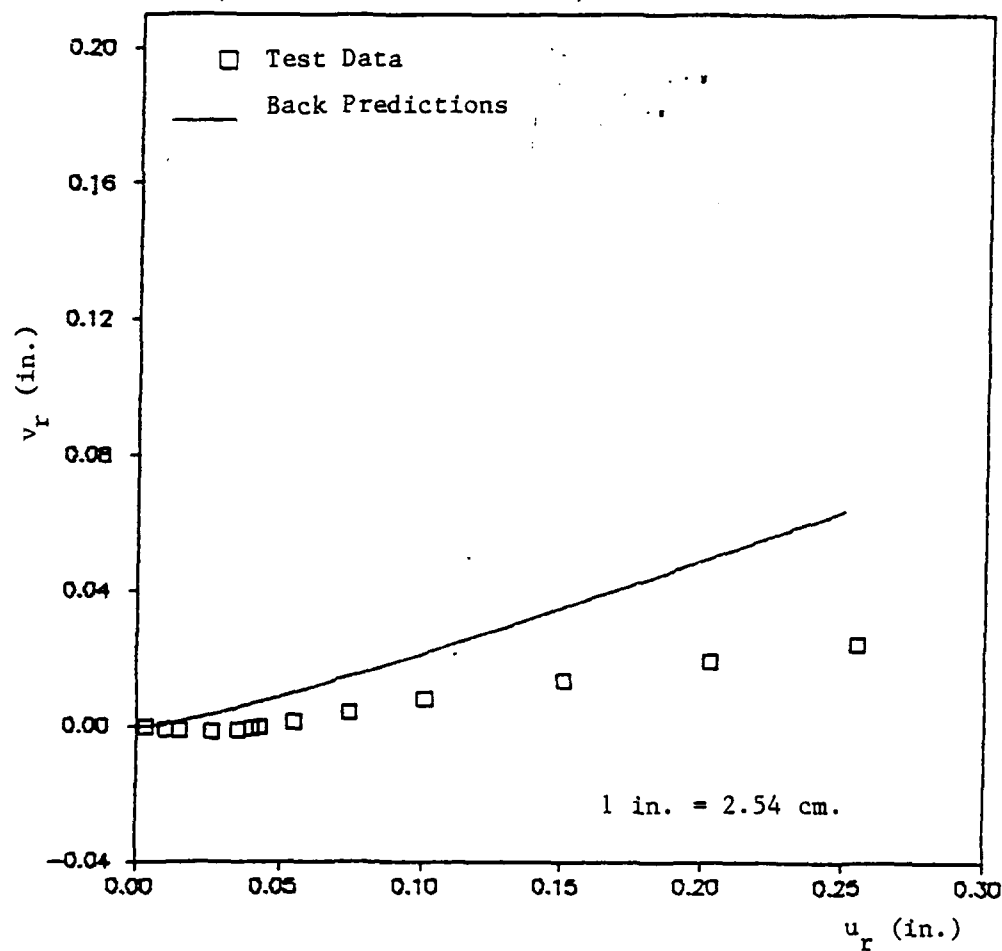


Figure 8-10. Test Data and Back Predictions of v_r versus u_r ; Quasi-Static Loading; Average Parameters; 9° Surface; $\sigma_n = 5$ psi; Nonassociative Case

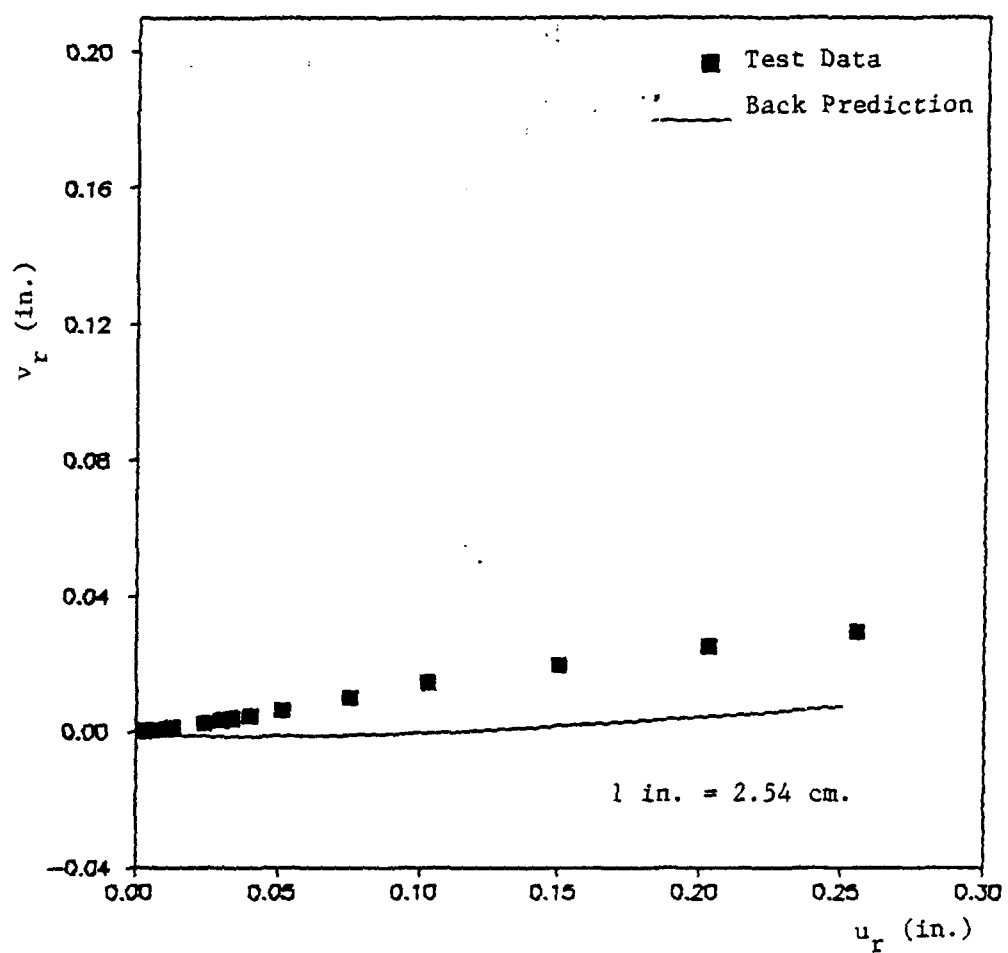


Figure 8-11. Test Data and Back Predictions of v_r versus u_r ; Quasi-Static Loading; Average Parameters; 9° Surface; $\sigma_n = 50$ psi; Nonassociative Case

that for the forward pass, previously described. The following section describes the determination of model parameters from the reverse pass data. A summary of all the parameters utilized in this section is presented in Table 8-3.

Determination of Parameters

Figure 8-12 is a plot of ultimate shear stress versus normal stress obtained from the reverse pass of quasi-static testing with the 9-degree surface. The square of the "best fit" line through these points yields a value of γ for the reverse pass of 0.45.

As previously discussed, it is assumed that the phase change parameter, n , is related to the characteristics of the microasperity pattern as opposed to the macroasperities. Assuming the microasperities are similar during travel up or down the asperity sides, the same value of $n - 2.5$ is employed for both the forward and reverse passes.

With the values of γ and n , the growth function parameters may be determined. Figure 8-13 is a plot of α versus ξ from data obtained during the reverse pass. Data from tests performed under four levels of normal stress 5, 10, 20, and 50 psi (34.5, 68.9, 137.8, and 344.5 KPa) is presented. Using this data, growth function constants a and b are 0.024 and -0.149, respectively. The solid line in Fig. 8-13 is a plot of the determined growth function.

Calculations for the nonassociative parameter κ during the reverse pass are presented in Appendix III.

Table 8-3. Summary of Parameters
for Reverse Pass;
9° Surface

γ	0.45
n	2.50
a	0.024
b	-0.149
κ	1.50

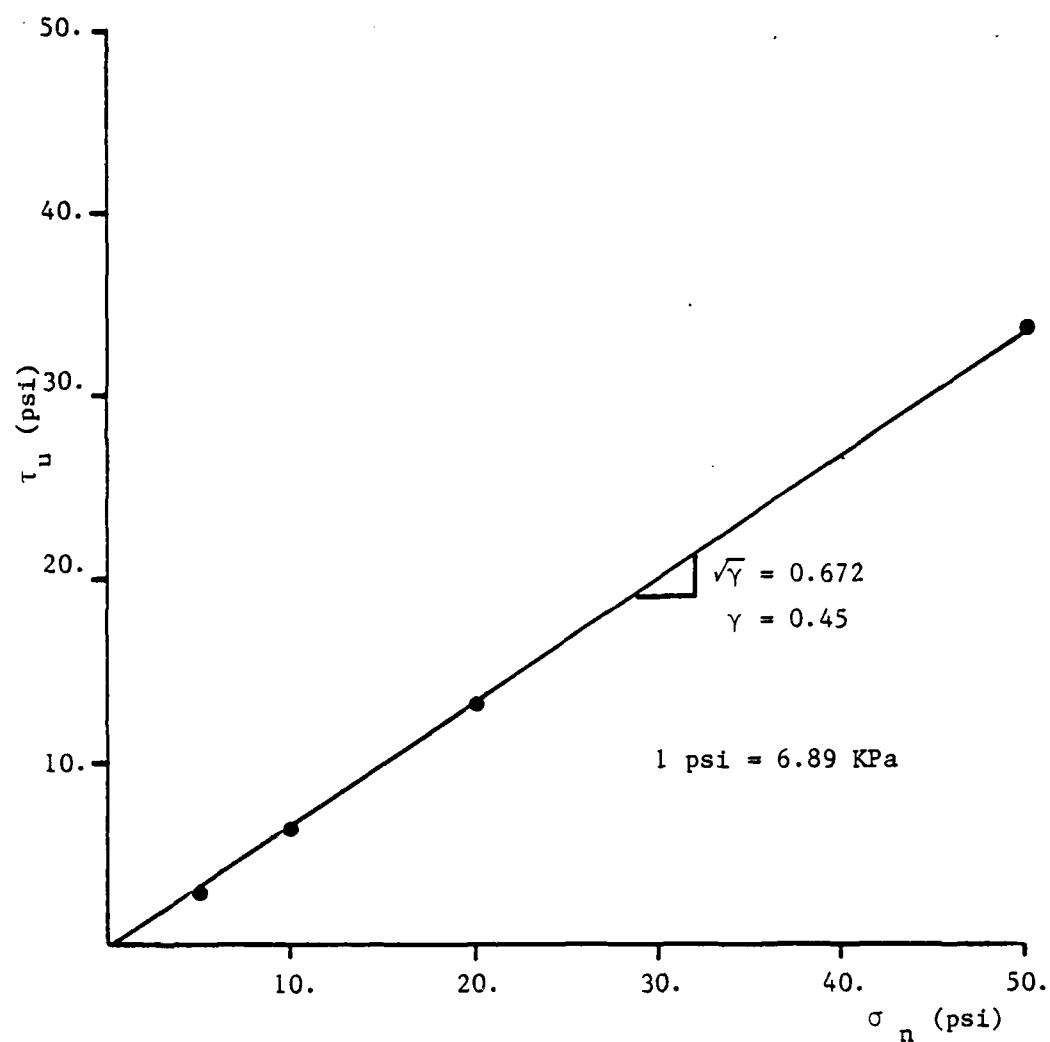
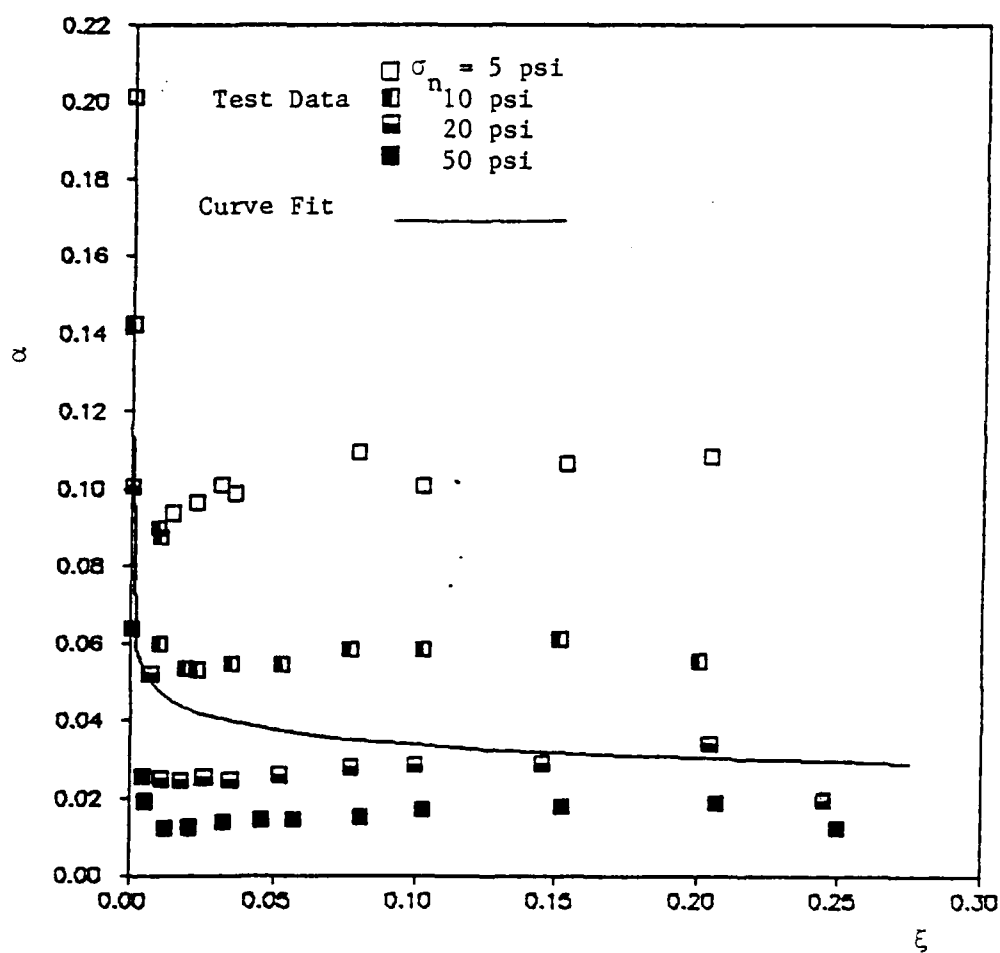


Figure 8-12. Ultimate Envelope; Reverse Pass;
9° Surface

Figure 8-13. α versus ξ ; Reverse Pass; 9° Surface

Back Predictions of Quasi-Static Loading With Unloading and Load Reversal

Using the parameters discussed in the preceding section, back predictions of both forward and reverse passes under four levels of normal stress on the 9-degree surface are computed and compared with test data. Both associative and nonassociative flow rules are employed.

Algorithm. The algorithm is similar in concept to the algorithm described in the section on quasi-static loading. The difference is that the back prediction continues after completion of the forward pass. Upon completion of the forward pass, unloading takes place prior to load reversal, as described in Chapter 7. Unloading is considered to be elastic.

After elastic unloading, parameters for the reverse pass are input, and the computations resume at Step 2 of the algorithm described in the section on quasi-static loading. Using this procedure, parameters which involve the history of deformation are reinitialized at the onset of reverse loading. However, the history of deformation is not erased since parameters for the reverse pass were determined from reverse pass test results obtained on a surface that previously underwent deformations of the forward pass.

Results. Figures 8-14 to 8-18 present results of back predictions of quasi-static shear tests with unloading and load reversal. Back predictions and test data are presented considering shear with the 9-degree surface under different levels of normal stress including 5, 10, 20, and 50 psi (34.5, 68.9, 137.8, and 344.5 KPa). Both associative and nonassociative flow rules are considered.

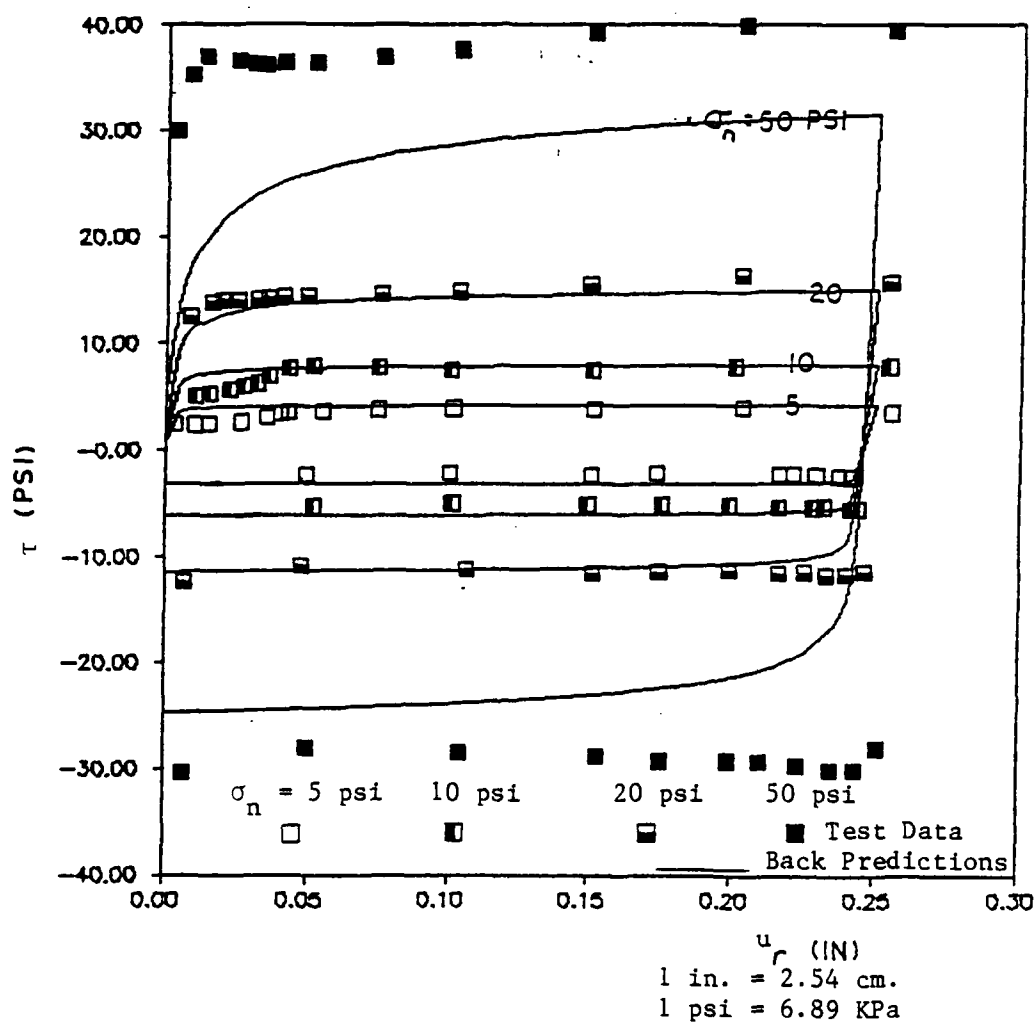


Figure 8-14. Test Data and Back Predictions of τ versus u_r ; Quasi-Static Tests With Unloading and Load Reversal; 9° Surface

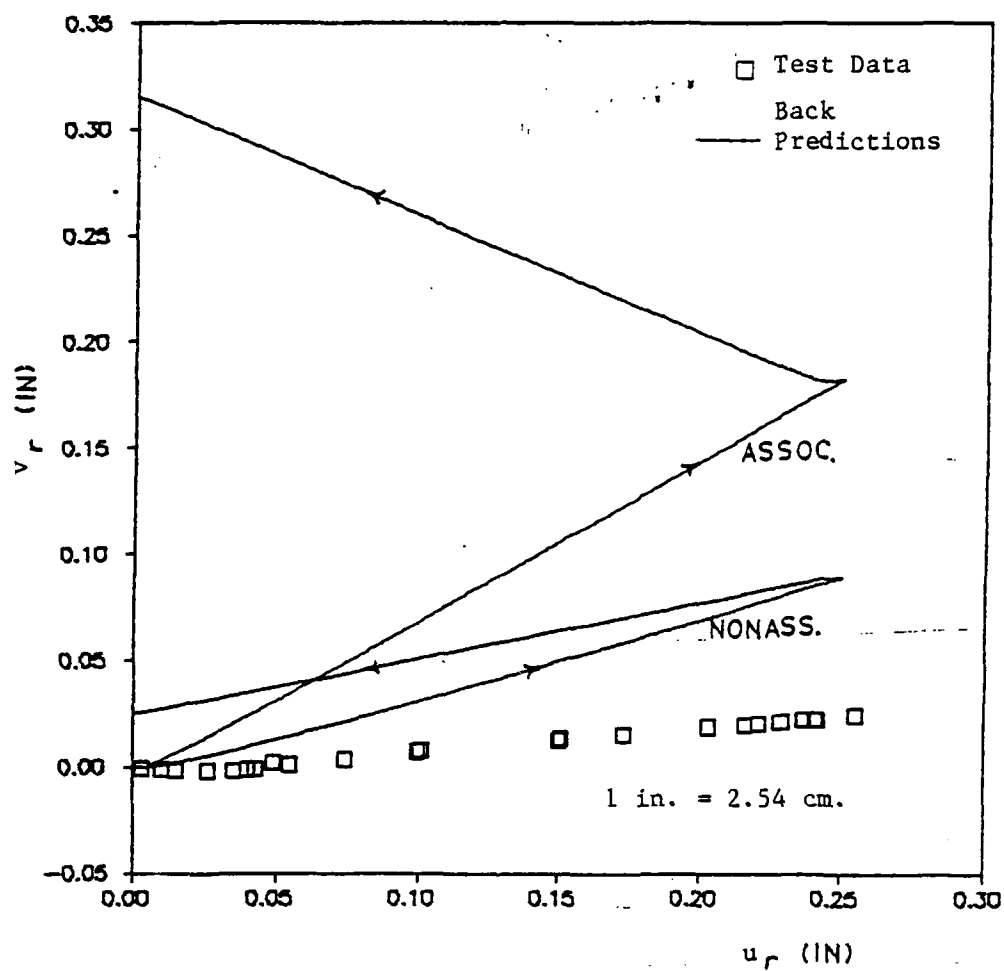


Figure 8-15. Test Data and Back Predictions of v_r versus u_r ; Quasi-Static Tests With Unloading and Load Reversal; 9° Surface; $\sigma_n = 5$ psi; Associative and Nonassociative Cases

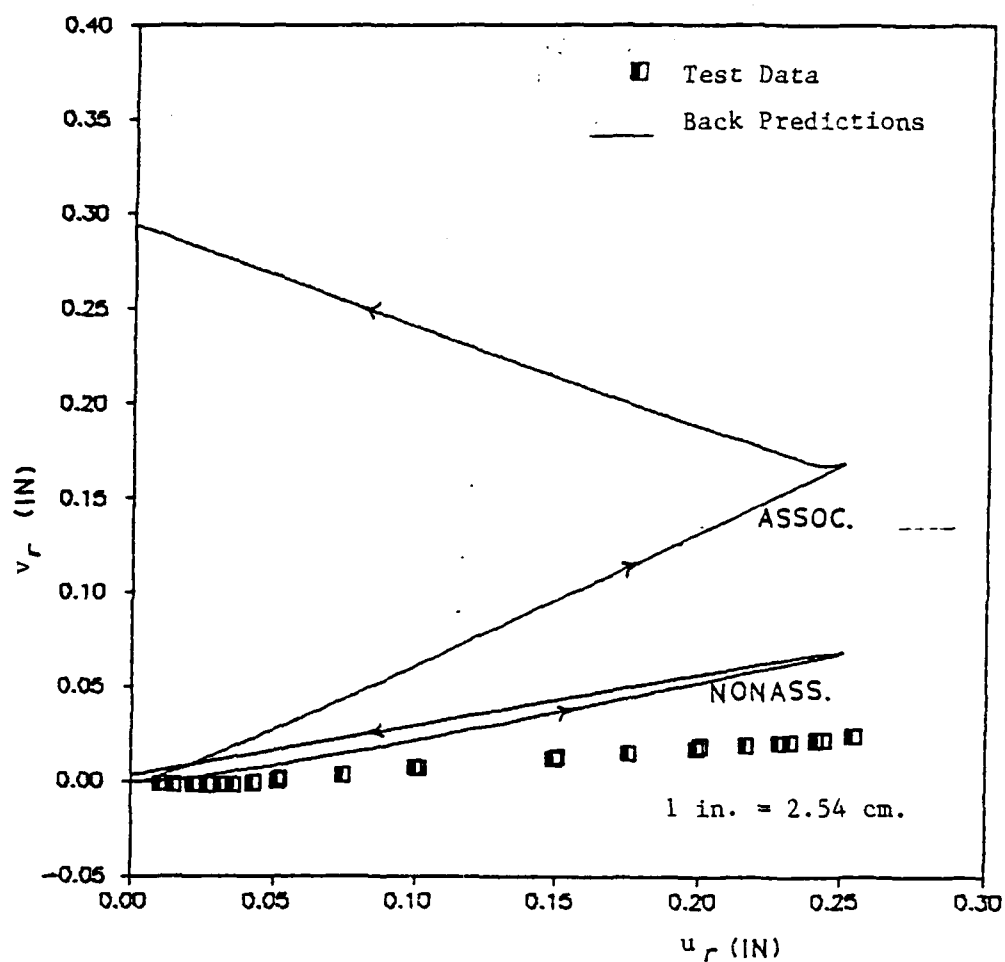


Figure 8-16. Test Data and Back Predictions of v_r versus u_r ; Quasi-Static Tests With Unloading and Load Reversal; 9° Surface; $\sigma_n = 10$ psi; Associative and Nonassociative Cases

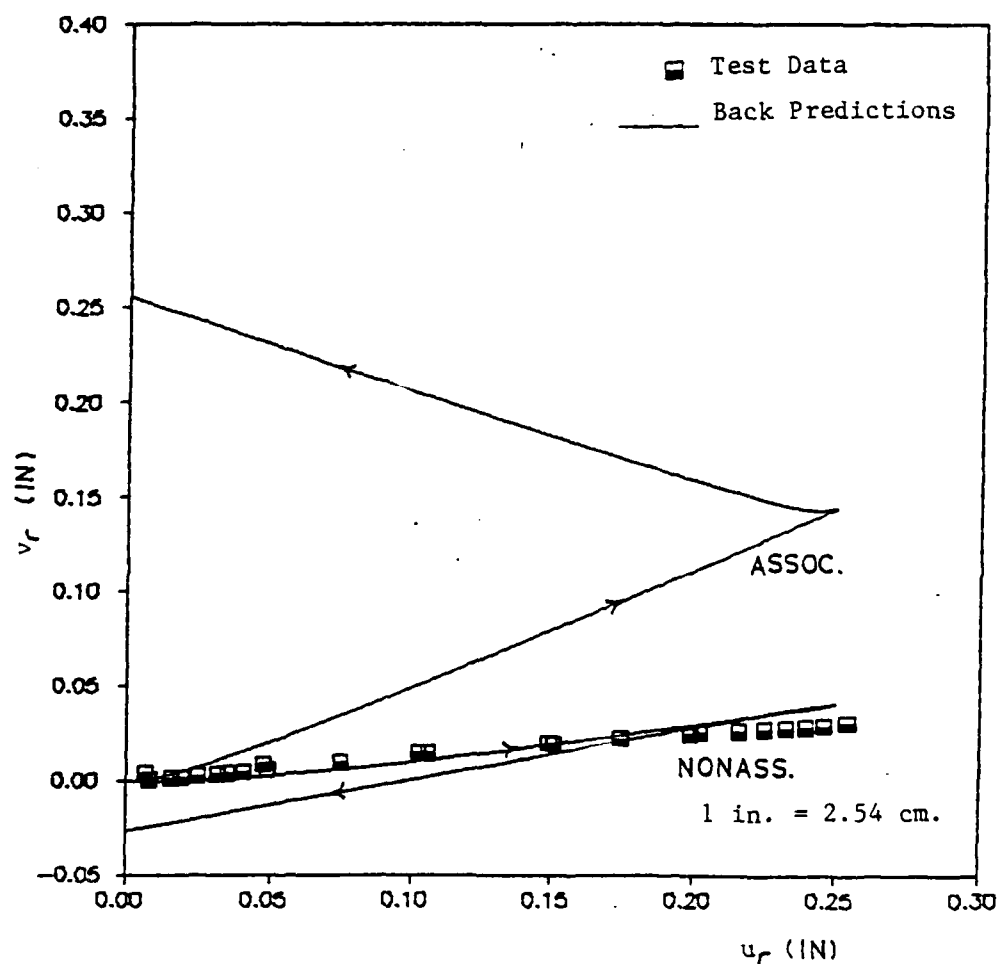


Figure 8-17. Test Data and Back Predictions of v_r versus u_r ; Quasi-Static Tests With Unloading and Load Reversal; 9° Surface; $\sigma_n = 20$ psi; Associative and Nonassociative Cases

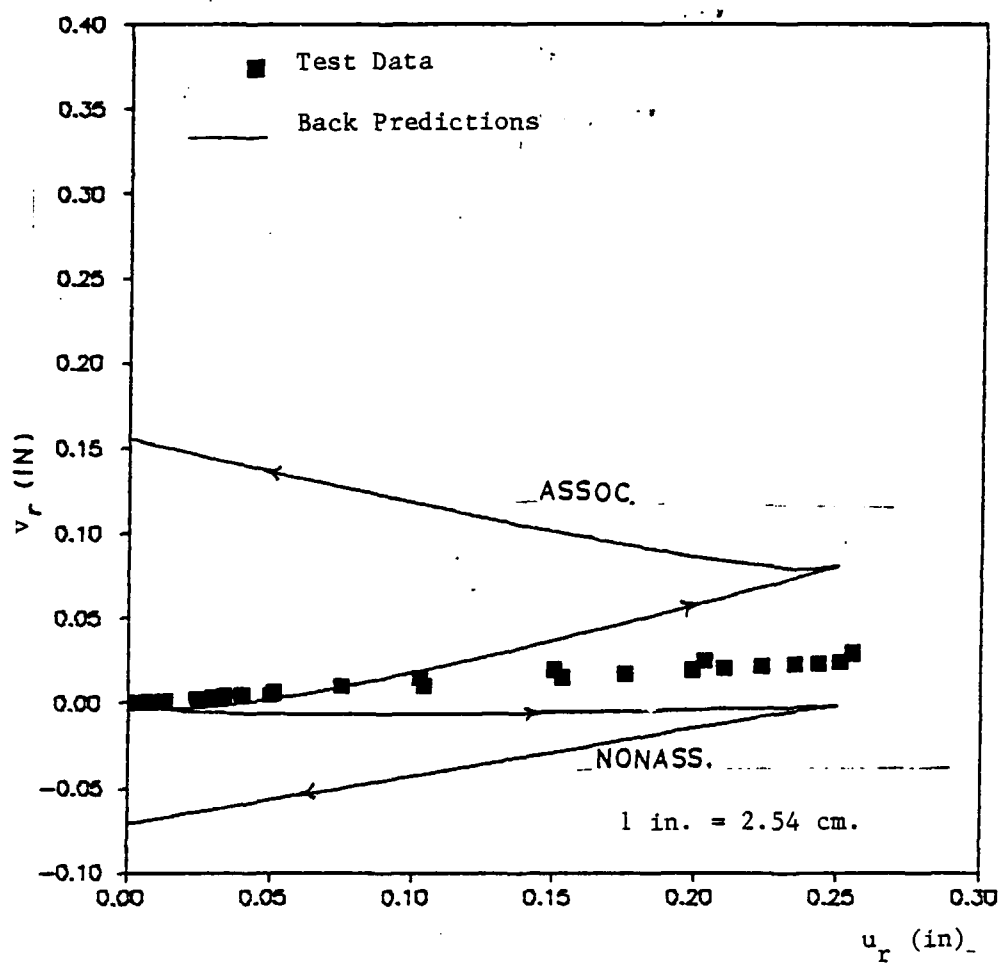


Figure 8-18. Test Data and Back Predictions of v_r versus u_r ; Quasi-Static Tests With Unloading and Load Reversal; 9° Surface; $\sigma_n = 50$ psi; Associative and Nonassociative Cases

Figure 8-14 is a plot of shear stress versus u_r with results from all levels of normal stress presented. The back predictions appear satisfactory with some significant error evident at normal stress level 50 psi (344.5 KPa).

Figures 8-15 to 8-18 are plots of u_r versus v_r considering unloading and load reversal. Each figure presents results from testing under one level of normal stress on the 9-degree surface, including back predictions utilizing associative and nonassociative flow rules and observations. Back predictions of the reverse pass utilizing the associative flow rule fail to indicate compression of the joint, and predict dilation, which is not a physical reality. Improved results are obtained with the introduction of the nonassociative flow rule although significant errors still prevail, particularly at normal stress levels of 5 and 50 psi (34.5 and 344.5 KPa). At the 5 psi (34.5 KPa) normal stress level, too much dilation is indicated at the conclusion of the reverse pass. At the 50 psi (344.5 KPa) normal stress level, too much compression is indicated. This is similar to the errors discussed with respect to u_r versus v_r curves, back predicted utilizing the nonassociative flow rule, for the case of quasi-static loading. The error at the end of the reverse pass is higher than that at the end of the forward pass because the errors of the forward and reverse passes are compounded.

Cyclic Shear

Cyclic shear is investigated with test results from the 9-degree surface under normal stress levels of 5, 10 and 20 psi (34.5, 68.9, and

137.8 KPa) with a maximum amplitude of cyclic displacement, u_r^m , of 0.1 in. (2.54 mm.). As described in Chapter 6, this case is modeled by considering four distinct phases of displacement defined by direction [refer to Fig. 6-6(b)]. By inspection of cyclic shear test results, it appears that the behavior during Phases 1 and 3 and 2 and 4 is similar. The direction of travel is different, but the tendency to compress or dilate is identical, and the hardening behavior and mobilized shear stress at the end of the phases are very close. Since the parameters determined for Phases 1 and 3 and 4 and 2 should be the same, only two sets of parameters need be determined to describe the four phases of displacement during a given cycle.

From the test results, the mobilized shear stress at the end of Phases 1 and 3 increases with number of cycles. This cyclic hardening shall be incorporated into the plasticity model by making the ultimate parameter, γ , a function of number of cycles. In this manner, γ includes the effects of the history of the deformation on the behavior from cycle to cycle, while during a given cycle the growth function, α , incorporates the effect of history of deformation.

The manner in which γ is made a function of number of cycles as well as the determination of the other parameters utilized in the model is discussed here. An algorithm for predicting results of cyclic tests is also presented, and a comparison of observed and back predicted results is made.

Determination of Parameters

Within each phase of a given displacement cycle, the same five parameters discussed in the section on quasi-static loading are utilized. In a sense, the isotropic hardening model developed for the case of quasi-static loading is applied independently to each phase of displacement. In the determination of parameters, consideration is given to the history of deformation so that the isotropic hardening model may incorporate the effect of cyclic shear. Table 8-4 presents a summary of the parameters used for the back prediction of cyclic shear tests.

Ultimate Parameter γ . Figure 8-19 presents plots of ultimate shear stress versus normal stress for Phases 1 and 3 at various displacement cycles. The solid lines in the figure are ultimate surfaces fitted through the data points via a linear regression analysis. As before, the square of the slope of these ultimate surfaces yields the value of γ . The manner in which γ increases with number of cycles is apparent. A plot of γ versus number of cycles, N , is depicted in Fig. 8-20. It appears that an expression of hyperbolic form would fit this data. An expression for γ during Phases 1 and 3 is determined as

$$\gamma = N/(1.67 + 0.7/N) \quad (8-1)$$

The solid line in Fig. 8-20 is a plot of this function indicating the closeness of fit to experimental points.

The peak shear stress during Phases 2 and 4 of the cyclic displacement is not consistently apparent from the test results. It is

Table 8-4. Parameters for Back Prediction of Cyclic Test

9° Surface

$$\sigma_n = 20 \text{ psi}$$

$$U_r^m = 0.1 \text{ in.}$$

	Phase 1 Cycle 1	Phase 1 (N≠1) and 3	Phase 2 + 4
γ	$N/(1.67 + 0.71 N)$	$N/(1.67 + .71 N)$	0.228
n	2.5	2.5	2.5
a	0.00455	$N/(200 + 50 N)$	0.0096
b	-0.364	-0.90	-0.206
κ	0.60	0.60	1.20

N is number of cycles.

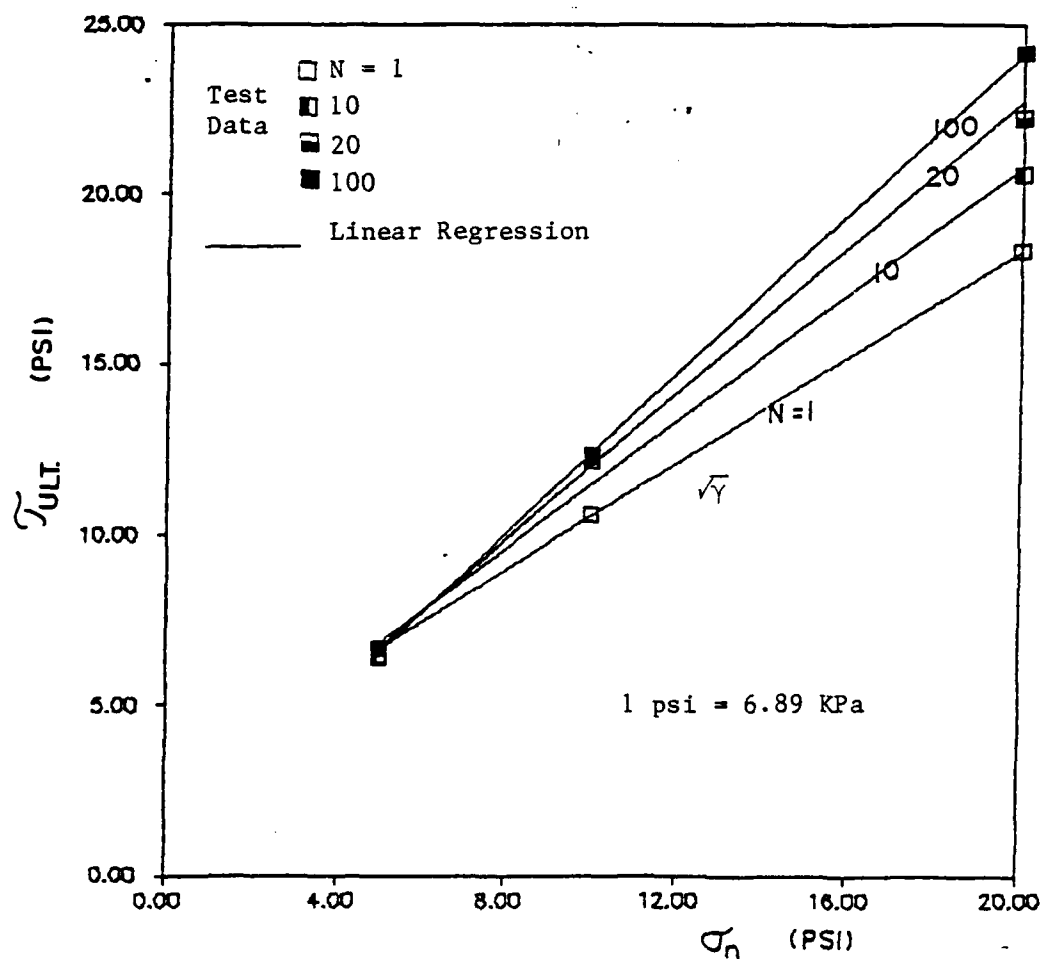


Figure 8-19. Ultimate Envelopes from Cyclic Test Results at Different Cycles of Displacement (N) for Phases 1 and 3; 9° Surface

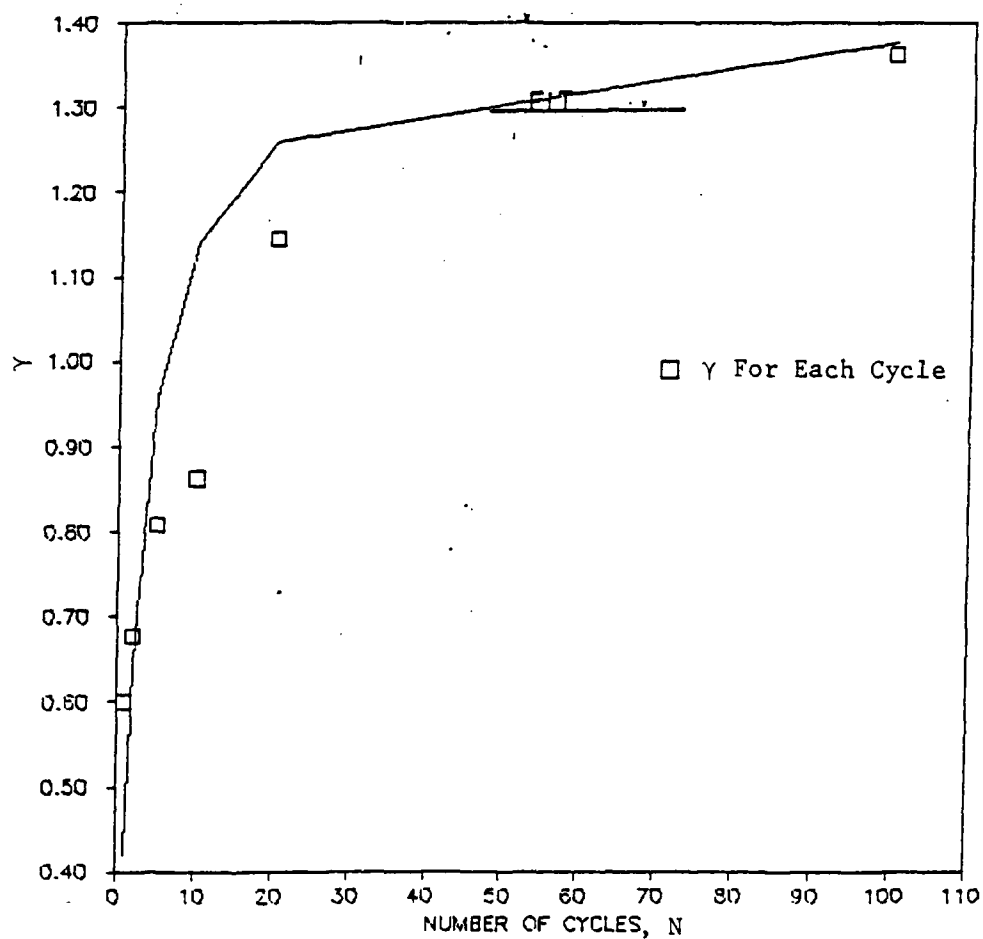


Figure 8-20. γ versus N from Cyclic Test Results;
Phases 1 and 3; 9° Surface

assumed that negligible surface wear occurs during "down asperity level" and that the maximum mobilized shear stress does not vary with number of cycles. This assumption is also made by Plesha (1986). Since the ultimate shear stress is computed directly from the peak shear stress, it also does not vary with number of cycles. The value of γ is determined from Fig. 8-21 which is a plot of ultimate shear stress versus σ_n from data obtained during Phases 2 and 4 of Cycle 1. The ultimate surface passed through these data points yields a value for γ of 0.228.

Phase Change Parameter n. The same value of $n = 2.5$, which was employed for the two previously discussed cases, will be used for the case of cyclic shear.

Growth Function Constants. Some special considerations in determining the proper growth function for different phases during a particular cycle of displacement need to be discussed. During deformation of a particular phase, hardening is described through the use of the growth function. The question arises, "What is the value of the growth function at the beginning of a particular phase?"

For the first phase of Cycle 1, the answer is more obvious than at other points in the deformation history. Since no previous shear displacement has occurred, the initial yield surface should be that corresponding to the state of stress after application of the normal stress but prior to the application of shear to the joint plane.

At the beginning of Phase 2, previous deformation has occurred during Phase 1 which must somehow be accounted for in the model. During

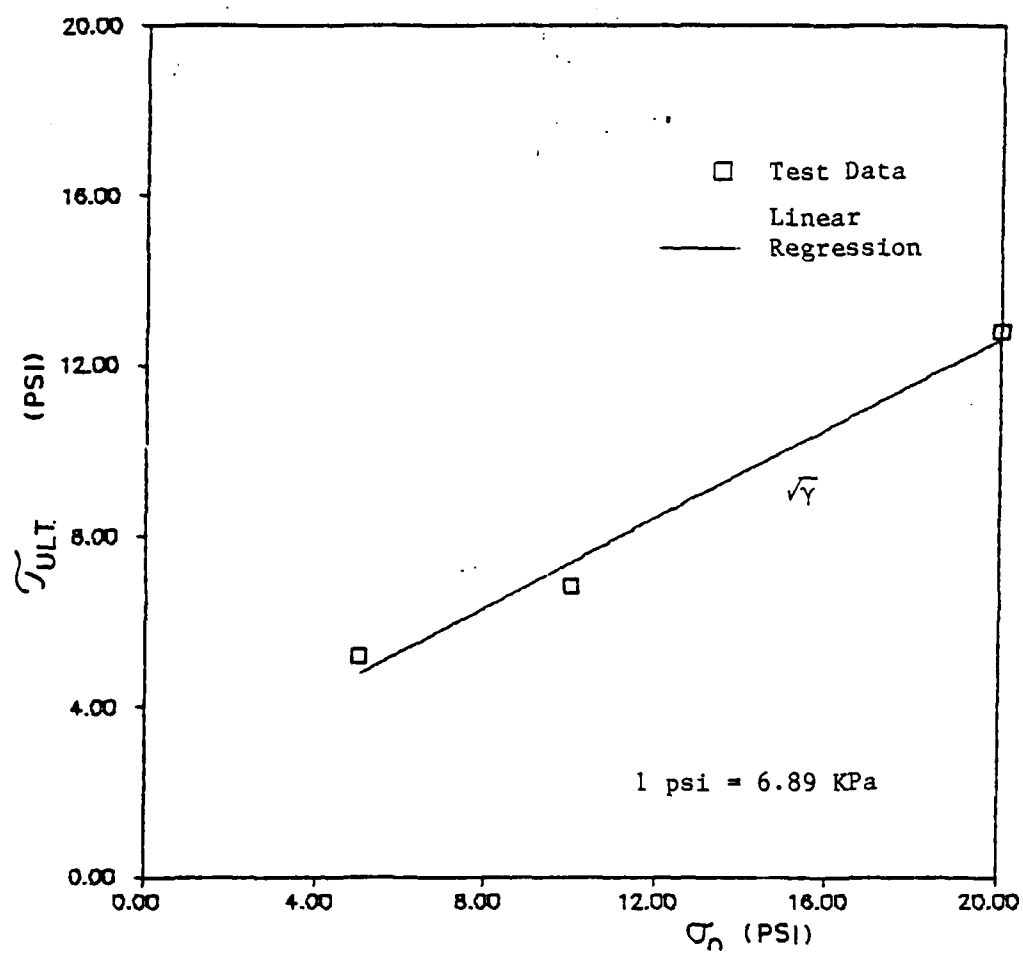


Figure 8-21. Ultimate Envelope; Phase 2 and 4; Cyclic Tests;
9° Surface, N = 1

Phase 2, unloading is assumed to be elastic. Therefore, the state of stress at the onset of plastic deformations is once again normal stress in the absence of shear along the joint plane. Thus the initial yield surface for Phase 2 should reflect this state of stress. Previous deformation of the joint surface, which occurred during Phase 1, is considered since determination of parameters for Phase 2 is based on deformations which occur to the surface after being disturbed during Phase 1. The same arguments presented in this paragraph hold for Phase 4 but with respect to Phase 3.

During Phase 1 (after Cycle 1) and Phase 3, the situation is a bit different. No loading in shear occurs at the beginning of these phases, and initially the state of stress is that which exists at the end of Phases 2 and 4, respectively. Therefore, the value of the growth function at the beginning of Phase 1 (after Cycle 1) and Phase 3 must be such that the initial yield surfaces reflect this state of stress.

A program was developed which computes the growth function parameters for each phase of displacement at various cycles. Required input for each cycle of interest consists of the values of γ , n , the elastic shear stiffness, and data points consisting of shear stress, normal stress, and relative vertical and tangential displacements from each phase of the displacement cycle. The program computes components of plastic deformation, the value of the growth function, α , and the trajectory of plastic strain for each data point of a phase. The program then creates a data file for plotting α versus ξ and performs a linear regression analysis of logarithmic transformed data points to determine

growth function constants for each phase of displacement. The program is entitled "GROCYC.FOR." Table 8-5 shows growth function constants a and b determined by the program from cyclic shear test data for the 9-degree surface with a normal stress of 20 psi (137.8 KPa).

Growth function parameters are determined based on the values of the ultimate parameters used for a given cycle of displacement and may be functions of number of cycles themselves. Growth function parameters from Phases 1 and 3 are a function of number of cycles while those from Phases 2 and 4 are considered constant. For Phases 2 and 4, average values of the growth function parameters determined from different cycles are employed. Expressions and values for growth function parameters employed in the back predictions may be seen in Table 8-4. Only data from the test with a normal stress of 20 psi was used to determine growth function constants, and these were used for back prediction of all tests considered herein.

Figures 8-22 to 8-28 are plots of α versus ξ for various phases and cycles of displacement. Experimental data points and plots of the growth function using both constants determined only from data pertaining to the cycle of interest, and those determined with expressions given in Table 8-4 are presented. From this information, the proximity of the employed growth function to observation may be ascertained.

Nonassociative Parameter κ . Computations for the values of the nonassociative parameter κ for different phases and cycles of displacement are presented in Appendix III. Since the plots of u_r versus v_r do not vary from cycle to cycle, the computations do not reflect significant

Table 8-5. Growth Function Constants Determined for
Cycles of Displacement; 9° Surface;
 $\sigma_n = 20$ psi

Cycle	Phase 1 & 3		Phase 2 & 4	
	a	b	a	b
1	0.0000	-4.22	0.0096	-0.206
2	0.0096	-0.851		
5	0.0116	-1.011		
10	0.0174	-0.914		
20	0.0157	-1.028		
100	0.0211	-0.892		

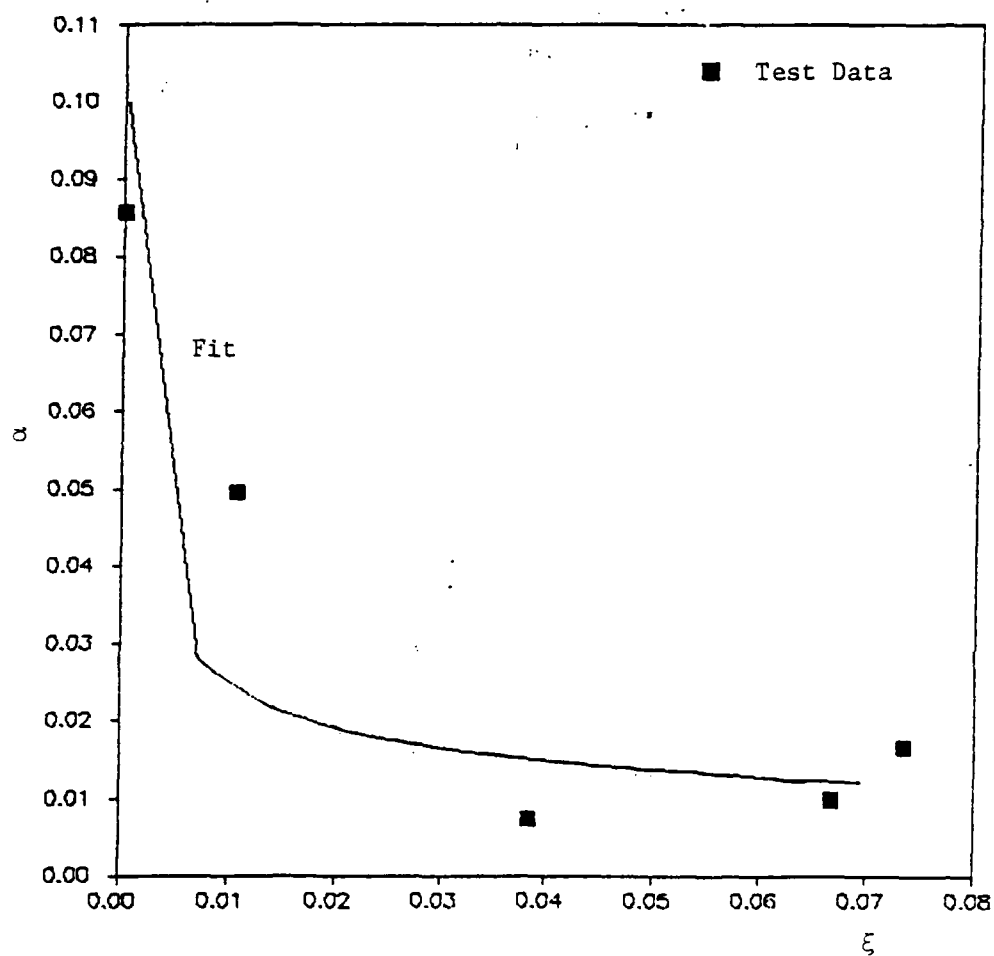


Figure 8-22. α versus ξ ; Phase 1; Cycle 1.
Cyclic Test; 9° Surface;
 $\sigma_n = 20$ psi

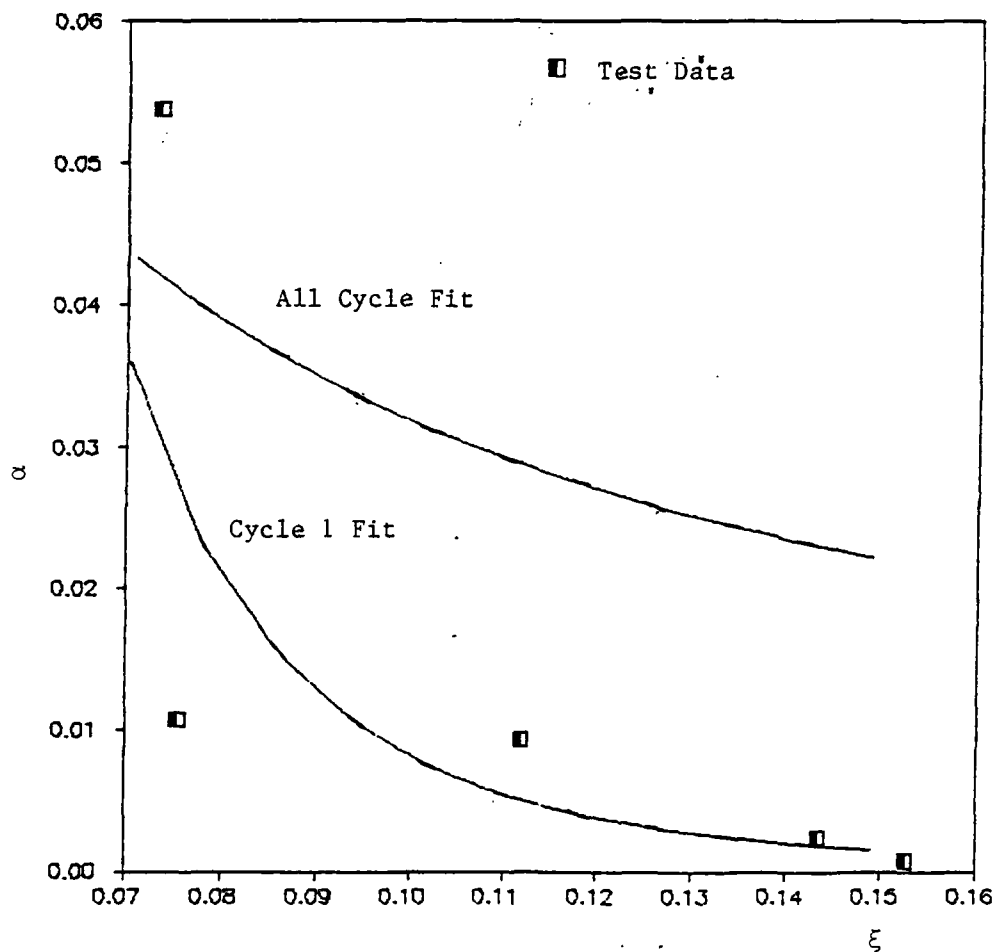


Figure 8-23. α versus ξ ; Phase 3; Cycle 1.
Cyclic Test; 9° Surface;
 $\sigma_n = 20$ psi

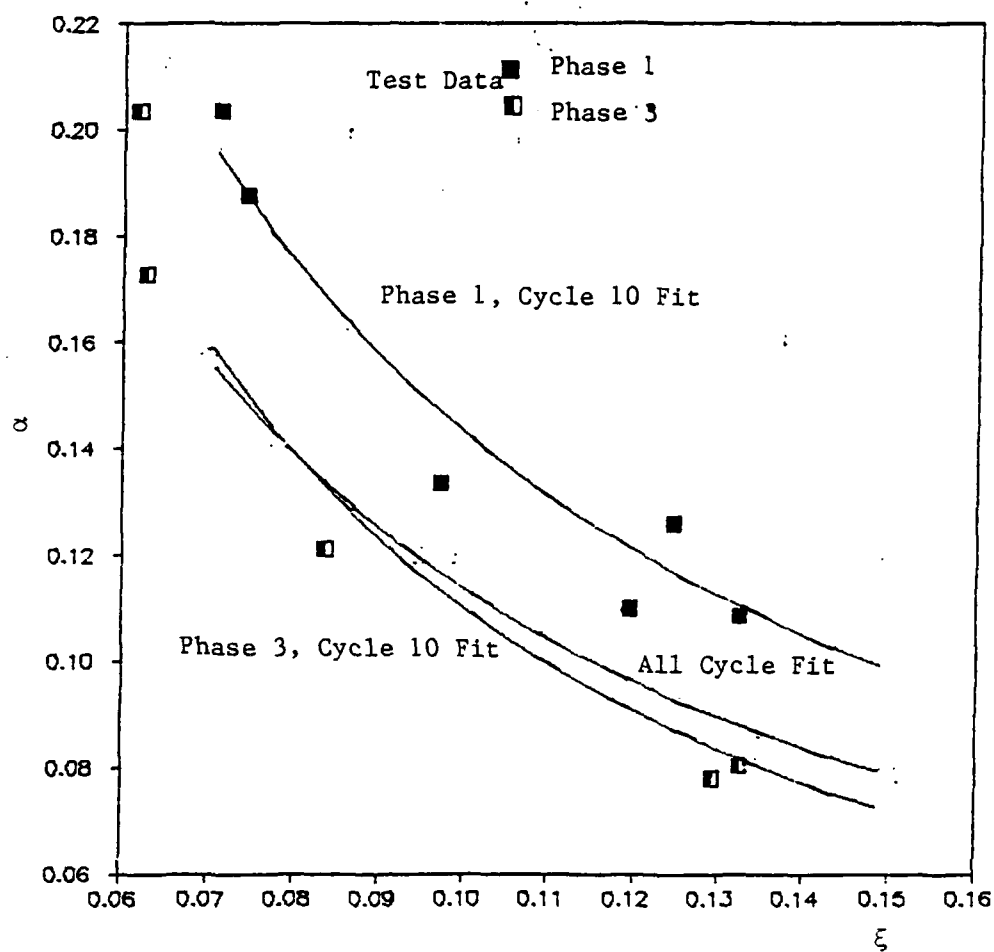


Figure 8-24. α versus ξ ; Phases 1 and 3; Cycle 10.
Cyclic Test; 9° Surface; $\sigma_n = 20$ psi

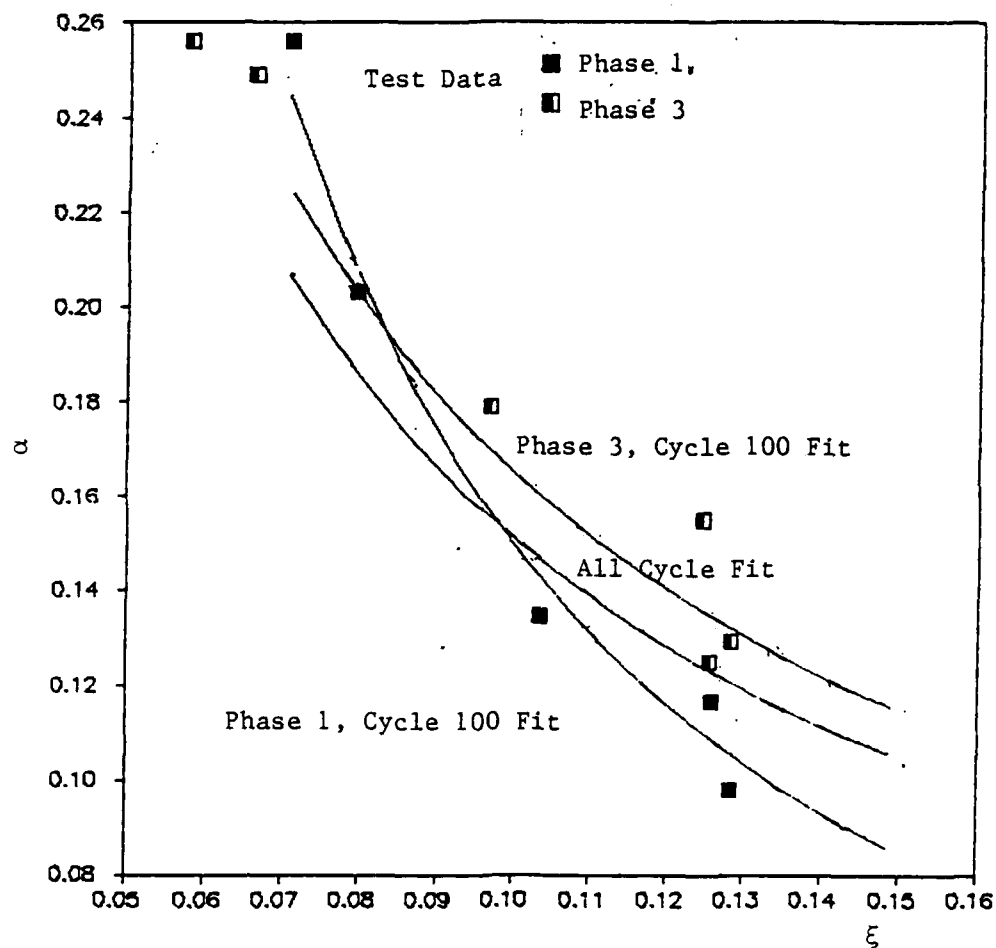


Figure 8-25. α versus ξ ; Phases 1 and 3; Cycle 100.
Cyclic Test; 9° Surface; $\sigma_n = 20$ psi

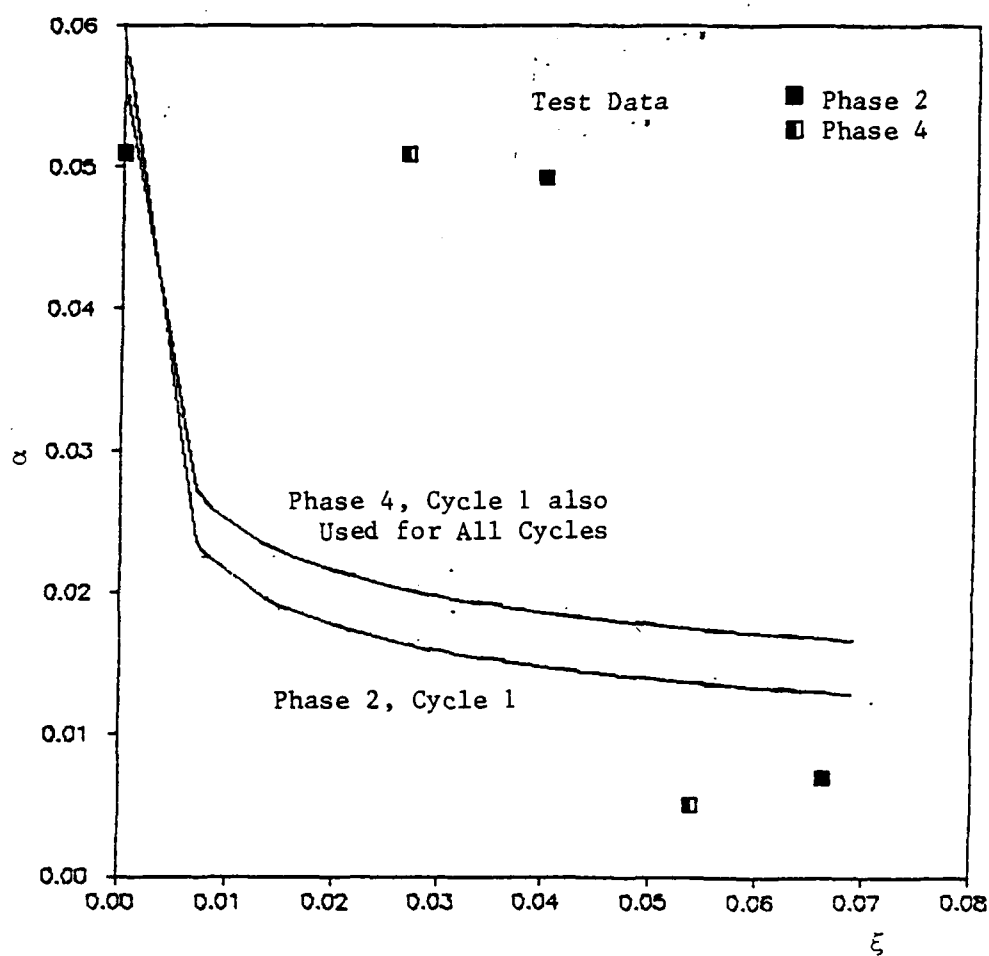


Figure 8-26. α versus ξ ; Phases 2 and 4; Cycle 1.
Cyclic Test; 9° Surface; $\sigma_n = 20$ psi

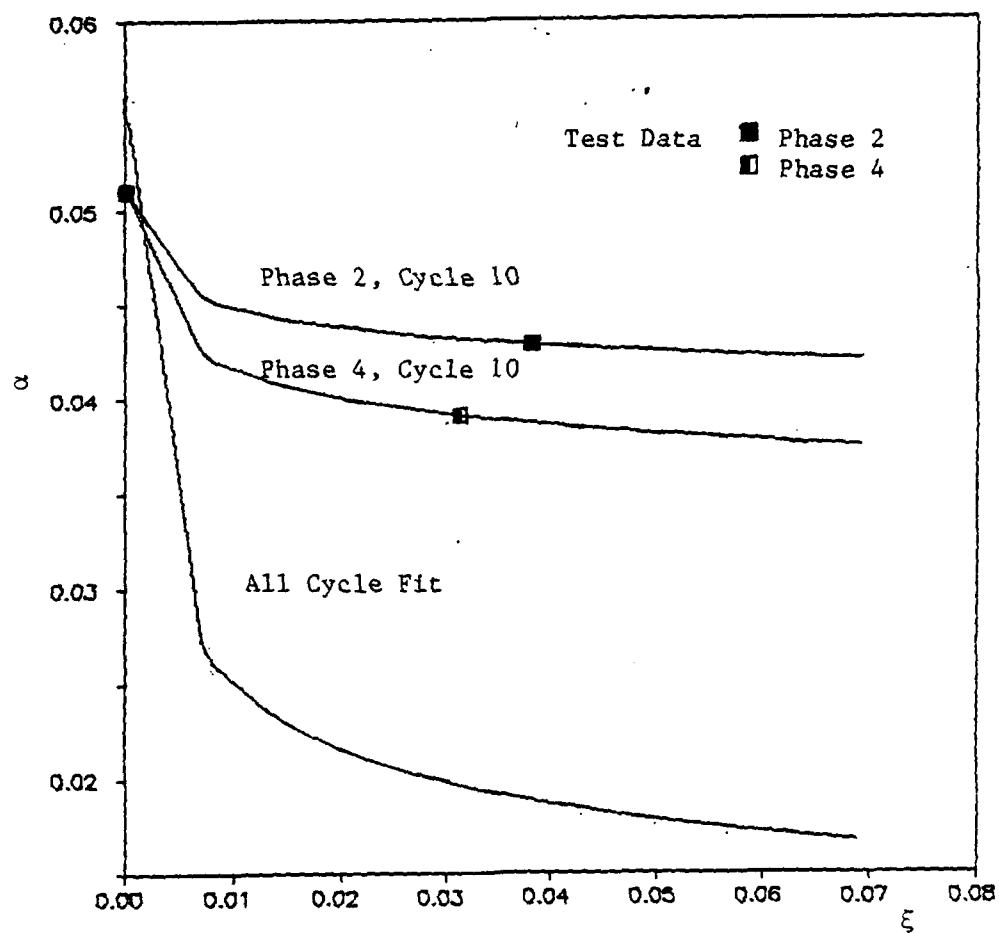


Figure 8-27. α versus ξ ; Phases 2 and 4; Cycle 10.
Cyclic Test; 9° Surface; $\sigma_n = 20$ psi

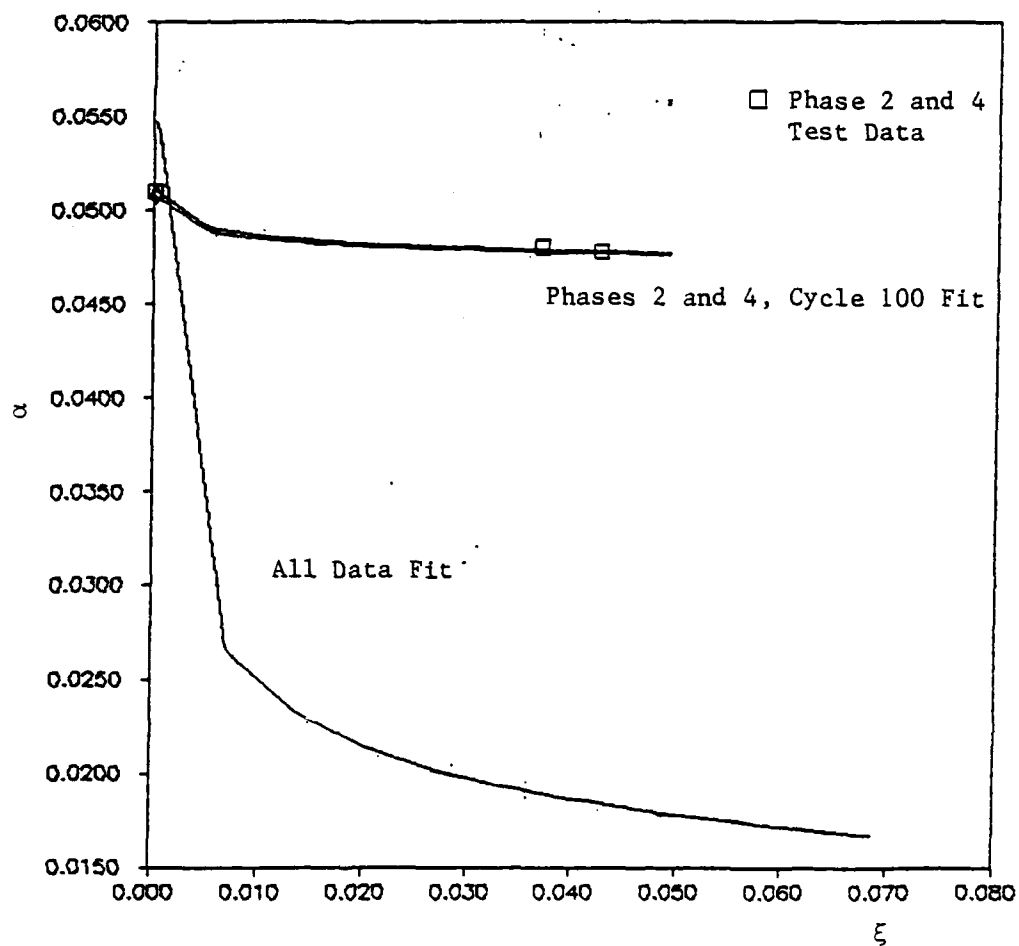


Figure 8-28. α versus ξ ; Phases 2 and 4; Cycle 100
Cyclic Test; 9° Surface; $\sigma_n = 20$ psi

variation of κ with N . Some variation may be predicted between cycles for Phases 1 and 3 due to variation in γ , but this does not appear to be significant. There is, however, significant difference in the values of κ between Phases 1 and 3 and Phases 2 and 4. Therefore, only two values of κ are required for all cycles of displacement, one for Phases 1 and 3 and one for Phases 2 and 4.

Back Predictions of Cyclic Shear Tests

Using the parameters discussed in the preceding section, back predictions of cyclic shear tests with the 9-degree surface are performed. The computations are carried out for 100 cycles of displacement, and compared with test data. Both associative and nonassociative flow rules are employed.

Algorithm. This section describes the algorithm used to determine increments of shear stress and relative vertical displacement based on applied increments of relative tangential displacement under the condition of constant normal stress. The algorithm describes the determination of the initial yield surface for a given phase; i.e., the initial value for the growth function, the formulation of the elastic-plastic constitutive matrix, and determination of the unknown quantities.

At the beginning of each phase of a cycle, parameters are determined from appropriate expressions. Using these parameters, the following algorithm is employed during each phase of the deformation history:

1. Calculate the value of the growth function at the beginning of the phase.

- a. Initially for Phase 1 of Cycle 1, the growth function is determined so that the initial yield function is equal to zero. The shear stress is zero and the normal stress is the applied normal stress.
- b. For Phases 2 and 4, after elastic unloading and just prior to load reversal, the initial value for the growth function is computed as in a.
- c. At the beginning of Phase 1 after Cycle 1, and Phase 3, the value of the growth function is determined based on the history of deformation at the end of Phases 4 and 2, respectively. However, if this value is greater than that required to satisfy the condition that the current yield surface equals zero, the growth function is modified so that this condition is satisfied given the current state of stress.
- d. The growth function at any point during the deformation of any phase of any cycle other than the initial condition is computed based on the history of deformation at the end of the previous increment.

2. Set the value of α_I equal to the value of α just after the application of normal stress, but prior to the initiation of shear. At this point, ξ is equal to ξ_v and r_v is unity.
3. Using these values of α , α_I , r_v and the parameters for the particular phase and cycle, compute α_Q , the derivatives of the yield and potential functions, and form the K^{ep} matrix.
4. Apply an increment of relative tangential displacement, $Du = 0.0001$ in.
5. Solve for increment of shear stress, $d\tau$, and relative vertical displacement, dv .
6. Compute elastic and plastic components of displacement using the associative or nonassociative flow rule.
7. Obtain updated values for ξ , ξ_v , r_v and α . If this is the first increment of shear, check to see that $F = 0$, and if F is negative, adjust the elastic shear stiffness, as described in the algorithm for quasi-static loading such that $F > 0$.
8. If the phase is not over, go to (3). If the phase is over, go to (1). If this is the end of Phase 4, Cycle 100, stop.

This algorithm was coded into a program entitled CYCDIS, which was then used for back predicting results from cyclic shear tests.

Results. Figures 8-29 to 8-33 present results of back predictions of a cyclic shear test performed on the 9-degree surface with $\sigma_n = 20$ psi (138 KPa). Back predictions are for the case of a nonassociative flow rule only. Results with $\sigma_n = 5$ and 10 psi (34.5 and 69 kPa) may be found in Appendix II.

Four figures of shear stress versus u_r are presented (Figures 8-29 to 8-32). The first of these depicts back predictions of cycles ranging from 1 to 100, and the remaining compare back predictions to test data for Cycles 1, 10 and 100. The transition between phases is readily apparent in these back predictions. Comparison of back prediction to observation is considered satisfactory although there is some error present for Cycle 1. This is due to the function which describes the variation of γ with number of cycles [Eq. (8-1)]. Inspection of Fig. 8-20, which compares this function to values of γ found for each cycle, indicates that the error between the data point and the "fitted" curve is greater for Cycle 1 than for Cycle 100. It is conservative to underpredict the shear strength of the first cycle; therefore, the relationship which describes the increase in γ with number of cycles is considered satisfactory.

Results of v_r versus u_r , Fig. 8-33, present back predictions for cycles ranging from 1 to 100, and compare these to test data. Since observations do not vary significantly from cycle to cycle, only observations from Cycle 1 are presented. Although back predictions of Cycle 1 are acceptable, considerable errors begin to predominate beyond the tenth cycle of displacement. It seems that at higher cycles the vertical

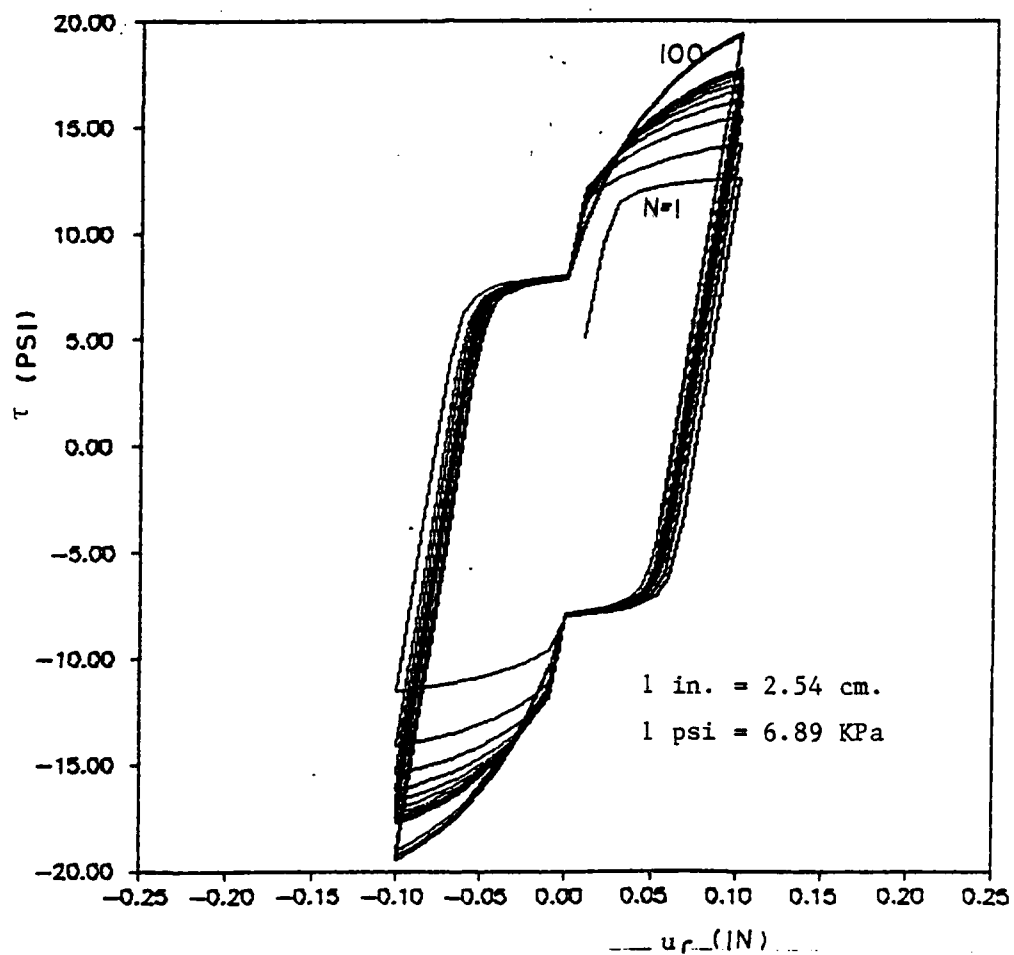


Figure 8-29. Back Predictions; Cyclic Test; τ versus i_r ;
 9° Surface; $\sigma_n = 20$ psi

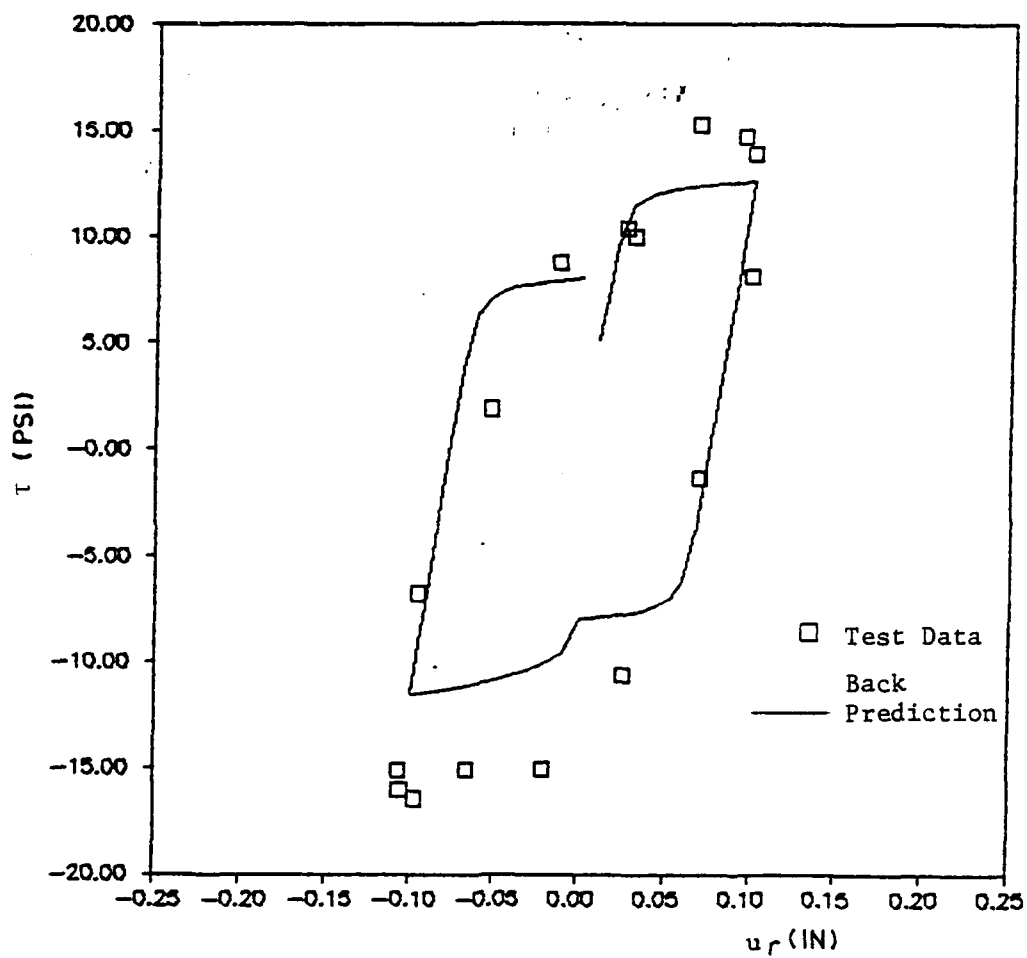


Figure 8-30. Test Data and Back Predictions; τ versus u_r ;
Cyclic Test; 9° Surface; $\sigma_n = 20$ psi;
Cycle 1

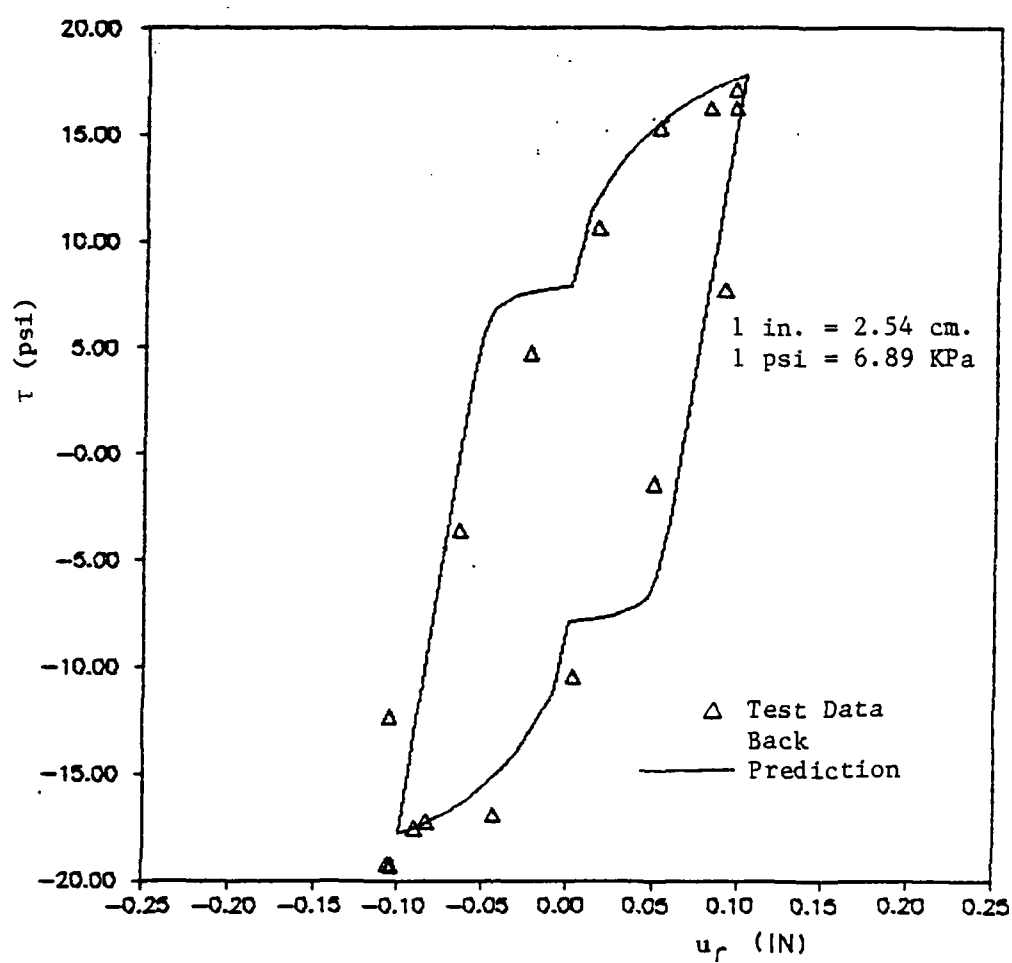


Figure 8-31. Test Data and Back Prediction; τ versus u_r ;
Cyclic Test; 9° Surface; $\sigma_n = 20$ psi;
Cycle 10

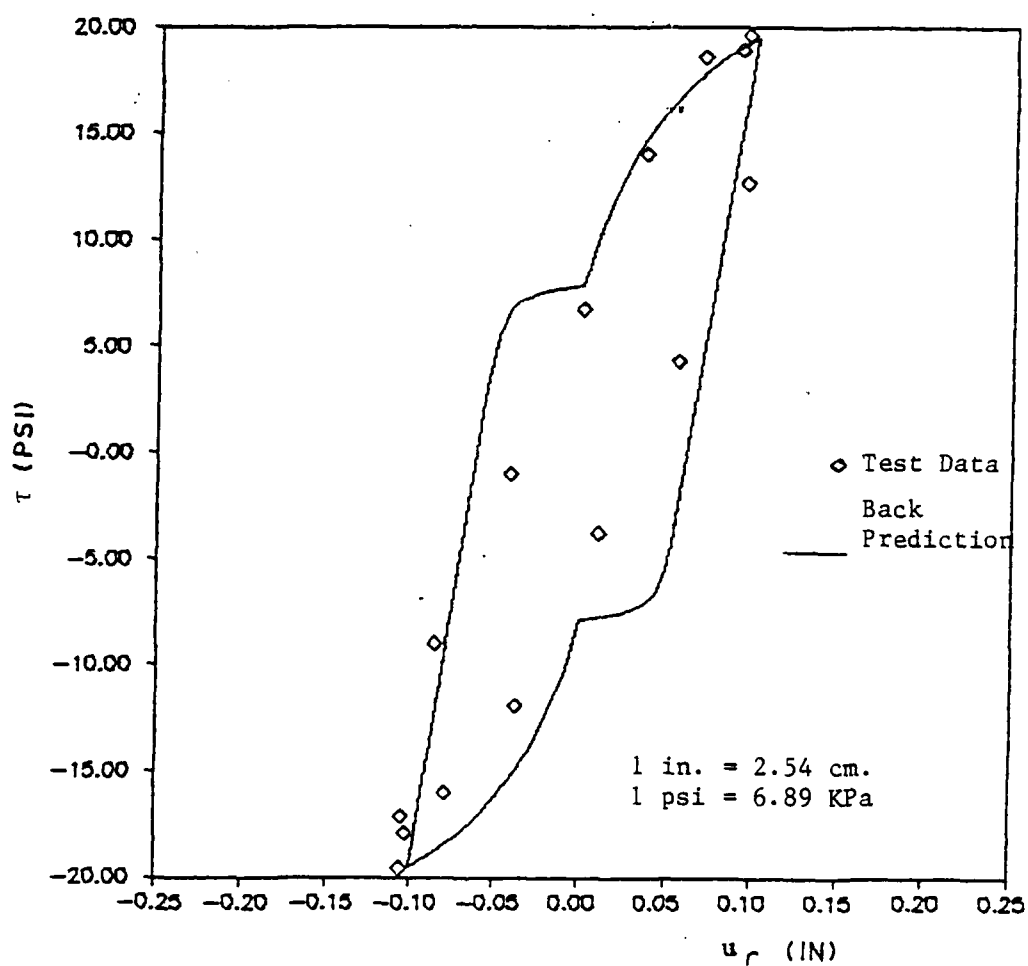


Figure 8-32. Test Data and Back Prediction; τ versus u_r ;
Cyclic Test; 9° Surface; $\sigma_n = 20$ psi;
Cycle 100

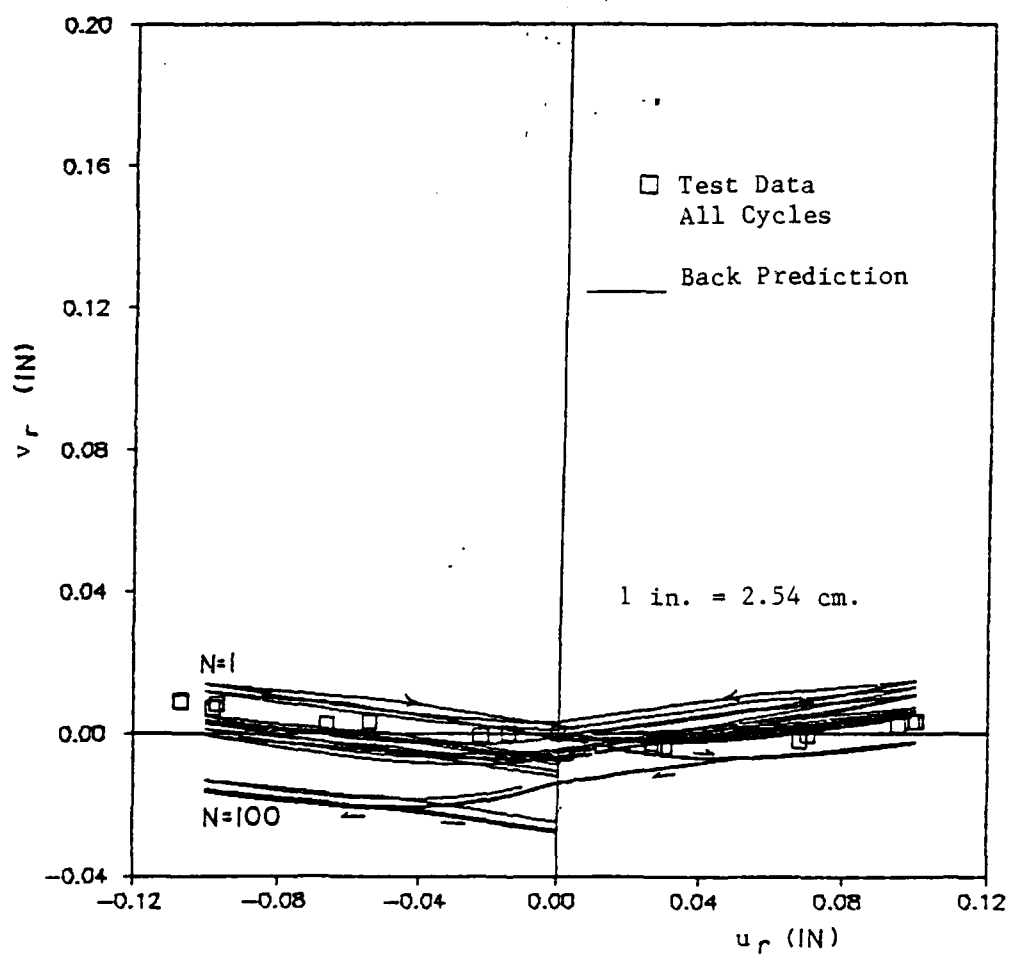


Figure 8-33. Test Data and Back Predictions; v_r versus u_r ;
Cyclic Test; 9° Surface; $\sigma_n = 20$ psi

displacements during Phases 1 and 3 are not predicted well so that at the conclusion of the cycle a significant net error persists. Since observations indicate no perceptible increase or decrease in joint thickness at the end of a cycle, these errors were corrected at the end of a cycle such that errors would not accumulate during back prediction.

CHAPTER 9

SUMMARY, CONCLUSIONS, AND RECOMMENDATIONS

Summary

A constitutive model to describe the behavior of individual rock joints during shear has been proposed. The model is based on the theory of incremental plasticity and is a specialization of the Generalized Plasticity Model developed for geologic solid materials. In its present form, the joint model can consider initial state of stress, states of shear and normal stress, plastic hardening, volume changes at joints, monotonic shear loading, unloading and load reversal, and cyclic shear loading.

A comprehensive program of shear testing was performed on idealized joint specimens. In order to perform these tests, certain modifications to the CYMDOF device were necessary. These modifications allowed the rock joint to compress, dilate, or rotate in the plane of shear. Quasi-static and cyclic shear tests were performed under variable conditions of joint geometry, initial state of stress, and cyclic displacement.

Inductance coils were employed for the measurement of vertical displacement at the center of the joint plane. To the author's knowledge, this is the first time these devices have been employed for this purpose. Special calibration and verification of the performance of

these instruments was necessary. The effects of coil misalignment during shear and the presence of the metal sample holders were considered in calibrating the instruments for this application.

Parameters for the plasticity model were determined from the test data and back predictions of the test data were performed. In order to determine parameters for cyclic tests, the displacement cycle was considered to consist of different phases of displacement. It was demonstrated that during back predictions this amounts to collapse or expansion and rotation of the yield surface at appropriate instants of time during the deformation process. Cyclic shear test results show an increase in mobilized peak shear stress with number of cycles. The increase in mobilized shear strength with number of cycles was described by making the ultimate parameter, γ , a function of number of cycles. Programs were written for determination of parameters and back predictions.

Conclusions

In conclusion, the plasticity model described in Chapter 7 is capable of predicting the behavior of rock joints during monotonic or cyclic shear loading. Displacement induced anisotropy and cyclic hardening behavior are incorporated in the model. Back predictions presented in Chapter 8 indicate that shear response of the joint is predicted well for both monotonic and cyclic shear. To reasonably predict the vertical behavior, a nonassociative flow rule must be employed or dilation will be overpredicted. Predictions of vertical response

indicate that the model is much more sensitive to changes in normal stress than test results indicate. Modifications are necessary to improve these predictions.

The inductance coils utilized for measurement of dilation/compression provide a very useful technique for taking measurements within the interface. The instruments must be calibrated for misalignment and the presence of metal sample holders, as described in Chapter 4.

Recommendations

The current research has considered the case of cyclic shear on dry, unfilled, structured joint surfaces. Although this is a significant contribution, many improvements and modifications in the model are required before the model can be applied to a wide range of problems. It is anticipated that these improvements and modifications will build upon the current model, utilizing the hierarchical approach, as outlined by Desai et al. (1986). To accomplish this, the following improvements are recommended:

1. The model needs to be modified to describe the effect of normal stress better. In the present model, the growth function was determined mainly on the basis of deformation which occurs during shear. A split form of the growth function, similar to that proposed by Faruque (1983), in which a portion is dependent on normal stress may predict the response more accurately at all levels of normal stress.

2. The model should be extended to the case of strain softening. It may be possible to describe strain softening by using the model proposed by Frantziskonis and Desai (1986) in which softening is described by considering some part of the material (joint) to be damaged. The behavior of the undamaged zone would still be described with the isotropic hardening model described in this report.

3. Tests should be performed on natural rock joints using the CYMDOF device to determine parameters for the plasticity model. The parameters should be compared to those obtained from testing of idealized joints. Back predictions should be performed to show that the model is still easily applied to the case of naturally occurring rock joints.

4. The effects of filler materials in rock joints should be considered. Naturally occurring rock joints may be filled with sand and clay which leach into the joint space.

5. The effect of water in the joint plane should be considered. Natural joints may be saturated with water. If free drainage is not allowed, pressure variations can occur during shear due to the tendency to compress or dilate. Changes in water pressure then contribute to changes in effective stress at the joint plane.

6. The model should be implemented in a finite element program.

7. Boundary value problems in which the presence of joints is a factor should be studied. Measurements could be made in the field or laboratory. Results from analysis using methods which incorporate the proposed joint model could be compared with measured results for verification purposes.

APPENDIX I

DERIVATION OF K^{ep} MATRIX

Define the following:

$$\{\sigma\} = \begin{Bmatrix} \sigma_n \\ \tau \end{Bmatrix} \quad \{\epsilon\}^e - \text{elastic strain}$$

$$\{\epsilon\} = \begin{Bmatrix} v_r \\ u_r \end{Bmatrix} \cdot \frac{1}{t} \quad \{\epsilon\}^p - \text{plastic strain}$$

$$[K] = \begin{bmatrix} K_n & 0 \\ 0 & K_s \end{bmatrix} \quad t - \text{joint thickness taken as unity}$$

The stress-elastic strain relationship may be written as

$$\{d\sigma\} = [K] \{d\epsilon\}^e \quad (I-1)$$

Decompose the total strain into elastic and plastic parts

$$\{d\epsilon\} = \{d\epsilon\}^e + \{d\epsilon\}^p \quad (I-2)$$

Rewrite Eq. (I-1) as

$$\{d\sigma\} = [K] (\{d\epsilon\} - \{d\epsilon\}^p) \quad (I-3)$$

Associative Case

Assuming associated plasticity, the flow rule may be written as

$$\{d\epsilon\}^p = \lambda \left\{ \frac{\partial F}{\partial \sigma} \right\} \quad (I-4)$$

Write the consistency condition, assuming α is a function of ξ ,

$$dF = \left\{ \frac{\partial F}{\partial \sigma} \right\}^T \{d\sigma\} + \frac{\partial F}{\partial \xi} d\xi = 0 \quad (I-5)$$

With

$$d\xi = (\{d\epsilon\}^P)^T \{d\epsilon\}^P)^{1/2}$$

and Eq. (I-4)

$$d\xi = \lambda \gamma_F \quad (I-6)$$

where

$$\gamma_F = \left(\left\{ \frac{\partial F}{\partial \sigma} \right\}^T \left\{ \frac{\partial F}{\partial \sigma} \right\} \right)^{1/2}$$

Utilizing Eqs. (I-3), (I-4), (I-5) and (I-6), obtain an expression for λ as follows:

$$\{d\sigma\} = [K] (\{d\epsilon\} - \lambda \left\{ \frac{\partial F}{\partial \sigma} \right\})$$

$$dF = \left\{ \frac{\partial F}{\partial \sigma} \right\}^T [K] (\{d\epsilon\} - \lambda \left\{ \frac{\partial F}{\partial \sigma} \right\}) + \frac{\partial F}{\partial \xi} \lambda \gamma_F = 0$$

$$\lambda = \frac{\left\{ \frac{\partial F}{\partial \sigma} \right\}^T [K] \{d\epsilon\}}{\left\{ \frac{\partial F}{\partial \sigma} \right\}^T [K] \left\{ \frac{\partial F}{\partial \sigma} \right\} - \frac{\partial F}{\partial \xi} \gamma_F} \quad (I-7)$$

By substituting Eqs. (I-4) and (I-7) into Eq. (I-3), the following expression is obtained:

$$\{d\sigma\} = ([K] - \frac{[K] \left\{\frac{\partial F}{\partial \sigma}\right\} \left\{\frac{\partial F}{\partial \sigma}\right\}^T [K]}{\left\{\frac{\partial F}{\partial \sigma}\right\}^T [K] \left\{\frac{\partial F}{\partial \sigma}\right\} - \frac{\partial F}{\partial \xi} \gamma_F}) \{d\varepsilon\} \quad (I-8)$$

Equation (I-8) may be rewritten as

$$\{d\sigma\} = [K]^{ep} \{d\varepsilon\} \quad (I-9)$$

where

$$[K]^{ep} = [K] - \frac{[K] \left\{\frac{\partial F}{\partial \sigma}\right\} \left\{\frac{\partial F}{\partial \sigma}\right\}^T [K]}{\left\{\frac{\partial F}{\partial \sigma}\right\}^T [K] \left\{\frac{\partial F}{\partial \sigma}\right\} - \frac{\partial F}{\partial \xi} \gamma_F} \quad (I-10)$$

Nonassociative Case

Assuming nonassociated plasticity, the flow rule may be written

as

$$\{d\varepsilon\}^P = \lambda \left\{\frac{\partial Q}{\partial \sigma}\right\} \quad (I-11)$$

and Eq. (I-5) becomes

$$dF = \left\{\frac{\partial F}{\partial \sigma}\right\}^T [K] (\{d\varepsilon\} - \lambda \left\{\frac{\partial Q}{\partial \sigma}\right\}) + \frac{\partial F}{\partial \xi} d\xi = 0 \quad (I-12)$$

Defining

$$\gamma_F = \left(\left\{\frac{\partial Q}{\partial \sigma}\right\}^T \left\{\frac{\partial Q}{\partial \sigma}\right\}\right)$$

and utilizing Eqs. (I-3), (I-11), (I-12) and (I-6), an expression for λ is obtained as

$$\lambda = \frac{\left\{\frac{\partial F}{\partial \sigma}\right\}^T [K] \{d\varepsilon\}}{\left\{\frac{\partial F}{\partial \sigma}\right\}^T [K] \left\{\frac{\partial Q}{\partial \sigma}\right\} - \frac{\partial F}{\partial \xi} \gamma_F} \quad (I-13)$$

As before, substituting Eqs. (I-11) and (I-13) into Eq. (I-3) yields

$$[K]^{ep} = [K] - \frac{[K] \left\{\frac{\partial Q}{\partial \sigma}\right\} \left\{\frac{\partial F}{\partial \sigma}\right\}^T [K]}{\left\{\frac{\partial F}{\partial \sigma}\right\}^T [K] \left\{\frac{\partial Q}{\partial \sigma}\right\} - \frac{\partial F}{\partial \xi} \gamma_F} \quad (I-14)$$

APPENDIX II

BACK PREDICTION FIGURES

Appendix II contains figures for determination of parameters and results including test data and back predictions which were not discussed in the main body of the text. These include results from quasi-static testing with flat, 5-degree and 7-degree surfaces, as well as cyclic testing with the 9-degree surface at normal stresses of 5 and 10 psi (34.5 and 69 KPa).

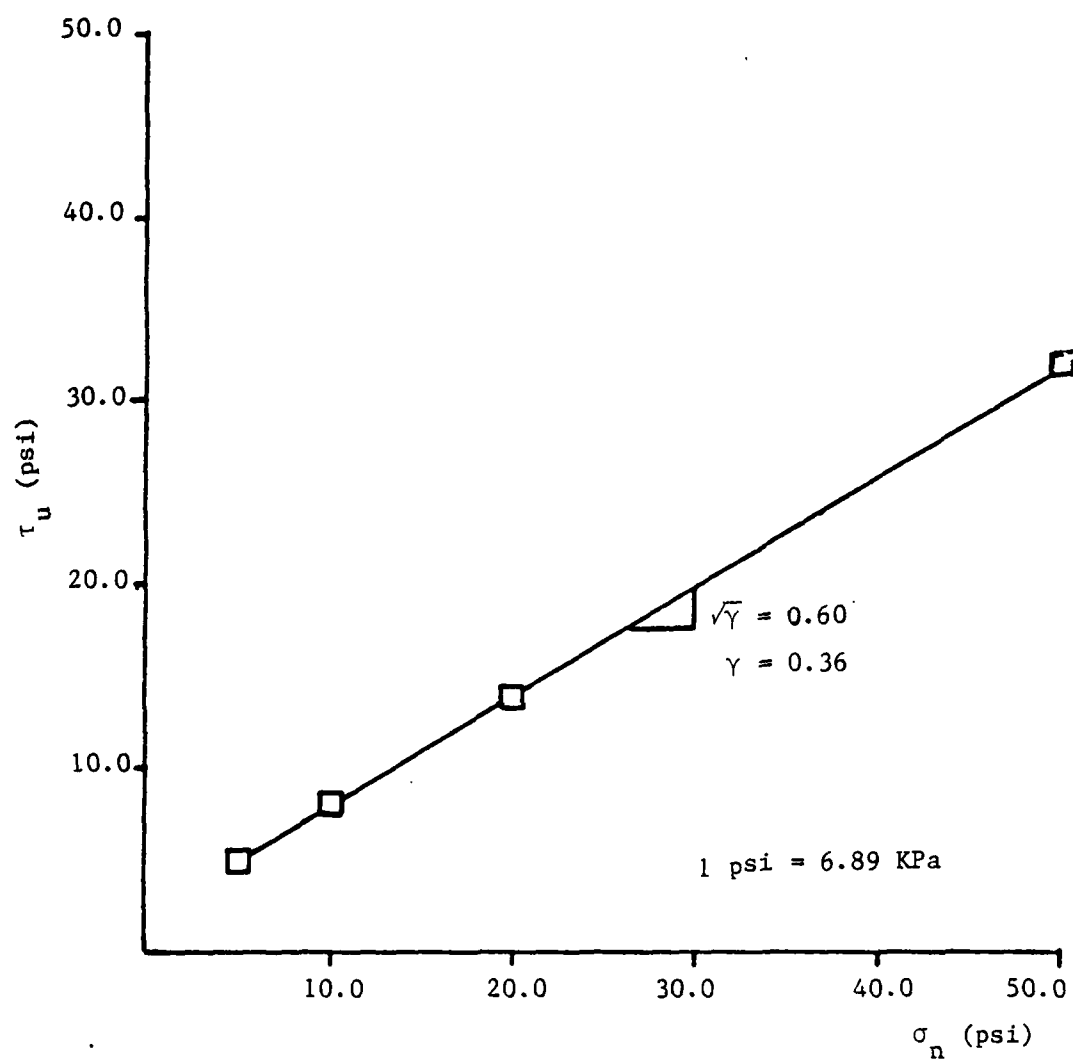


Figure II-1. Ultimate Envelope; Quasi-Static Test Series, Forward Pass; Flat Surface

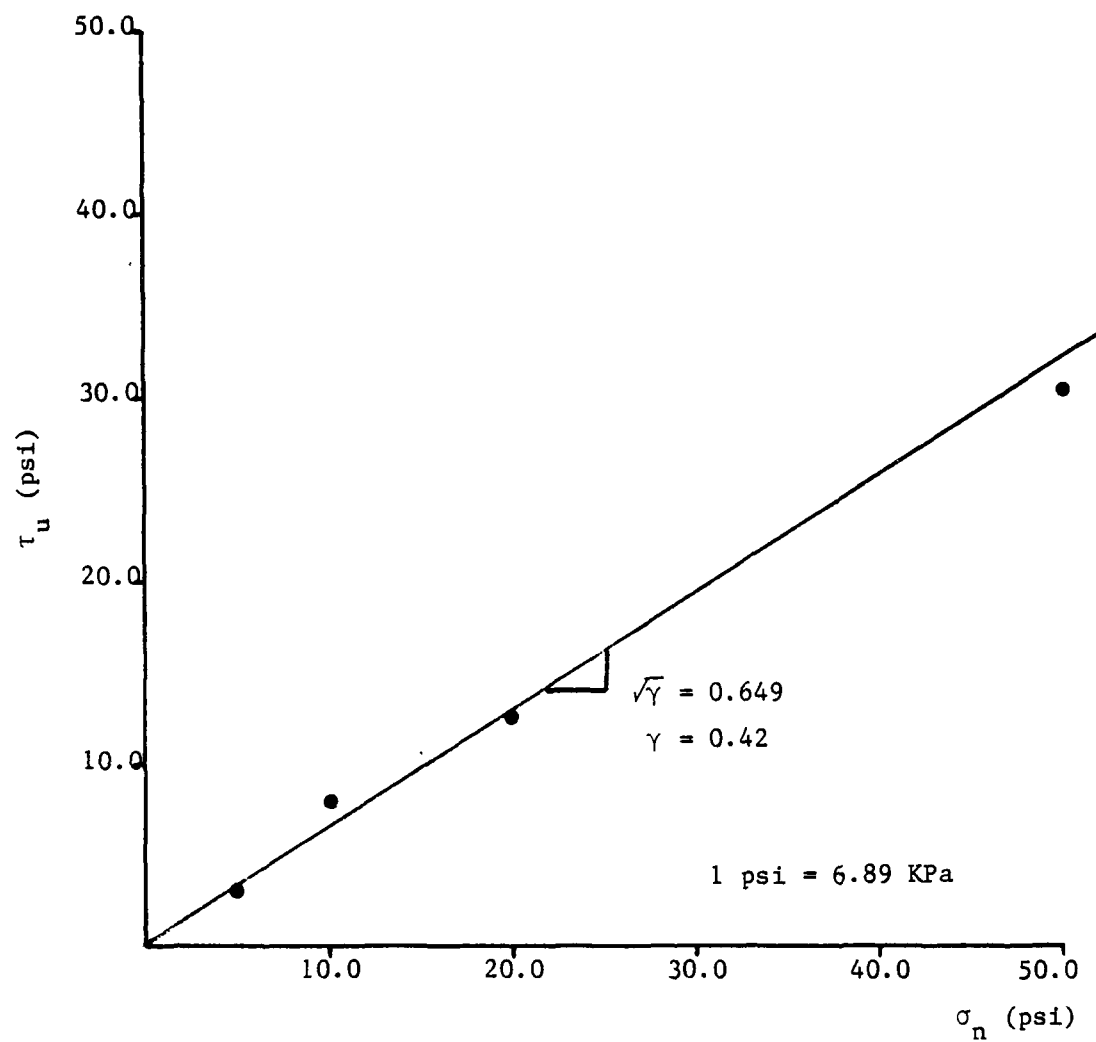


Figure II-2. Ultimate Envelope; Quasi-Static Test Series;
Forward Pass; 5° Surface

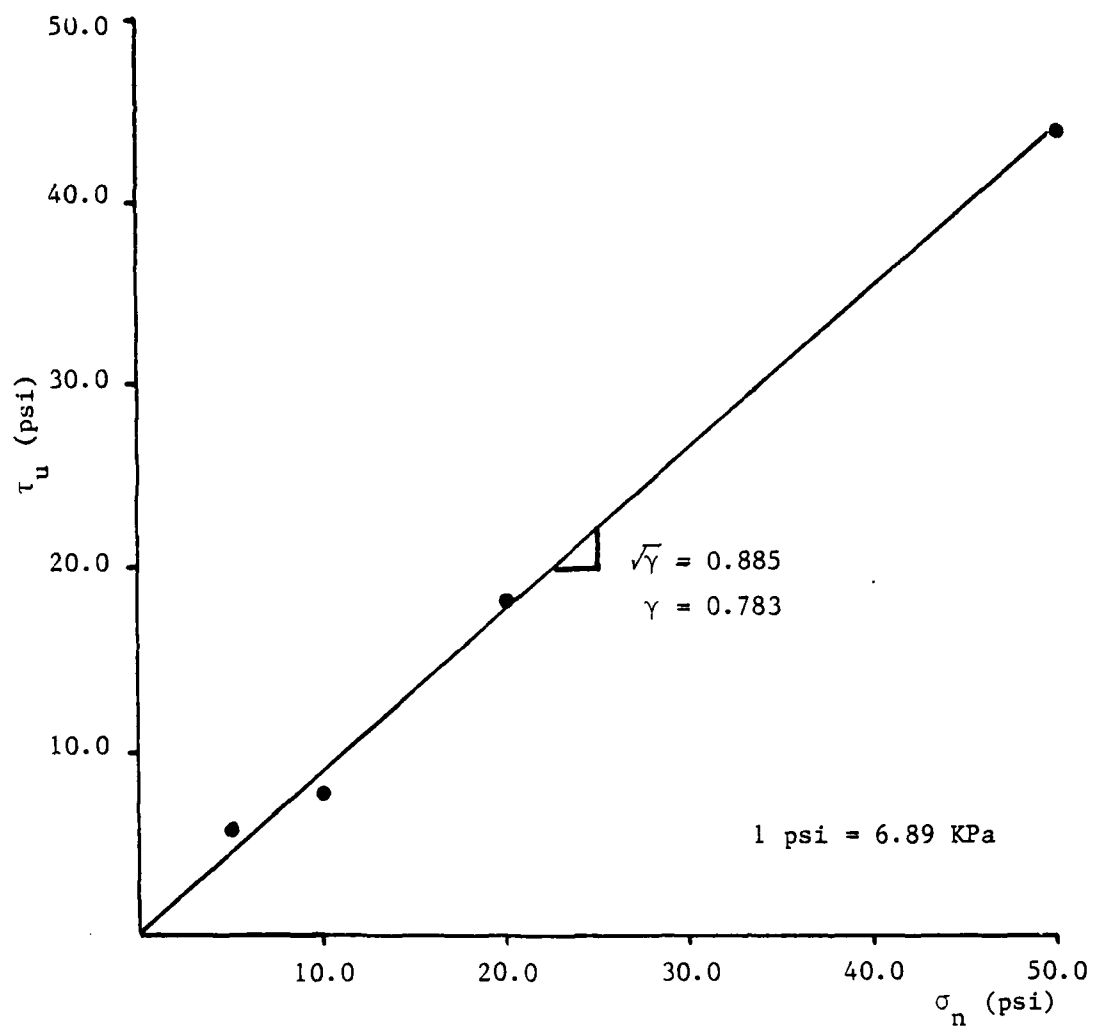


Figure II-3. Ultimate Envelope; Quasi-Static Test Series;
Forward Pass; 7° Surface

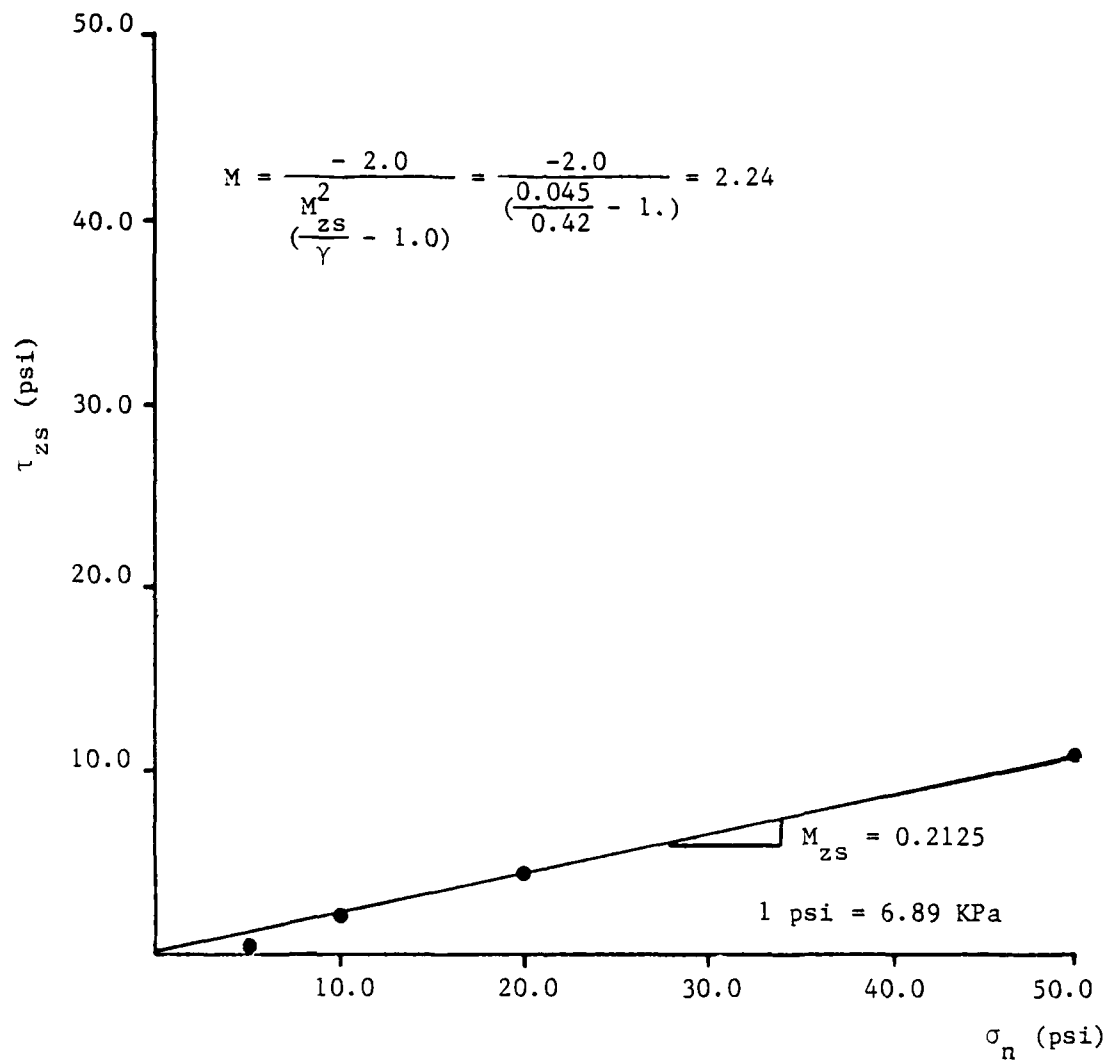


Figure II-4. Phase Change Envelope; 5° Surface

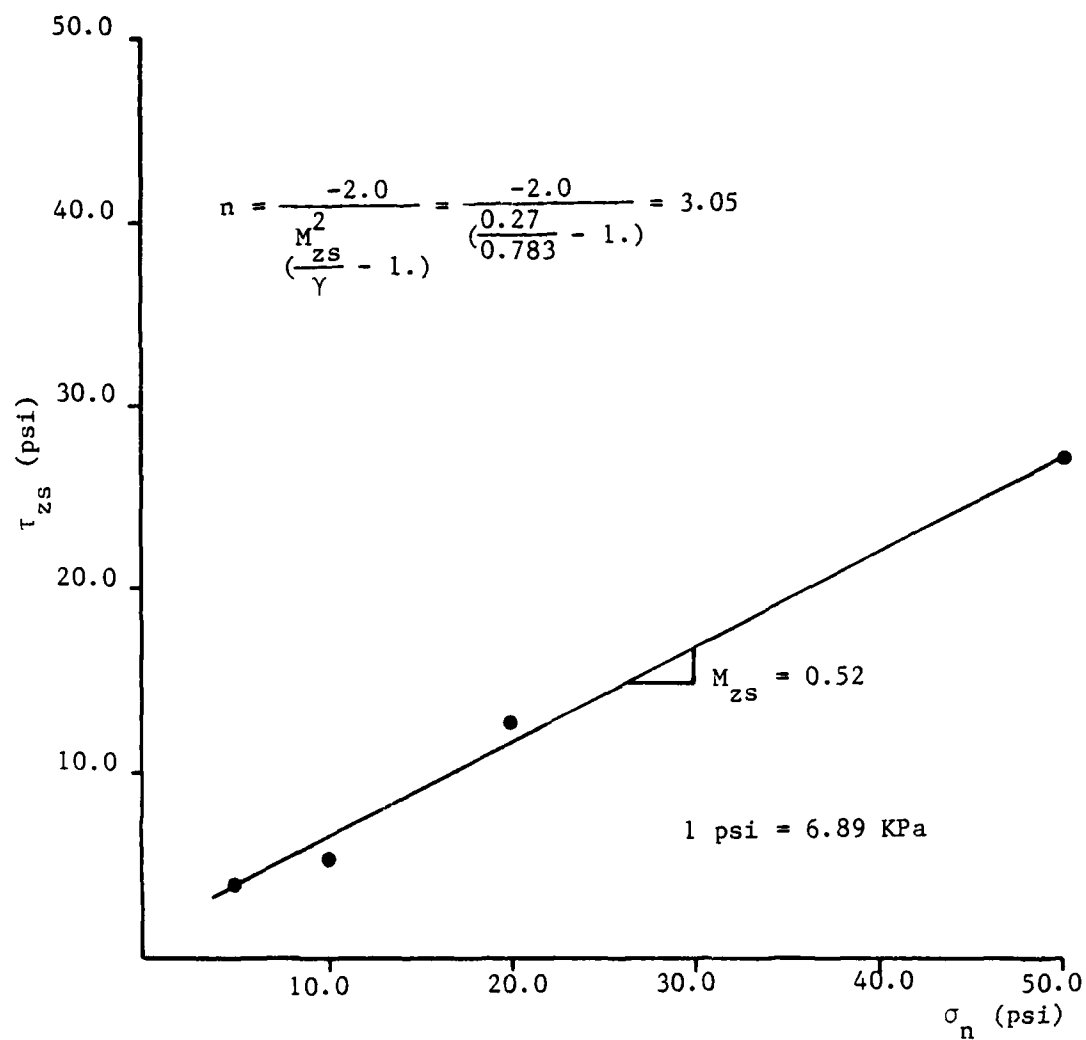


Figure II-5. Phase Change Envelope; 7° Surface

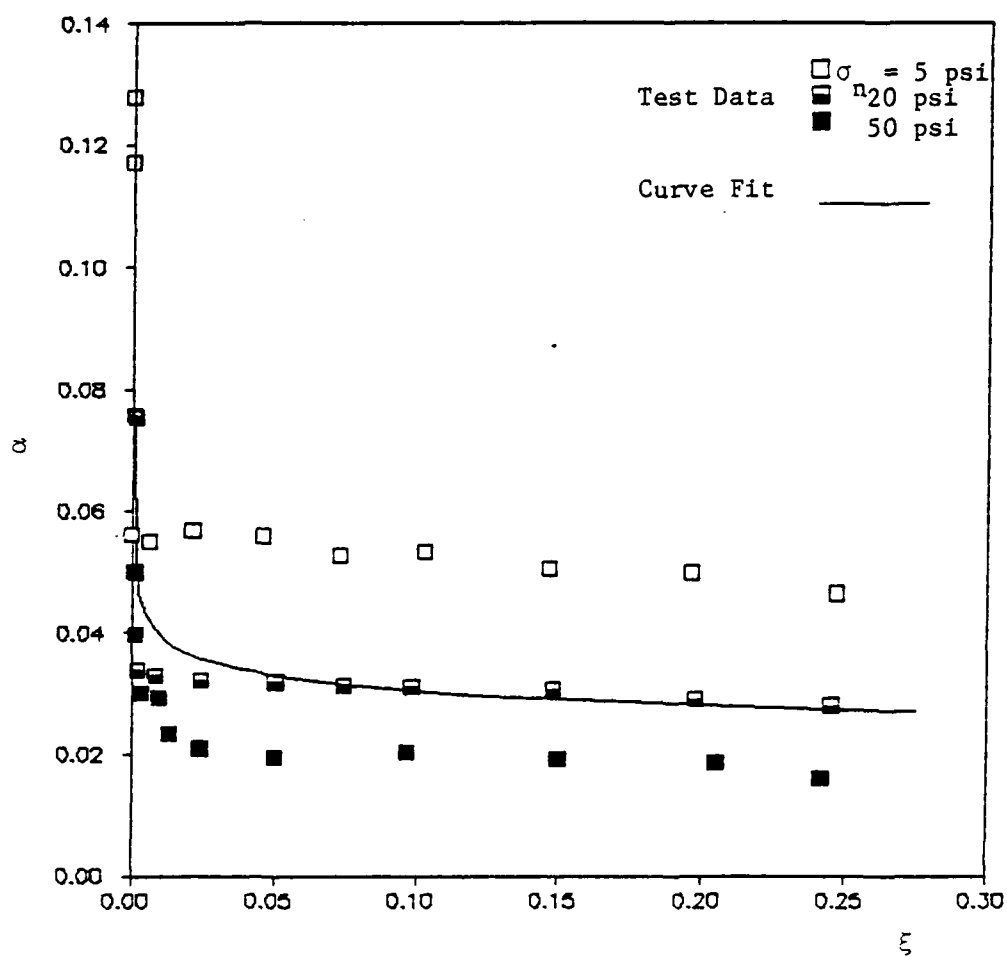


Figure II-6. α versus ξ ; Quasi-Static Test Series; Flat Surface

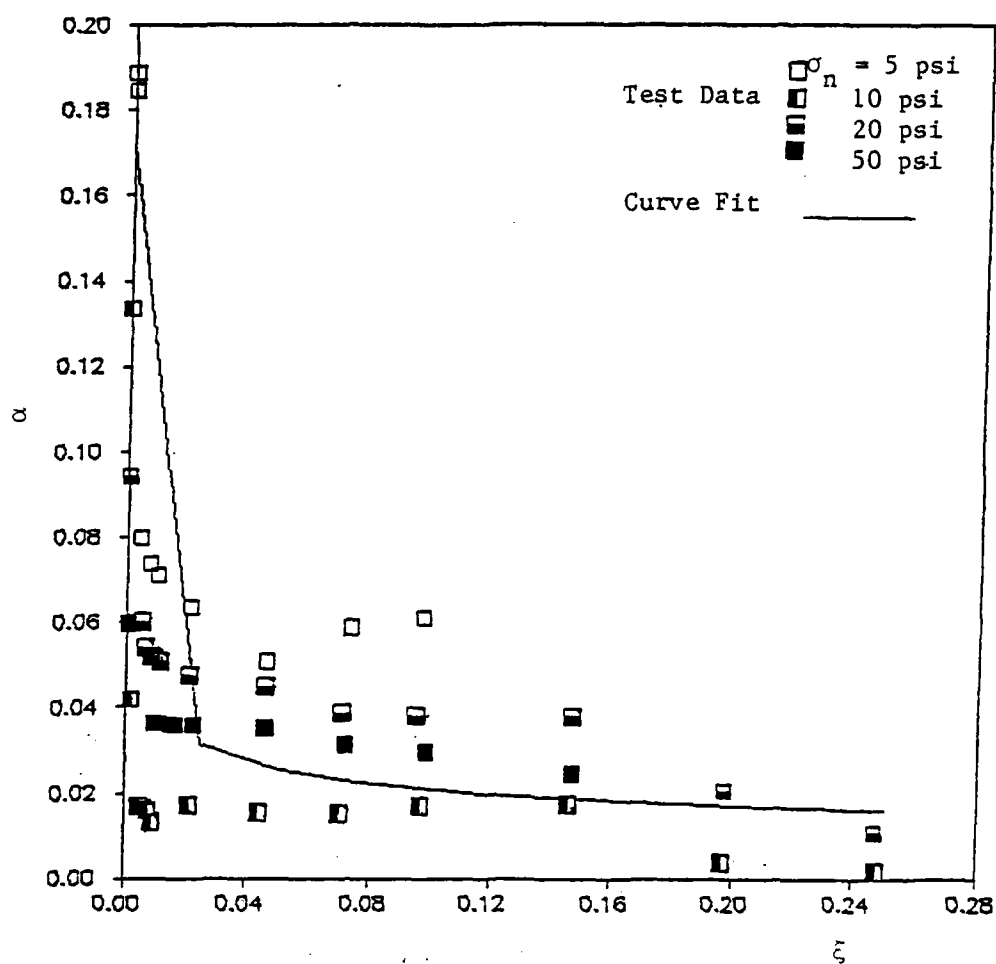


Figure II-7. α versus ξ ; Quasi-Static Test Series; 5° Surface

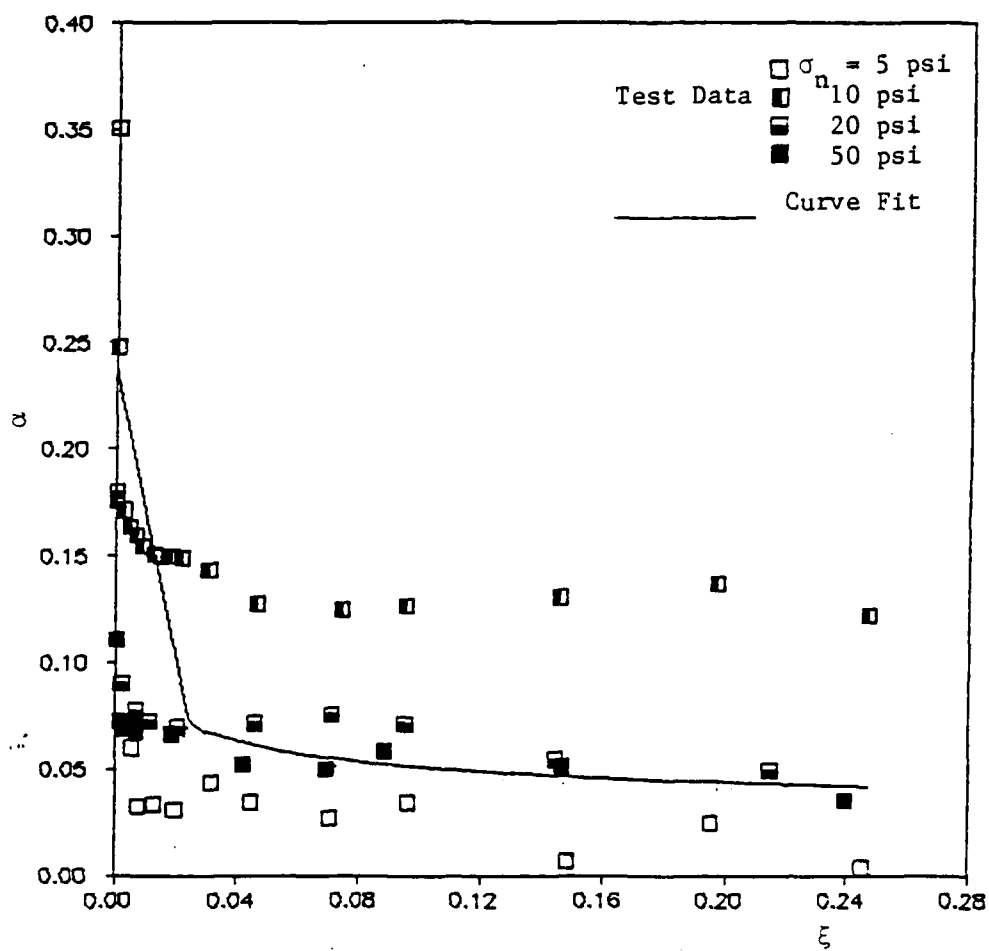


Figure II-8. α versus ξ ; Quasi-Static Test Series; 7° Surface

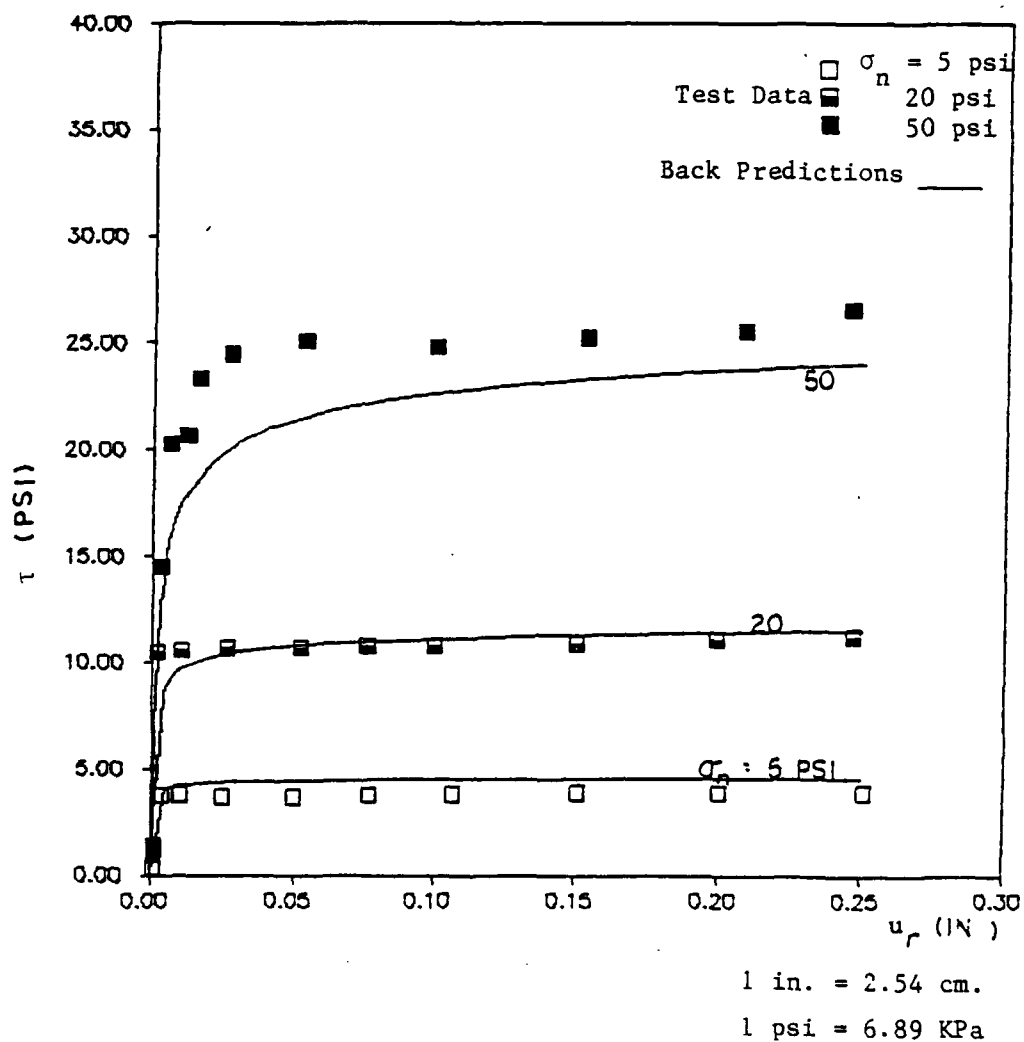


Figure II-9. Test Data and Back Predictions of τ versus u_r ; Quasi-Static Loading; Flat Surface

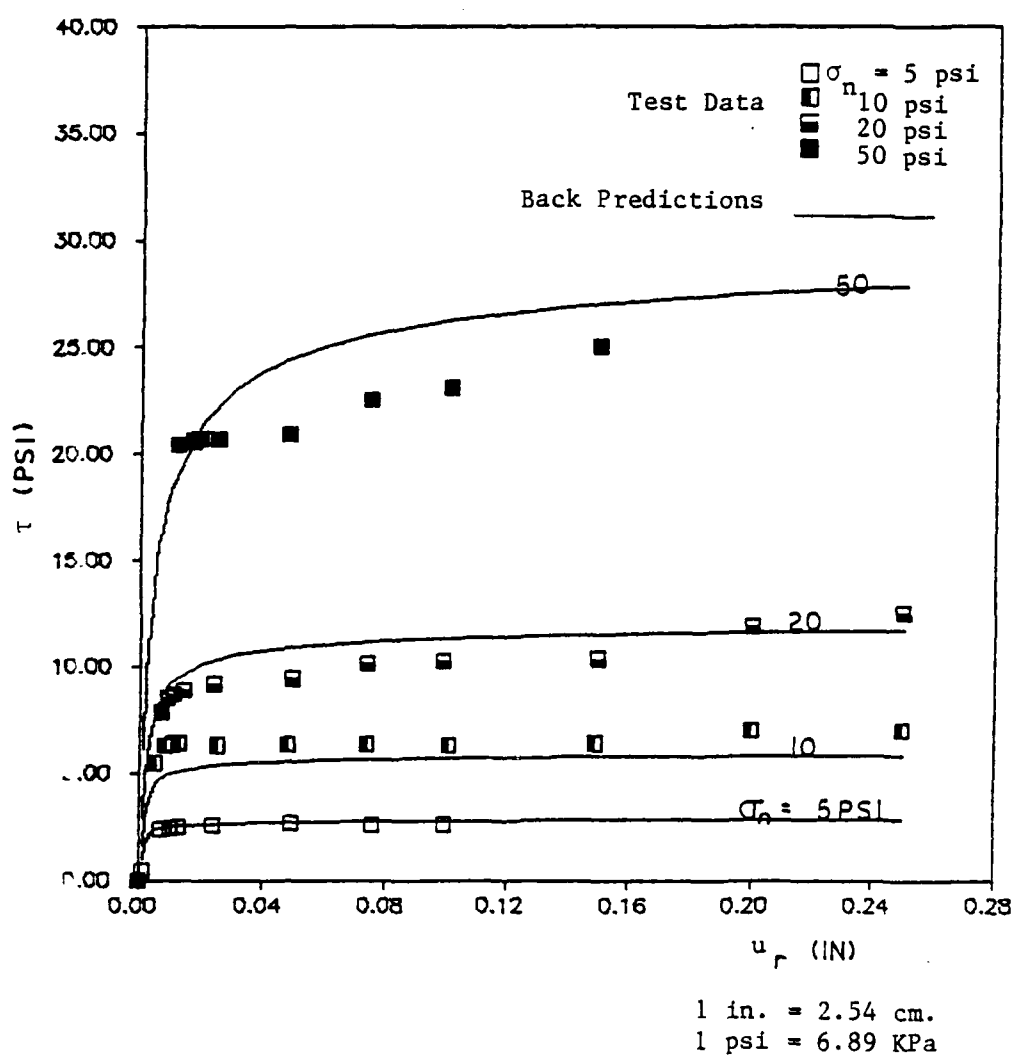


Figure II-10. Test Data and Back Predictions of τ versus u_r ; Quasi-Static Loading; 5° Surface

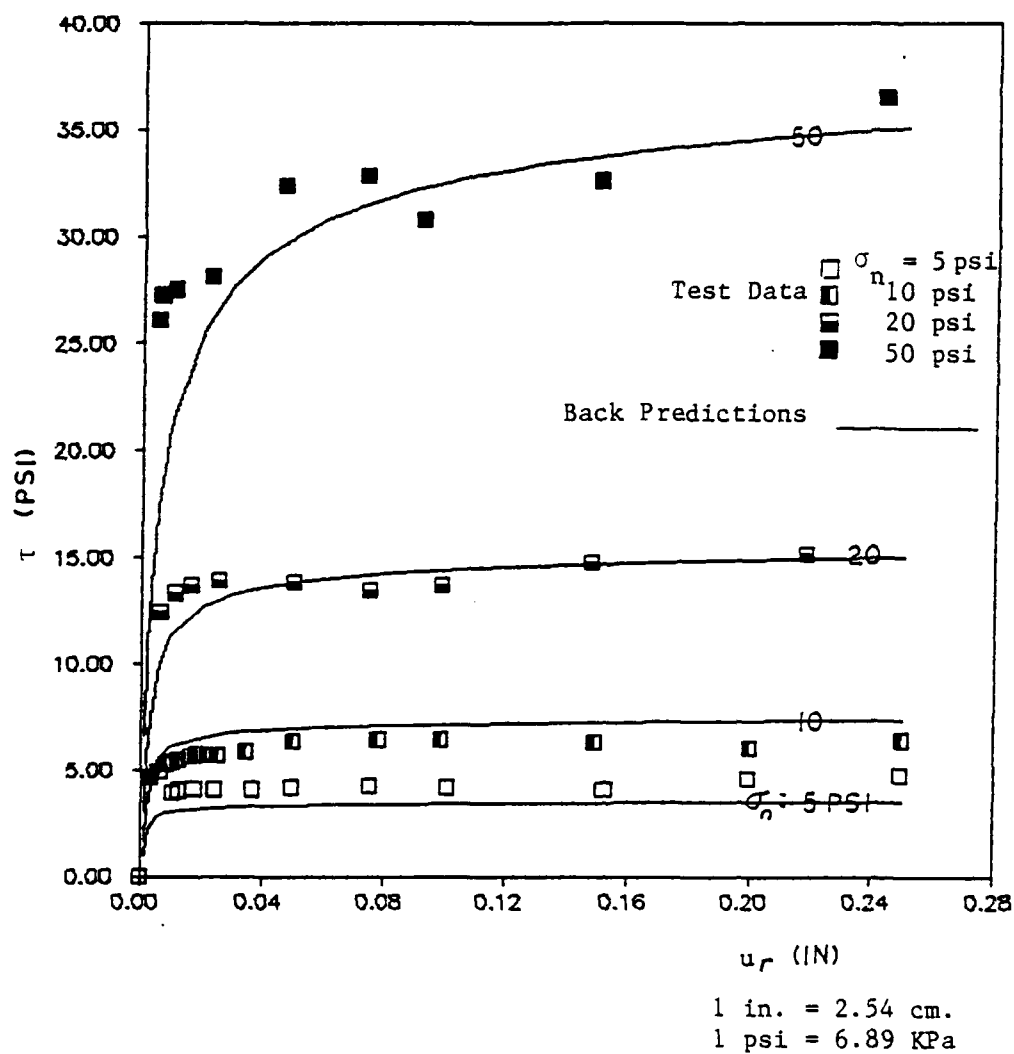


Figure II-11. Test Data and Back Predictions of τ versus u_r ; Quasi-Static Loading; 7° Surface

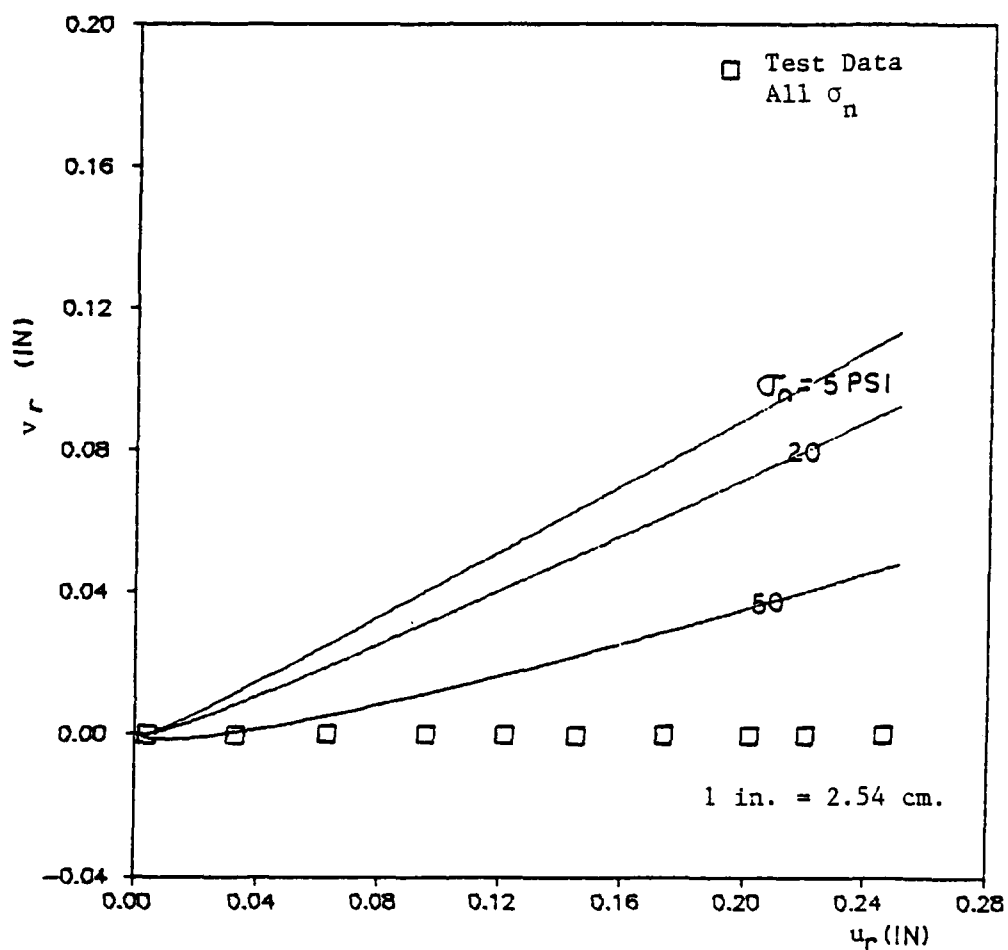


Figure II-12. Test Data and Back Predictions of v_r versus u_r ; Quasi-Static Loading; Flat Surface; Associative Case

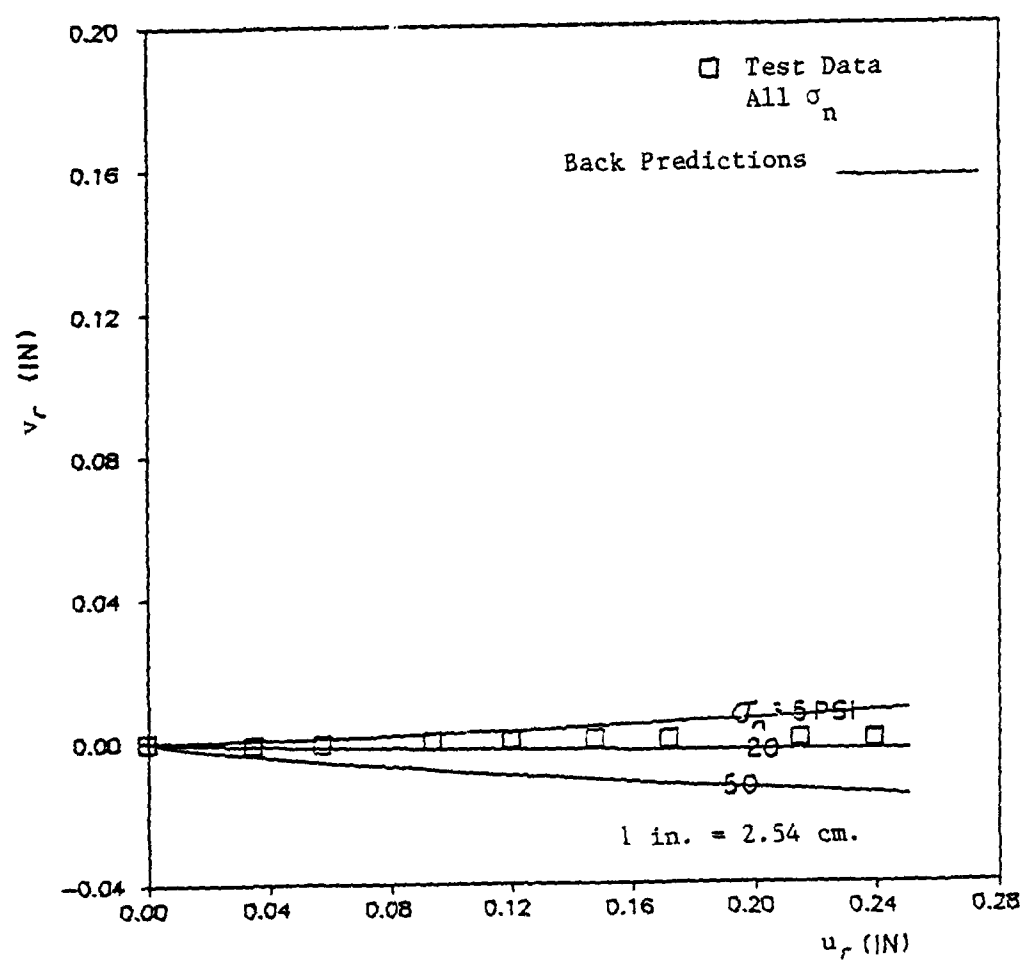


Figure II-13. Test Data and Back Predictions of v_r versus u_r ; Quasi-Static Loading; Flat Surface; Nonassociative Case

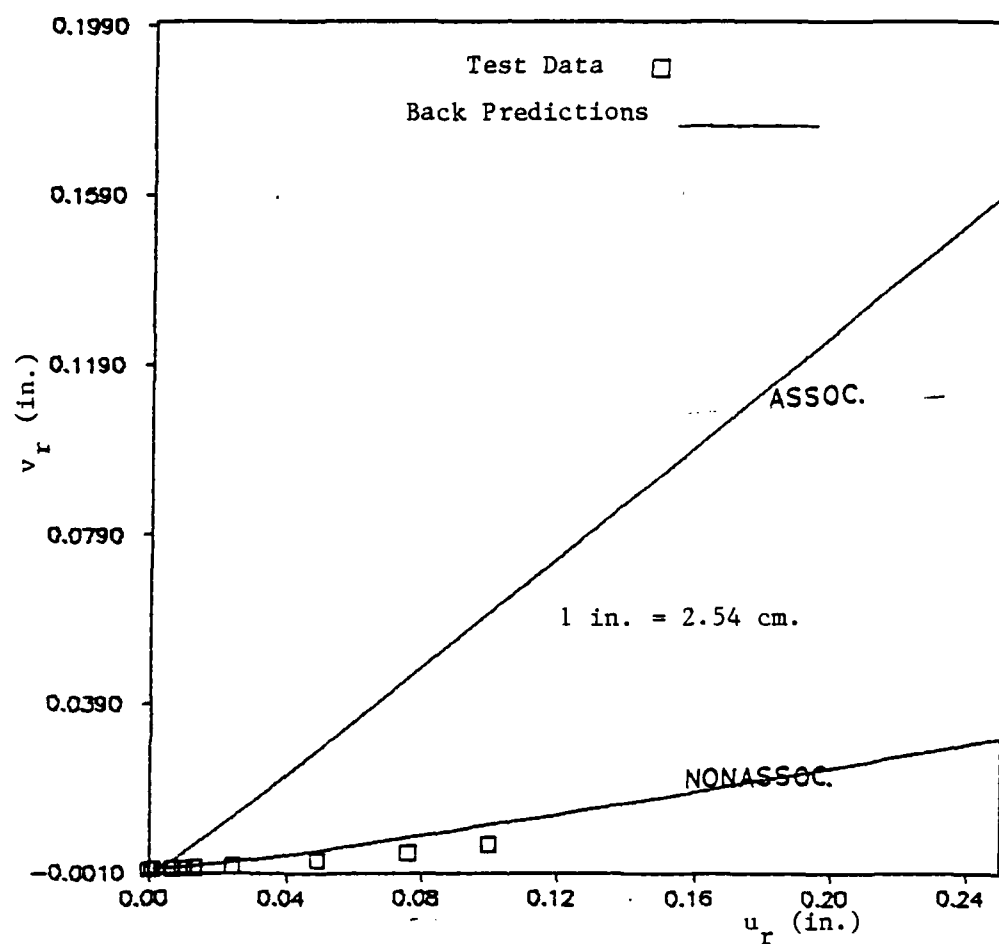


Figure II-14. Test Data and Back Predictions of v_r versus u_r ; Quasi-Static Loading; $\sigma_n = 5$ psi; 5° Surface; Associativeⁿ and Nonassociative Case

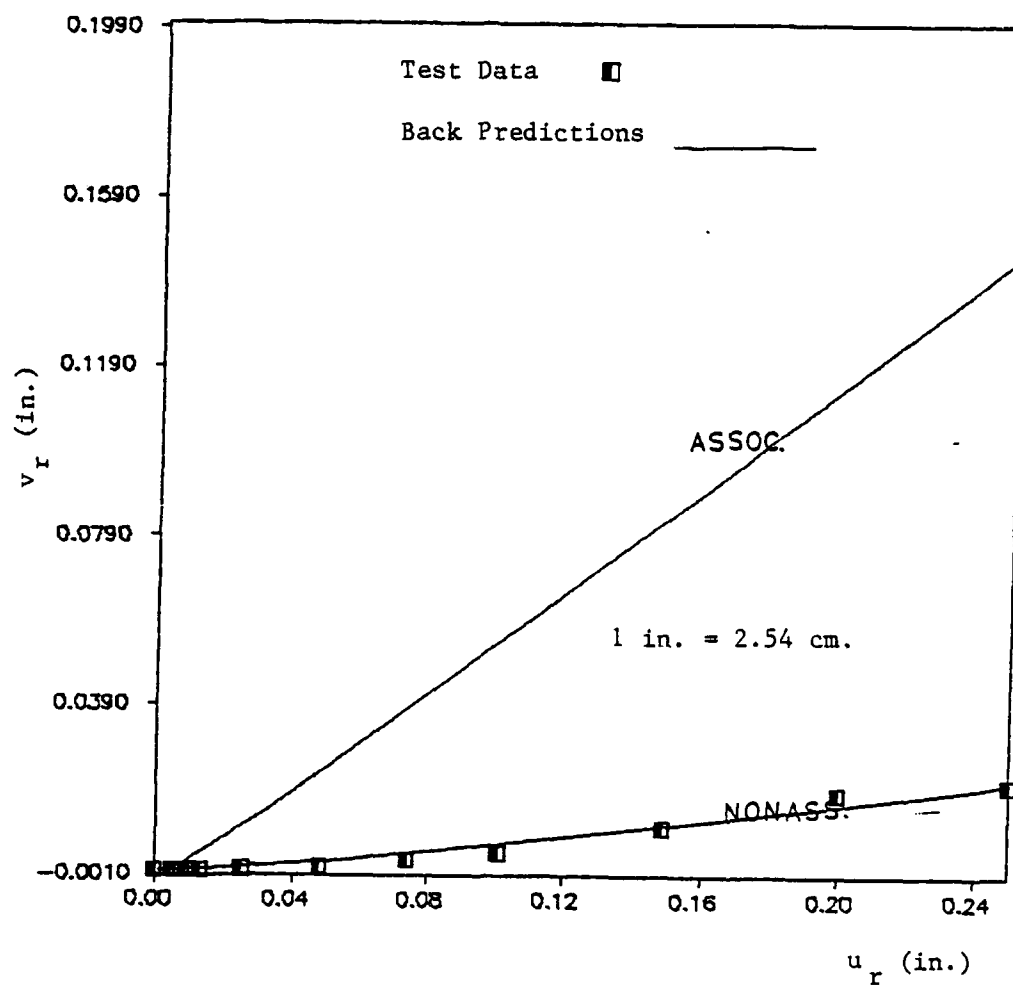


Figure II-15. Test Data and Back Predictions of v_r versus u_r ; Quasi-Static Loading; $\sigma_n = 10$ psi; 5° Surface; Associativeⁿ and Nonassociative Case

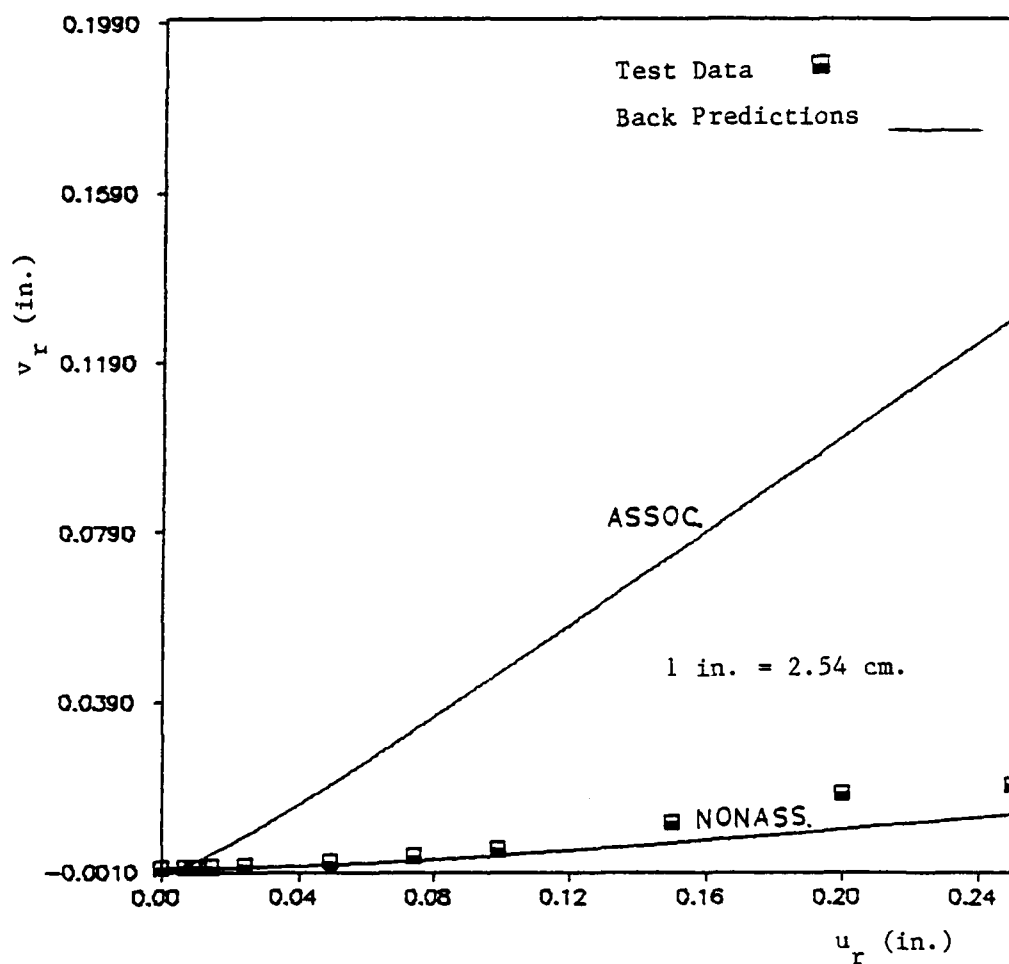


Figure II-16. Test Data and Back Predictions of v_r versus u_r ; Quasi-Static Loading; $\sigma_n = 20$ psi; 5° Surface; Associative and Nonassociative Case

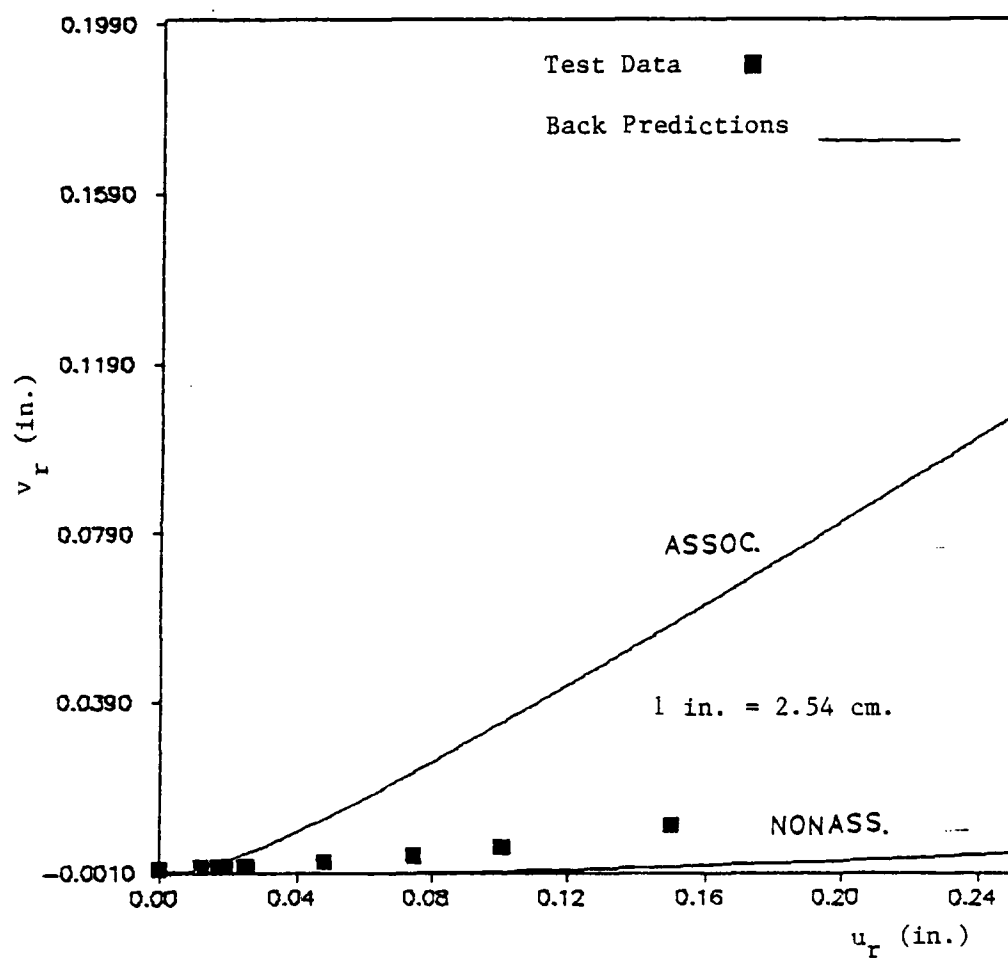


Figure II-17. Test Data and Back Predictions of v_r versus u_r ; Quasi-Static Loading; $\sigma_n = 50$ psi; 5° Surface; Associativeⁿ and Nonassociative Case

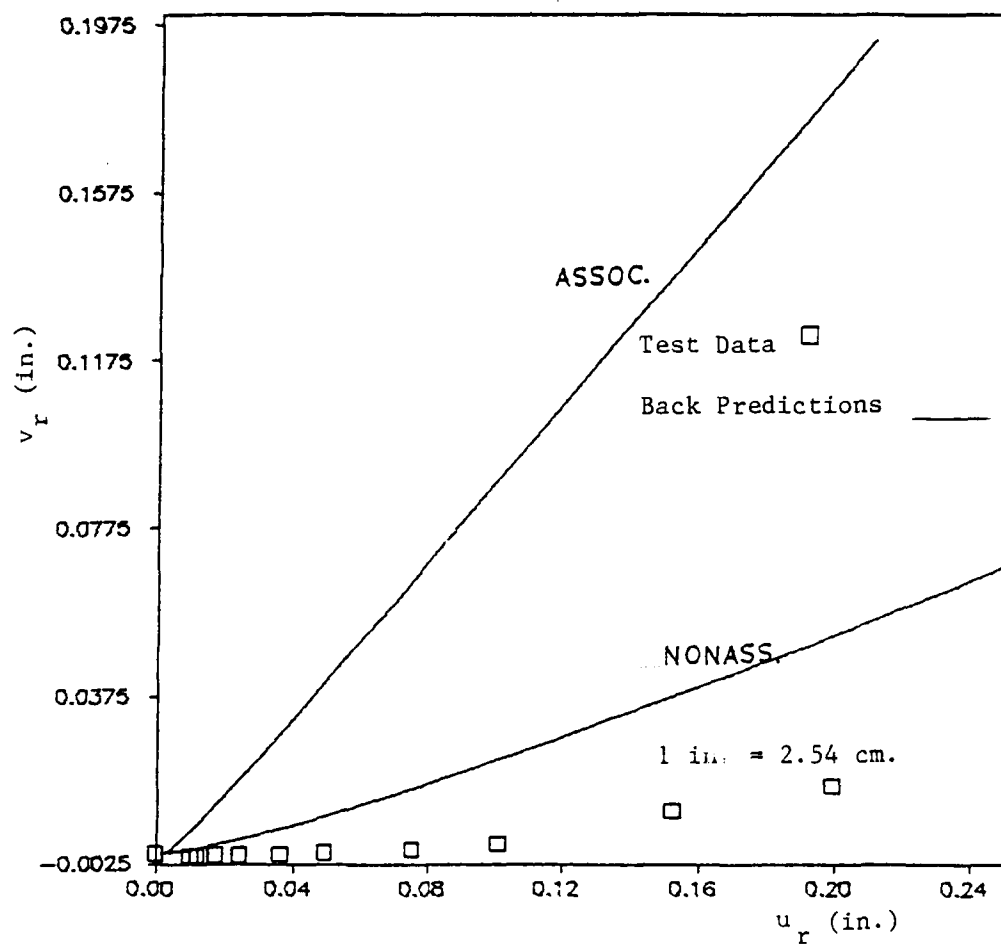


Figure II-18. Test Data and Back Predictions of v_r versus u_r ; Quasi-Static Loading; $\sigma_n = 5$ psi; 7° Surface; Associative and Nonassociative Case

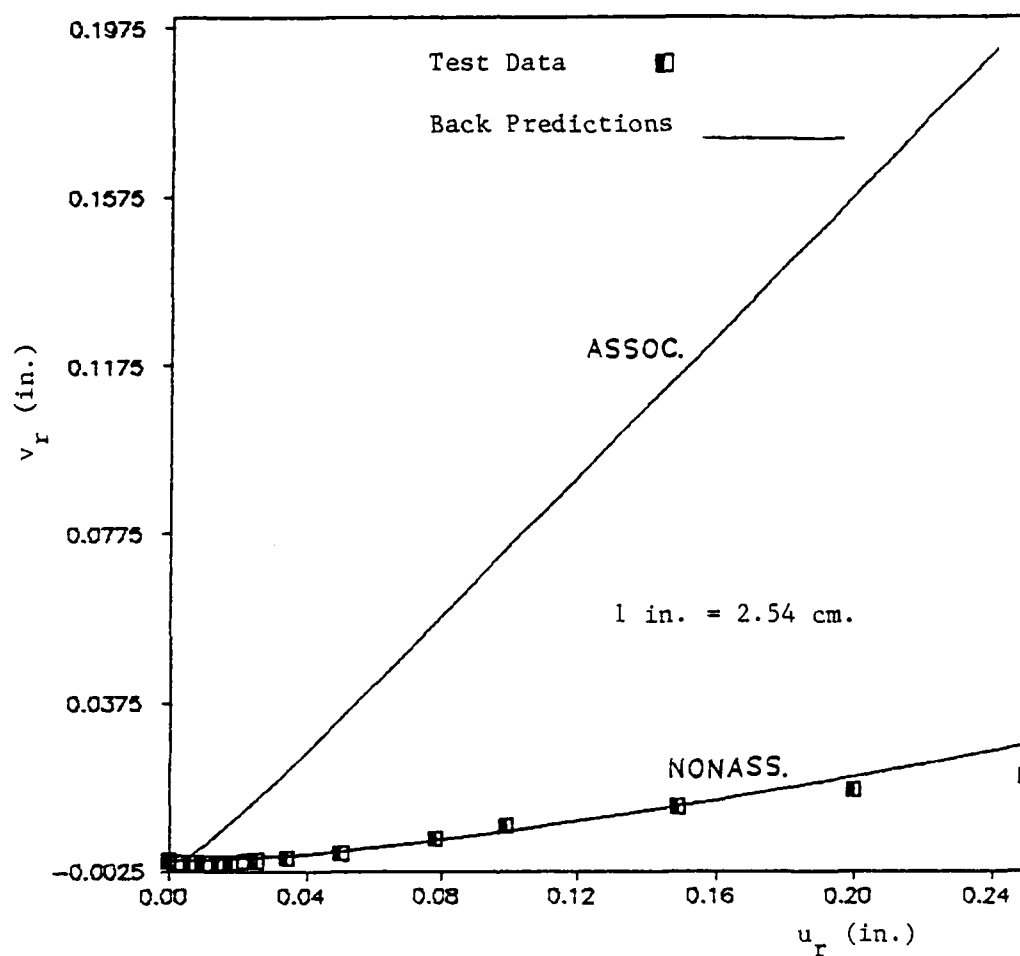


Figure II-19. Test Data and Back Predictions of v_r versus u_r ; Quasi-Static Loading; $\sigma_n = 10$ psi; 7° Surface; Associativeⁿ and Nonassociative Case

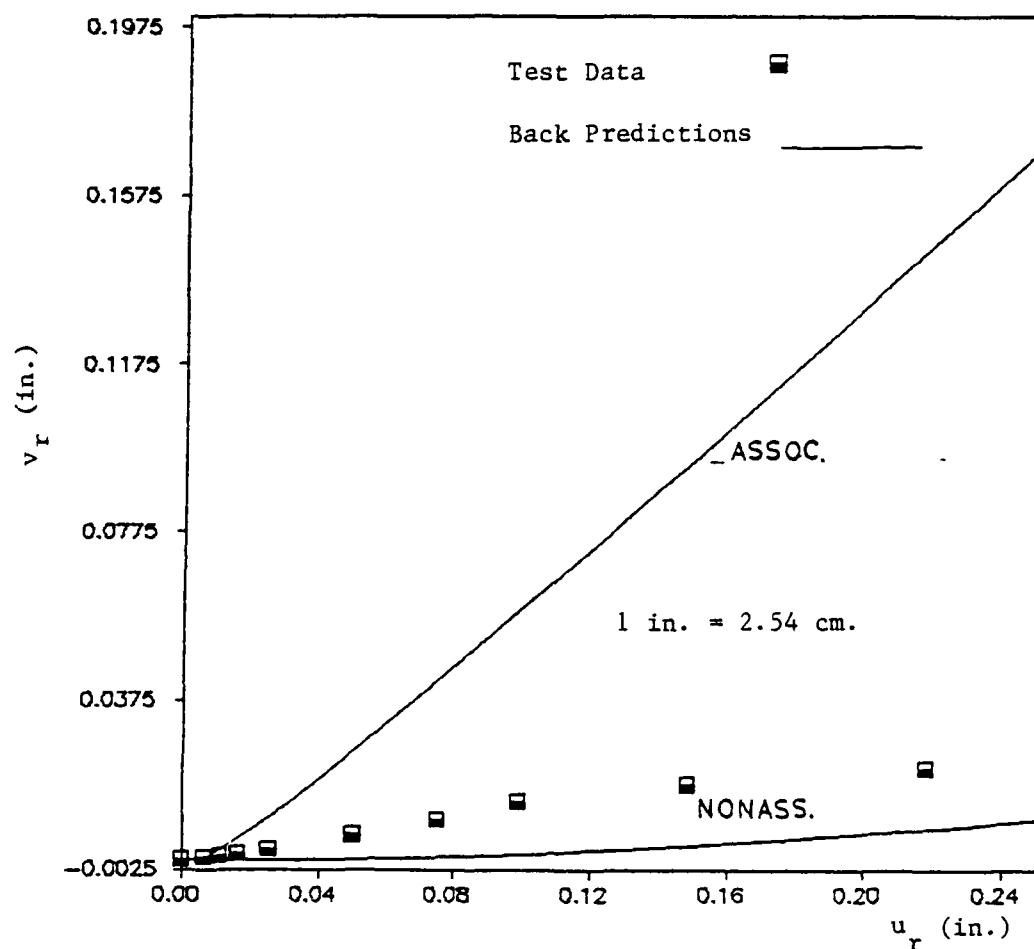


Figure II-20. Test Data and Back Predictions of v_r versus u_r ; Quasi-Static Loading; $\sigma_n = 20$ psi; 7° Surface; Associativeⁿ and Nonassociative Case

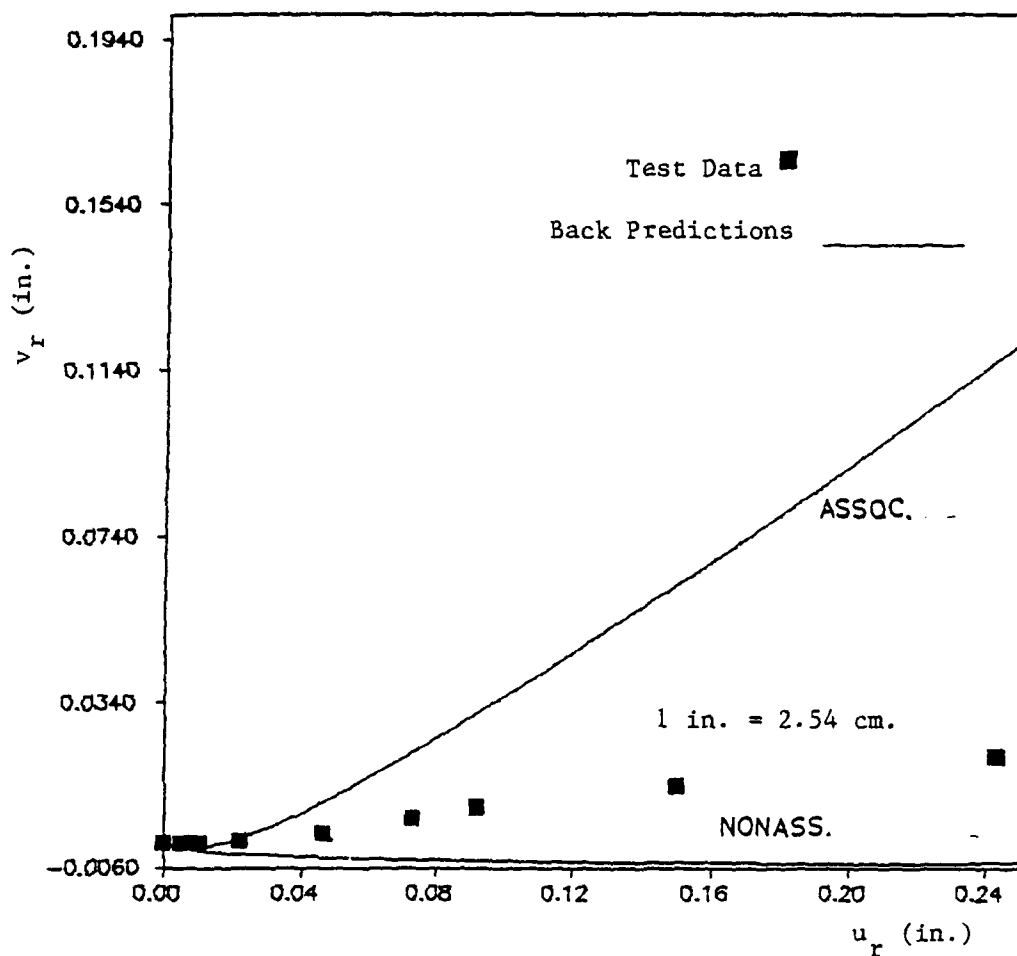


Figure II-21. Test Data and Back Predictions of v_r versus u_r ; Quasi-Static Loading; $\sigma_r \approx 50$ psi; 7° Surface; Associativeⁿ and Nonassociative Case

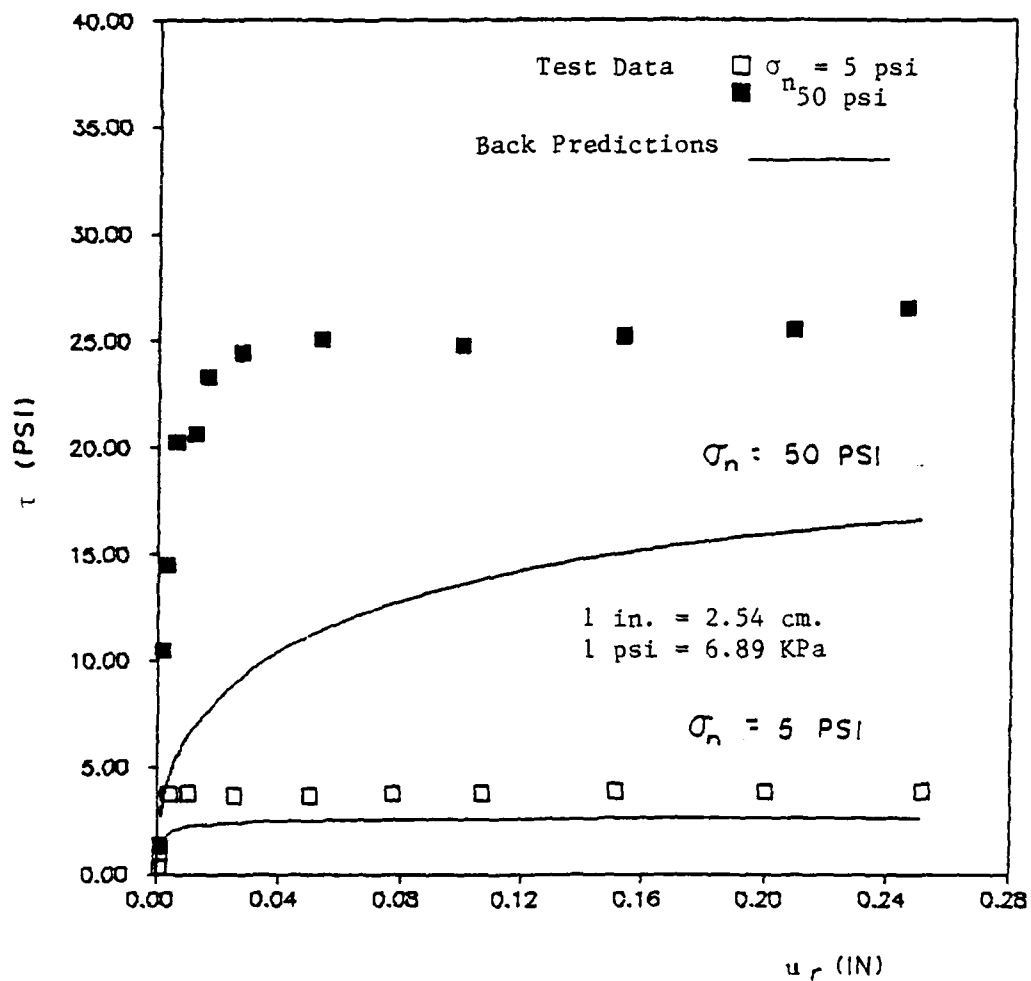


Figure II-22. Test Data and Back Predictions of τ versus u_r ; Quasi-Static Loading; Average Parameters; Flat Surface; Nonassociative Case

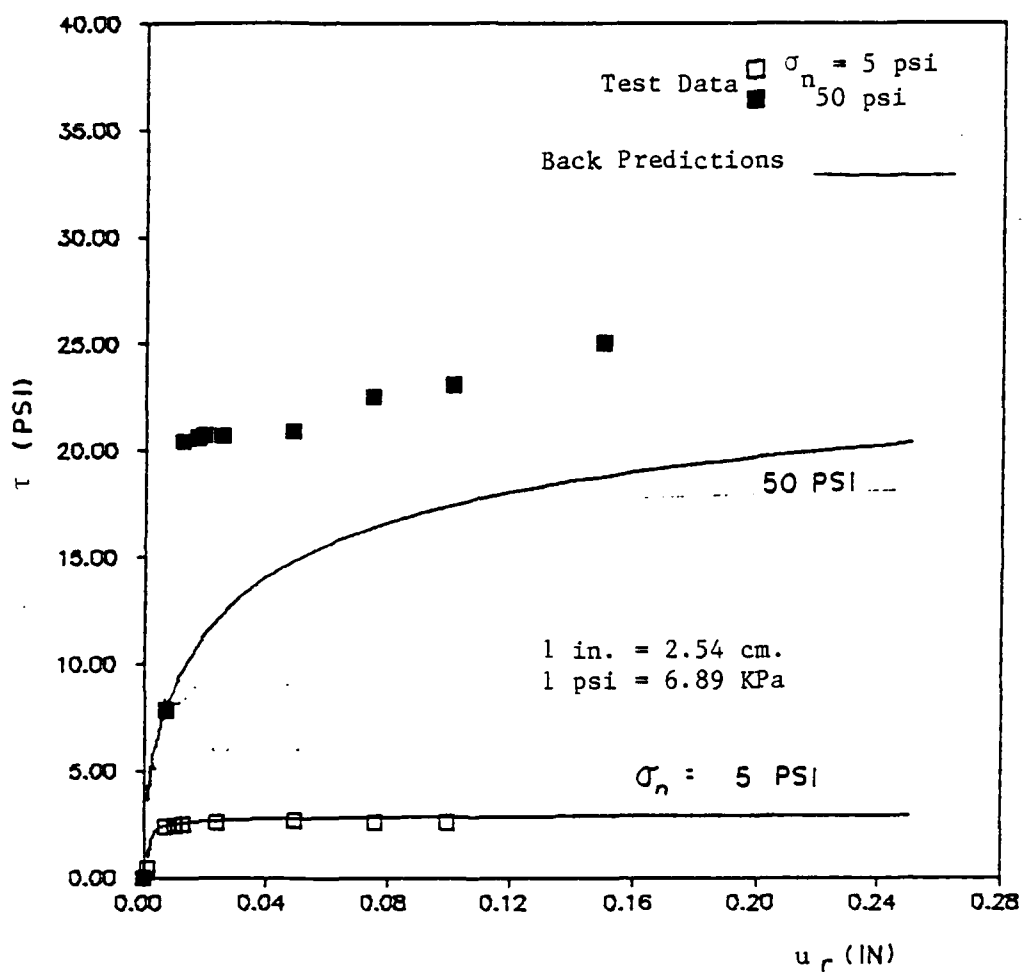


Figure II-23. Test Data and Back Predictions of τ versus u_r ; Quasi-Static Loading; Average Parameters; 5° Surface; Nonassociative Case

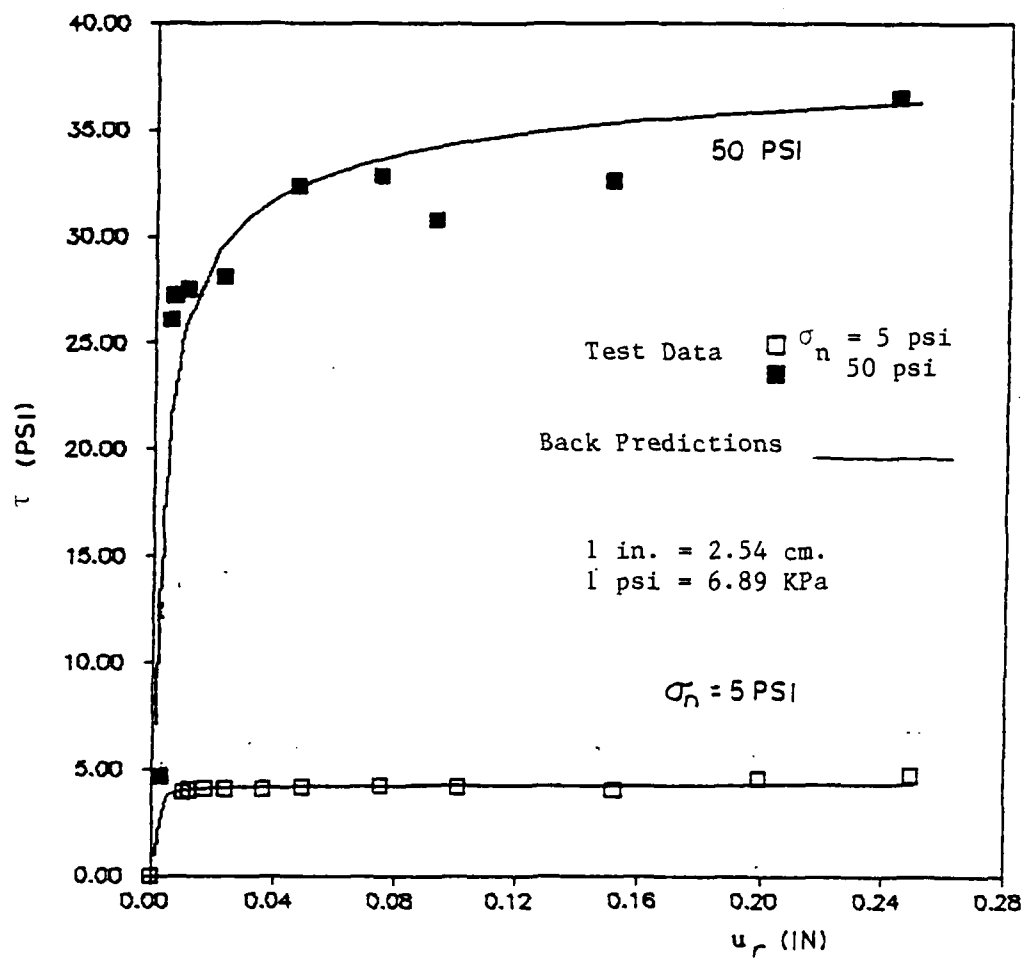


Figure II-24. Test Data and Back Predictions of τ versus u_r ; Quasi-Static Loading; Average Parameters; 7° Surface; Nonassociative Case

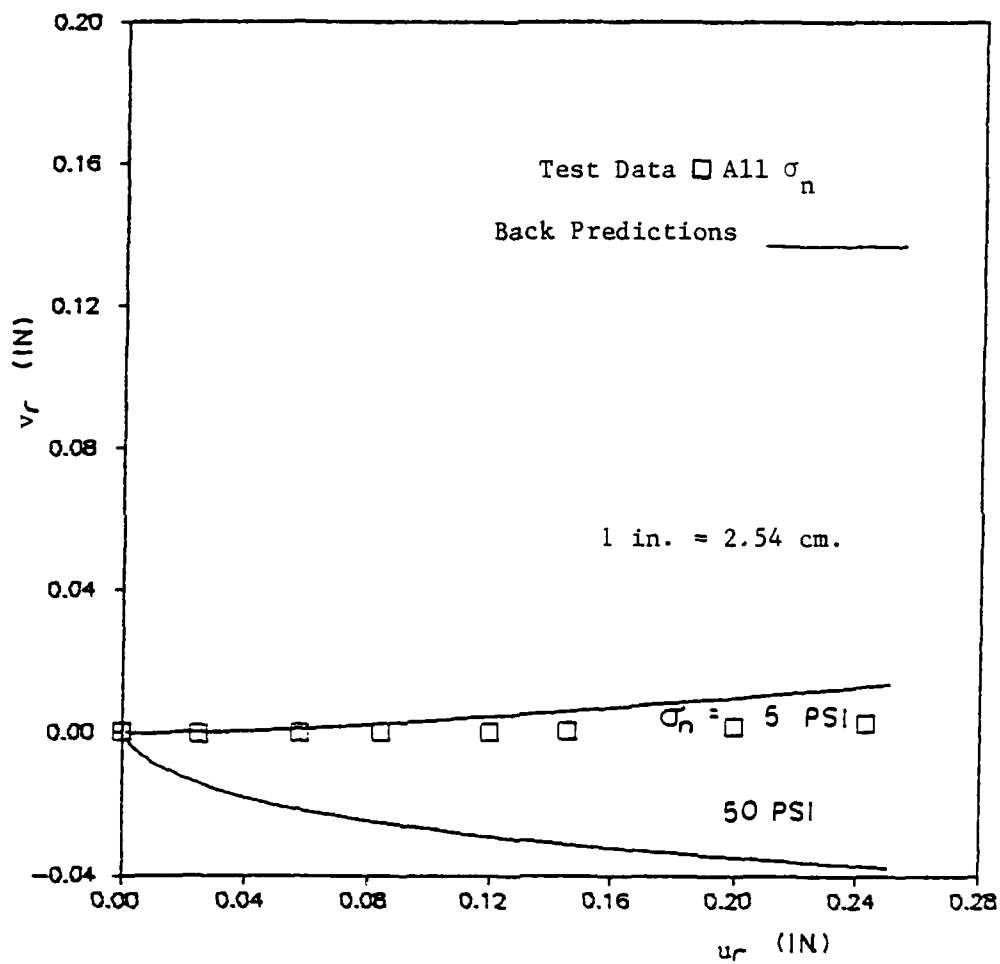


Figure II-25. Test Data and Back Predictions of v_r versus u_r ; Quasi-Static Loading; Average Parameters; Flat Surface; Nonassociative Case

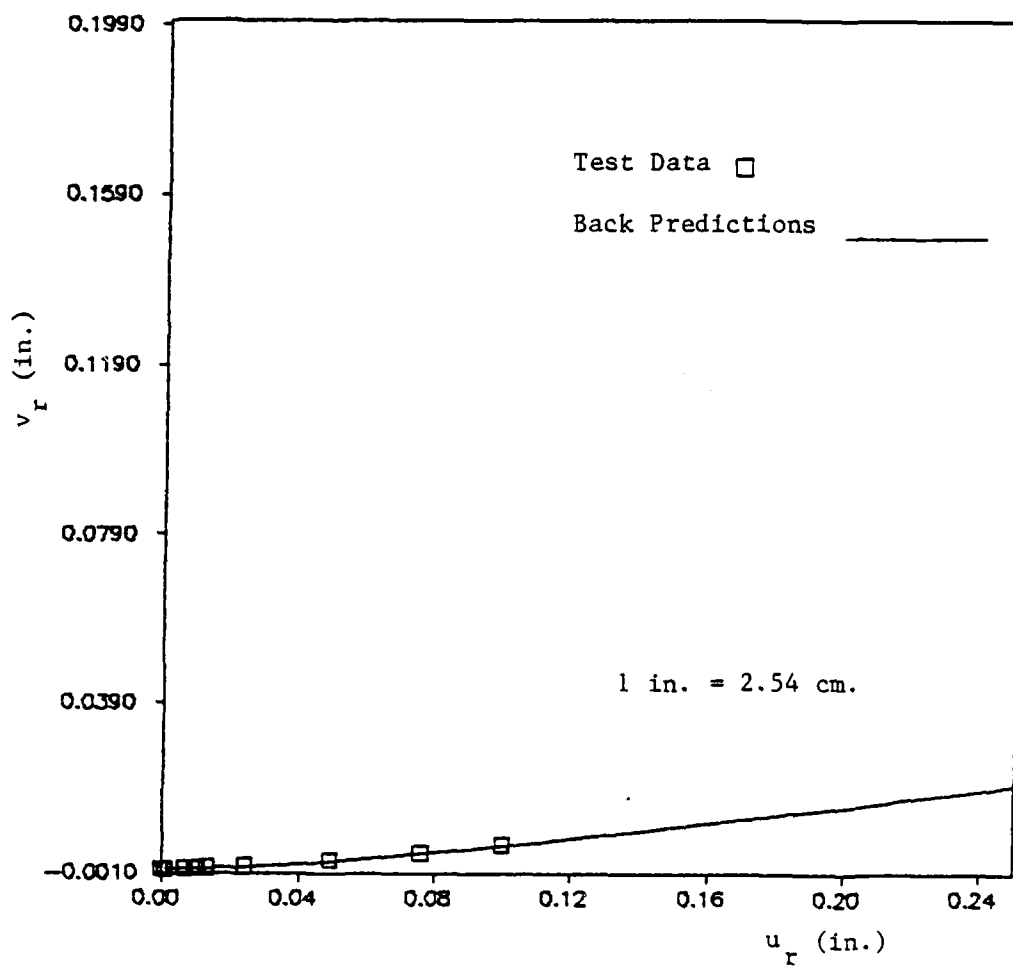


Figure II-26. Test Data and Back Predictions of v_r versus u_r ; Quasi-Static Loading; Average Parameters; 5° Surface; $\sigma_n = 5$ psi; Nonassociative Case

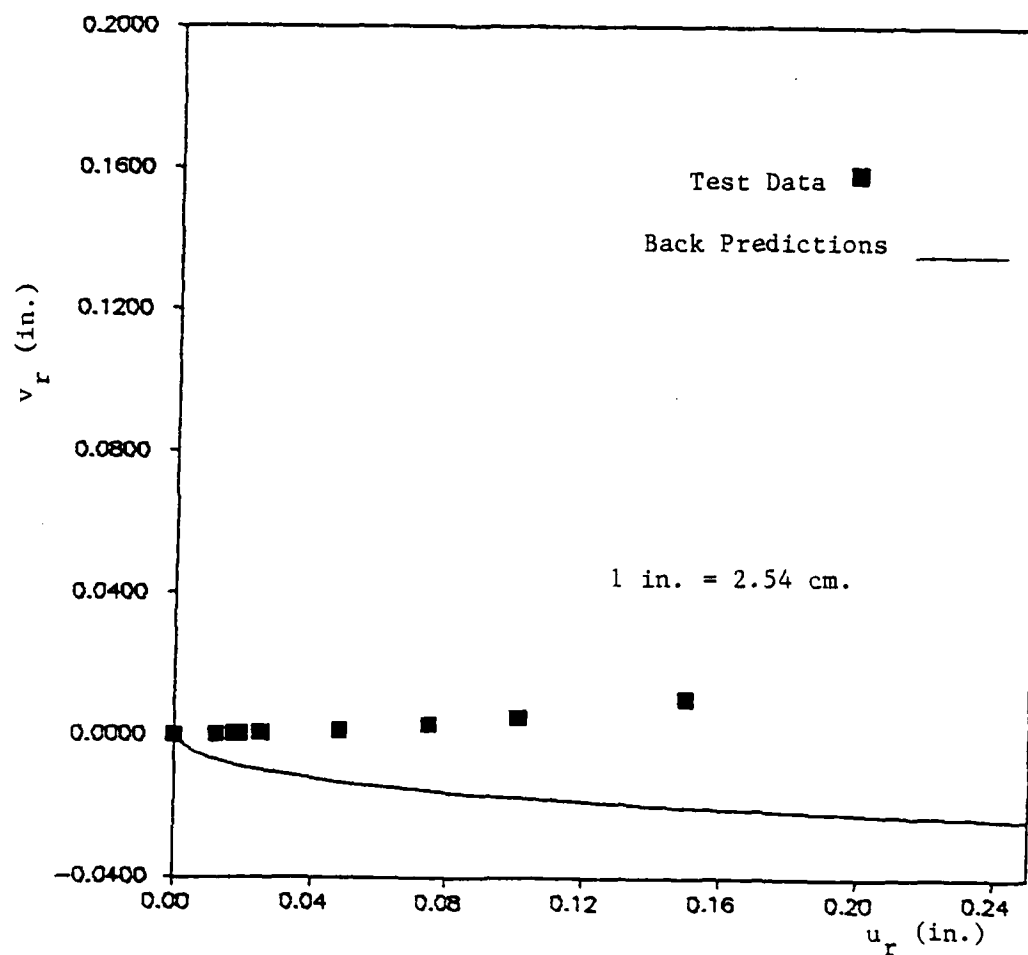


Figure II-27. Test Data and Back Predictions of v_r versus u_r ; Quasi-Static Loading; Average Parameters; 5° Surface; $\sigma_n = 50$ psi; Nonassociative Case

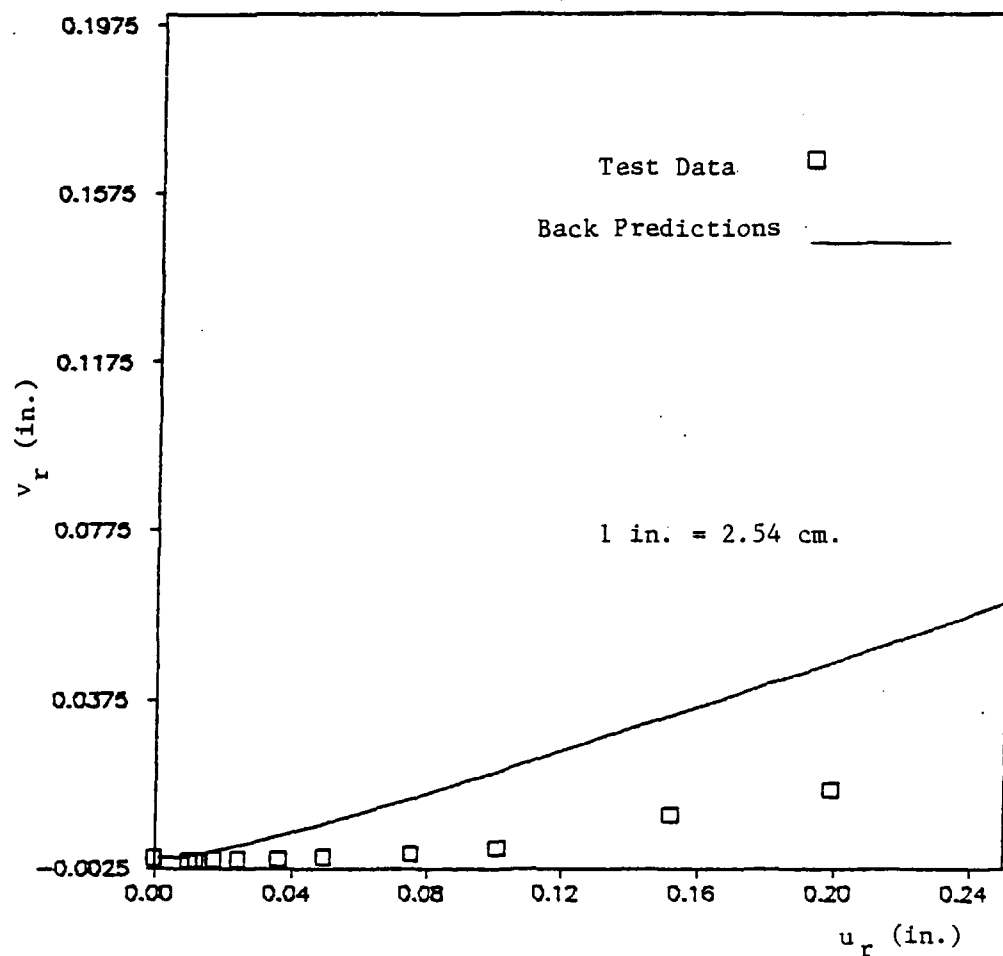


Figure II-28. Test Data and Back Predictions of v_r versus u_r ; Quasi-Static Loading; Average Parameters; 7° Surface; $\sigma_n = 5$ psi; Nonassociative Case

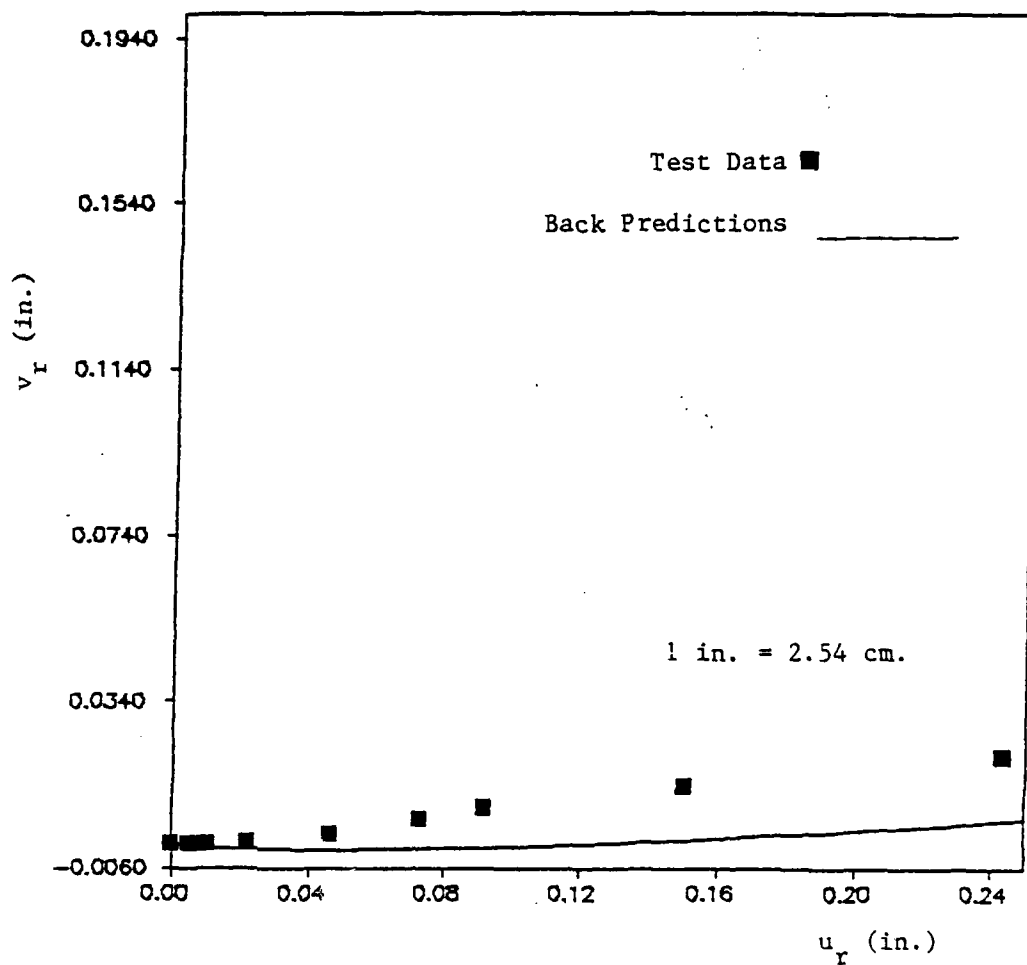


Figure II-29. Test Data and Back Predictions of v_r versus u_r ; Quasi-Static Loading; Average Parameters; 7° Surface; $\sigma_n = 50$ psi; Nonassociative Case

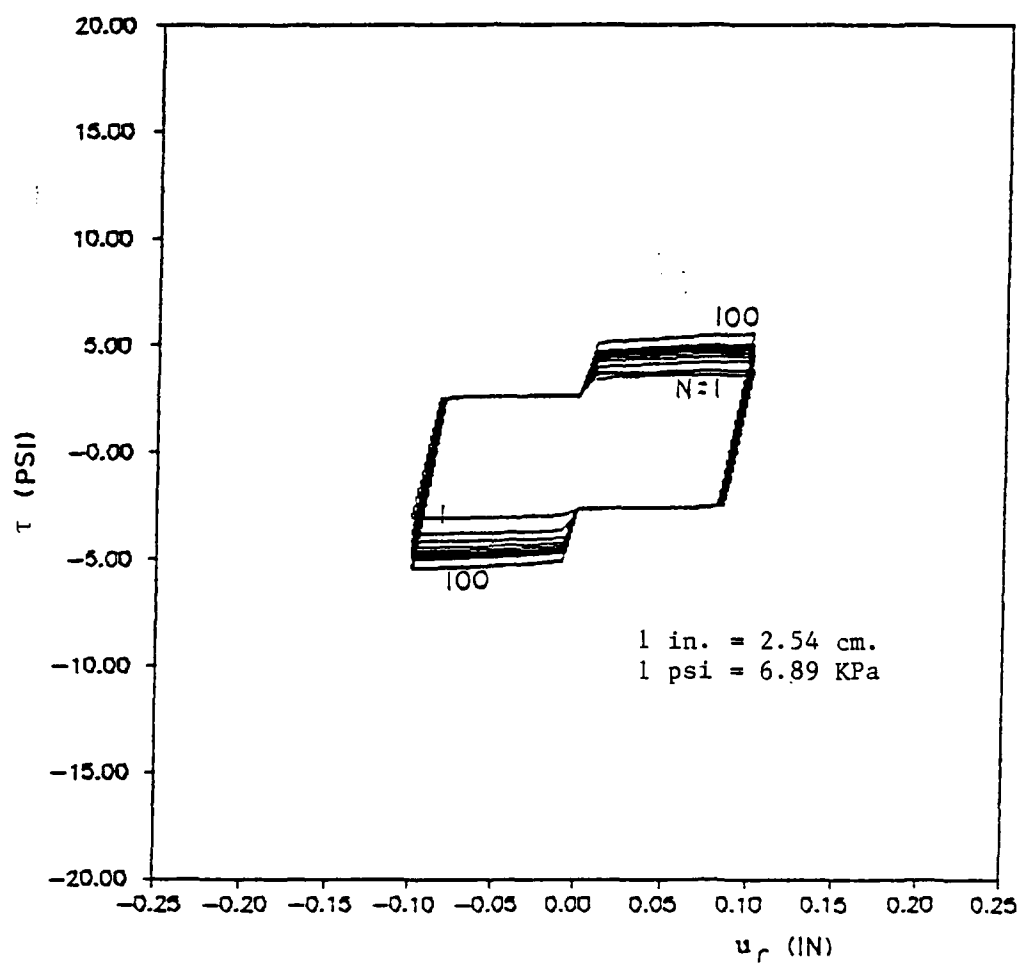


Figure II-30. Back Predictions; Cyclic Test; τ versus u_r ;
9° Surface; $\sigma_n = 5$ psi

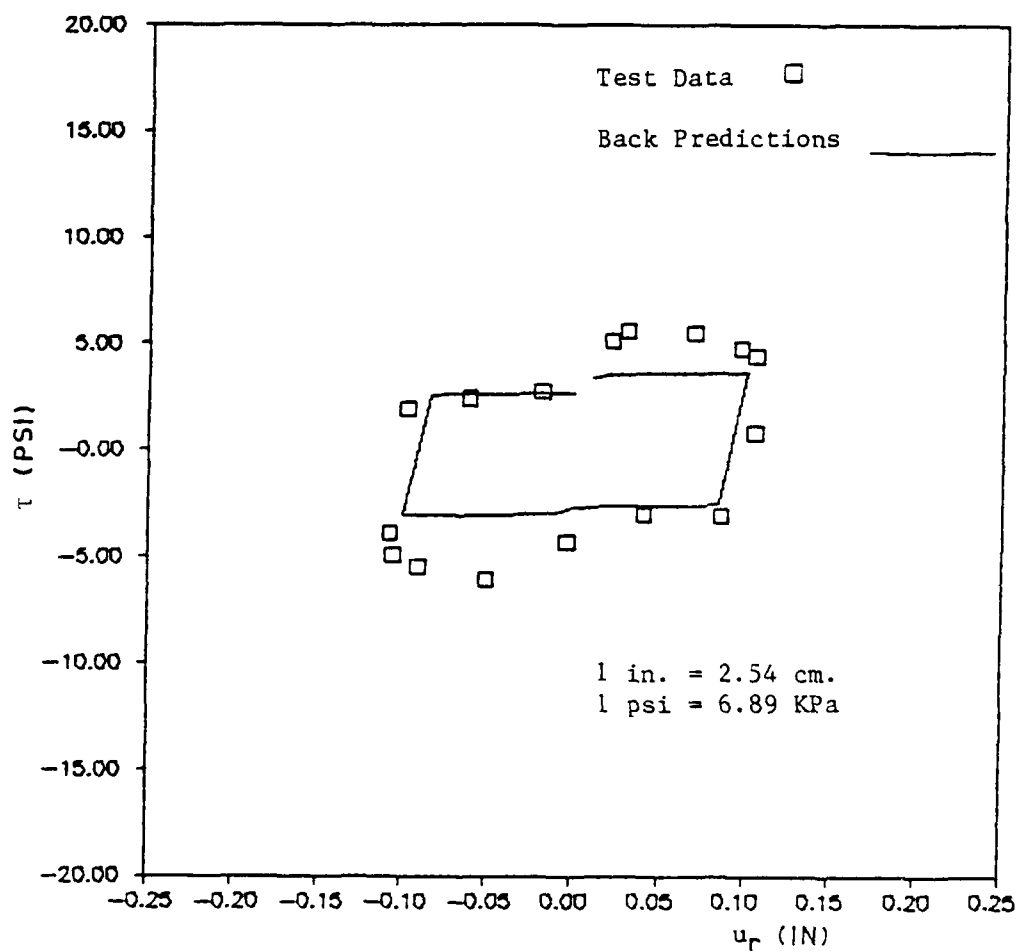


Figure II-31. Test Data and Back Predictions; τ versus u_r ; Cyclic Test; 9° Surface; $\sigma_n = 5$ psi; Cycle r_1

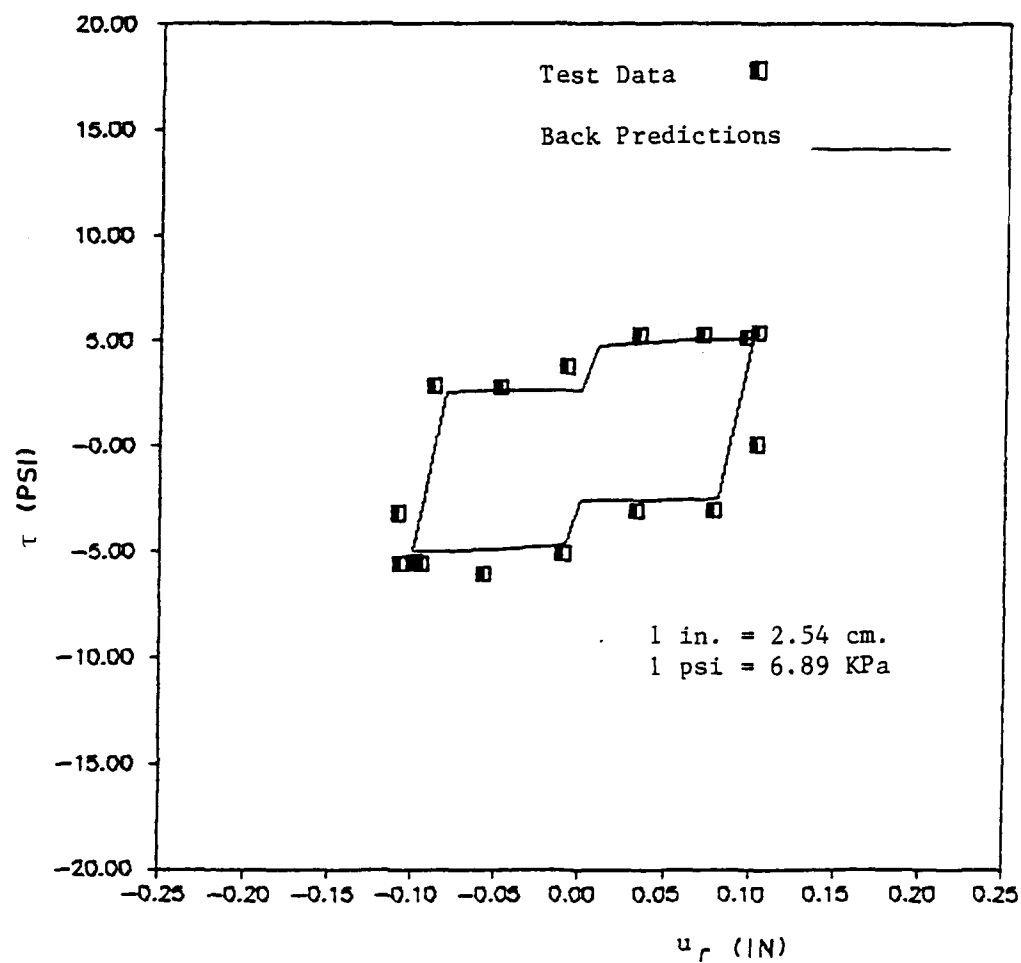


Figure II-32. Test Data and Back Predictions; τ versus u_r ;
Cyclic Test; 9° Surface; $\sigma_n = 5$ psi; Cycle 10

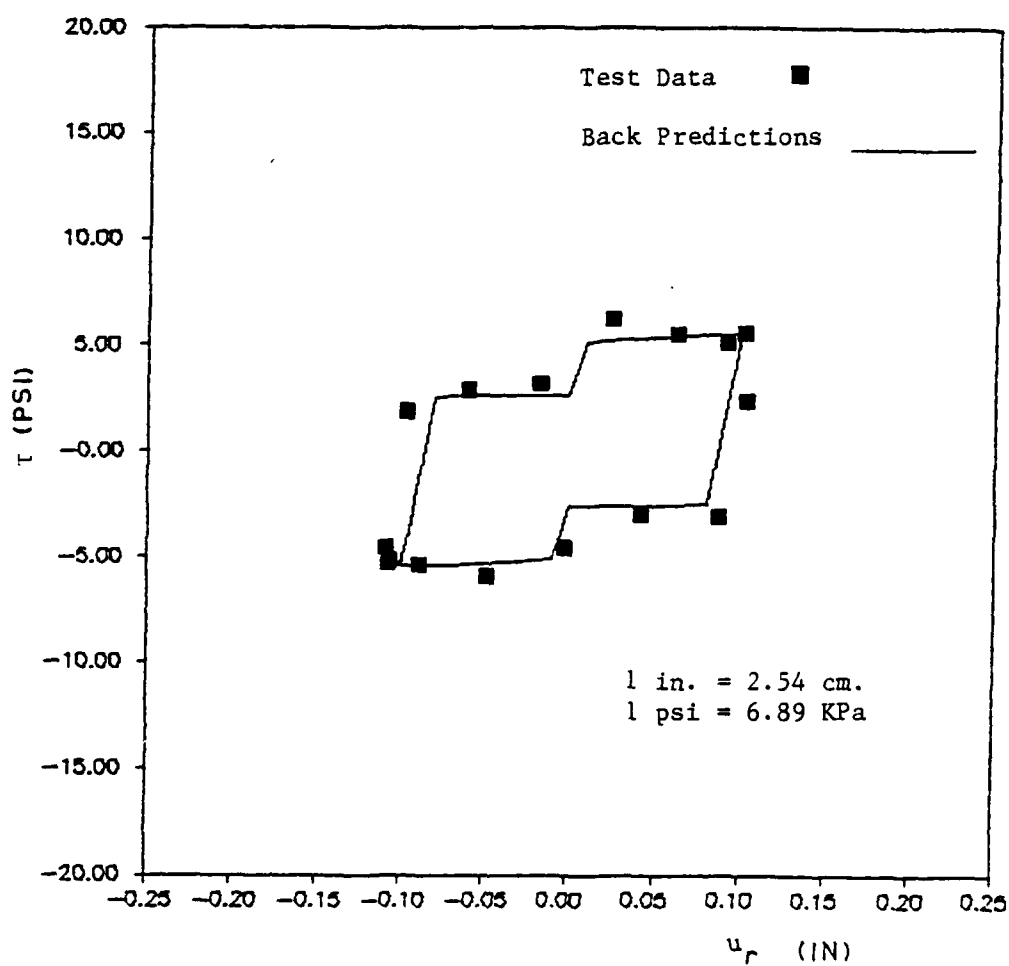


Figure II-33. Test Data and Back Predictions; τ versus u_r ;
Cyclic Test; 9° Surface; $\sigma_n = 5$ psi; Cycle^r100

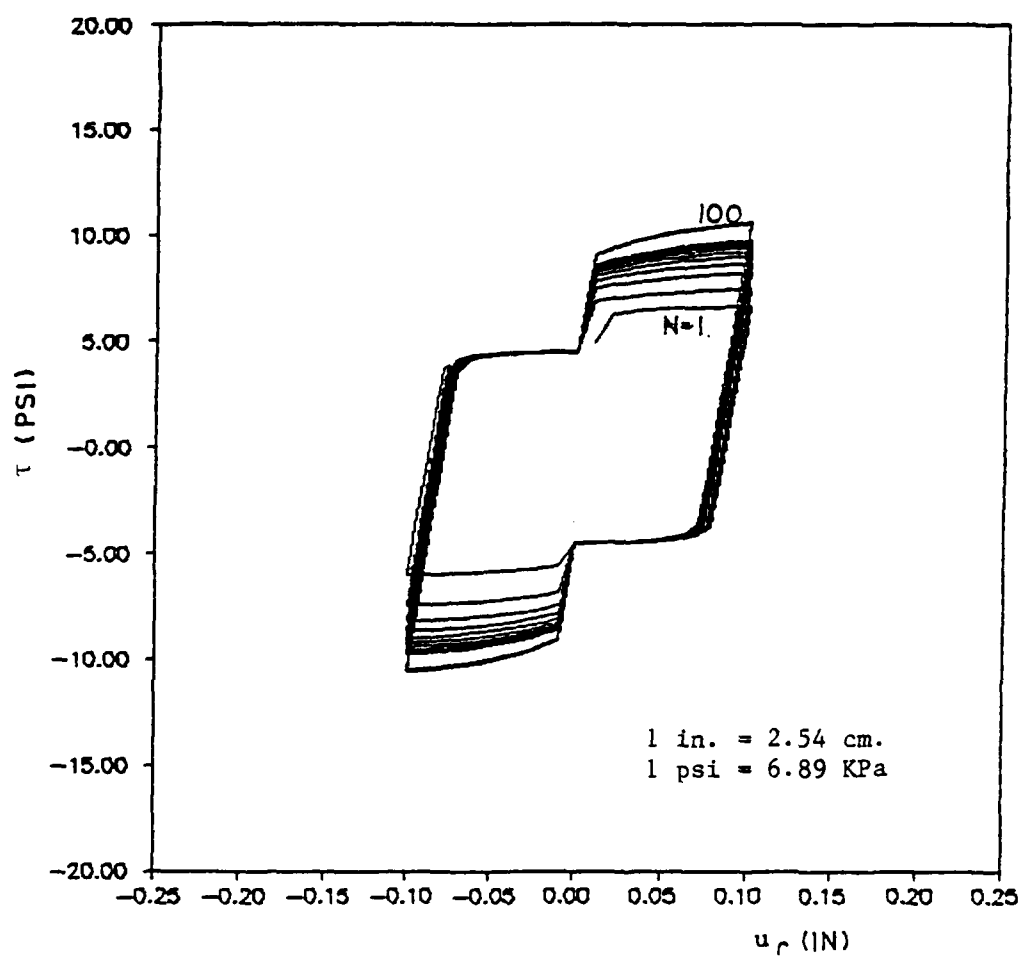


Figure II-34. Back Predictions; Cyclic Test; τ versus u_r ;
9° Surface; $\sigma_n = 10$ psi

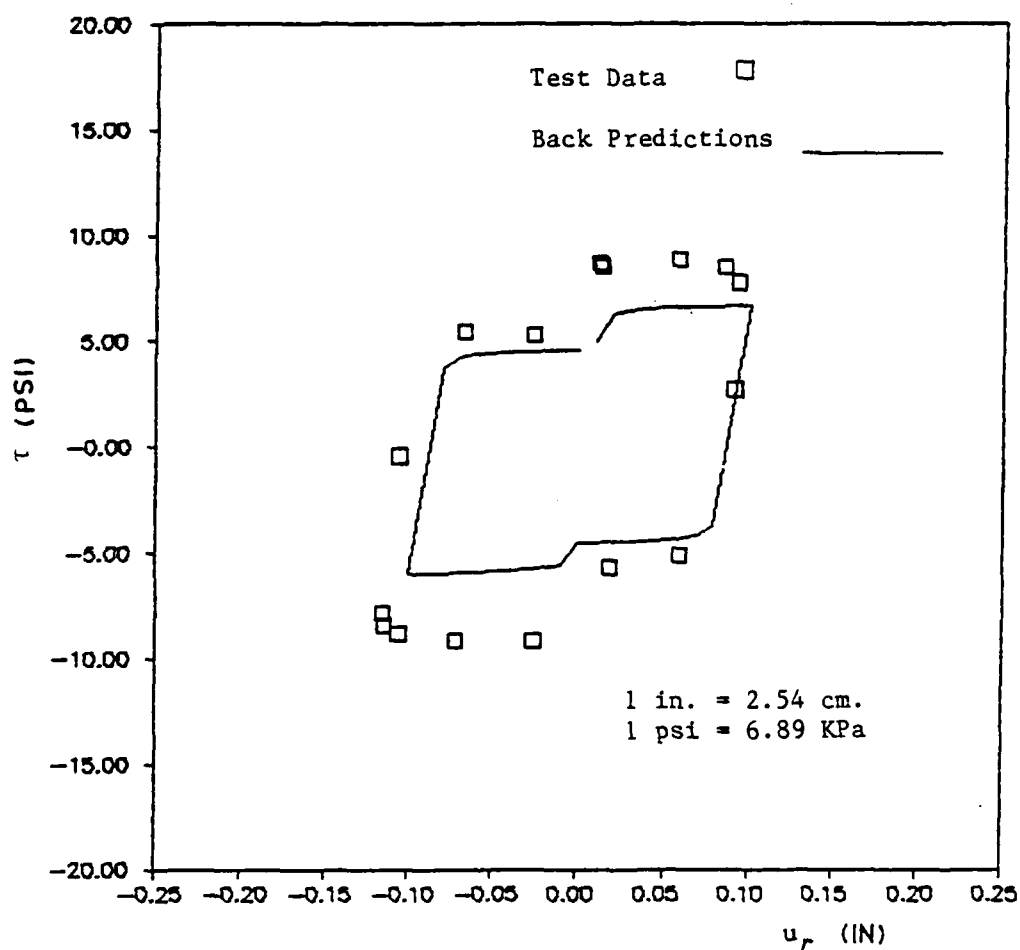


Figure II-35. Test Data and Back Predictions; τ versus u_r ; Cyclic Test; 9° Surface; $\sigma_n = 10$ psi; Cycle 1

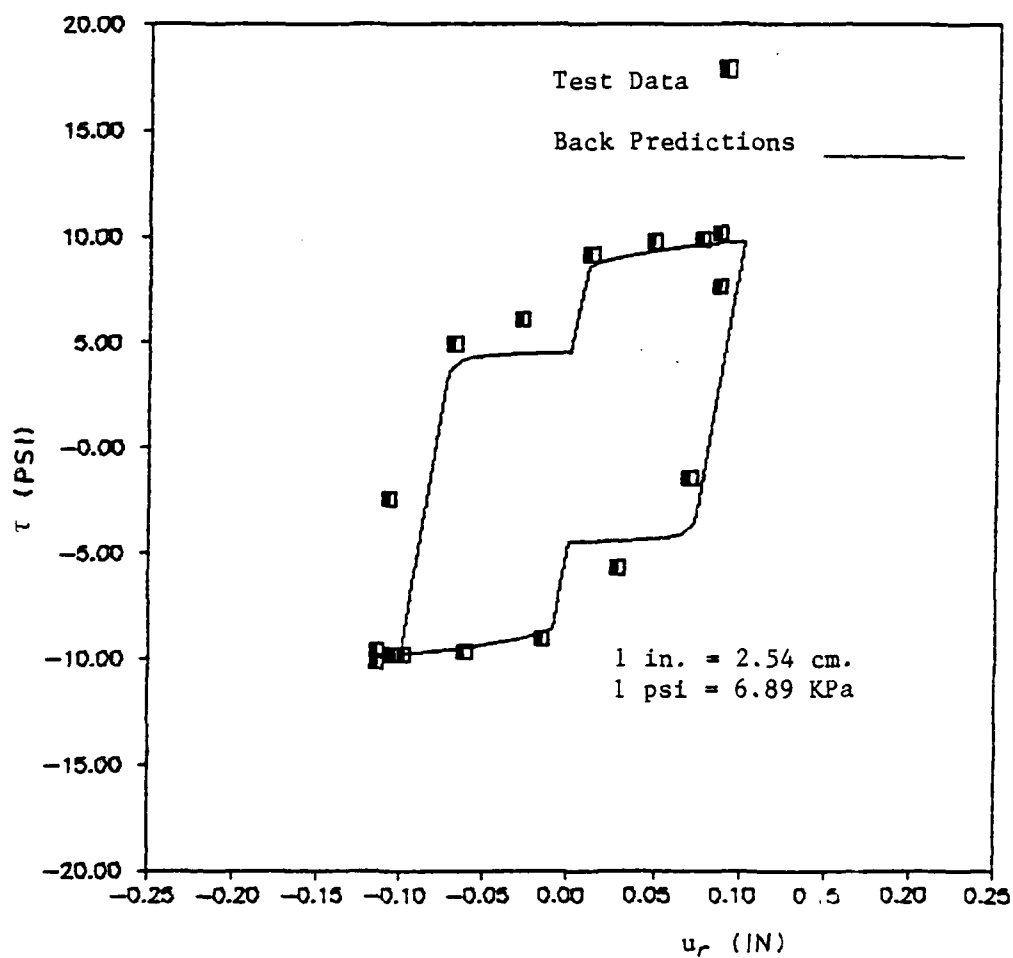


Figure II-36. Test Data and Back Predictions; τ versus u_r ; Cyclic Test; 9° Surface; $\sigma_n = 10$ psi; Cycle 10

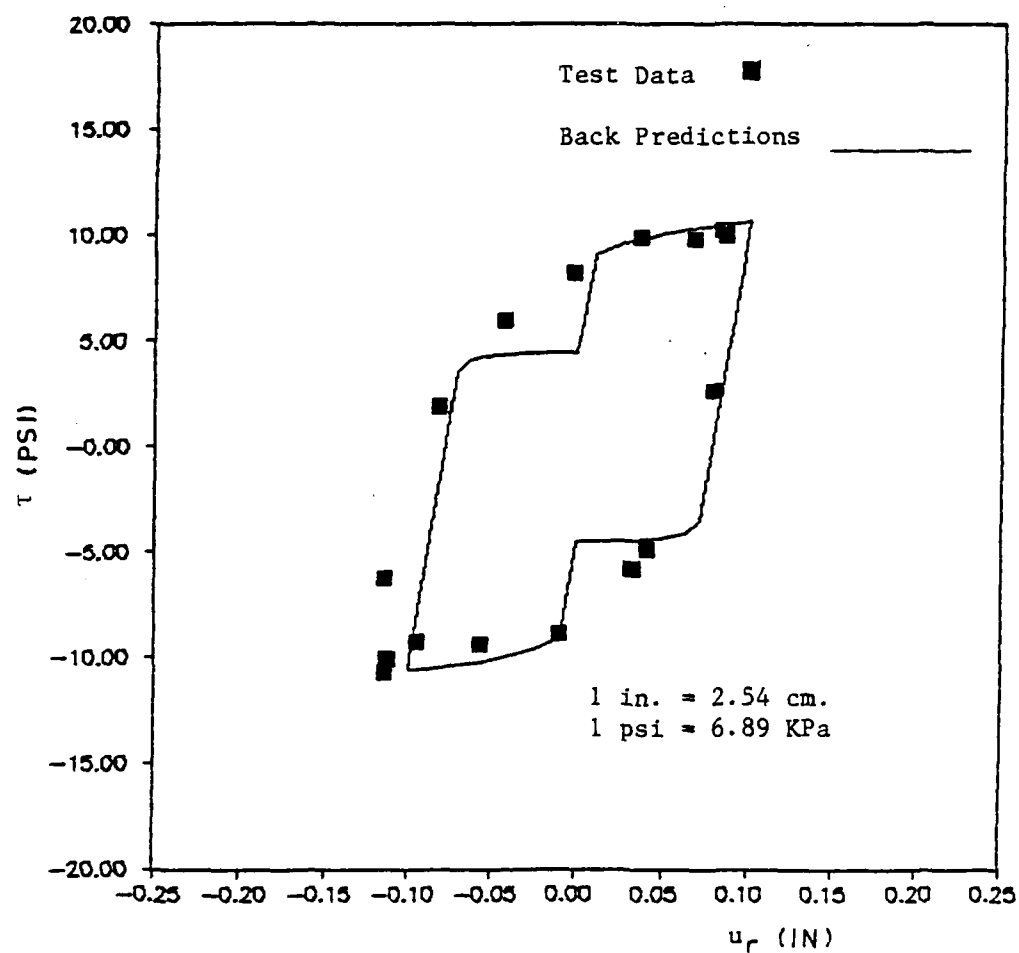


Figure II-37. Test Data and Back Predictions; τ versus u_r ;
Cyclic Test; 9° Surface; $\sigma_n = 10$ psi; Cycle 100

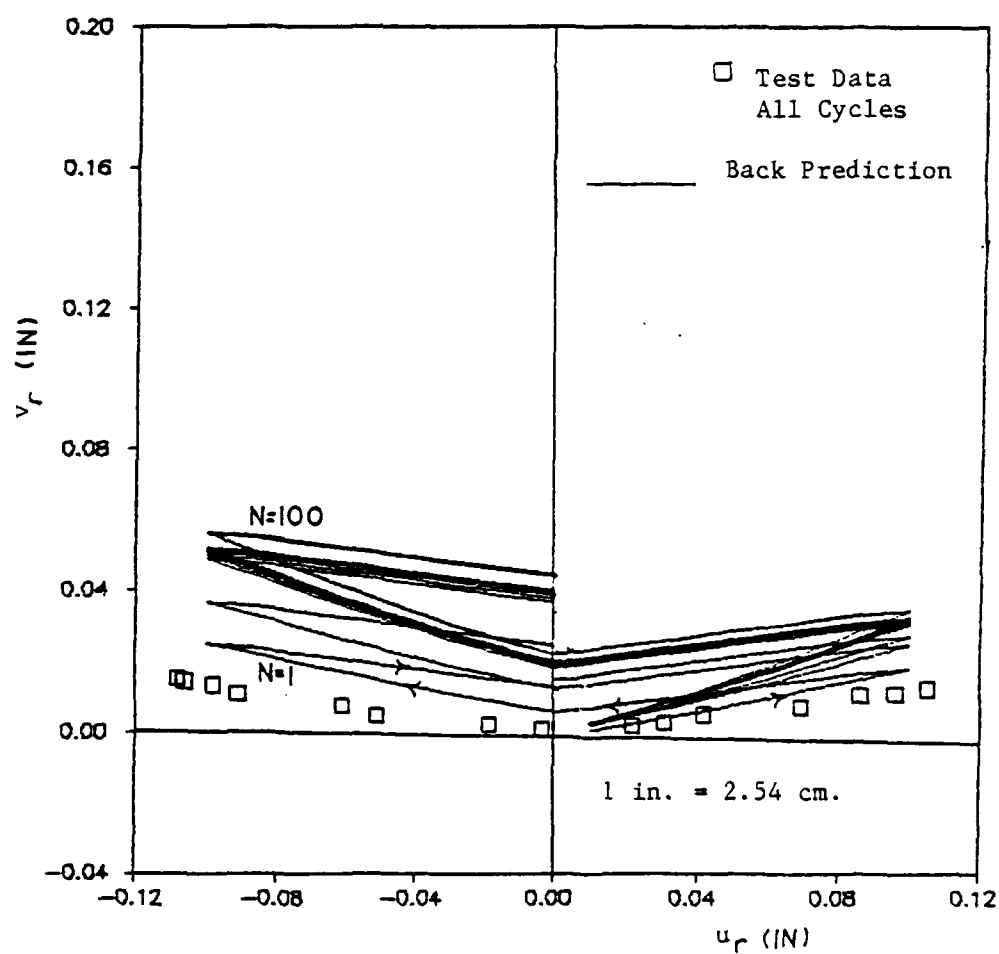


Figure II-38. Test Data and Back Predictions; v_r versus u_r ; Cyclic Test; 9° Surface; $\sigma_n = 5$ psi

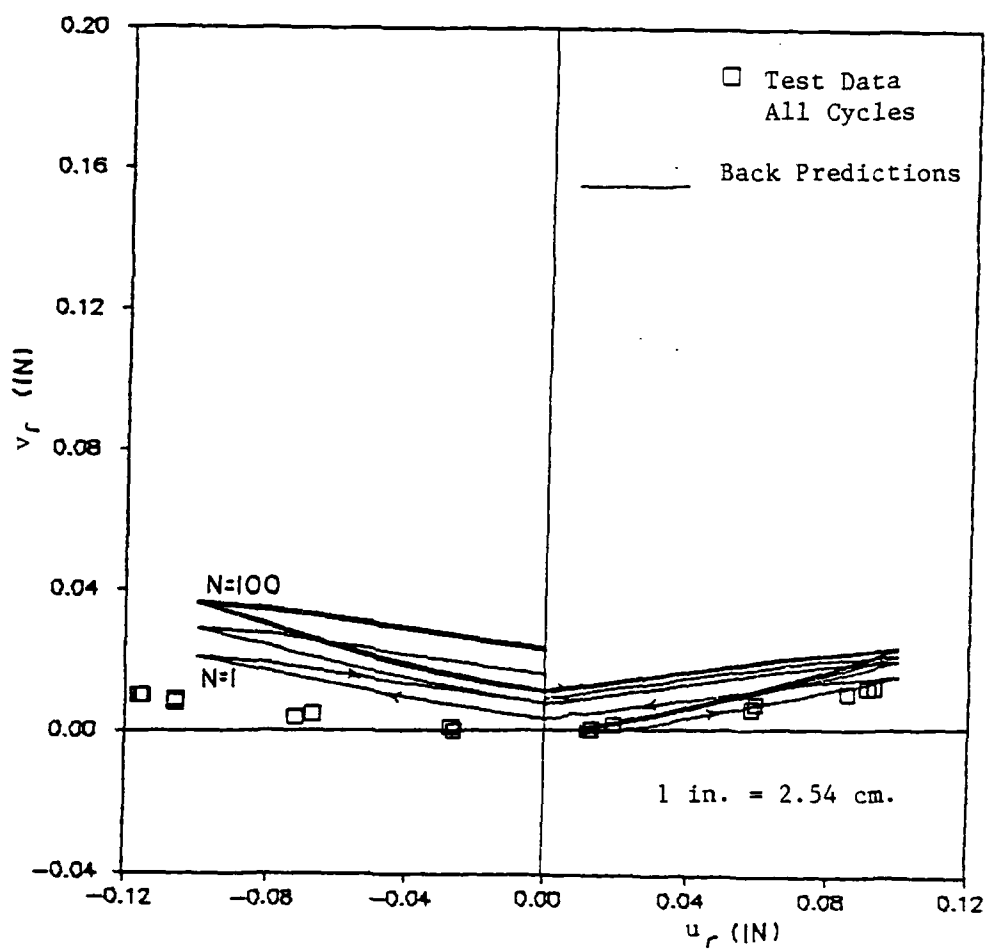


Figure II-39. Test Data and Back Predictions; v_r versus u_r ; Cyclic Test; 9° Surface; $\sigma_n = 10$ psi

APPENDIX III

COMPUTATIONS FOR κ

Equation (7-16) is an expression for determination of κ

$$\kappa = \alpha_Q / \alpha_I (1 - r_v) \quad (7-16)$$

where α_Q given by Eq. (7-18) is

$$\alpha_Q = \left[\left(\frac{du}{dv} \right)_u^p \cdot 2.0 (\tau_u) + 2\gamma\sigma_n \right] / n\sigma_n^{(n-1)} \quad (7-18)$$

Derivation of these expressions can be found in Chapter 7 and all parameters have been previously defined.

Tables III-1 and III-3 show the determination of κ from test data and the parameters used in the calculations. The parameter κ is determined using data from the following:

1. The forward pass of the quasi-static test series (Table III-1).
2. The reverse pass of quasi-static testing with the 9-degree surface (Table III-2).
3. Cyclic testing at different cycles and phases of displacement (Table III-3).

Table III-1. Determination of κ ; Quasi-Static Test Series, Forward Pass

Surface	γ	σ_n (psi)	τ_u (psi)	$\left(\frac{dv}{du}\right)_u^P$	α_Q	α_I	r_v	κ
Flat	0.364	8.10	4.88	0.0	0.1023	0.1279	0.0000	0.7999
5°	0.42	5.0	3.24	-0.077	0.1324	0.1887	0.0593	0.746
	0.42	10.0	6.48	-0.065	0.0956	0.1334	0.0515	0.755
	0.42	20.0	12.96	-0.066	0.0674	0.0943	0.0502	0.753
	0.42	50.0	34.40	-0.076	0.0419	0.0551	0.0551	0.744
7°	0.783	5.0	4.42	-0.080	0.2547	0.3502	0.0872	0.797
	0.783	10.0	8.85	-0.064	0.1839	0.2476	0.0860	0.812
	0.783	20.0	17.69	-0.057	0.1310	0.1751	0.1013	0.832
	0.783	50.0	44.24	-0.077	0.0809	0.1107	0.0946	0.806
9°	0.81	5.0	4.50	-0.110	0.2544	0.3622	0.1022	0.782
	0.81	10.0	9.00	-0.0995	0.1823	0.2561	0.1050	0.795
	0.81	20.0	18.00	-0.090	0.1303	0.1811	0.1208	0.818
	0.81	50.0	45.00	-0.086	0.0839	0.11455	0.1182	0.820

$n = 2.5$ for all tests.

Table III-2. Determination of κ ; Reverse Pass;
9° Surface

Surface	γ	σ_n psi	τ_u psi	$\left(\frac{dv}{du}\right)_u^p$	α_Q	α_I	r_v	κ
9°	0.45	5.0	-3.35	-0.0979	0.1634	0.2012	0.1100	0.91
	0.45	50.0	-33.54	-0.1052	0.0589	0.0636	0.1200	1.05

$$n = 2.5$$

Table III-3. Determination of κ ; Cyclic Test;
 9° Surface; $\sigma_n = 20$ psi

Phase	γ	σ_n psi	τ_u psi	$(\frac{dv}{du})^p_u$	α_Q	α_I	r_v	κ
<u>Cycle 1</u>								
1	0.42	24.0	15.60	-0.221	0.0450	0.0857	0.1126	0.59
2 and 4	0.228	20.0	± 9.54	-0.0507	0.0450	0.0510	0.0904	0.970
3	0.42	24.0	-15.60	0.202	0.047	0.0857	0.1259	0.625
<u>Cycle 100</u>								
1 and 3	1.376	20.75	24.34	-0.309	0.1780	0.3021	0.1453	0.689

$n = 2.5$ for all cycles and phases of displacement

LIST OF REFERENCES

- Amontons, G., "De la resistance caus'ee dans les machines: Memoires de l'Academie Royale, A," (Chez Gerard Kuyper, Amsterdam, 1706), pp. 257-282, 1699.
- Archaud, "Elastic Deformation and the Laws of Friction," Proc. Roy. Soc. London, A 243, pp. 190-205, 1958.
- Barton, N. R., "Review of a New Shear-Strength Criterion for Rock Joints," Engineering Geology, Vol. 7, pp. 287-232, 1973.
- Barton, N. R., "Estimating the Shear Strength of Rock Joints," Proc. 3rd Cong. Int. Soc. Rock Mech., Denver, Vol. 2, Part A, pp. 219-220, 1974.
- Barton, N. and Bandis, S. C., "Rock Joint Model for Analyses of Geologic Discontinua," Proceedings Conference on Constitutive Laws for Engineering Materials: Theory and Application, University of Arizona, Tucson, AZ, January 1987.
- Barton, N. and Choubey, V., "The Shear Strength of Rock Joints in Theory and Practice," Rock Mechanics, Vol. 10, pp. 1-54, 1977.
- Bowden, F. P. and Tabor, D., The Friction and Lubrication of Solids, Oxford University Press, London, 337 pp., 1950.
- Byerlee, J. D., "Frictional Characteristics of Granite Under High Confining Pressure," Journal Geophysical Research, Vol. 72, No. 14, pp. 3639-3648, 1967a.
- Byerlee, J. D., "Theory of Friction Based on Brittle Fracture," J. Appl. Physics, Vol. 38, No. 7, pp. 2928-2934, 1967b.
- Christensen, R. J., Swanson, S. R. and Brown, W., "Torsional Shear Measurement of the Frictional Properties of Westerly Granite," Proc. 3rd Cong. Int. Soc. Rock Mech., Vol. 2, Part A, pp. 221-225, 1974.
- Coulson, J. H., "Shear Strength of Flat Surfaces in Rock," Proc., 13th Symp. on Rock Mech., Urbana, Illinois, Am. Soc. Civ. Eng., N. Y., N. Y., pp. 77-105, 1972.

- Crawford, A. M. and Curran, J. H., "The Influence of Shear Velocity on the Frictional Resistance of Rock Discontinuities," Int. J. Rock Mech. & Min. Sci., Vol. 18, No. 6, pp. 505-515, 1981.
- Desai, C. S., "A Dynamic Multi-Degree-of-Freedom Shear Device," Report No. 8-36, Department of Civil Engineering, Virginia Tech., Blacksburg, VA, 1980a.
- Desai, C. S., "A General Basis for Yield, Failure and Potential Functions in Plasticity," Int. J. Num. Analyt. Meth. in Geomech., Vol. 4, pp. 361-375, 1980b.
- Desai, C. S., "Behavior of Interfaces Between Structural and Geologic Media," A State-of-the-Art Paper, Proc., Int. Conf. on Recent Advances in Geotech. Earthquake Eng. and Soil Dynamics, St. Louis, MO, 1981.
- Desai, C. S., Eitani, I. M. and Haycocks, C., "An Application of Finite Element Procedure for Underground Structures with Nonlinear Materials and Joints," Proc., 5th Int. Eng. Soc. of Rock Mech., Melbourne, April 1983.
- Desai, C. S. and Faruque, M. O., "A Generalized Basis for Modelling Plastic Behavior of Materials," Proc., Int. Conf. Constitutive Laws for Eng. Materials, Tucson, AZ, 1983.
- Desai, C. S. and Faruque, M. O., "Constitutive Model for (Geologic) Materials," J. of Eng. Mech., ASCE, Vol. 110, No. 9, pp. 1391-1408, 1984.
- Desai, C. S., Galagoda, H. M., and Wathugala, G. W., "Hierarchical Modelling for Geologic Materials and Discontinuities," Proc., 2nd Int. Conf. on Const. Laws for Eng. Mat.: Theory and Application, University of Arizona, Tucson, AZ, 1987.
- Desai, C. S., Lightner, J. G. and Sargand, S. M., "Mixed and Hybrid Procedures for Nonlinear Problems in Geomechanics," Proc., 4th Int. Conf. Num. Meth. in Geomech., Edmonton, Canada, 1982.
- Desai, C. S. and Siriwardane, H. J., "A Concept of Correction Functions to Account for Nonassociative Characteristics of Geologic Media," Int. J. Num. Analyt. Meth. in Geomech., Vol. 4, 1980.
- Desai, C. S. and Siriwardane, H. J., Constitutive Laws for Engineering Materials With Emphasis on Geologic Materials, Prentice-Hall, Inc., Englewood Cliffs, NJ, 1984.

- Desai, C. S., Siriwardane, H. J. and Janardhanam, R., "Interaction and Load Transfer Through Track Support Systems, Parts I and 2," U. S. Dept. of Transportation, Washington, D. C., 1983.
- Desai, C. S., Somasundaram, S. and Frantziskonis, G., "A Hierarchical Approach for Constitutive Modelling of Geologic Materials," Int. J. Num. Analyt. Meth. in Geomechanics, Vol. 10, No. 3, 1986.
- Desai, C. S., Zaman, M. M., Lightner, J. G., and Siriwardane, H. J., "Thin-Layer Element for Interfaces and Joints," Int. J. Num. Analyt. Meth. in Geomech., Vol. 8, pp. 19-43, 1984.
- Dieterich, J. H., "Preseismic Fault Slip and Earthquake Prediction," Journal of Geophysical Research, Vol. 83, No. B8, pp. 3940-3947, 1978.
- Dieterich, J. H., "Modeling of Rock Friction, Experimental Results and Constitutive Equations," Journal of Geophysical Research, Vol. 84, No. B5, pp. 2161-2168, 1979a.
- Dieterich, J. H., "Modeling of Rock Friction, Simulation of Preseismic Slip," Journal of Geophysical Research, Vol. 84, No. B5, pp. 2169-2175, 1979b.
- Dieterich, J. H., "Constitutive Properties of Faults with Simulated Gauge," Reprinted from Mechanical Behavior of Crustal Rocks, Geophysical Monograph, 24, pp. 103-119, 1981a.
- Dieterich, J. H., "Potential for Geophysical Experiments in Large Scale Tests," Geophysical Research Letters, Vol. 8, No. 7, pp. 633-636, 1981b.
- Dieterich, J. H. and Okubo, P. G., "Fracture Energy of Stick Slip Events in a Large Scale Biaxial Experiment," Geophysical Research Letters, Vol. 8, No. 8, pp. 887-890, 1981.
- DiMaggio, F. L. and Sandler, I., "Material Model for Granular Soils," J. of the Eng. Mech. Div., ASCE, Vol. 97, No. EM3, pp. 935-950, 1971.
- Divakar, M. P., Fafitis, A., and Shah, S. P., "Constitutive Modeling of Rough Interfaces in Sliding Shear," Proceedings, Conf. on Constitutive Laws for Engineering Materials: Theory and Application, University of Arizona, Tucson, AZ, 1987.
- Drumm, E. C., "Testing, Modelling and Applications of Interface Behavior in Dynamic Soil Structure Interaction," Ph.D. Thesis, Dept. of Civil Eng. & Eng. Mech., University of Arizona, Tucson, AZ, 1983.

- Drumm, E. C. and Desai, C. S. "Testing, Modelling and Applications of Interface Behavior in Dynamic Soil-Structure Interaction," Report, Department of Civil Engineering and Engineering Mechanics, University of Arizona, Tucson, AZ, 1983.
- Faruque, M. O., "Development of a Generalized Constitutive Model and Its Implementation in Soil-Structure Interaction," Ph.D. Dissertation, University of Arizona, Tucson, AZ, 1983.
- Frantziskonis, G. and Desai, C. S., "Constitutive Model with Strain Softening," Int. J. Solids & Structures, Vol. 23, No. 6, pp. 733-750, 1987.
- Frantziskonis, G., Desai, C. S. and Somasundaram, S., "Constitutive Model for Nonassociative Behavior," J. of Eng. Mech. Div., ASCE, Vol. 9, No. 6, 1986.
- Ghaboussi, J. and Wilson, E. L., "Finite Element for Rock Joints and Interfaces," J. of Soil Mech. and Found. Div., ASCE, Vol. 99, No. SM10, pp. 833-848, October 1973.
- Gillette, D. R., "Undrained Behavior of Rock Joints Under Dynamic Loading," M.S. Thesis, University of Colorado, Boulder, CO, 1983.
- Giuseppe, B., "The Shear Strength of Some Rocks by Laboratory Tests," Proc., 2nd Cong. Int. Soc. Rock Mech., Belgrade, Vol. 2, pp. 3-24, 1970.
- Goodman, R. E., "The Mechanical Properties of Joints," Proc., 3rd Cong. Int. Soc. of Rock Mech., Denver, CO, Vol. 1, Part A, pp. 127-140, 1974.
- Goodman, R. E., Methods of Geological Engineering in Discontinuous Rocks, West Publishing Co., St. Paul, MN, 472 pp., 1976.
- Goodman, R. E. and Ohnishi, Y., "Undrained Shear Testing of Jointed Rock," Rock Mechanics, Vol. 5, p. 129, 1973.
- Goodman, R. E., Taylor, R. L. and Brekke, T. L., "A Model for the Mechanics of Jointed Rock," J. of Soil Mech. and Found. Div., ASCE, Vol. 94, No. SM3, pp. 637-659, May 1968.
- Gould, M. C., "Development of High Capacity Dynamic Direct Shear Apparatus and Its Application to Testing Sandstone Rock Joints," M.S. Thesis, University of Colorado, Boulder, CO, 1982.
- Heuze, F. E. and Barbour, T. G., "New Models for Rock Joints and Interfaces," J. of Geotech. Eng. Div., ASCE, Vol. 108, No. GT5, pp. 757-776, May 1982.

- Hoek, E. and Bray, J., "Rock Slope Engineering," J. of Min. and Metallurgy, London, p. 84, 1974.
- Horn, H. M. and Deere, D. U., "Frictional Characteristics of Minerals," Geotechnique, Vol. 12, No. 4, pp. 319-335, 1962.
- Hsu-Jun, K., "Nonlinear Analysis of the Mechanical Properties of Joint and Weak Intercalation in Rock," Proc., 3rd Int. Conf. Num. Meth. Geomech., Aachen, West Germany, pp. 523-532, 1979.
- Jaeger, J. C., "The Frictional Properties of Joints in Rock," Pure Applied Geophysics, Vol. 43, pp. 148-158, 1959.
- Jaeger, J. C., "Friction of Rocks and Stability of Rock Slopes," Geotechnique, Vol. 21, pp. 97-134, 1971.
- Jaeger, J. and Cook, N.G.W., Fundamentals of Rock Mechanics, 2nd Ed., Chapman and Hall Ltd., London, 1976.
- Kane, W. F., "Direct Shear Behavior of Rock Joints in a Granite Gneiss," M.S. Thesis, Department of Civil Engineering, Virginia Tech, Blacksburg, VA, 1981.
- Kane, W. F. and Drumm, E. C., "A Modified 'Cap' Model for Rock Joints," Rock Mechanics: Proceedings of the 28th U. S. Symposium, University of Arizona, Tucson, AZ, 1987.
- Krsmonovic, D. and Popovic, M., "Large Scale Tests of the Shear Strength of Limestone," Proc., 1st Cong. of ISRM, Lisbon, Vol. 1, pp. 773-779, 1967.
- Kulhawy, F. K. and Peterson, M. S., "Behavior of Sand-Concrete Interfaces," Proc., 6th Pan American Conf. on Soil Mech., Found. Eng., 1979.
- Kutter, H. K., "Rotary Shear Testing of Rock Joints," Proc., 3rd Cong. Int. Soc. Rock Mech., Denver, CO, Vol. 2, Part A, pp. 254-262, 1974.
- Lajtain, E. Z., "Unconfined Shear Strength of Discontinuous Rocks," Proc., 2nd Cong. Int. Soc. Rock Mech., Belgrade, Vol. 2, pp. 3-39, 1970.
- Locker, H. G., "Some Results of Direct Shear Tests on Rock Discontinuities," Proc., Int. Symp. on Rock Mech., Madrid, pp. 171-173, 1968.

- Locker, H. G. and Rieder, V. G., "Shear Tests on Layered Jurassic Limestone," Proc., 2nd Cong. Int. Soc. Rock Mech., Belgrade, Vol. 2, pap. 3-1, 1970.
- Martin, G. R. and Miller, P. J., "Joint Strength Characteristics of a Weathered Rock," Proc., 3rd Cong. Int. Soc. Rock Mech., Denver, CO, Vol. 2, Part A, pp. 263-270, 1974.
- Mogilevskaya, S. E., "Effects of Geologic Factors on the Shearing Resistance Along Joints in Rock," Proc., 3rd Cong. Int. Soc. Rock Mech., Denver, CO, Vol. 2, Part A, pp. 276-281, 1974.
- Nagaraj, B. K., "Modelling of Normal and Shear Behavior of Interfaces in Dynamic Soil-Structure Interaction," Ph.D. Dissertation, University of Arizona, Tucson, AZ, 1986.
- Nikitin, A. A., Sapegin, D. C., Uvarov, "Shear Resistance of Rock Along Joint Planes Under Static and Impulse Loads," Proc., 3rd Cong. Int. Soc. Rock Mech., Denver, CO, Vol. 2, Part A, 1974.
- O'Conner, K., Zubelewicz, C. H., Dowding, C. H., Belytschko, T. B. and Plesha, M., "Cavern Response to Earthquake Shaking With and Without Dilation," Rock Mechanics: Key to Energy Production, Proc., 27th U. S. Symp. on Rock Mech., University of Alabama, Tuscaloosa, AL, 1986.
- Pande, G. N., "Numerical Modelling of Rocks: Possibilities and Problems," Proc., 3rd Int. Conf. Num. Meth. Geomech., Aachen, West Germany, April 1979.
- Patton, F. D., "Multiple Modes of Shear Failure in Rock," Proc., 1st Int. Cong. of Rock Mech., Lisbon, Vol. 1, pp. 509-513, 1966.
- Plesha, M. E., "Constitutive Models for Rock Discontinuities With Dilatancy and Surface Degradation," Int. J. Num. and Analyt. Meth. in Geomech., Vol. 11, No. 4, pp. 345-362, 1987.
- Pratt, H. R., Black, A. D. and Brace, W. F., "Friction and Deformation of Jointed Quartz Diorite," Proc., 3rd Cong. Int. Soc. Rock Mech., Denver, CO, Vol. 2, Part A, pp. 306-310, 1974.
- Roberds, W. J. and Einstein, H. H., "Comprehensive Model for Rock Discontinuities," J. of Geotech. Eng. Div., ASCE, Vol. 104, No. GT5, pp. 553-569, May 1978.
- Ross-Brown, D. M. and Walton, G., "A Portable Shear Box for Testing Rock Joints," Rock Mechanics, Vol. 7, pp. 129-153, 1975.

- Salami, M. R., "Multiaxial Behavior and Modelling for Concrete,"
Ph.D. Dissertation, University of Arizona, Tucson, AZ, 1984.
- Schneider, H. J., "Rock Friction--A Laboratory Investigation," Proc.,
3rd Cong. Int. Soc. Rock Mech., Denver, CO, Vol. 2, Part A,
pp. 311-315, 1974.
- Selig, E. T., "A Review of Stress and Strain Measurement in Soil,"
Proceedings of the Symposium on Soil-Structure Interaction,
University of Arizona, Tucson, AZ, September 1964.
- Truesdale, W. B. and Anderson, M. E., "A New Device for Soil Strain
Measurement," Proceedings of the Symposium on Soil-Structure
Interaction, University of Arizona, Tucson, AZ, September 1964.
- Truesdale and Schwab, "Soil Strain Gage Instrumentation," Final Report
for Air Force Weapons Laboratory, New Mexico, June 1965.
- Zaman, M. M. and Desai, C. S., "Influence of Interface Behavior in
Dynamic Soil-Structure Interaction Problems," Report, Dept. of
Civil Eng. and Eng. Mech., University of Arizona, Tucson, AZ,
1982.
- Zienkiewicz, O. C. and Pande, G. N., "Time Dependent Multilaminate Model
of Rocks - A Numerical Study of Deformation and Failure of Rock
Masses," Int. J. for Num. and Analyt. Meth. in Geomech., Vol. 1,
pp. 219-247, 1977.